NNT : 2016SACLS263

THÈSE DE DOCTORAT
DE
L'UNIVERSITÉ PARIS-SACLAY
PRÉPARÉE À
L'UNIVERSITE PARIS-SUD

ÉCOLE DOCTORALE N° 576
Particules, Hadrons, Énergie, Noyau, Instrumentation, Imagerie, Cosmos et Simulation (PHENIICS)

Spécialité de doctorat : Physique des particules

Par

Mme Maria Hoffmann

Recherche d'un boson de Higgs additionnel de plus haute masse via sa désintégration en une paire de bosons de jauge Z avec le détecteur ATLAS au LHC

Thèse présentée et soutenue au CEA Saclay, le 7 Octobre 2016

Composition du Jury :

M.	Patrick	Puzo	Professeur, Centre scientifique d'Orsay	Président
M.	Nikolaos	Konstantinidis	Professeur, University College London	Rapporteur
Mme	Chiara	Mariotti	Professeur (contrat), INFN	Rapporteur
M.	Michael	Duehrssen-Debling	Docteur, CERN	Examinateur
Mme	Chiara	Roda	Professeur, Università di Pisa	Examinatrice
M.	Reisaburo	Tanaka	Chargé de recherche, Centre scientifique d'Orsay	Examinateur
Mme	Rodanthi	Nikolaidou	Ingénieur chercheur, CEA Saclay IRFU/SPP	Directrice de thèse

"*It was the secrets of heaven and earth that I desired to learn; and whether it was the outward substance of things or the inner spirit of nature and the mysterious soul of man that occupied me, still my inquiries were directed to the metaphysical, or in its highest sense, the physical secrets of the world.*"

– Mary Shelley, *Frankenstein*

Thèse préparée à
l'Institut de recherche sur les lois fondamentales de l'Univers
Service de Physique des Particules, Bât. 141
CEA-Saclay
91191 Gif-sur-Yvette CEDEX

Acknowledgements

Conducting research at the frontiers of physics has been a truly humbling experience, and the past years have been tremendously valuable to me.

Above all, I want to express my gratitude to my supervisor, friend and mentor, Rosy. I am sincerely thankful for the multiple opportunities you have given me to work at CERN and thereby letting me realise a long-lasting dream of conducting particle physics research. Thank you for always supporting me and consistently fighting my case, for caring about my well-being and for being indulgent with my rebellious nature. Your technical expertise, human insightfulness and kindness is admirable, and I could not have asked for a better supervisor to get me through my PhD.

Secondly, I want to thank all members of my jury, Chiara Mariotti, Chiara Roda, Michael Duerhssen-Debling, Nikolaos Konstantinidis, Patrick Puzo and Reisaburo Tanaka, for their assistance in turning my original manuscript into a finalised thesis and for ultimately helping me graduate. Also a big thanks to my group leader, Claude Guyot, and all colleagues from the Irfu/SPP group for welcoming me in the lab and hosting me for the past years.

The work presented in this thesis could not have been conducted without my many colleagues. From the ATLAS Higgs working groups I owe thanks to Alessandro, Arthur, Carl, Dimitris, Denys, Haider, Hideki, Joao, Jochen, Kerry, Lailin, Lei, Nan, Nick, Robert, Rosy, Stefan and many more. Furthermore, thanks to Anna and Stathes, without whom the project on compositeness would not have been orchestrated. I would also like to thank Sune and all colleagues from the Tile community who assisted in the characterisation of the MBTS. A special thanks to Eirini Vichou (1964 – 2016) – I will remember you as an exceptional physicist and a role-model to all young female scientists in the community.

Thanks to all CERN friends for being part of the particle physics adventure. Fabian – I hope we frequently will be able to share a bottle of wine in the future. Super girls, Katha and Lydia – thanks for always having my back and for holding a special place in my heart. Vince, Carsten and Stefan – thank you for being faithful companions of the super girl squad. Kate, Rosanna, Suzanne, Terhi, and all remaining members of the CERN Uterus Network Team – thank you for our many dinner parties. Thanks my the Slav Squad, AJ, Christine, Leo, Vito, Thea, and more, for dating advice and tequila. Alessandro – thanks for our many hang-outs on Hearth and lively chats about physics and life in general. Arthur – thanks for sharing ups and down in physics with me, and for teaching me to love (or at least accept!) the way of the French. Thank you, Denys, for our many coffee breaks and interesting discussions. Sophia – thank you for providing political inspiration and for introducing me to the coolest places in Paris. A special shout-out to Remie for taking on the role as my secretary, French interpreter, judicial advisor, accountant, psychologist, bed and breakfast host, cook, religious and cultural eye-opener, fellow cynophile and nail-enthusiast. Thank you Matthias, Martha, and all fellow SPP students for making my stays in Paris enjoyable. Fellow Danes – I am deeply thankful for having had you by my side and for making Geneva feel like home. Sune, a special thanks to you for your company in countless lunch breaks, unlimited supply of coffee and Orangina, and for giving me the opportunity to conduct hardware studies. Thank you Gorm, Chris, Therkel and Ingrid, for bid til bolle, gedesimulator, smeltet ost and ansigtsmaling. Eva, thank you for brightening my days at Casa Vuache.

Finn, Merete, and Johan – thank you for always being there for me, despite the distance. Hass, thank you for always making me laugh and for giving me a future to be excited about.

Contents

Acknowledgements v

1 Introduction 1

2 The Standard Model and Beyond 3

2.1 The Standard Model of Particle Physics . . . 3
2.2 Electroweak Symmetry Breaking . . . 5
2.3 Constraints on the Higgs Boson Mass . . . 6
2.4 The Discovery . . . 9
2.5 Production and Decay . . . 9
2.6 The Narrow Width Approximation and Interference . . . 13
2.7 Shortcomings of the Standard Model . . . 14
2.8 The 2 Higgs Doublet Model . . . 15
2.8.1 Phenomenology . . . 17

3 Experimental Facilities 23

3.1 The Large Hadron Collider . . . 23
3.1.1 Luminosity and Operation . . . 24
3.2 The LHC Experiments . . . 26
3.3 The ATLAS Detector . . . 27
3.4 The Inner Detector . . . 29
3.4.1 Semiconductor Trackers . . . 31
3.4.2 The Transition Radiation Tracker . . . 32
3.4.3 Solenoid Magnet . . . 32
3.5 Calorimeters . . . 32
3.5.1 Liquid Argon Calorimeters . . . 33
3.5.2 Tile Calorimeter . . . 34
3.6 Muon Spectrometer . . . 37

3.6.1 Monitored Drift Tubes . . . 38
3.6.2 Cathode Strip Chambers . . . 39
3.6.3 Thin Gap Chambers . . . 39
3.6.4 Resistive Plate Chambers . . . 40
3.6.5 Run-2 Updates . . . 40
3.6.6 Toroidal Magnets . . . 41
3.7 Trigger and Data Acquisition . . . 41
3.7.1 Minimum Bias Trigger Scintillators . . . 42
3.8 ATLAS Data Processing and Simulation . . . 43

4 Overview of Heavy Higgs Boson Searches 45
4.1 Overview . . . 45
4.2 Author's Contribution . . . 46

5 Search for an Additional, Heavy Higgs Boson in the $H \to ZZ^{(*)} \to 4l$ Decay Channel Using $\sqrt{s} = 8$ TeV Data 47
5.1 Introduction . . . 47
5.2 The $\sqrt{s} = 8$ TeV Data-Set . . . 48
5.3 Event Selection . . . 49
5.3.1 Triggering . . . 50
5.3.2 Object Reconstruction . . . 51
5.3.3 Lepton Pre-Selection . . . 55
5.3.4 Di-lepton Pairing and Quadruplet Selection . . . 56
5.3.5 Double Z Mass Constraint Studies . . . 57
5.3.6 Event Categorisation . . . 61
5.4 Signal Modelling . . . 64
5.4.1 The Narrow Width Approximation . . . 64
5.4.2 Monte Carlo Samples . . . 64
5.4.3 Shape Parametrisation . . . 65
5.4.4 Acceptance and Yield . . . 66
5.5 Background Modelling . . . 70
5.5.1 Irreducible Backgrounds . . . 70
5.5.2 Reducible Backgrounds . . . 74
5.6 Systematic Uncertainties . . . 81
5.6.1 Experimental Uncertainties . . . 81
5.6.2 Theoretical Uncertainties . . . 84

5.7 Statistical Procedures . . . 87
5.7.1 Including Nuisance Parameters . . . 88
5.7.2 The Fitting Model . . . 89
5.7.3 The CL_S Technique . . . 90
5.7.4 Nuisance Parameter Rankings and Pulls . . . 92
5.8 Results . . . 98
5.8.1 Post-fit Yields and Distributions . . . 98
5.8.2 Upper Limits on Heavy Higgs Boson Production Rate . . . 103
5.9 Conclusion and Further Work . . . 103

6 Combination of Heavy Higgs Boson Searches in the $H \to ZZ^{(*)}$ Decay Channels Using $\sqrt{s} = 8$ TeV Data 109

6.1 Introduction . . . 109
6.2 The $H \to ZZ^{(*)} \to 2l2\nu$ Decay Channel . . . 110
6.2.1 Missing Transverse Energy Reconstruction . . . 110
6.2.2 Event Categorisation . . . 111
6.2.3 Backgrounds . . . 112
6.2.4 Statistical Modelling . . . 113
6.3 The $H \to ZZ^{(*)} \to 2l2q$ Decay Channel . . . 115
6.3.1 b-tagging . . . 115
6.3.2 Event Categorisation . . . 115
6.3.3 Backgrounds . . . 116
6.3.4 Statistical Modelling . . . 117
6.4 The $H \to ZZ^{(*)} \to 2\nu2q$ Decay Channel . . . 120
6.4.1 Event Selection and Categorisation . . . 120
6.4.2 Backgrounds . . . 120
6.4.3 Statistical Modelling . . . 122
6.5 Combination . . . 124
6.5.1 Input . . . 125
6.5.2 Correlation Scheme . . . 125
6.6 Nuisance Parameter Rankings and Pulls . . . 130
6.6.1 Nuisance Parameters From the 4l and 2l2ν Decay Channels . . . 141
6.6.2 Nuisance Parameters From the 2l2q and 2ν2q Decay Channels . . . 142
6.7 Results . . . 143
6.7.1 Upper Limits on Heavy Higgs Boson Production Rate . . . 143

6.7.2 2HDM Interpretation . . . 146
6.8 Conclusion . . . 149

7 Search for an Additional, Heavy Higgs Boson in the H→ZZ$^{(*)}$→4l Decay Channel Using √s = 13 TeV Data 151

7.1 Introduction . . . 151
7.2 The √s = 13 TeV Data-Set . . . 152
7.3 Monte Carlo Samples . . . 153
7.4 Analysis Changes Since Run-1 . . . 153
7.4.1 Impact of IBL . . . 154
7.4.2 Muon Reconstruction and Identification . . . 154
7.4.3 Triggers . . . 155
7.4.4 Optimization of Isolation and d_0 Significance . . . 155
7.4.5 Event Categorisation . . . 156
7.4.6 Signal Shape Parametrisation . . . 157
7.4.7 Signal Acceptance . . . 158
7.4.8 Background Modelling . . . 158
7.4.9 Systematic Uncertainties . . . 164
7.4.10 Systematic Rankings . . . 164
7.5 Results . . . 169
7.5.1 Post-fit Yields and Distributions . . . 169
7.5.2 Upper Limits on Heavy Higgs Boson Production Rate . . . 171
7.6 Conclusion and Further Work . . . 174

8 Conclusion of Heavy Higgs Boson Searches 175

8.1 Summary . . . 175
8.1.1 Comparison of Combined Run-1 Results . . . 176
8.1.2 Sensitivity Comparison of the H → ZZ$^{(*)}$ → 4l Searches . . . 177

9 Characterization of Run-2 Minimum Bias Trigger Scintillators 181

9.1 Introduction . . . 181
9.1.1 Objectives . . . 182
9.1.2 Author's Contribution . . . 182
9.2 Run-2 Upgrades of the MBTS . . . 183
9.3 Calibrating the Photomultiplier to One Photoelectron . . . 183
9.4 Cosmic Setup . . . 187

9.5 Measurement Series . . . 187
9.6 Correcting for Light Loss in Connector . . . 188
9.7 Results . . . 190
9.7.1 Fiber Attenuation . . . 191
9.7.2 MBTS Yield . . . 191
9.8 Summary and Implications . . . 194

10 Sommaire de la thése en français **197**
10.1 Introduction . . . 197
10.2 Recherches dans le canal du Higgs se désintégrant en ZZ en quatre leptons, avec les données à 8 TeV . . . 198
10.3 Combinaison des recherches avec les données à 8 TeV . . . 200
10.4 Recherches dans le canal du Higgs se désintégrant en ZZ en quatre leptons, avec les données à 13 TeV . . . 204
10.5 Caractérisation des scintillateurs du déclencheur à biais minimum . . . 205

A Auxiliary Material for the Combination of the four $H \to ZZ^{(*)}$ Searches **207**

B Minimum Bias Trigger Scintillators for ATLAS: Commissioning and Run-2 Initial Operation **211**

C Probing Compositeness with Higgs Boson Decays at the LHC **213**

Bibliography **221**

List of Figures

2.1 Illustration of the Higgs potential in Equation 2.1. 5

2.2 Theoretical limits on the Higgs boson mass imposed by the triviality bound (upper bound) and vacuum stability bound (lower bound), as a function of the cut-off scale Λ. 8

2.3 Summary of electroweak precision measurements obtained at experiments at the LEP, the SLC and the Tevatron. 8

2.4 Exclusion limits imposed as a function of m_h by the LEP and Tevatron experiments. 9

2.5 Results presented by the ATLAS and CMS collaborations in July 2012 in relation to the SM Higgs boson discovery [6, 7]. 10

2.6 Leading-order diagrams for the four dominant Higgs production mechanisms at the LHC. (A): gluon-fusion (ggF). (B): vector boson-fusion (VBF). (C): associated production with a vector boson (VH). (D): associated production with a top-quark pair (ttH). 11

2.7 SM Higgs boson production cross-section broken down by production mechanism at $\sqrt{s} = 8$ TeV (A) and inclusively for $\sqrt{s} = 7$ TeV, $\sqrt{s} = 8$ TeV and $\sqrt{s} = 14$ TeV (B) [36]. 12

2.8 SM Higgs boson branching ratios (A) and total width as a function of m_h (B) [36]. . 12

2.9 Differential cross-sections as a function of the discriminating variable, the four-lepton invariant mass ($m_{4\ell}$), for the $gg \to (h \to) ZZ \to 2e2\mu$ process at parton level, the non-resonant $gg \to ZZ^{(*)}$ continuum and the $gg \to (h \to) ZZ^{(*)}$ process, assuming SM Higgs boson couplings [37]. 13

2.10 A fermion loop contributing to the Higgs mass. 14

2.11 Contours of $\sigma_H \cdot BR(H \to VV)/\sigma_h \cdot BR(h \to VV)$ at $\sqrt{s} = 8$ TeV, shown as a function of $\cos(\beta - \alpha)$ and β for Type-1 (A) and Type-2 (B) 2HDM. 19

2.12 Contours of the ratio between the ggF production cross-section of H (σ_{ggF}) and the sum of the production cross-section for the ggF and VBF mechanisms at $\sqrt{s} = 13$ TeV as function of $\tan(\beta)$ and $\cos(\beta - \alpha)$ for Type-1 and Type-2 2HDM. 20

2.13 Contours of the ratio between the width of H, Γ_H, and its mass as function of $\tan(\beta)$ and $\cos(\beta-\alpha)$ for Type-1 (left) and Type-2 (right) 2HDM at $m_H = 200$ GeV, $m_H = 300$ GeV, and $m_H = 400$ GeV. 21

3.1 Overview of the CERN accelerator complex. 24
3.2 Cross-sections for specific physics processes in pp or $p\bar{p}$ collisions as function of $\sqrt{s}$. 26
3.3 Schematic of the full ATLAS detector 28
3.4 Illustration of the barrel and end-cap regions of the Inner Detector. 30
3.5 Illustration of a track traversing the three detectors in the ID. 30
3.6 Illustration of the ATLAS calorimeters. 35
3.7 Cumulative amount of material in the ATLAS calorimeter components in units of interaction length as a function of η. 35
3.8 lllustration of the accordion-like arrangement of the absorber employed in the EMB and EMEC. 36
3.9 Illustration of a Tile calorimeter wedge and the implementation of the optical read-out. 36
3.10 Illustration of the MS in the $y-z$-plane. 38
3.11 Layout of the CSC chambers. 39
3.12 Schematic of the central solenoid and the three toroidal magnet. 41
3.13 Layout of a Run-1 MBTS disk. 42

5.1 Integrated luminosity versus time delivered by the LHC and recorded by ATLAS, among the distribution of $\langle\mu\rangle$. 49
5.2 he $m_{4\ell}$ distribution in the $2e2\mu$ final-state after having applied the ZMC to either or both di-lepton pairs at two different thresholds of $m_{4\ell} \geq 190$ GeV and $m_{4\ell} \geq 210$ GeV. 60
5.3 The $m_{\ell\ell}$ distribution of the leading (A) and sub-leading (B) di-lepton pair in the $2e2\mu$ final-state for $m_H = 190$ GeV before and after applying the ZMC at a threshold of $m_{4\ell} \geq 190$ GeV. The distribution on generator (truth) level is shown for comparison. All distributions are normalised to unity. 60
5.4 Schematic of the sequential event categorisation employed in this analysis. 61
5.5 Selection efficiency for the ggF (inclusive), VBF and VH event categories as a function of m_H for a Higgs boson originating from the ggF (A), VBF (B) and VH (C) production mechanisms. 63
5.6 Signal shapes obtained with KEYS in the six event categories at $m_H = 300$ GeV, overlaid with the generated MC events. 67

5.7 Signal PDFs ($f_S(x_e)$) presented at select m_H values in the six event categories with the signal originating from the ggF production mechanism. . . . 68
5.8 The signal acceptance in the six event categories segmented according to production mechanism. . . . 69
5.9 Leading-order diagram for the non-resonant process $q\bar{q} \to ZZ^{(*)}$. . . . 70
5.10 Leading-order diagram for the non-resonant process $gg \to ZZ^{(*)}$. . . . 71
5.11 The background shapes obtained with the KEYS procedure for the $q\bar{q} \to ZZ^{(*)}$ process in the six event categories, overlaid with the generated MC events. The cyan band indicates the MC statistical uncertainty. The red lines show the boundaries of the bins used in the adaptive binning procedure. . . . 72
5.12 The background shapes obtained with the KEYS procedure for the $gg \to ZZ^{(*)}$ process in the six different event categories, overlaid with the generated MC events. The cyan band indicates the MC statistical uncertainty. The red lines show the boundaries of the bins used in the adaptive binning procedure. . . . 73
5.13 Examples of lowest-order Feynman diagrams contributing to Z+jets ((A) and (B)) and $t\bar{t}$ production (C). . . . 74
5.14 The observed m_{12} distributions in data and the results of the maximum likelihood fit imposed to the four control regions described in the text. . . . 79
5.15 Fits applied to $n_{hits}^{B-layer}$, the number of hits in the innermost pixel detector layer, and r_{TRT}, the ratio of the number of high-threshold to low-threshold hits in the TRT, for the $2e2\mu$ final-state. . . . 80
5.16 $f_B(x_e)$ for the $\ell\ell\mu\mu$ (A) and $\ell\ell ee$ (B) background in the signal region, overlaid with systematic variations. . . . 80
5.17 Nuisance parameter ranking performed with μ_{ggF}. The ranking was performed at $m_H = 200$ GeV with an Asimov data-set generated with $\mu = 0.1$. . . . 94
5.18 Nuisance parameter ranking performed with μ_{VBF}. The ranking was performed at $m_H = 200$ GeV with an Asimov data-set generated with $\mu = 0.1$. . . . 95
5.19 Nuisance parameter ranking performed with μ_{ggF}. The ranking was performed at $m_H = 900$ GeV with an Asimov data-set generated with $\mu = 0.1$. . . . 96
5.20 Nuisance parameter ranking performed with μ_{VBF}. The ranking was performed at $m_H = 900$ GeV with an Asimov data-set generated with $\mu = 0.1$. . . . 97
5.21 Post-fit $m_{4\ell}$ distributions for all six event categories. . . . 99
5.22 Post-fit $m_{4\ell}$ distributions for the four ggF event categories (inclusively). . . . 99
5.23 Post-fit $m_{4\ell}$ distributions for the ggF event categories. . . . 100
5.24 Post-fit $m_{4\ell}$ distributions for the VBF and VH event categories. . . . 102

5.25 95% CL_S upper limits on $\sigma \times BR(H \to ZZ^{(*)})$ as a function of m_H in the ggF (A) and VBF (B) event categories. . . . 104

6.2 Leading-order diagram of WZ production. . . . 112
6.1 The distribution of m_T obtained in the $H \to ZZ^{(*)} \to 2\ell 2\nu$ decay channel in the ggF event category ((A) and (B)) and the VBF event category ((C) and (D)). . . . 114
6.3 Distribution of the discriminating variables in the four signal regions; $m_{\ell\ell jj}$ ((A), (B) and (D)) and $m_{\ell\ell j}$ ((C)). . . . 119
6.4 The distributions of m_T used in the $H \to ZZ^{(*)} \to 2\nu 2q$ search in the untagged ((A), (C)) and tagged ((B), (D)) event categories for a Higgs boson of $m_H = 400$ GeV ((A), (B)) and $m_H = 900$ GeV ((C), (D)). . . . 121
6.5 Nuisance parameter ranking for the combined fit performed at $m_H = 200$ GeV with Asimov data generated with $\mu_{\text{ggF}} = 0.1$. . . . 131
6.6 Nuisance parameter ranking for the combined fit performed at $m_H = 200$ GeV with Asimov data generated with $\mu_{\text{VBF}} = 0.1$. . . . 132
6.7 Nuisance parameter ranking for the combined fit performed at $m_H = 900$ GeV with Asimov data generated with $\mu_{\text{ggF}} = 0.1$. . . . 133
6.8 Nuisance parameter ranking for the combined fit performed at $m_H = 900$ GeV with Asimov data generated with $\mu_{\text{VBF}} = 0.1$. . . . 134
6.9 Ranking of the 20 most pulled NPs performed with the combined likelihood function on data for $m_H = 200$ GeV. . . . 135
6.10 Ranking of the 20 most constrained NPs performed with the combined likelihood function on data for $m_H = 200$ GeV. . . . 136
6.11 Ranking of the 20 most pulled NPs performed with the combined likelihood function on data for $m_H = 900$ GeV. . . . 137
6.12 Ranking of the 20 most constrained NPs performed with the combined likelihood function on data for $m_H = 900$ GeV. . . . 138
6.13 95% CL_S upper limits on $\sigma \times \text{BR}(H \to ZZ^{(*)})$ as a function of m_H, resulting from the combination of all four searches in the ggF (A) and VBF (B) event categories. . . . 144
6.14 95% CL_S exclusion contours in the 2HDM Type-1 (A) and Type-2 (B) models for $m_H = 200$ GeV, shown as a function of the parameters $\cos(\beta - \alpha)$ and $\tan(\beta)$. . . . 147
6.15 95% CL_S exclusion contours in the 2HDM Type-1 (A) and Type-2 (B) models for $\cos(\beta - \alpha) =$ -0.1 and $\cos(\beta - \alpha) = 0.1$ (C) and (D), shown as a function of m_H and the parameter $\tan(\beta)$. . . . 148

7.1 Integrated luminosity versus time delivered by the LHC and recorded by ATLAS (A) among the distribution of $\langle\mu\rangle$ (B) in LHC Run-2 [141]. 153
7.2 The function in Equation 7.2 (blue curve) fitted to MC samples for the $4e$, 4μ and $2e2\mu$ final-states at $m_H = 200$ GeV and 900 GeV. Both the Crystal Ball (dashed green) and Gaussian components (dashed grey) of the fit are shown. 160
7.3 Examples of signal shapes $f_S(x_e)$ obtained with the analytical parametrisation at select m_H values for the 4μ final-state (A), the $4e$ final-state (B) and the mixed final-states $2\mu2e$+$2e2\mu$ (C). 161
7.4 The signal acceptance as a function of m_H for ggF (A) and VBF (B) production. For each production mechanism, the acceptance of the final-states is determined separately. 161
7.5 The observed m_{12} distributions in data in the three control regions described above. The data is fitted simultaneously in the the inverted d_0 (A) and the $e\mu$+$\mu\mu$ (B) CRs. The dashed lines correspond to the Z+heavy jets and $t\bar{t}$ components of the fit. The fitted Z+heavy jets yield is fixed when fitting the inverted isolation CR (C) to extract the yield of the Z+light jets component. 162
7.6 Fits applied to the number of hits in the B-layers, $n_{hits}^{B-layer}$, (A) and the TRT electron probability, p_{TRT}^{e}, (B) for the $4e$ and $2\mu2e$ final-states. The histograms show the light-flavoured jets mistakenly identified as an electron (f), electrons from photon conversion of from FSR (γ) and electrons from heavy-flavoured quark decays (f). . 163
7.7 Distribution of $m_{4\ell}$ obtained from the irreducible ZZ background for the 4μ (top), $2e2\mu$+$2\mu2e$ (middle) and $4e$ (bottom) final-states. The red line represents the smoothed shape obtained with KEYS. 163
7.8 Nuisance parameter ranking performed with Asimov data generated at $\mu = 0$ at $m_H = 300$ GeV. 166
7.9 Nuisance parameter ranking performed with Asimov data generated at $\mu = 0$ at $m_H = 600$ GeV. 167
7.10 Nuisance parameter ranking performed with Asimov data generated at $\mu = 0$ at $m_H = 900$ GeV. 168
7.11 Post-fit $m_{4\ell}$ distributions broken down according to final-state: $4e$ (A), 4μ (B), $2\mu2e$ (C), $2e2\mu$ (D) and inclusively (E). The hashed band on the MC distributions represent the systematic uncertainty on the expectation. 170
7.12 95% CL_S upper limits on $\sigma \times BR(H \to ZZ^{(*)} \to 4\ell)$ as a function of m_H. 171

9.1 Layout of the Run-1 and Run-2 WLS routing scheme in the inner and outer sector of each MBTS wedge. . . . 183
9.2 The detecting medium from a Run-2 MBTS wedge. . . . 184
9.3 The edges of a scintillating tile from an inner sector – the grooves used to embed the WLS are visible (A). A bundle of 8 WLS mounted onto a read-out connector before installation in the grooves (B). . . . 184
9.4 A Hamamtsu R7877 PMT mounted to a TileCal VD (A). The PMT signal is extracted directly from the VD (B). . . . 185
9.5 The 1PE calibration spectra recorded with Configuration 1 (A) and 2 (B) from Table 9.1. . . . 186
9.6 Cosmic rays impinging the inner sector are selected by positioning the trigger scintillators at the centre of the inner sector (A). The clear fiber connected to the MBTS is routed to the PMT and kept in position with appropriate support structures (B). . . 188
9.7 Illustration of the MBTS connector seen from the front (left). The yellow area represents the area of the MBTS connector, while the grey area represents the area of the light cone at the position of the PMT. Cross-section of the MBTS connector from the side (right). The green line represents the WLS, the yellow area the light being emitted from the WLS, and the grey area the connector material. . . . 189
9.8 The setup used to measure the light loss in the connector consisting of a WLS bundle, an LED, and a pin-diode (A), and a close-up of the WLS bundle facing the pin-diode (B). . . . 190
9.9 Spectra obtained with the inner sector of the MBTS with measurement D (A) and E (B). The orange histogram is the pedestal recorded with a random trigger after each measurement, used to define the baseline of the experimental setup. The black histogram is the data recorded with the MBTS counter. A fit with Equation 9.1 is imposed to the data (blue curve). . . . 192
9.10 The fitted curves from Measurements A – E. The measurements performed with no use of clear fiber have been scaled with the light loss correction factor from Section 9.3. The x-axis is displayed in units of photoelectrons. The pedestal from all measurements has been centred around 0. . . . 192
9.11 The upper and lower boundary on the light yield obtained from Measurement D and E in Table 9.4. The obtained attenuation lengths are 2.49 ± 0.65 m (blue) and 2.85 ± 0.84 m (red). . . . 193

9.12 Relative timing of the rising edge of the 50 ns trigger signal from the different Minimum Bias Trigger Scintillator (MBTS) counters in units of 25 ns Bunch Crossing (BC) with respect to the bunch crossing position where beams were colliding in ATLAS. 195

10.1 Limites sur $\sigma \times BR(H \rightarrow ZZ^{(*)})$ pour un CL de 95% en fonction de m_H dans les catégories (A) ggF et (B) VBF. La courbe noire et les points indiquent les limites observées. La ligne pointillée noire représente les limites prédites, alors que les bandes verte et jaune symbolisent les déviations à 1σ et 2σ sur la limite attendue. 199

10.2 Limites supérieures sur $\sigma \times \mathrm{BR}(H \rightarrow ZZ)$ en utilisant la méthode des $\mathrm{CL_S}$, en fonction de m_H, obtenues par combinaison des quatre recherches dans les catégories (A) ggF et (B) VBF. La courbe noire et les points indiquent la limite observée. La courbe noire en pointillés représente la limite attendue, tandis que les bandes verte et jaune matérialisent les incertitudes à 1σ et 2σ sur la limite attendue. Les courbes colorées en pointillés symbolisent les limites obtenues pour les différentes recherches individuelles. 201

10.3 Contours d'exclusion dans les 2HDM de (A) Type-1 et (B) Type-2 pour $m_H = 200$ GeV, dans les espaces de paramètres $\cos(\beta-\alpha)$ et $\tan(\beta)$. Les aires rouges hachurées montrent les limites d'exclusion obersvées, avec les bords soulignés par les courbes rouges. La courbe bleue en pointillés représente le contour d'exclusion attendu, et les bandes verte et jaune les incertitudes à 1σ et 2σ sur la valeur attendue. L'échelle de l'axe vertical est choisie de telle sorte que des régions pour lesquelles les couplages du boson de Higgs lèger sont trois fois plus grand que ceux du Modèle Standard, sont exclues. 202

10.4 Contours d'exclusion dans 2HDM de (A) Type-1 et (B) Type-2 pour (C) $\cos(\beta - \alpha) =$ -0.1 et (D) $\cos(\beta - \alpha) = 0.1$, en fonction de m_H et de $\tan(\beta)$. L' aire rouge hachurée montre la région d'exclusion observée. La courbe bleue représente le contour d'exclusion attendu et les bandes verte et jaune symbolisent les incertitudes à 1σ et 2σ sur ce contour. L'aire grise masque les régions pour lesquelles la largeur du boson est supérieure à 0.5% de m_H. 203

10.5 Limites supérieures à 95% $\mathrm{CL_S}$ sur le produit $\sigma \times BR(H \rightarrow ZZ^{(*)} \rightarrow 4\ell)$ en fonction de m_H. La courbe noire et les points présentent les limites observées. La courbe noire en pointillés indique la limite attendue et les bandes verte et jaune montrent les déviations à 1σ et 2σ sur la prédiction. 204

A.1 The distributions of $m_{\ell\ell jj}$ or $m_{\ell\ell j}$ in the Z+jets control region of the $H \to ZZ^{(*)} \to 2\ell 2q$ search. 208
A.2 The distribution of the MV1c b-tagging event categories, based on the two signal jets, in the Z+jets control region in the untagged ggF (A) and tagged ggF (B) channels of the $H \to ZZ^{(*)} \to 2\ell 2q$ search. 209
A.3 The distribution of the MV1c b-tagging event categories, based on the two signal jets, in the $W^{\pm}$+jets 0-b-tag (A) and 1-b-tag (B) control regions of the $H \to ZZ^{(*)} \to 2\nu 2q$ search. 209

List of Tables

2.1 Properties of the quarks [5]. . . . 4
2.2 Properties of the leptons [5]. . . . 4
2.3 Properties of the gauge bosons [5]. . . . 4
2.4 Overview of couplings in the four most common types of 2HDM models. κ_u, κ_d and κ_ℓ denote the coupling to up-type quarks, down-type quarks and leptons, respectively [45]. . . . 16

3.1 Performance requirements of the ATLAS detector systems 28
3.2 Precision of the Inner Detector trackers. . . . 29
3.3 An overview of the ATLAS calorimeter components. . . . 33
3.4 Overview of the specifications of the ATLAS Muon Spectrometer. . . . 37

5.1 Percentage of data recorded during Run-1 by the ATLAS detector systems that is classified as suitable for physics analysis. . . . 49
5.2 Summary of the Run-1 triggers used in the $H \to ZZ \to 4\ell$ analysis using $\sqrt{s} = 8$ TeV data. . . . 51
5.3 The discriminating variables used in the LH electron identification approach for the LOOSE working point. . . . 53
5.4 Summary of the lepton pre-selection requirements. . . . 58
5.5 Summary of the requirements imposed in the di-lepton pairing and quadruplet selection. . . . 58
5.6 Transfer factors for the $Z + b\bar{b}$, Z+light jets and $t\bar{t}$ background components. . . . 76
5.7 Probability for the three $\ell\ell ee$ background components to pass the nominal event selection in the $4e$ and $2\mu 2e$ final-states. These three components originate from light-flavoured quarks faking an electron (f), photon conversion and FSR contribution (γ), and the semi-leptonic decays of heavy-flavoured quarks (q). The quoted errors include systematic uncertainties and the statistical uncertainty arising from the MC estimation. . . . 77

5.8 Experimental systematic uncertainties on the signal yield per event category at $m_H = 400$ GeV. Only uncertainties resulting in a variation of at least 0.5% for at least one m_H value are shown. The combined uncertainty for the four ggF event categories, folded in quadrature, is 6.81%. 81
5.9 Uncertainties on the acceptance of the signal arising from variations in the underlying theoretical parameters used in the generation of the signal samples. 86
5.10 Uncertainties on the backgrounds arising from variations in the underlying theoretical parameters used in the generation of the signal samples. 87
5.11 Expected and observed background yields pre- and post-fit. 101
5.12 Expected and observed limits on $\sigma \times BR(H \to ZZ^{(*)})$ obtained in the ggF event category 105
5.13 Expected and observed limits on $\sigma \times BR(H \to ZZ^{(*)})$ obtained in the ggF event category 106
5.14 Expected and observed limits on $\sigma \times BR(H \to ZZ^{(*)})$ obtained in the VBF event category 107
5.15 Expected and observed limits on $\sigma \times BR(H \to ZZ^{(*)})$ obtained in the VBF event category 108

6.1 Branching ratios for a SM Higgs boson in the four decay modes considered in this combination at selected m_h values. In this table $\ell = e, \mu$, $\nu = \nu_e, \nu_\mu, \nu_\tau$ and $q = u, d, c, s, b$ [36]. 110
6.2 Expected background yields and observed number of events in data after the full selection of the ggF and VBF event categories of the $H \to ZZ^{(*)} \to 2\ell 2\nu$ search. The first and second uncertainty corresponds to the statistical and systematic component, respectively. 113
6.3 Number of events observed in data compared to the fitted background predictions for the $H \to ZZ^{(*)} \to 2\ell 2q$ search in the untagged, tagged, and merged-jet ggF event categories, along with the VBF event category. 118
6.4 Summary of the signal- and control-regions among the discriminants entering the likelihood fit in the $2\ell 2q$ decay channel in the signal region (SR) and control regions (CR). 118
6.5 Number of observed events in data compared to the fitted background predictions for the $H \to ZZ^{(*)} \to 2\nu 2q$ search in the untagged and tagged ggF event categories for the $m_H = 400$ GeV and $m_H = 900$ GeV selection. 122

6.6 Summary of the regions and input distributions entering the likelihood fit in the $2\nu 2q$ channel. . . . 123
6.7 Summary of the distributions entering the likelihood fit for each event category of the four searches.The control regions shared between the $2\ell 2q$ and $2\nu 2q$ decay channels are marked with grey. . . . 124
6.8 Overview of the input to the combination from the four decay channels as a function of m_H. The m_H spacing specifies the distance between the m_H values where input is available. . . . 125
6.9 Correlation of nuisance parameters between the four channels. . . . 127
6.10 Percentage change in the ggF limits when correlating JES systematics between all channels. An increment indicates that the limit decreased in value. . . . 128
6.11 Percentage change in the VBF limits when correlating JES systematics between all channels. An increment indicates that the limit decreased in value. . . . 129
6.12 Overview of the nuisance parameters appearing in Figure 6.5 to Figure 6.12 listed in alphabetical order. The symbol "×" signifies which decay channel(s) the NP is affiliated to. A subset of the NPs appearing in Table 6.9 have been assigned a new name in the combination. When an NP appears more than once for more than one decay channel, the reason is that the NP was not combined between the respective channels, which could be due to the NP being pruned of the channel not contributing at the respective m_H point. . . . 139
6.13 Expected and observed limits on $\sigma \times BR(H \to ZZ^{(*)})$ obtained in the ggF event category (left) and the VBF event category (right). . . . 145

7.1 Percentage of data recorded during Run-2 by the ATLAS detector systems that is signified as suitable for physics analysis. . . . 153
7.2 Summary of the triggers used during the 2015 data-taking for $4e$, 4μ and mixed final-state, $2e2\mu$. When multiple chains are indicated a logical OR is requested among them. The naming convention follows that of Chapter 5. . . . 155
7.3 Summary of the effects of the experimental systematic uncertainties on the signal yield and on the peak position, expressed in %, on the 4μ, $4e$ and $2\mu 2e$ final-states. `MUON_MS`, `MUON_MS_RES_ID` and `MUON_MS_RES_MS` denote the muon momentum scale uncertainty and the momentum resolution uncertainty in the ID and MS, respectively. `EG_SCALE` and `EG_RESOLUTION` denote the uncertainty on the electron energy scale and on the electron energy resolution, respectively. . . . 165

7.4 Expected and observed events yields for the four-lepton final-states obtained in this search over the full considered mass range. The expected yields are shown post-fit for an integrated luminosity of 3.2 fb^{-1} at $\sqrt{s} = 13$ TeV. 169
7.5 Expected and observed limits on $\sigma \times BR(H \to ZZ^{(*)} \to 4\ell)$ in fb. 172
7.6 Expected and observed limits on $\sigma \times BR(H \to ZZ^{(*)} \to 4\ell)$ in fb. 173

8.1 Obtained number of signal (S) and background (B) events at $\sqrt{s} = 8$ TeV at select m_H values. S is calculated from the SM Higgs boson production cross-section obtained from the LHC Higgs Cross-Section Working Group [36], multiplied with the signal acceptance obtained in Chapter 5. B is calculated from the simulation of the $q\bar{q} \to ZZ^{(*)}$ and $gg \to ZZ^{(*)}$ backgrounds in Chapter 5 in a window around the signal of $m_H \pm 50$ GeV. 178
8.2 Obtained number of signal (S) and background (B) events at $\sqrt{s} = 13$ TeV at select m_H values. S is calculated from the SM Higgs boson production cross-section obtained from the LHC Higgs Cross-Section Working Group [36], multiplied with the signal acceptance obtained in Chapter 7. B is calculated from the simulation of the $q\bar{q} \to ZZ^{(*)}$ and $gg \to ZZ^{(*)}$ backgrounds in Chapter 7 in a window around the signal of $m_H \pm 50$ GeV. 179
8.3 S/B ratio per fb^{-1} at $\sqrt{s} = 13$ TeV divided by the corresponding quantity obtained at $\sqrt{s} = 8$ TeV. 179

9.1 Configurations of PMT and VD used for the measurements presented in this chapter. 185
9.2 Parameters of Equation 9.1. 186
9.3 Parameters obtained from fitting the calibration spectra in Figure 9.5. The quoted errors originate from the fit. 187
9.4 Results obtained from the different measurements with the MBTS counter. The value μ denotes the average number of photoelectrons. The measurements performed with no use of clear fiber have been scaled with the light loss correction factor from Section 9.6. 190

10.1 Résultats des mesures avec le compteur MBTS. Le rendement lumineux est mesuré en unités de nombre de photoélectrons. 206

Til Finn og Merete

CHAPTER 1

Introduction

Elementary particle physics is the scientific discipline dedicated to the study of the smallest constituents of matter and their interactions. Modern day particle physics relies on the Standard Model (SM), an enormously successful theory that for the past 50 years has accurately predicted the existence of a broad spectrum of elementary particles and their fundamental properties. Currently, the state-of-the-art facility for conducting particle physics research at the energy frontier is the Large Hadron Collider (LHC) and its associated experiments, situated at the European Organisation for Nuclear Research (CERN). At these facilities, the discovery of a new boson was announced on July 4th 2012 by the ATLAS and CMS collaborations. Following this, a great amount of work was put into verifying the compatibility of this new particle with the Higgs boson appearing in the SM.

The work presented in this thesis was initiated in Fall 2013, one year after the discovery. Upon this, a new question had become relevant; is the newly found Higgs boson one of its kind, or part of larger, extended Higgs sector? Several theories predict physics beyond the SM (BSM), which may include additional Higgs bosons. An example of such a theory is the 2 Higgs Doublet Model (2HDM), which is a simple extension of the SM containing five Higgs bosons. The scope of this thesis is to search for an additional Higgs boson, H, using the $H \to ZZ^{(*)}$ decay channels and proton-proton collision data from the LHC recorded with the ATLAS detector. The Higgs boson of interest is assumed to be CP-even, have no electric charge and to be heavier than the particle discovered in 2012. Although such a Higgs boson would be compatible with the predictions from 2HDM, the search is made as general as possible in order to be sensitive to a wide range of signals.

As introduction and motivation for the heavy Higgs boson searches, a brief review of the underlying theory is given in Chapter 2. The aim of this chapter is to give an overview of the origin of the Higgs boson as described by the SM, as well as its phenomenological behaviour at the LHC. Afterwards, the heavy, CP-even Higgs boson appearing in 2HDM is described. Following this,

Chapter 3 gives an overview of the experimental facilities upon which this thesis is based on, including a description of the functionality and operation of the LHC and a review of the ATLAS experiment.

The search for an additional, heavy Higgs boson is presented in Chapter 4 to Chapter 8. These chapters contain three analyses, which rely on one or more of the $H \to ZZ^{(*)}$ decay channels and two different LHC data-sets. Chapter 5 describes the search for a heavy Higgs boson in the $H \to ZZ^{(*)} \to 4\ell$ decay channel using a data-set of 20.3 fb^{-1} recorded at $\sqrt{s} = 8$ TeV. In the following chapter, Chapter 6, the search in the $H \to ZZ^{(*)} \to 4\ell$ decay channel is combined with corresponding searches conducted in the three additional $H \to ZZ^{(*)}$ decay channels, $ZZ^{(*)} \to 2\ell 2\nu$, $2\ell 2q$ and $2\nu 2q$, performed with the same data-set. Lastly, in Chapter 7 the search is performed once more in the $H \to ZZ^{(*)} \to 4\ell$ decay channel, but this time using a data-set of 3.2 fb^{-1} recorded at $\sqrt{s} = 13$ TeV. Chapter 8 concludes the three analyses.

In addition to the Higgs boson searches described above, a project of more technical character was conducted as part of this thesis. As will be described in Chapter 3, the ATLAS detector employs a set of scintillation detectors for triggering with minimal bias in the forward region, the Minimum Bias Trigger Scintillators (MBTS). Due to material degradation caused by radiation damage in the early phases of LHC operation, the MBTS had to be replaced during the LHC shutdown taking place in 2014. Before installation in ATLAS, these detectors were characterised in appropriate laboratory facilities using cosmic radiation. This effort is documented in Chapter 9.

In addition to the studies mentioned above, the work conducted during this thesis included a study of the feasibility of probing compositeness, another viable BSM theory, with Higgs boson decays. This study is documented in Appendix C.

CHAPTER 2

The Standard Model and Beyond

2.1 The Standard Model of Particle Physics

The Standard Model (SM) of particle physics describes a panorama of elementary particles, their fundamental properties, as well as their interaction via three of the four known fundamental forces; the electromagnetic, the weak and the strong force, the latter two unifying into the electroweak (EW) force at sufficiently large energy scales. The SM is a locally gauge invariant theory of the form $SU_C(3)\times SU_L(2)\times U_Y(1)$. In this notation C refers to the colour charge of the strong force, Y refers to the weak hypercharge, while L refers to the fact that only left-handed fermions interact in the weak force. The strong interaction, also known as quantum chromo dynamics (QCD), transforms according to the group $SU_C(3)$, while the electroweak interaction obeys invariance under $SU_L(2)\times U_Y(1)$ transformations [1, 2, 3, 4].

According to the SM, the visible matter surrounding us is constituted by fermions, i.e. particles carrying spin-1/2[1]. Two types of fermions are distinguished: quarks and leptons, the properties of which are discussed in Table 2.1 and Table 2.2. The SM describes six quarks, up (u), down (d), strange (s), charm (c), beauty (b) and top (t), and six leptons, the electron (e), the muon (μ), the tau (τ) and three neutrinos (ν_e, ν_μ, ν_τ), among their corresponding anti-particles. As indicated in Table 2.1 and Table 2.2, both quarks and leptons are segmented into three generations, which are characterised by vastly different masses spanning over 5 orders of magnitude. The three forces that are described by the SM are mediated by the spin-1 gauge bosons. The massless photon (γ) mediates the electromagnetic force, the W^+, W^- and Z bosons, collectively known as the vector bosons (V) mediate the weak interactions, while the massless gluons (g) mediate the strong force. The properties of the gauge bosons are summarised in Table 2.3.

[1] Throughout this thesis, natural units are used, i.e. $\hbar = c = 1$. In this notation, spin is a dimensionless quantity and mass is measured in electron volts (eV).

Despite the unparalleled success and marvellous predictive power of the SM, it fails to explain an essential and obvious fact of nature: the W and Z bosons have mass. When adding mass-terms for the electroweak gauge bosons to the quantum field theoretical formulation of the SM, the local gauge symmetry of the $SU_L(2)\times U_Y(1)$ group is broken. The riddle of the origin of the gauge boson masses remained unanswered until the year 2012, where the two LHC experiments ATLAS and CMS announced the discovery of the Higgs boson [6, 7]. As will be explained below, this discovery verified the existence of the Higgs mechanism, which allows for the gauge bosons

TABLE 2.1: Properties of the quarks [5].

Quark properties			
Generation	Flavour	Electric charge [e]	Mass [MeV]
I	u	+2/3	2.3
	d	-1/3	4.8
II	c	+2/3	1275
	s	-1/3	95
III	t	+2/3	173.21×10^3
	b	-1/3	4.18×10^3

TABLE 2.2: Properties of the leptons [5].

Lepton properties			
Generation	Flavour	Electric charge [e]	Mass [MeV]
I	e	-1	0.511
	ν_e	0	$<2 \times 10^{-3}$
II	μ	-1	105.66
	ν_μ	0	$<2 \times 10^{-3}$
III	τ	-1	1776.82
	ν_τ	0	$<2 \times 10^{-3}$

TABLE 2.3: Properties of the gauge bosons [5].

Gauge boson properties			
Boson	Electric charge [e]	Mass [GeV]	Interaction
g	0	0	strong
γ	0	0	electromagnetic
$W^\pm$	± 1	80.385	weak
Z	0	91.188	weak

to obtain mass without breaking the gauge symmetry of the $SU_L(2)\times U_Y(1)$ group.

2.2 Electroweak Symmetry Breaking

A mechanism explaining the gauge boson masses was delivered in the 1960s more or less simultaneously by three independent research groups composed of P. Higgs, R. Brout, F. Englert, G.S. Guralnik, C. R. Hagen and T. W. B. Kibble [8, 9, 10, 11, 12]. In modern day physics, the proposed mechanism is popularly known as the Higgs mechanism. As mentioned above, the Higgs mechanism proposes spontaneous symmetry breaking as a mean to introduce mass to the $W^{\pm}$ and Z bosons without breaking the local gauge invariance of the $SU_L(2)\times U_Y(1)$ group.

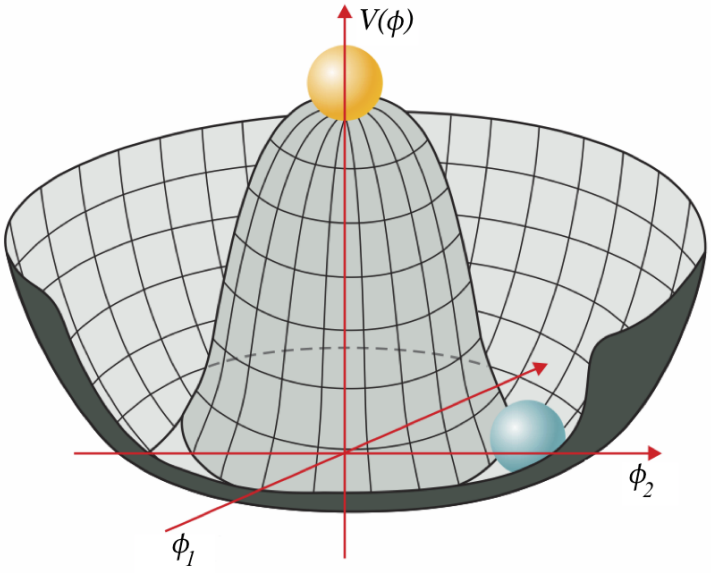

Figure 2.1: Illustration of the Higgs potential in Equation 2.1.

The principle behind spontaneous symmetry breaking can be understood from the illustration in Figure 2.1. In the Higgs mechanism, the complex scalar field ϕ, also known as the Higgs field, is introduced. This field contains two components and therefore has the form of $\phi = \phi_1 + i\phi_2$. Figure 2.1 shows a potential, the so-called Higgs potential, for the field ϕ of the form:

$$V(\phi_1^2 + \phi_2^2) = \frac{1}{4}\lambda^2(\phi_1^2 + \phi_2^2)^2 - \frac{1}{2}\mu^2(\phi_1^2 + \phi_2^2), \quad \mu^2 < 0, \quad \lambda^2 > 0. \tag{2.1}$$

In this equation μ is a mass-term and λ an undetermined, free parameter known as the quartic self-coupling. The ground state, i.e. the value of the field that minimises the potential, is known as

the vacuum expectation value (v). If the ground state of the potential in Equation 2.1 is located at the center of the potential, i.e. at $(\phi_1, \phi_2) = 0$, rotational symmetry would be present. However, as seen from Figure 2.1 this is not the case – the minimum is continuous and follows the ring around the bottom of the potential. Thus, the symmetry of the potential would be spontaneously broken if one of the infinite number of degenerate ground states is chosen. In the Higgs mechanism, the spontaneous symmetry breaking leads to the Higgs potential acquiring a vacuum expectation value of 246 GeV, which defines the electroweak scale [13, 14].

Goldstone's theorem [15] states that the spontaneous breaking of a continuous, global symmetry is accompanied by the appearance of a massless scalar, a so-called Goldstone boson. By spontaneously breaking the symmetry of the Higgs field, a total of four Goldstone bosons appear. In the SM, three of these add a third, longitudinal polarisation state to the gauge fields W_μ and B_μ, which corresponds to giving mass to the W and Z bosons, while the fourth Goldstone boson manifests as a Higgs boson. This Higgs boson is electrically neutral, has spin-0 (meaning that it is a scalar), is CP-even, and will in the following be referred to as the SM Higgs boson. After spontaneous symmetry breaking, in addition to providing mass to the gauge bosons, the Higgs field gives mass to the fermions through their mutual couplings, the so-called Yukawa couplings [16].

2.3 Constraints on the Higgs Boson Mass

In the SM, the mass of the Higgs boson, m_h, is specified by:

$$m_h = \sqrt{2\lambda v^2}. \tag{2.2}$$

Since λ is a free parameter in the SM, m_h is not predicted from theory. However, prior to the Higgs boson discovery in 2012, constraints on m_h were imposed from theoretical arguments and observations from experiments at the Stanford Linear Collider (SLC) [17] at SLAC, the Large Electron-Positron Collider (LEP) [18] at CERN and at the Tevatron [19] at Fermilab. The following constraints had been obtained:

- **Theoretical constraints** on m_h were derived from assumptions on the energy range in which the SM is valid before perturbation theory breaks down and new phenomena emerge. One constraint can be obtained by requiring that the scattering of W bosons obeys unitarity. Without the existence of a Higgs boson of $m_h < 870$ GeV acting as a propagator in these processes (or the existence of new physics at a similar scale), the cross-section diverges at a high center-of-mass-energy. Another theoretical constraint

arises from the triviality bound. Since the quartic Higgs self-coupling is expected to increase with the energy scale of a given process, a cut-off scale, Λ, must be defined, where new physics is expected to appear. If the validity of the SM extends up to 10^{16} GeV, masses above $m_h = 200$ GeV are not permitted. However, if restricted to the electroweak scale, m_h could reach 1 TeV. Lastly, a theoretical constraint is set by the vacuum stability bound. The Higgs self-coupling is impacted by contributions from fermion and gauge bosons loops, some of which have negative sign. If the value of m_h is too low, the sign of the quartic term in Equation 2.1 becomes negative, the result being that the minimum of the potential disappears. Thus, m_h must be above a certain threshold, depending on the value of cut-off scale Λ. The allowed values of m_h taking the latter two effects into account are presented in Figure 2.2. A recent discussion of these two effects is given in [20].

- **Indirect experimental constraints** on m_h were imposed from electroweak precision measurements, an approach made possible by the fact that the SM Higgs boson contributes to the radiative corrections appearing in electroweak theory. For example, by incorporating the electroweak precision data obtained with the experiments at the SLC, LEP and Tevatron displayed in Figure 2.3a in a combined fit, the constraint on m_h presented in Figure 2.3b was derived. This latter exhibit shows the $\Delta\chi^2$ of the fit to the combined measurements as a function of m_h, with the most likely value being $m_h = 114^{+69}_{-45}$ GeV. Furthermore, a 95% upper Confidence Level (CL)[2] of $m_h < 260$ GeV was imposed [21].

- **Direct experimental constraints** on m_h were imposed by Higgs boson searches performed at LEP and at the Tevatron. As seen in Figure 2.4, the LEP experiments established a lower bound of $m_h > 114.4$ GeV at 95% CL [22], while the Tevatron experiments excluded the presence of a SM Higgs boson in the interval $90 < m_h < 109$ GeV and $149 < m_h < 182$ GeV at 95% CL [23].

[2] The experimental terminology used in this section is reviewed in Chapter 5.

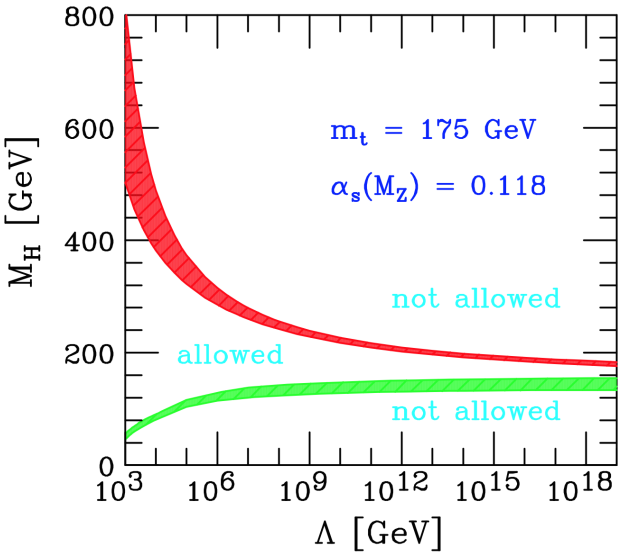

FIGURE 2.2: Theoretical limits on the Higgs boson mass imposed by the triviality bound (upper bound) and vacuum stability bound (lower bound), as a function of the cut-off scale Λ. The coloured bands illustrate the impact of various uncertainties. The allowed region for m_h lies between the uncertainty bands [24].

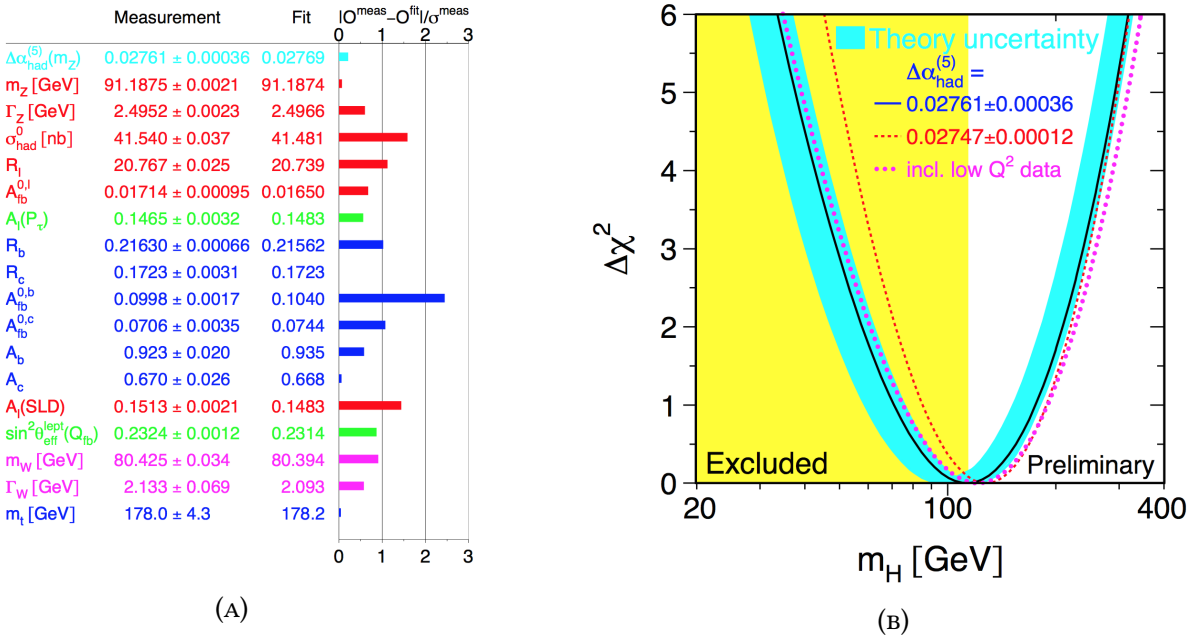

FIGURE 2.3: (A): Summary of electroweak precision measurements obtained at experiments at LEP, the SLC and the Tevatron. An explanation of the electroweak parameters can be found in [21]. (B): The $\Delta\chi^2$ of the fit to the electroweak precision data as a function of m_h. The solid line represents the results when all data are included, while the blue/shaded band is the estimated theoretical error from unknown higher-order corrections [21].

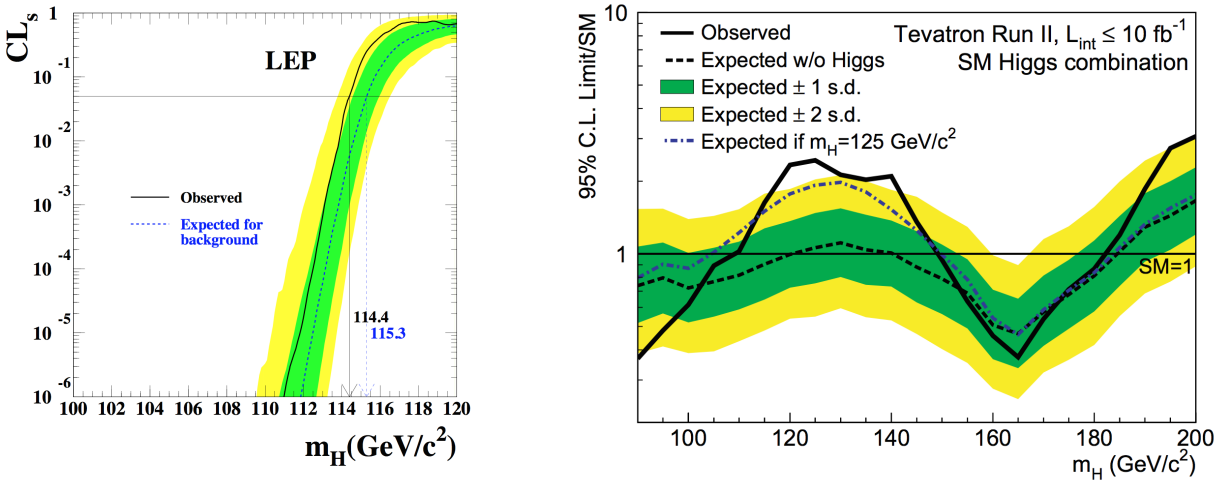

(A) (B)

FIGURE 2.4: (A): Exclusion limits imposed as a function of m_h by the LEP experiments (ALEPH, DELPHI, L3 and OPAL [25, 26, 27, 28]), establishing a lower bound of $m_h > 114.4$ GeV at 95% CL [22]. (B): Exclusion limits imposed as a function of m_h by the Tevatron experiments (CDF and D0 [29, 30]), excluding a SM Higgs boson in the interval $90 < m_h < 109$ GeV and $149 < m_h < 182$ GeV at 95% CL [23].

2.4 The Discovery

Given that the mass of the SM Higgs boson is not predicted from theory, the task of experimentalists prior to its discovery was to search for it in the widest possible range. As will be explained in more detail in Chapter 3, LHC operation was initiated in 2008 and data-taking by the ATLAS and CMS experiments in 2010. During 2011 and 2012, the LHC delivered enough data for these two experiments to announce the discovery of a new boson in July 2012 [6, 7]. A selection of the figures presented at this occasion is shown in Figure 2.5. The subsequent measurements of the properties of this particle revealed that it indeed is consistent with the scalar Higgs boson appearing in the SM [31, 32, 33, 34], and possesses a mass measured to be $m_h = 125.09 \pm 0.21$ (stat) ± 0.11 (syst) GeV [35]. The phenomenological behaviour of the SM Higgs boson at the LHC is described below.

2.5 Production and Decay

As will be explained in Chapter 3, the LHC is designed to collide protons at a collision energy between $\sqrt{s} = 7$ TeV and $\sqrt{s} = 14$ TeV. The production of a SM Higgs boson at the LHC happens mainly via four mechanisms: gluon-fusion (ggF), vector boson-fusion (VBF), associated production

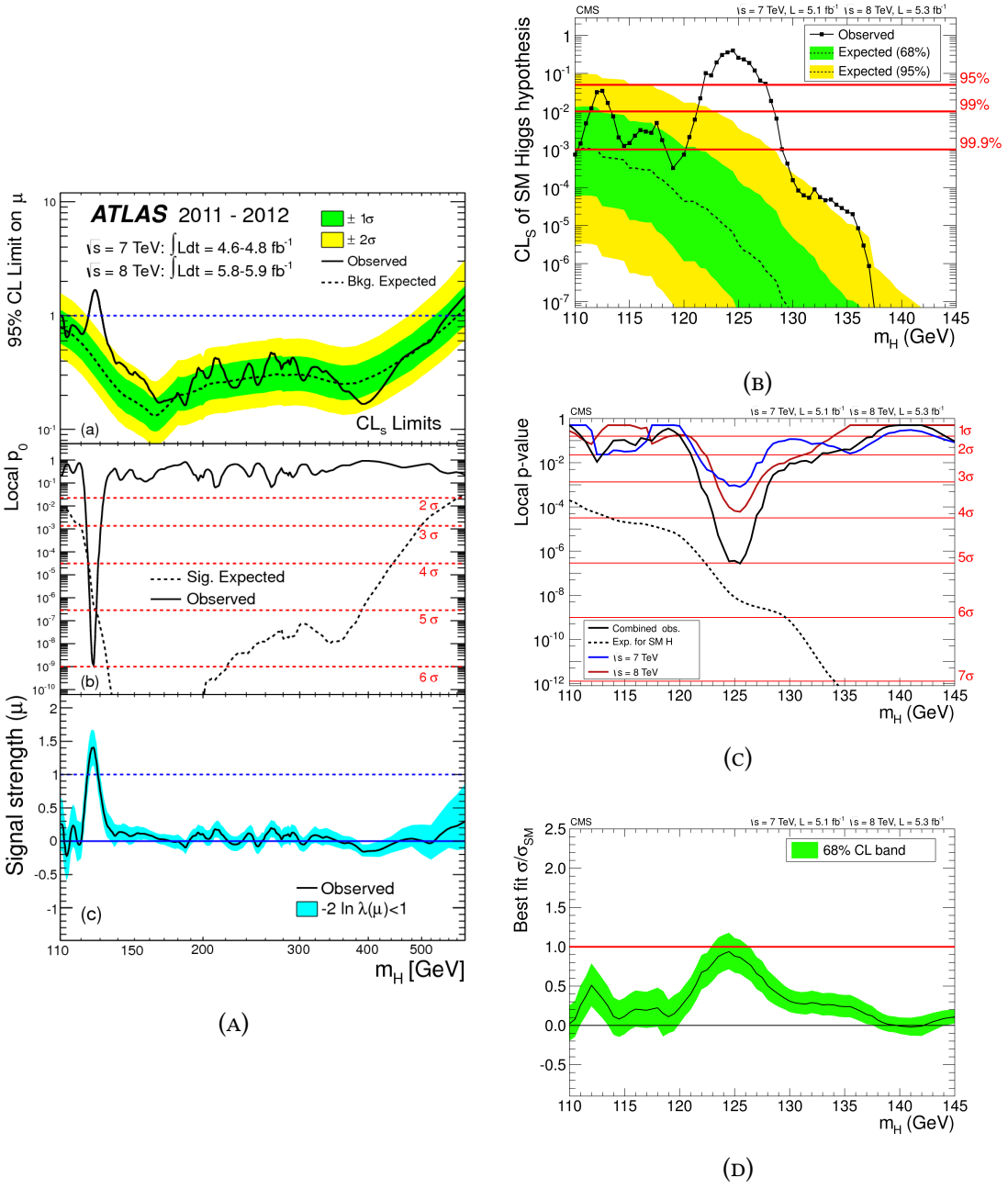

FIGURE 2.5: Results presented by the ATLAS and CMS collaborations in July 2012 in relation to the SM Higgs boson discovery [6, 7]. The experimental terminology appearing in this figure is reviewed in Chapter 5. (A)(a) and (B): The observed upper limit on the signal strength, μ, as a function of m_h, and the expectation under the background-only hypothesis for ATLAS and CMS. (A)(b) and (C): The observed local p_0 value as a function of m_h and the expectation for a SM Higgs boson signal hypothesis at the given m_h value for ATLAS and CMS. (A)(c) and (D): The best-fit signal strength, $\hat{\mu}$, as a function of m_h for ATLAS and CMS.

with a vector boson (VH) and associated production with a top-quark pair (ttH). The leading-order diagrams of these processes are shown in Figure 2.6. As will be demonstrated throughout this thesis, the absence or presence of byproducts created with the Higgs boson, such as jets from the VBF mechanism or a decaying vector boson from the VH mechanism, can be exploited in experimental studies to distinguish the different production mechanisms.

Figure 2.7 shows the SM Higgs boson production cross-section of the four mechanisms as a function of the Higgs boson mass in the range $80 \leq m_h \leq 1000$ GeV at $\sqrt{s} = 8$ TeV. As seen, the ggF and VBF mechanisms dominate the production, with ggF being more than an order of magnitude larger than VBF in the low-mass regime where the SM Higgs boson was discovered. Also observed from Figure 2.7 is the very modest contribution from associated production, which falls steeply with m_h and becomes negligible above masses of 300 GeV. The contribution from the ttH mechanism is approximately a factor of two smaller than the VH mechanism, and is therefore not considered in the analyses of this thesis. Figure 2.7 also displays the inclusive Higgs boson production cross-section at $\sqrt{s} = 7$ TeV, $\sqrt{s} = 8$ TeV and $\sqrt{s} = 14$ TeV, which correspond to the collision energies in the different data-taking periods of the LHC. As seen in this exhibit, the total production cross-section of the SM Higgs boson increases by up to one order of magnitude between $\sqrt{s} = 8$ TeV and $\sqrt{s} = 14$ TeV.

The coupling strength of the SM Higgs boson is proportional to the mass of the particle it interacts with. More specifically, the coupling strength is proportional to the fermion mass and proportional to the square of the boson mass. Therefore, for a given value of m_h, the dominant

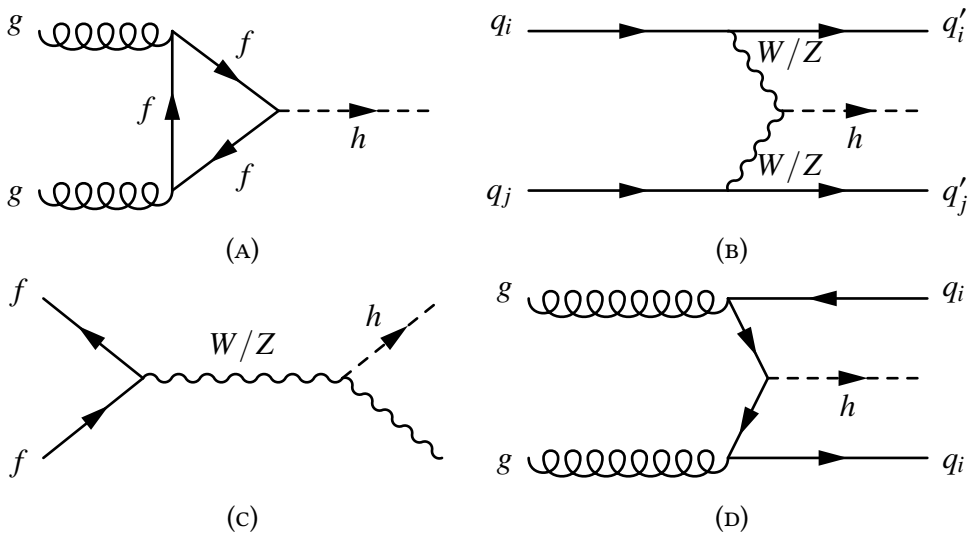

Figure 2.6: Leading-order diagrams for the four dominant Higgs production mechanisms at the LHC. (A): gluon-fusion (ggF). (B): vector boson-fusion (VBF). (C): associated production with a vector boson (VH). (D): associated production with a top-quark pair (ttH).

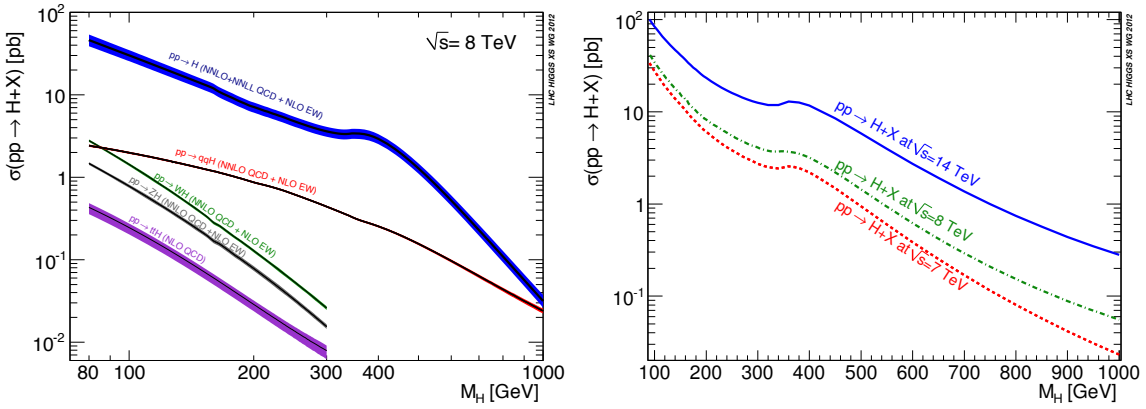

(A) (B)

FIGURE 2.7: SM Higgs boson production cross-section broken down by production mechanism at $\sqrt{s} = 8$ TeV (A) and inclusively for $\sqrt{s} = 7$ TeV, $\sqrt{s} = 8$ TeV and $\sqrt{s} = 14$ TeV (B) [36].

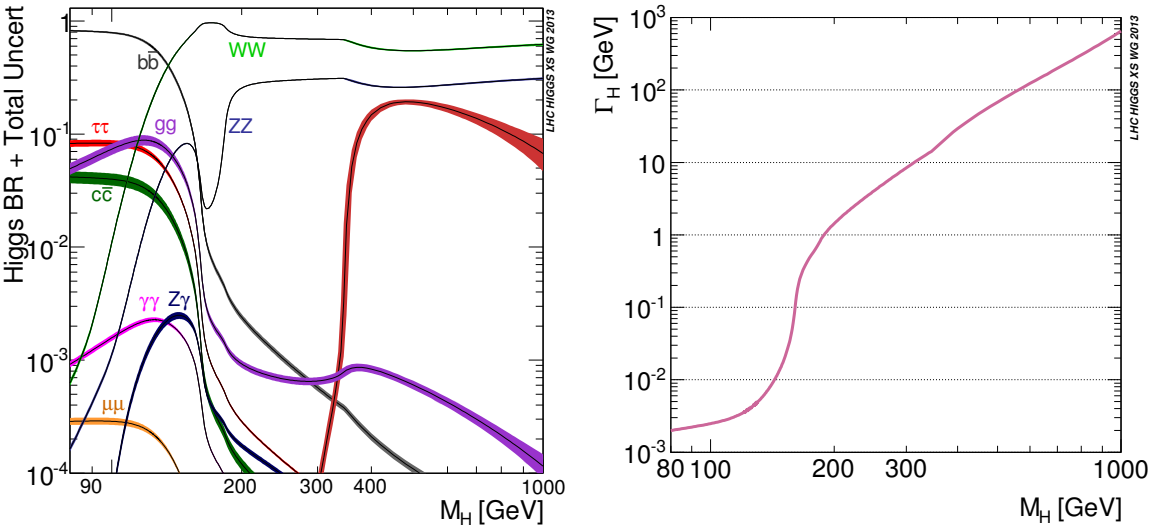

(A) (B)

FIGURE 2.8: SM Higgs boson branching ratios (A) and total width as a function of m_h (B) [36].

decay of the SM Higgs boson will be to the heaviest, kinematically accessible final-state, however, the decays to the massive gauge bosons are favoured. This behaviour is illustrated in Figure 2.8a, which presents the branching ratio of the SM Higgs boson as a function of m_h. As observed, the $h \to b\bar{b}$ decay dominates at low mass, while the di-boson channels $h \to ZZ$ and $h \to WW$ dominate from $m_h \sim 180$ GeV and up, which is the threshold where these decays become permitted by kinematics. The $h \to ZZ$ decay, which is the decay of interest to this thesis, is the second-most

dominant at large m_h values.

Figure 2.8b displays the total width of the Higgs boson, Γ_h, as described by the SM as a function of its mass in the interval $80 \leq m_h \leq 1000$ GeV. Given that a heavier Higgs boson has more allowed decay modes and a larger kinematical phase space to decay into, its width increases with mass. As seen, this quantity varies with up to six orders of magnitude. At the observed value of $m_h = 125$ GeV, the width of the Higgs boson is $\Gamma_h^{SM} = 4.07$ MeV.

2.6 The Narrow Width Approximation and Interference

An interesting phenomenon that scales with Γ_h, and thus becomes increasingly important for larger values of m_h, is the quantum mechanical interference occurring between the resonant Higgs processes and the non-resonant SM processes. Within the context of a Higgs boson decaying to two Z bosons, for ggF production the interference happens between the processes $gg \to h \to ZZ^{(*)}$ and $gg \to ZZ^{(*)}$, while for VBF production, it occurs between the $q\bar{q} \to h \to ZZ^{(*)} + q\bar{q}$ and $q\bar{q} \to ZZ^{(*)} + q\bar{q}$ processes. This interference impacts the overall production cross-section of the Higgs boson, and as well its line-shape and kinematic distributions. The impact of the interference on the differential cross-section of the SM Higgs boson as a function of the invariant mass of the four leptons in the $h \to ZZ^{(*)} \to 4\ell$ decay as documented by ATLAS in [37] is shown in Figure 2.9.

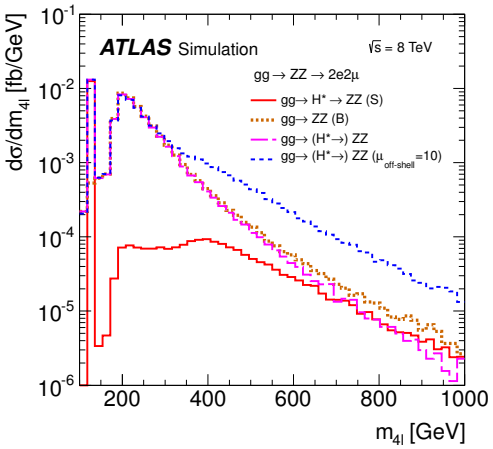

FIGURE 2.9: Differential cross-sections as a function of the discriminating variable, the four-lepton invariant mass ($m_{4\ell}$), for the $gg \to (h \to)ZZ \to 2e2\mu$ process at parton level, the non-resonant $gg \to ZZ^{(*)}$ continuum and the $gg \to (h \to)ZZ^{(*)}$ process, assuming SM Higgs boson couplings [37].

In this exhibit, the process denoted $gg \to (h \to)ZZ^{(*)}$ contains the resonant $gg \to h \to ZZ^{(*)}$ Higgs production, the non-resonant process $gg \to ZZ^{(*)}$, and the interference occurring between these two processes. As observed, the net impact of the interference is an alteration of the $ZZ^{(*)}$ line-shape.

Since the interference described above is non-trivial to model, one can employ the Narrow Width Approximation (NWA) (or Zero Width Approximation (ZWA)) and thus avoid it. In this approximation, the width is kept constant as a function of m_h at a value significantly smaller than the given value of m_h, and significantly below the experimental resolution of the analysis in question. Under these circumstances, the interference is considered negligible and can hence safely be ignored. Furthermore, given that the model-specific relation between Γ_h and m_h is removed,

the NWA is frequently used in experimental studies in order to depend on the fewest possible assumptions about the underlying model. More details on this will be given in Chapter 5. Although practical, the use of the NWA is obviously limited in scope to theoretical circumstances where the Higgs boson width is predicted to be very narrow. As will be explained in Section 2.8, an example of a framework where this assumption is valid is the 2HDM.

2.7 Shortcomings of the Standard Model

Nowadays, the SM is considered in terms of an effective field theory, meaning that its validity is constrained – rather than being a complete theory in itself, it is considered an approximation with validity limited to the sensitivity of present experiments. Furthermore, despite the enormous success of the SM, a series of deficiencies and unresolved issues emphasise that it is not complete in its current form and hence cannot be a final theory of nature, implying that physics beyond the SM (BSM) must exist. This section and Section 2.8 give a brief overview of the most severe shortcomings of the SM and describe the 2 Higgs Doublet Model, which is a BSM framework that can alleviate some of these existing shortcomings.

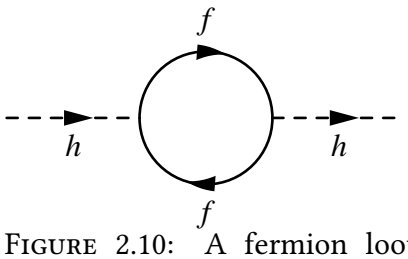

FIGURE 2.10: A fermion loop contributing to the Higgs mass.

The SM quite accurately describes physics near the electroweak scale, however, it breaks down near the Planck scale of $\sim 10^{19}$ GeV. At this energy scale, the effects of gravity at the quantum mechanical level cannot be ignored and must be accounted for. Incorporating this into the SM necessitates a quantum mechanical description of gravity, the development of which has been unsuccessful so far. As a result, the validity of the SM is currently constrained to the low-energy regime near the electroweak scale and misses a description of gravity [38].

Another theoretical issue is the so-called hierarchy problem, which arises because there are 16 orders of magnitude between the electroweak scale and the Planck scale. The natural mass of the Higgs boson is impacted by contributions from fermion loops, such as the one illustrated in Figure 2.10. The contribution from these loops on the bare Higgs mass is proportional to a cut-off scale, where new physics is expected to exist. This means, that if no new physics exists up until the Planck scale, the natural mass of the Higgs boson would be at the order of 10^{19} GeV. This is obviously not the case, entailing that some mechanism must be in place which preserves the SM Higgs boson mass at the observed value of 125 GeV. One possibility is that certain uncorrelated counterterms in the SM are tuned such that the loop-corrections exactly cancel out. This requires that the parameters are adjusted to a level of 10^{-15} – a degree of fine-tuning that one may argue is highly improbable and a coincidence that borders on being magical. Various BSM theories, such as

Supersymmetry (SUSY), offer a solution to this problem by expanding the spectrum of particles in the SM, thereby making the above-mentioned counterterms cancel, leaving the Higgs boson mass at the electroweak scale. This latter possibility is one of the strong arguments for searching for BSM physics at the TeV scale.

In addition to the theoretical issues listed above, a series of experimental observations highlight shortcomings of the SM. Astronomical data suggests that the matter described by the SM only constitutes ~5% of the total mass-energy content in the universe. Approximately 27% of the content, so-called dark matter, is a type of matter which does not interact via the electromagnetic force, while the remaining ~68%, so-called dark energy, is attributed to causing the accelerating expansion of the universe. The presence of these two place-holders is a strong indication of the existence of BSM physics [39, 40].

Another puzzle demonstrating the inadequacy of the SM in its current form are the experimentally verified neutrino oscillations, which can only occur if the neutrinos have mass. This is in direct opposition to the SM, which predicts them to be massless. However, neutrino masses can be introduced into the SM by relatively simple theoretical means such as the Seesaw mechanism [41, 42].

2.8 The 2 Higgs Doublet Model

A BSM theory that is of high interest to the LHC community is the 2 Higgs Doublet Model (2HDM), which is a reasonably simple extension of the SM that introduces a minimal set of new parameters. Within the 2HDM framework, the Higgs sector of the SM is extended by adding a second electroweak doublet to the one described in Section 2.2, meaning that two electroweak doublets, Φ_1 and Φ_2, are present. When assuming CP conservation in the Higgs sector, the most general scalar potential for these two doublets with hypercharge +1 can be written:

$$\begin{aligned} V = m_{11}^2\Phi_1^\dagger\Phi_1 + m_{22}^2\Phi_2^\dagger\Phi_2 - m_{12}^2\left(\Phi_1^\dagger\Phi_2 + \Phi_2^\dagger\Phi_1\right) + \frac{\lambda_1}{2}\left(\Phi_1^\dagger\Phi_1\right)^2 + \frac{\lambda_2}{2}\left(\Phi_2^\dagger\Phi_2\right)^2 \\ +\lambda_3\Phi_1^\dagger\Phi_1\Phi_2^\dagger\Phi_2 + \lambda_4\Phi_1^\dagger\Phi_2\Phi_2^\dagger\Phi_1 + \frac{\lambda_5}{2}\left[\left(\Phi_1^\dagger\Phi_2\right)^2 + \left(\Phi_2^\dagger\Phi_1\right)^2\right], \end{aligned} \tag{2.3}$$

where all parameters are real.

By adding the second electroweak doublet, four additional Goldstone bosons appear after spontaneous symmetry breaking, three of which give mass to the W and Z bosons. The remaining Goldstone bosons manifest as physical Higgs bosons, the result being that the 2HDM framework contains five Higgs bosons. Two of these have no electric charge and are CP-even (h and H), one has no electric charge and is CP-odd (A), while the remaining two are charged (H^+ and H^-) [43].

The 2HDM framework contains seven free parameters; the Higgs boson masses, m_h, m_H, m_A, $m_{H^\pm}$, the ratio of the vacuum expectation value of the two doublets, $\tan(\beta) = v_2/v_1$, the mixing angle between h and H, named α, and the potential parameter m_{12}^2 from Equation 2.3 that mixes the two Higgs doublets. The vacuum expectation values of the two doublets satisfies the relation $v_1^2 + v_2^2 = v^2 = 246^2$ GeV^2. The specific masses of the five Higgs bosons are not predicted, however, their relative values are constrained. Of particular relevance to this thesis is the relation between the mass of h and H, which is heavily dependent on the values of the remaining parameters of the theory, but which allows for H to be heavier than h. Following this convention, the Higgs boson discovered in 2012 can be interpreted as h. This thesis revolves around the search for a heavy, electrically neutral, CP-even boson consistent with the 2HDM Higgs boson H[3] [44, 45, 46].

The 2HDM model does not refer to one specific theory, but is rather a theoretical framework that constitutes the basis for multiple BSM theories, a popular example being the Minimal Supersymmetric Standard Model (MSSM). The most frequently encountered types of 2HDM are summarised in Table 2.4. These differ in how the SM fermions couple to the two electroweak doublets. In the Type-1 model, the doublet Φ_2 couples to both the up- and down-type quarks, as well as the leptons, whereas for Type-2, Φ_1 couples to down-type quarks and leptons and Φ_2 couples to up-type quarks. Type-2 is also known as MSSM-like. The lepton-specific model (also known as Type-3) is similar to Type-1, except for the fact that the leptons couple to Φ_1 instead of Φ_2. The flipped model (also known as Type-4) is similar to Type-2, except that the leptons couple to Φ_2 instead of Φ_1. Within the context of the $H \to ZZ$ decay, there is no direct coupling of the heavy Higgs boson to leptons. Therefore, the lepton-specific and -flipped types will not be considered, but only Type-1 and -2 interpretations will be performed throughout this thesis.

TABLE 2.4: Overview of couplings in the four most common types of 2HDM models. κ_u, κ_d and κ_ℓ denote the coupling to up-type quarks, down-type quarks and leptons, respectively [45].

	Type-1	Type-2	Lepton-specific	Flipped
κ_u	$\sin(\alpha)/\sin(\beta)$	$\sin(\alpha)/\sin(\beta)$	$\sin(\alpha)/\sin(\beta)$	$\sin(\alpha)/\sin(\beta)$
κ_d	$\sin(\alpha)/\sin(\beta)$	$\cos(\alpha)/\cos(\beta)$	$\sin(\alpha)/\sin(\beta)$	$\cos(\alpha)/\cos(\beta)$
κ_ℓ	$\sin(\alpha)/\sin(\beta)$	$\cos(\alpha)/\cos(\beta)$	$\cos(\alpha)/\cos(\beta)$	$\sin(\alpha)/\sin(\beta)$

[3] Throughout this thesis, h refers to the SM Higgs boson, whereas H refers to a heavier scalar, such as that appearing in 2HDM.

2.8.1 Phenomenology

Within the context of 2HDM, the phenomenological behaviour of h and H are similar to that of the SM Higgs boson described in Section 2.5 – they are expected to be produced via the same mechanisms and able to decay via the same channels. However, since the couplings of h and H can be parametrised entirely in terms of α and β, their production and decay rates may differ from the SM. The couplings of h and H to vector bosons defined with respect to the SM are given by:

$$g_{\mathrm{hVV}}^{\mathrm{2HDM}}/g_{\mathrm{hVV}}^{\mathrm{SM}} = \sin(\beta-\alpha) \tag{2.4}$$

$$g_{\mathrm{HVV}}^{\mathrm{2HDM}}/g_{\mathrm{hVV}}^{\mathrm{SM}} = \cos(\beta-\alpha) \tag{2.5}$$

Here $g_{\mathrm{hVV}}^{\mathrm{2HDM}}$ and $g_{\mathrm{HVV}}^{\mathrm{2HDM}}$ are the couplings of h and H in the 2HDM framework defined with respect to the corresponding coupling in the SM, $g_{\mathrm{hVV}}^{\mathrm{SM}}$.

Constraints on the 2HDM parameter space have been imposed by experimental studies such as the measurement of the SM Higgs boson couplings. Currently, the studies performed with LHC data [47, 48] favour the benchmark scenario known as the alignment limit, which is at the point in the 2HDM parameter space where $\cos(\beta-\alpha)=0$, $\sin(\beta-\alpha)=1$. In this scenario, the 2HDM Higgs boson h couples like the SM Higgs boson and is therefore by itself indistinguishable from it. Since proximity to the alignment limit causes the vector couplings of H to vanish, the rates of the VBF and VH production mechanisms, and the rate of the $H \to VV$ decays, are suppressed. This behaviour is illustrated in Figure 2.11, which presents the parametric variation of the production cross-section of H, σ_H, multiplied with the $H \to VV$ branching ratio, $BR(H \to VV)$, as a function of $\cos(\alpha-\beta)$ and β, normalised to the value of the same quantity for the SM Higgs boson. This dependence is presented for both Type-1 and Type-2 2HDM at $m_H = 300$ GeV. As observed, the production rate of H diminishes near the alignment limit. This behaviour is further illustrated in Figure 2.12, which displays the ratio of the production cross-section of H via the ggF mechanism to the production cross-section of both the ggF and VBF mechanisms for three different m_H values in both Type-1 and -2 2HDM. As seen, the ggF production mechanism dominates over the majority of the 2HDM phase-space at both low and high mass.

In addition to a dependence on the 2HDM parameter space, the width of H varies with its mass. The width of H expressed as a fraction of its mass is presented in Figure 2.13 for Type-1 and -2 2HDM for $m_H = 200$ GeV, $m_H = 300$ GeV and $m_H = 400$ GeV under the assumption of $m_h = 125$ GeV. From this exhibit, it is seen that the width of H is quite narrow in certain regions

of the parameter space, at the order of <1% of m_H. This fact legitimises the use of the NWA, mentioned in Section 2.6, which is employed in the heavy Higgs boson searches documented in Chapter 4 to Chapter 8.

The interference described in Section 2.6 between the Higgs boson and the various non-resonant SM processes is also expected to be present for the heavy Higgs boson, as well as interference between the heavy and the light Higgs boson. These effects can safely be ignored in this thesis due to the fact that the NWA is employed. Furthermore, recent studies show that the effect of the interference on the heavy Higgs boson cross-section reaches $\mathcal{O}(10)$% at maximum, and that the approximation to neglect the interference can be justified in view of the experimental sensitivity that has been reached during the first data-taking period of LHC operation [49]. A more detailed summary of the interference effects impacting the heavy Higgs boson is given in [50].

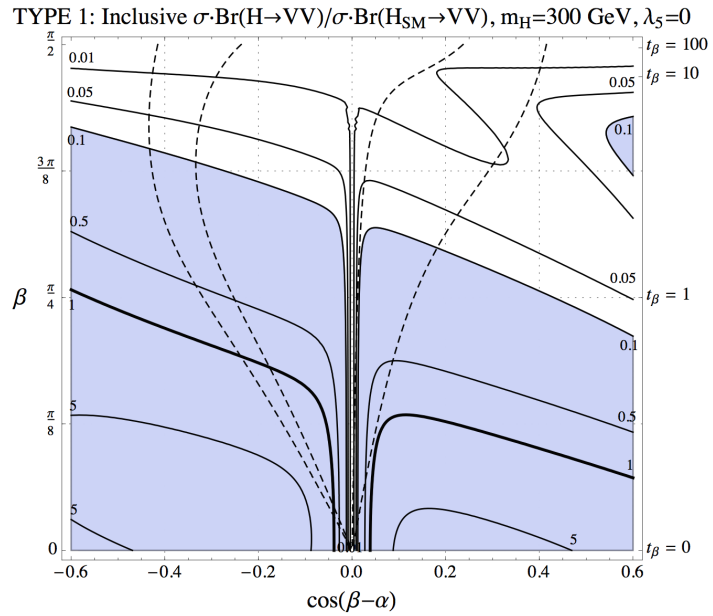

(A)

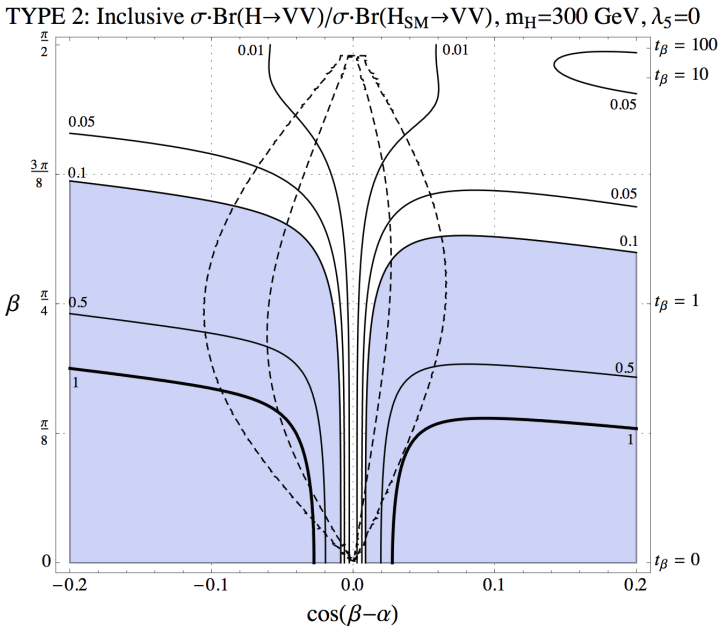

(B)

FIGURE 2.11: Contours of $\sigma_H \cdot BR(H \to VV)/\sigma_h \cdot BR(h \to VV)$ at $\sqrt{s} = 8$ TeV, shown as a function of $\cos(\beta-\alpha)$ and β for Type-1 (A) and Type-2 (B) 2HDM. The inner (outer) dashed contour denotes the 68% (95%) CL best fit to the signals of the SM Higgs boson. The values of $\tan(\beta)$, here denoted t_β, corresponding to the displayed values of β are shown as well. The violet shaded region denotes the parameter space excluded by the CMS experiment using LHC data corresponding to 5.1 fb^{-1} recorded at $\sqrt{s} = 7$ TeV and 5.3 fb^{-1} recorded at $\sqrt{s} = 8$ TeV [48, 51].

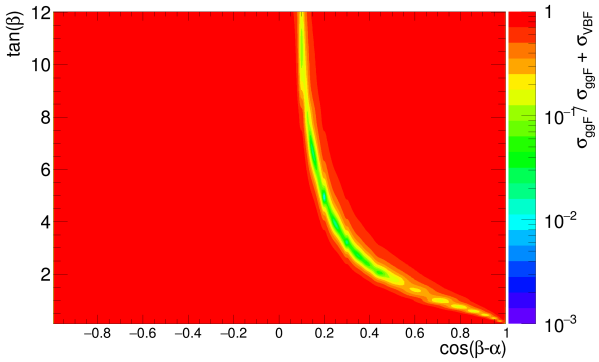

(A) Type-1, $m_H = 200$ GeV

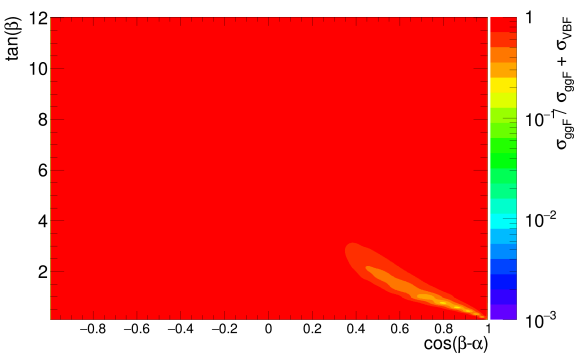

(B) Type-2, $m_H = 200$ GeV

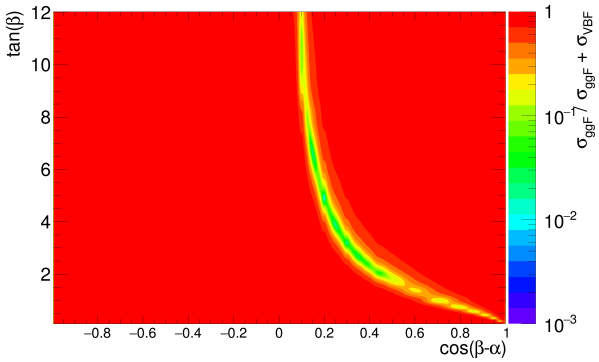

(C) Type-1, $m_H = 600$ GeV

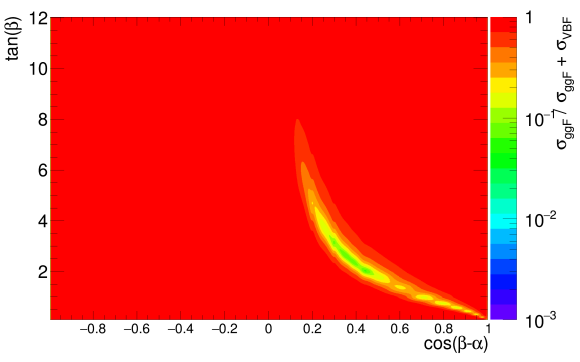

(D) Type-2, $m_H = 600$ GeV

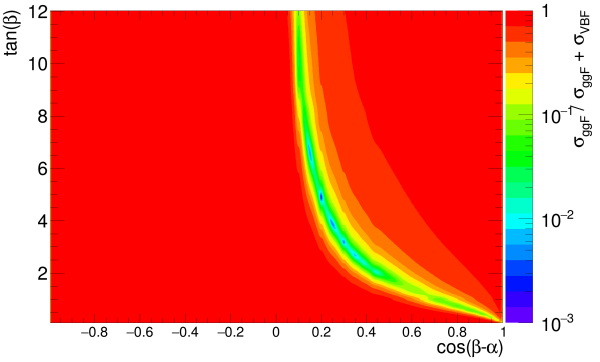

(E) Type-1, $m_H = 1000$ GeV

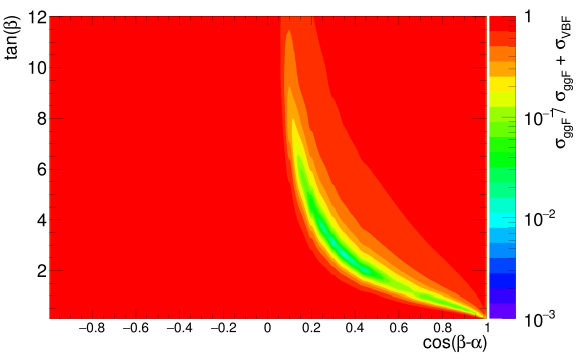

(F) Type-2, $m_H = 1000$ GeV

FIGURE 2.12: Contours of the ratio between the ggF production cross-section of H (σ_{ggF}) and the sum of the production cross-section for the ggF and VBF mechanisms ($\sigma_{\text{ggF}}+\sigma_{\text{VBF}}$) at $\sqrt{s} = 13$ TeV as function of $\tan(\beta)$ and $\cos(\beta-\alpha)$ for Type-1 (left) and Type-2 (right) 2HDM at $m_H = 200$ GeV, $m_H = 600$ GeV, and $m_H = 1000$ GeV.

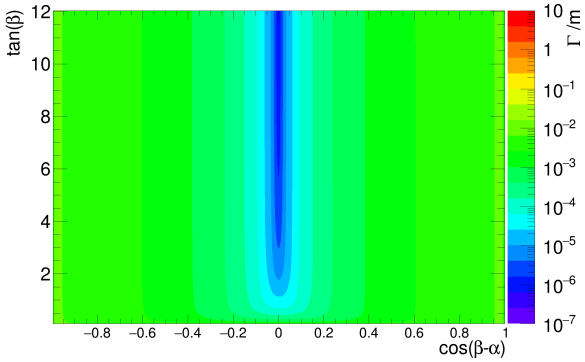

(A) Type-1, $m_H = 200$ GeV

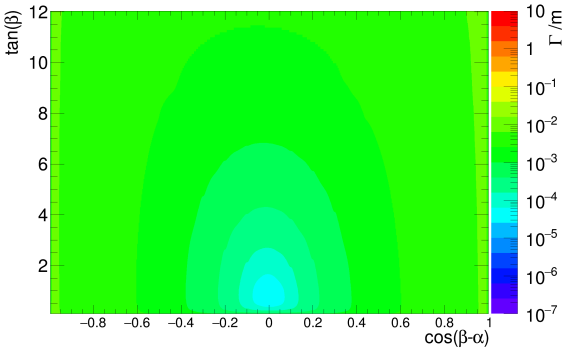

(B) Type-2, $m_H = 200$ GeV

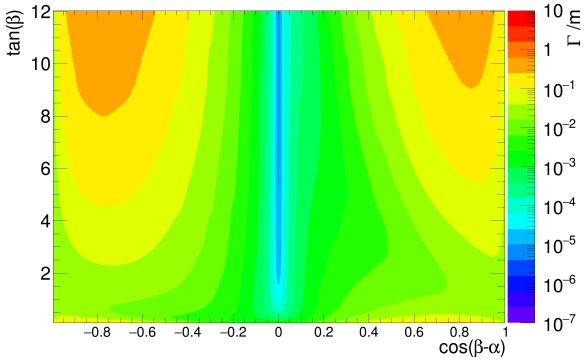

(C) Type-1, $m_H = 300$ GeV

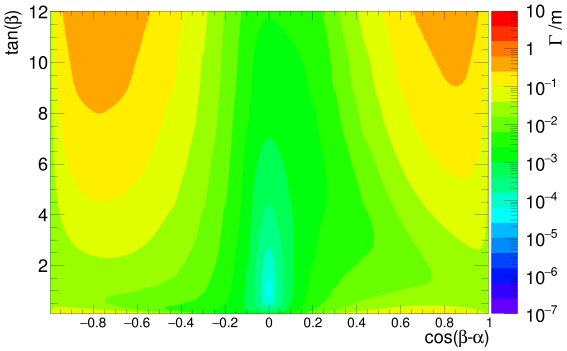

(D) Type-2, $m_H = 300$ GeV

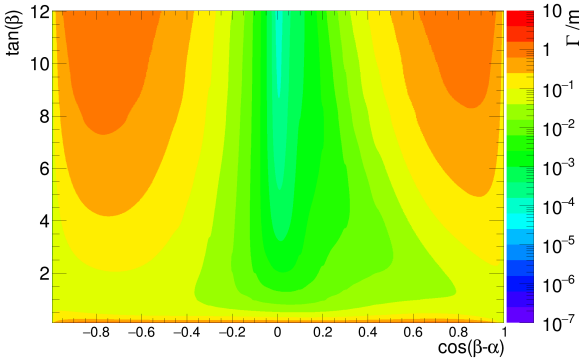

(E) Type-1, $m_H = 400$ GeV

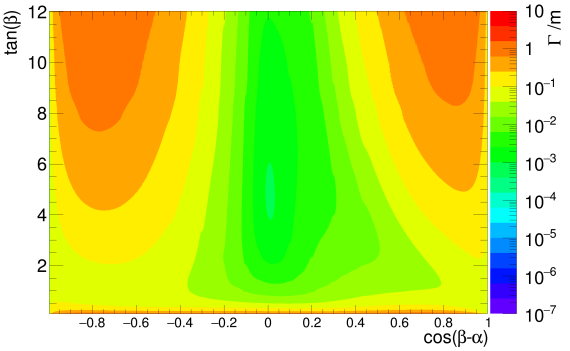

(F) Type-2, $m_H = 400$ GeV

FIGURE 2.13: Contours of the ratio between the width of H, Γ_H, and its mass as function of $\tan(\beta)$ and $\cos(\beta-\alpha)$ for Type-1 (left) and Type-2 (right) 2HDM at $m_H = 200$ GeV, $m_H = 300$ GeV, and $m_H = 400$ GeV.

CHAPTER 3

Experimental Facilities

3.1 The Large Hadron Collider

The Large Hadron Collider (LHC) [52] is a 26.7 km long storage ring constructed at The European Organization for Nuclear Research (CERN) near Geneva, Switzerland. The LHC was built in the tunnel of its predecessor, the Large Electron-Positron collider (LEP), with the objective to probe previously inaccessible kinematic regimes via hadron collisions at unprecedented energies. Four large experiments, described in Section 3.2, attached to the LHC record the particles emanating from these collisions. The design and operation of the LHC is tailored to the physics goals of these experiments, in particular to a research programme relying on high-luminosity proton-proton (pp) collisions.

The proton beams in the LHC are accelerated to the appropriate energy in multiple steps facilitated by the CERN accelerator complex illustrated in Figure 3.1. Protons are initially extracted from hydrogen atoms and accelerated to an energy of 50 MeV by the linear accelerator Linac 2. Subsequently, the protons are fed to the booster, which raises the energy to 1.4 GeV and feeds them to the Proton Synchotron (PS). The PS increases the energy to 25 GeV and passes the beam on to the Super Proton Synchrotron (SPS). Injection to the LHC happens from this ring at an energy of 450 GeV in both clockwise and counter-clockwise direction. In the LHC the beams are contained in two separate pipes, which intersect at four insertion regions where the experiments are positioned. Oppositely oriented magnetic dipole fields sustained at 8 T by helium-cooled superconducting magnets bend the proton beams as they travel around the ring. A total of 1232 dipole magnets are installed in the LHC ring. Acceleration of the beams is provided by 8 superconducting radio frequency (RF) cavities operated at 400 MHz, located at a single point on the LHC ring. Due to the specifications of the RF cavities and the dimensions of the LHC, the beams are segmented into 2808 proton bunches.

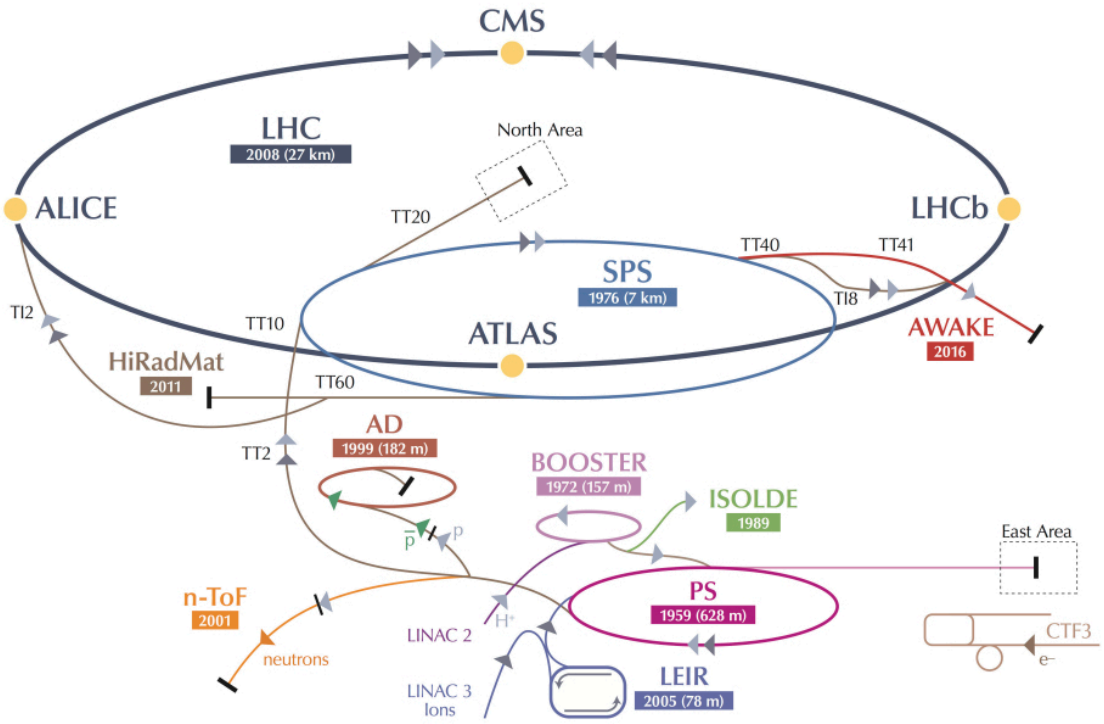

FIGURE 3.1: Overview of the LHC injector complex among the position of the four experiments (indicated with yellow markers) on the LHC ring [53].

3.1.1 Luminosity and Operation

Collider performance is often quantified by two metrics, the instantaneous and integrated luminosity. The instantaneous luminosity, $\mathcal{L}_{\text{inst}}$, reflects the rate at which events are produced per unit time. This quantity can be parametrised as:

$$\mathcal{L}_{\text{inst}} = \frac{f_r n_1 n_2 n_b}{2\pi \Sigma_x \Sigma_y} \quad [\text{cm}^{-2}\text{s}^{-1}] \tag{3.1}$$

Here f_r is the machine revolution frequency (11245 Hz), $n_{1,2}$ are the number of protons in the colliding bunches ($\sim 10^{11}$), n_b is the number of colliding bunches, while $\Sigma_{x,y}$ are the convoluted transverse beam profiles describing the transverse area of the beams. The latter parameter is related to two optical functions, the transverse emittance, ϵ, and the amplitude function at the interaction point, $\beta^*_{x,y}$, via the relation $\Sigma_{x,y} = \sqrt{\epsilon \beta^*_{x,y}}$. As will be described shortly, the instantaneous luminosity obtained at the LHC at nominal pp operation is adjusted by varying the parameter n_b, resulting in a change in the time between two occurring collisions (the bunch-spacing), and by changing the transverse area of the beams by varying β^* [54].

The integrated luminosity, L, refers to the instantaneous luminosity integrated over time and is therefore used to signify the size of a given data sample. Knowledge of the integrated luminosity is absolutely essential for collider physics, since it relates the produced number of events from a given process, N, to the production cross-section of the process, σ, via the relation:

$$N = L \times \sigma \tag{3.2}$$

Given the fundamental role of L, the precision with which it is determined is of great importance for any physics analysis including event yields. In the first LHC data-taking period, which will be defined below, the ATLAS experiment constrained the uncertainty on the luminosity down to 2.8%.

Due to its pioneering specifications, the LHC will exceed the performance of all preceding colliders in terms of both luminosity and collision energy. The preceding hadron collider comparable to the LHC, the Tevatron at Fermilab, delivered $L \approx 10$ fb^{-1} of $p\bar{p}$ collisions at $\sqrt{s} = 1.96$ TeV at a peak luminosity of 4×10^{32} cm^{-2}s^{-1}. In comparison, the LHC is expected to deliver a total of $L \approx 300$ fb^{-1} around the year 2020 with a collision energy of $\sqrt{s} = 14$ TeV and peak luminosity of 3×10^{34} cm^{-2}s^{-1}. Figure 3.2 compares the production cross-section for various physics processes at these two colliders, which, as observed, are several orders of magnitude larger at the LHC.

Operation of the LHC was initiated in 2008. The first two years were dedicated to rectifying technical problems which occurred in the start-up phase and to machine commissioning. Data-taking was successfully started in 2010. Run-1 denotes the period from 2011 – 2012 where the LHC delivered collisions at $\sqrt{s} = 7$ TeV to $\sqrt{s} = 8$ TeV with a peak luminosity of 8×10^{33} cm^{-2}s^{-1}. As explained in Chapter 2, the successful delivery and recording of data in this period constituted the foundation for the discovery of the Higgs boson in 2012. After a shutdown period lasting 2013 – 2014, operation was resumed in 2015. In this period, known as Run-2, collisions were delivered at $\sqrt{s} = 13$ TeV at an expected peak luminosity of $1 - 2 \times 10^{34}$ cm^{-2}s^{-1}. This increase in instantaneous luminosity was achieved by reducing the bunch-spacing from 50 ns to 25 ns and by reducing β^* by a factor of almost two. Data from both Run-1 and Run-2 will be presented throughout this thesis [55, 56, 57].

The high instantaneous luminosity achieved at the LHC results in the obvious advantage of more data being delivered, but not without complications. The phenomenon known as pile-up, signifying the occurrence and/or read-out of multiple interactions per bunch-crossing, is inevitable and is significant enough that large efforts are dedicated to taking it into account. This effect and its implications will be described in more detail in Chapter 5 to Chapter 7 .

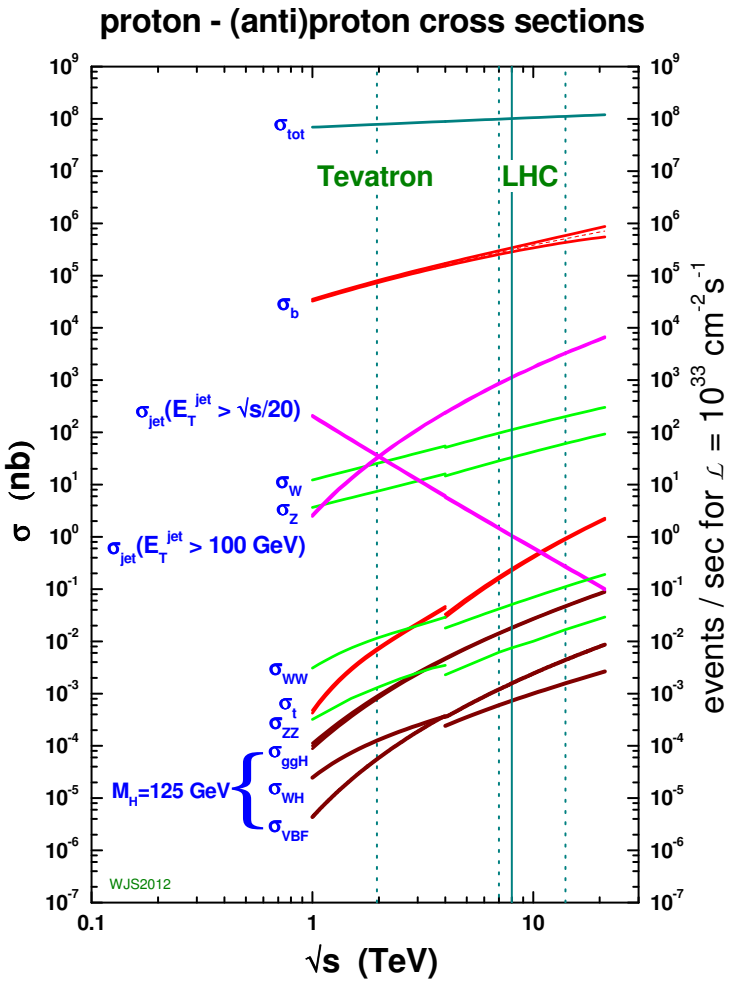

FIGURE 3.2: Cross-sections for specific physics processes in pp or $p\bar{p}$ collisions as function of $\sqrt{s}$. The vertical lines annotate the Tevatron and LHC collision energies of $\sqrt{s} = 1.96$ TeV and $\sqrt{s} = 8$ TeV, respectively [58].

3.2 The LHC Experiments

The four large experiments installed at the LHC ring are **A** **T**oroidal **L**HC **A**pparatu**S** (ATLAS) [59], **C**ompact **M**uon **S**olenoid (CMS) [60], **A** **L**arge **I**on **C**ollider **E**xperiment (ALICE) [61] and **LHC**-**b**eauty (LHCb) [62]. These experiments are located at the four LHC interaction points illustrated in Figure 3.2 and are dedicated to very different physics programmes. ATLAS and CMS are general purpose experiments, meaning that they are designed for a broad variety of measurements and searches for new physics in pp collisions. As will be explained in Section 3.3, this necessitates an apparatus that can accommodate a large variety of final-state objects over a broad kinematic spectrum. The ALICE experiment is designed to conduct heavy-ion physics, for which reason the LHC collides heavy nuclei instead of protons every year for a few weeks. LHCb is dedicated to the

study of b-physics through measurements involving B-meson decays. Three smaller experiments are installed on the LHC ring in addition to the above; **TOT**al cross section, **E**lastic scattering and diffraction dissociation **M**easurement at the LHC (TOTEM) [63], **Mo**nopole and **E**xotics **D**etector **A**t the **L**HC (MoEDAL) [64] and **LHC f**orward (LHCf) [65]. As their names indicate, TOTEM is designed to conduct a measurement of the total elastic pp cross-section, MoEDAL searches for magnetic monopoles and exotic, highly ionising stable particles, while LHCf studies high-energy neutral pions created by the collisions in the very forward region.

3.3 The ATLAS Detector

ATLAS is the largest-volume detector ever constructed at a collider, measuring an impressive 44 m in length and 25 m in height. To conduct a diverse physics programme and thus maximally benefit from the LHC collisions, the detector has been designed as a general purpose experiment, meaning that it is capable of accurately detecting a broad range of final-states. To facilitate this approach, three independent detector systems are used – the Inner Detector, the Calorimeters and the Muon Spectrometer. As will be elaborated in Section 3.4 to Section 3.6, these are dedicated to separate tasks. The trigger and data acquisition systems are described in Chapter 3.7. An illustration of the full ATLAS detector is presented in Figure 3.3.

The performance requirements of ATLAS were defined by an ambitious physics programme spanning from QCD and electroweak precision measurements to potential discoveries of new elementary particles, calling for sensitivity to different signals in a wide variety of final-states with vastly different topologies. Fulfilling this objective necessitates excellent tracking, particle identification and charge measurement, precise calorimetry for electromagnetic and hadronic showers, precise muon momentum measurement and efficient triggering over a large kinematic range. The required performance of the ATLAS detector systems is summarised in Table 3.1. In addition to the above, the intensity of the LHC collisions demands tolerance for high occupancies and robustness to radiation damage. To accommodate these immensely challenging tasks, ATLAS employs instrumentation operating at the boundaries of existing technology.

The ATLAS coordinate system is defined as right-handed with origin at the proton-proton interaction point (IP), the z-axis pointing in the direction of the beamline, and the $x-y$-plane transverse to the beam direction. The positive x-axis points towards the centre of the LHC and the positive y-axis upwards. The two geometric halfs of ATLAS located at $z > 0$ and $z < 0$ are denoted side-A and side-C, respectively. Due to the cylindrical geometry of the detector, position is often specified in cylindrical coordinates. The azimuthal angle ϕ is measured about the z-axis with $\phi = 0$ defined on the positive x-axis, and the polar angle θ defined from the positive z-axis.

Commonly, instead of the variable θ, the pseudorapidity η is used, defined as:

$$\eta = -\ln\left[\tan\left(\frac{\theta}{2}\right)\right] \tag{3.3}$$

In the context of physics analysis, the angular distance ΔR is frequently used, which is defined as:

$$\Delta R = \sqrt{\Delta\eta^2 + \Delta\phi^2} \tag{3.4}$$

TABLE 3.1: The targeted resolution requirements of the ATLAS detector systems defined in the design phase among their geometrical coverage [59].

Detector	**Resolution**	**Measurement**	**Trigger**
Tracking	$\sigma_{p_T}/p_T = 0.05\%\ p_T \oplus 1\%$	$\lvert\eta\rvert < 2.5$	–
EM Calorimetry	$\sigma_E/E = 10\%/\sqrt{E} \oplus 0.7\%$	$\lvert\eta\rvert < 3.2$	$\lvert\eta\rvert < 2.5$
Hadronic Calorimetry			
Barrel and end-cap	$\sigma_E/E = 50\%/\sqrt{E} \oplus 3\%$	$\lvert\eta\rvert < 3.2$	$\lvert\eta\rvert < 3.2$
Forward	$\sigma_E/E = 100\%/\sqrt{E} \oplus 10\%$	$3.1 < \lvert\eta\rvert < 4.9$	$3.1 < \lvert\eta\rvert < 4.9$
Muon Spectrometer	$\sigma_{p_T}/p_T = 11\%$ @ $p_T = 1$ TeV	$\lvert\eta\rvert < 2.7$	$\lvert\eta\rvert < 2.4$

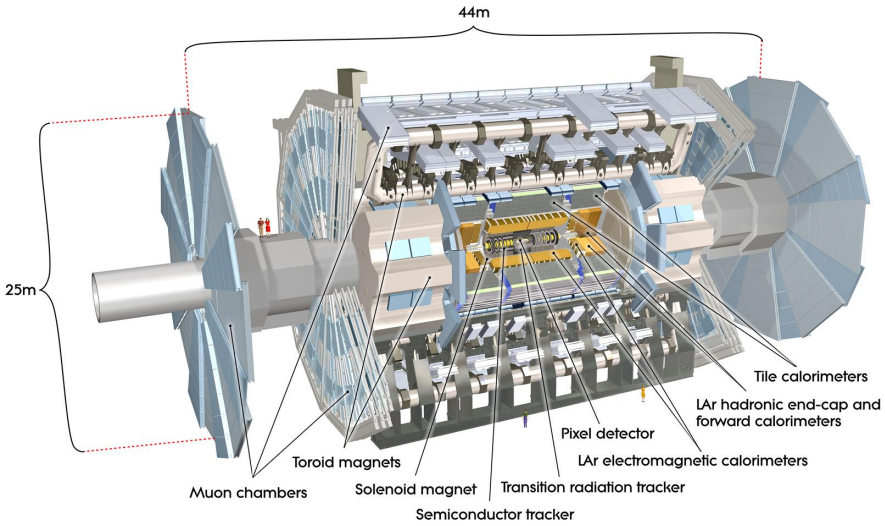

FIGURE 3.3: Schematic of the full ATLAS detector. The individual detector components of the Inner Detector, the Calorimeters and Muon Spectrometer are marked [66].

3.4 The Inner Detector

The detector system closest to the beam-pipe, the Inner Detector (ID), is dedicated to the tracking of charged particles with a p_T greater than 0.5 GeV. Generally, a track is defined by five parameters; its azimuthal and polar angle (η and ϕ), the charge of the particle divided by its momentum (q/p) determined from the track curvature, and its coordinate of origin specified by the transverse and longitudinal impact parameter (d_0 and z_0). The ID is designed to provide independent measurements of all five variables, a task that requires excellent spatial resolution in both the η- and ϕ-coordinate, among the presence of a magnetic field. This is achieved with a composition of three independent detectors, the Pixel Detector (Pixel), the Semiconductor Tracker (SCT) and the Transition Radiation Tracker (TRT). The former two are similar in terms of technology and layout, and both serve the purpose of providing space-point measurements with high precision close to the interaction point. These are supplemented by a large number of space-point measurements delivered by the TRT. To enable the measurement of p_T and charge, the entire ID is immersed in a 2 T solenoidal magnetic field. Illustrations of the ID are given in Figure 3.4 and Figure 3.5, and its specifications are summarised in Table 3.2. The three separate detectors are described in the following.

Table 3.2: Overview of the targeted spatial resolution of the Inner Detector Trackers defined in the design phase of ATLAS [59, 67, 68].

Detector	**Coverage**	**Composition**	**Resolution** [μm]
Pixel	$\lvert\eta\rvert < 2.5$		
Barrel		3 cylindrical layers	10 $(R-\phi) \times 115$ (z)
End-cap		2×3 disks	10 $(R-\phi) \times 115$ (R)
SCT	$\lvert\eta\rvert < 2.5$		
Barrel		4 cylindrical layers	17 $(R-\phi) \times 580$ (z)
End-cap		2×9 disks	17 $(R-\phi) \times 580$ (R)
TRT	$\lvert\eta\rvert < 2.0$		
Barrel		73 straw planes	130 $(R-\phi)$
End-cap		160 straw planes	130 $(R-\phi)$

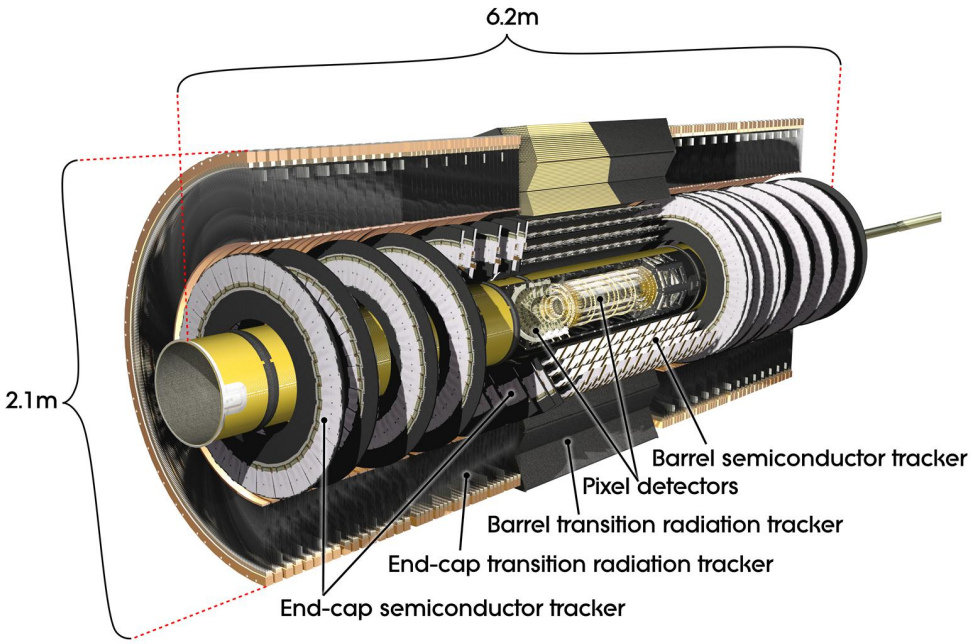

FIGURE 3.4: Illustration of the barrel and end-cap regions of the Inner Detector. The individual detector components are marked [59].

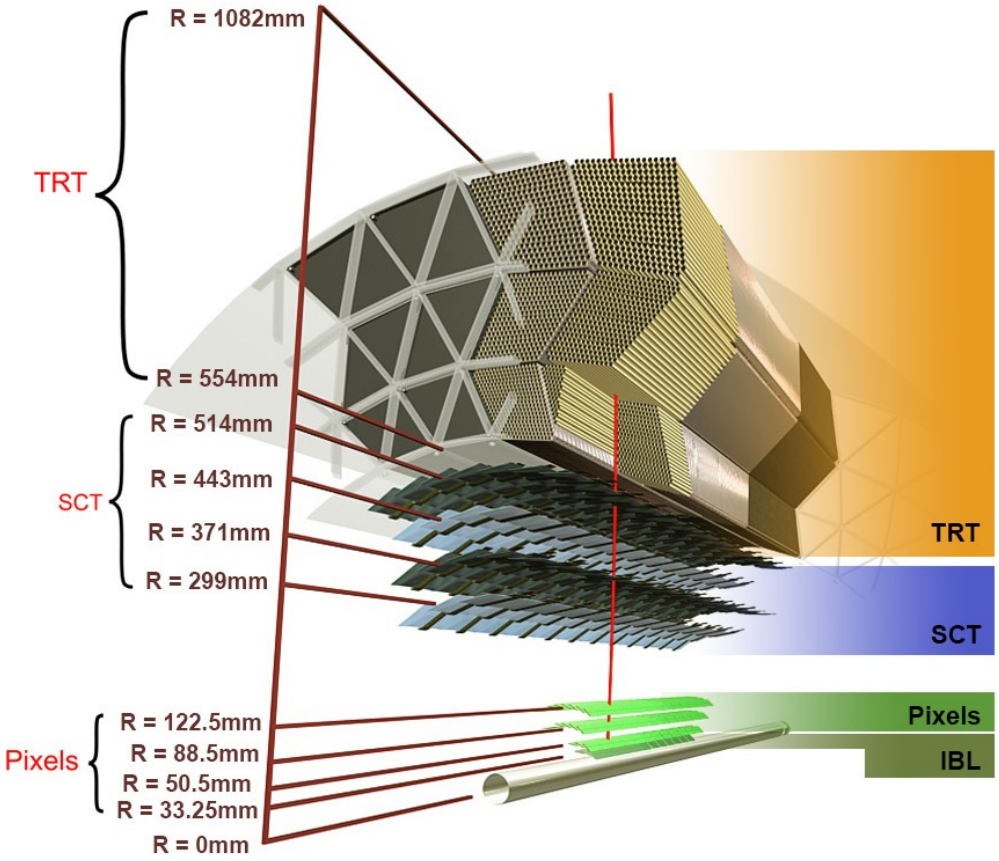

FIGURE 3.5: Illustration of a track traversing the three detectors in the ID [69].

3.4.1 Semiconductor Trackers

Both the Pixel detector and the SCT use semiconductor sensors for detection, allowing for space-point resolution in the sub-μm range and sensor granularity fine enough to maintain robust pattern recognition at the high occupancies anticipated close to the interaction point. Furthermore, both detectors measure in both the $R-\phi$- and z-coordinate. On average, a traversing particle will register 3 space-point measurement in the Pixel detector and 4 in the SCT.

The Pixel detector is composed of 256 μm thick sensors segmented into read-out pixels. As seen in Figure 3.5, in the barrel region, the sensors are mounted as cylindrical layers around the beam-pipe. The pixels in these three layers have dimensions of 50×400 μm^2 (in $\phi \times z$). In the end-cap region, the pixels are organised as disks mounted perpendicularly to the beam-pipe and also measure 50×400 μm^2 (in $\phi \times r$). Three disks are opted for in each end-cap.

In the SCT, space-point determination is done with 285 μm thick, 6.4 cm long micro-strip sensors mounted back-to-back in stereo pairs with a pitch of 80 μm. The SCT is composed of four cylindrical layers in the barrel and 9 disks mounted perpendicular to the beam-pipe in each end-cap. In the barrel, one layer of strips is aligned in the beam direction, while the other strip layer is rotated 40° in order to provide stereo-coordinate information. The same principle applies in the end-caps, however, the nominal strip layer is aligned in the radial direction.

3.4.1.1 The Insertable B-Layer

In the early phases of LHC operation, three layers were installed in the barrel region of the Pixel detector. However, in order to maintain adequate performance at an instantaneous luminosity greater than 10^{34} $\text{cm}^{-2}\text{s}^{-1}$, a fourth layer, the insertable B-layer (IBL), was integrated before the start of Run-2. As illustrated in Figure 3.5, the IBL is positioned at radial distance $R = 33$ mm, and is constructed with the same geometry and detecting medium as the existing three layers. By adding the IBL, one extra space-point measurement per traversing particle is foreseen. The IBL pixels measure 50×250 μm^2 (in $\phi \times z$), which makes it able to withstand occupancies three times higher than in the original layers. Furthermore, the IBL improves the precision of track parameters. Specifically, it is expected to reduce the error on the transverse impact parameter, which leads to an improved background rejection in physics analysis, since the discriminating power of this variable is enhanced [69].

3.4.2 The Transition Radiation Tracker

The TRT delivers a high number of space-point measurements, 36 on average, in the $R - \phi$-coordinate and it furthermore provides e/π separation. As summarised in Table 3.2, the spatial resolution is significantly lower than that of the Pixel detector and the SCT, however, this is offset by the longer distance over which a track is measured. The TRT is built as a matrix of straw tubes with a 4 mm diameter, containing a 31 μm gold-plated tungsten read-out wire along the center. The detecting medium in the TRT, a gas-mixture consisting of $Xe/CO_2/O_2$ (in the ratio 70/27/3), is filled into these straws. In its barrel region, the TRT consists of 73 planes of straws aligned with the beam-axis, while in the end-cap, it consists of 160 planes positioned parallel to the radial direction. The e/π separation is achieved with 7 – 10 high-threshold hits induced by transition radiation from electrons with energies above 2 GeV. To enhance the emission of transition radiation, polypropylene is woven between the straws.

3.4.3 Solenoid Magnet

The ID is able to measure the p_T of traversing charged particles due to the application of a solenoidal magnetic field that deflects particles in the transverse plane. This 2 T field is provided by the solenoid magnet, which surrounds the ID. The solenoid is composed of a 10 cm thick tube with a diameter of 2.56 m, length of 5.8 m, and weight of 5.4 tonnes. Despite its apparent immensity, a key aspect when design it was limiting the amount of material in front of the calorimeters in order to minimise the probability of initiating electromagnetic and hadronic showers. The 2 T field is induced by 222 windings/m of NbTi/Cu superconducting cable cooled to 4.5 K, supported by an aluminium structure. The solenoid is charged and discharged in approximately 30 minutes.

3.5 Calorimeters

As illustrated in Figure 3.6, the ATLAS calorimeters surround the ID. Overall, they can be segmented into three parts; the electromagnetic calorimeter, the hadronic calorimeters and the presampler. In order to limit their size, the ATLAS calorimeters are constructed as sampling calorimeters, meaning that an absorber is inserted into the area of energy deposition in order to enhance the stopping power, which entails that only a part of the total deposited energy is sampled and read out. The amount of material in the calorimeters in units of interaction lengths as function of η is displayed in Figure 3.7. As summarised in Table 3.3, four types of absorber and two types of detecting media are utilised. A description of the calorimeters is presented in the following sections.

Table 3.3: An overview of the ATLAS calorimeter components [59, 70].

Component	Absorber	Active medium	Coverage
Electromagnetic			
Barrel	Lead	Liquid argon	$\|\eta\| < 1.475$
End-cap	Lead	Liquid argon	$1.375 < \|\eta\| < 3.2$
Forward	Copper	Liquid argon	$3.1 < \|\eta\| < 4.9$
Hadronic			
Barrel	Steel	Scintillating tiles	$\|\eta\| < 1.7$
End-cap	Copper	Liquid argon	$1.5 < \|\eta\| < 3.2$
Forward	Tungsten	Liquid argon	$3.1 < \|\eta\| < 4.9$
Presampler			
Barrel	None	Liquid argon	$\|\eta\| < 1.475$
End-cap	None	Liquid argon	$1.5 < \|\eta\| < 1.8$

3.5.1 Liquid Argon Calorimeters

Liquid argon (LAr) is frequently used as detecting medium due to its intrinsic linear behaviour, radiation-hardness, stability, and low cost. Liquid argon is used in four different calorimeter components; the electromagnetic barrel calorimeter (EMB), electromagnetic end-cap calorimeter (EMEC), the hadronic end-cap calorimeter (HEC) and the forward calorimeter (FCal). To keep it liquid, all these components are installed inside cryostats maintaining an operating temperature of 88.5 K [70].

The EMB and EMEC share the same distinct layout; The liquid argon is contained between stacks of absorbing material, lead, which is conformed into accordion-like shapes, as illustrated in Figure 3.8. Readout electrodes are located in the gap between the absorbers. This specific geometry is advantageous because it naturally provides full coverage in ϕ without any cracks. In the EMB, the accordion waves are axial and arranged in ϕ, whereas in the EMEC, they are rotated 90° to ensure full coverage. In both the EMB and EMEC, three calorimeter layers at different depths are distinguished and read out separately. As illustrated in Figure 3.8, the granularity decreases as a function of depth; the front layer provides a finely segmented description of the lateral shower profile, the middle layer gives the bulk of the energy measurement, while the rear layer is meant to capture the tail end of the electromagnetic showers. Similar principles apply to the HEC modules, however, the absorber plates of this calorimeter component are flat instead of accordion-shaped and made from copper instead of lead.

The FCal is located in the very forward region of ATLAS. Because of the high rates impinging in

this region, it is designed significantly different compared to the other LAr components. The FCal is a combined electromagnetic and hadronic calorimeter consisting of three cylinders of absorber (divided in z), the first made from copper (FCal1) and the other two made from tungsten (FCal2, FCal3). Holes are drilled into the absorber in the beam direction, and read-out rods are positioned in these holes. The liquid argon is contained in the gaps surrounding these rods.

Lastly, liquid argon is also used in the presampler, which is an individual component that has been added to detect the rarely occurring showers initiated by material interaction before the calorimeters, for example in the ID, support structures or the cryostat. The presampler does not have its own cryostat, but is instead integrated into the existing barrel and end-cap cryostat.

3.5.2 Tile Calorimeter

The Tile Calorimeter (TileCal) is positioned outside of the LAr calorimeter and is designed to measure hadronic activity in the central region of ATLAS. This detector employs steel as an absorber and scintillating tiles as detecting medium. Slices of these two materials are arranged into wedge-like structures installed inside a steel support structure, a so-called girder, as illustrated in Figure 3.9. The scintillating tiles are oriented radially to the beam-axis. Upon the incidence of an ionising particle in a scintillating tile, ultraviolet light is emitted from the base material (polystyrene) and subsequently converted to visible light by wavelength shifting flours. This light is collected at the edges of each scintillating tile using two wavelength shifting fibres (WLS), also illustrated in Figure 3.9. These WLS have a diameter of 1 mm and are equipped with double-cladding. The WLS are grouped together in bundles and coupled to photo-multipliers (PMTs). These PMTs are housed at the outer edge of the mechanical girder in so-called drawers, which also contain the TileCal front-end electronics. The grouping of the WLS bundles define the read-out granularity in $\Delta\eta \times \Delta\phi$. Likewise the LAr calorimeters, the read-out of the TileCal is segmented according to depth, also with granularity decreasing with radial distance [71].

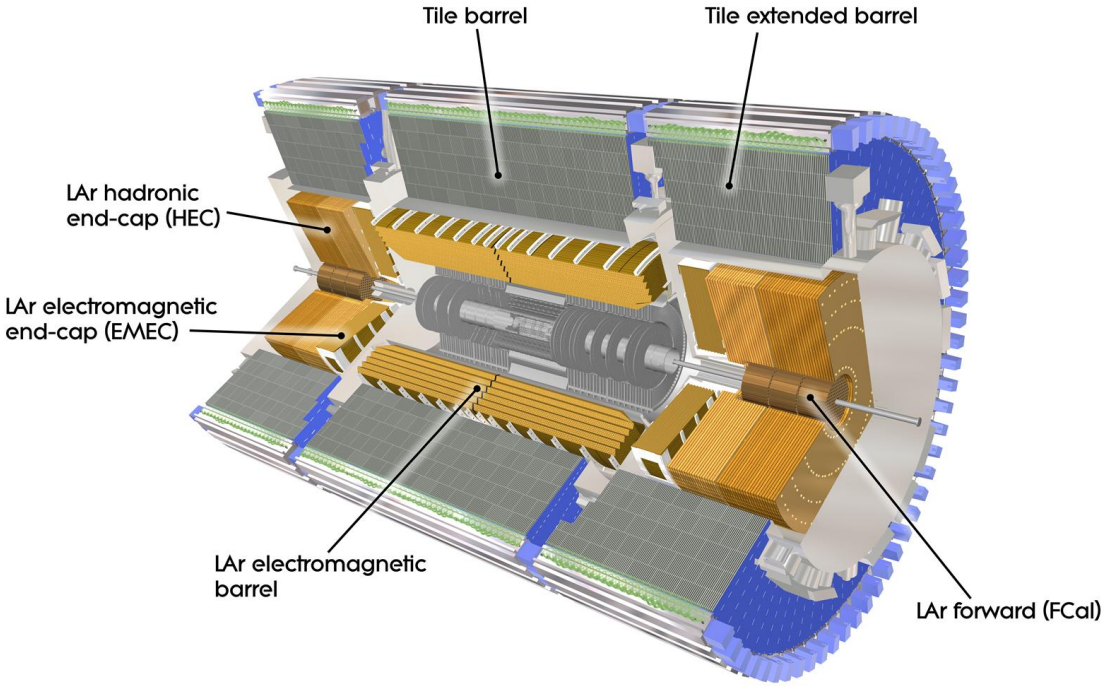

Figure 3.6: Illustration of the ATLAS calorimeters. The individual components of the various calorimeters are marked [59].

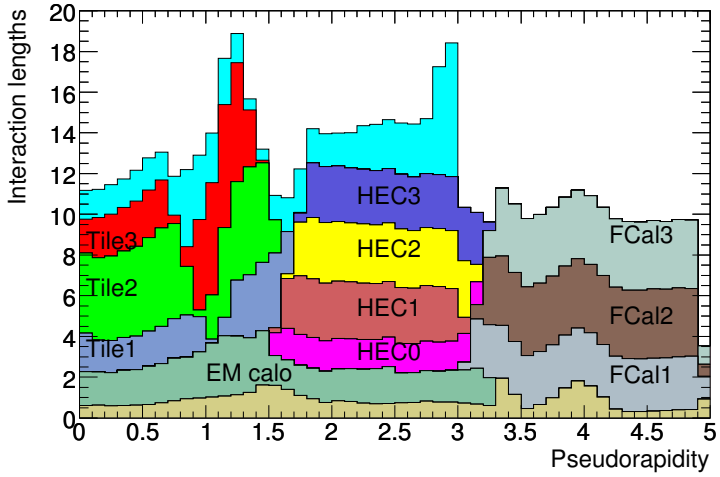

Figure 3.7: Cumulative amount of material in the ATLAS calorimeter components in units of interaction length as a function of η [59].

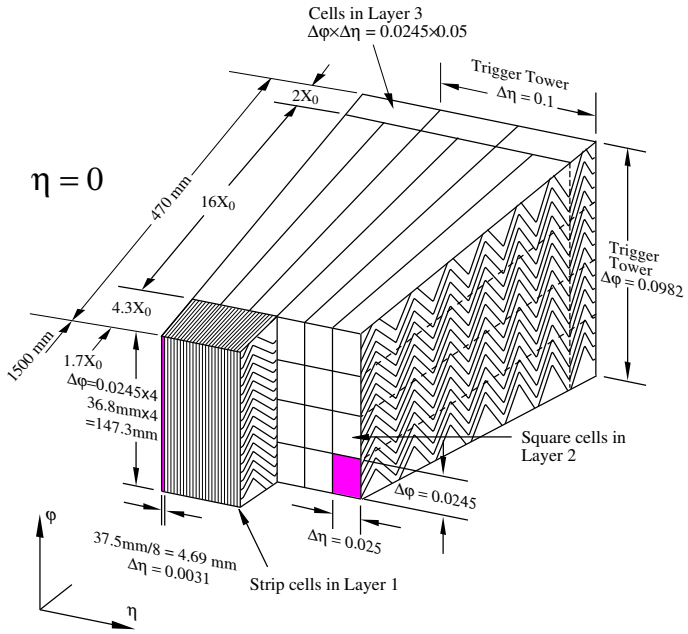

FIGURE 3.8: lllustration of the accordion-like arrangement of the absorber employed in the EMB and EMEC [59].

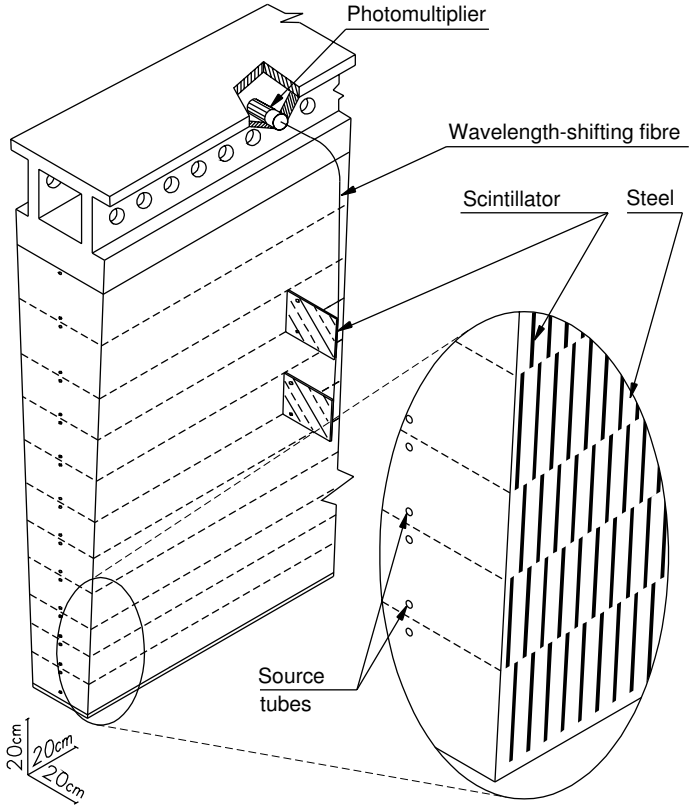

FIGURE 3.9: lllustration of a Tile Calorimeter wedge and the implementation of the optical read-out [59].

3.6 Muon Spectrometer

As illustrated in Figure 3.3 and Figure 3.10, the Muon Spectrometer (MS) constitutes the outermost layers of the ATLAS detector. With its volume of 16.000 m^3 and surface area of 5.000 m^2 it is the largest detector system.

A series of physics benchmark processes were used to define its necessary performance. Of particular importance was the decay of a Higgs boson into the four-lepton final-state via the process $H \rightarrow ZZ^{(*)} \rightarrow 4\ell$, which is of special interest to this thesis. To enable a measurement of momentum, the system is immersed in a 0.5 – 1 T toroidal magnetic field bending the traversing particles in the η-plane. The tremendous size of the MS was motivated by requirements on its capabilities as a magnetic spectrometer; the long lever arm results in a more accurate momentum measurement, the benchmark being a relative resolution of 3% over a wide p_T range and a maximum of 11% at $p_T = 1$ TeV. In addition to the above, the spectrometer was also designed to provide level-1 triggering [72].

The detector technologies used in the MS were chosen for their ability to cost-effectively cover the large area, provide space-point measurements accurate enough to satisfy the requirements for momentum resolution, and provide a response fast enough to be used as a triggering detector. Four different technologies, all gas-based, are employed; two dedicated to precision measurements and two to triggering, as summarised in Table 3.4. Like the other ATLAS systems, the MS is divided into a barrel region and an end-cap region. The arrangement of the muon chambers is similar to that of the semiconductor trackers; the detectors are arranged as three cylindric layers around the beam-pipe in the barrel region, and three disks in each end-cap region. The barrel layers are positioned at radial distance of $R = 5$ m, 7.5 m and 10.5 m and the end-cap disks at $z = 7.4$ m, 14 m and 21.5 m. The four detector technologies in the MS are described in the following sections.

Table 3.4: Overview of the specifications of the ATLAS Muon Spectrometer. The quoted resolution is for a full chamber of the given technology, i.e. multiple detector planes [59].

Technology	**Coverage**	**Resolution**
Precision		
MDT	$\lvert\eta\rvert < 2.7$	35 μm (z)
CSC	$2.0 < \lvert\eta\rvert < 2.7$	40 μm $(R) \times 5$ mm (ϕ)
Trigger		
TGC	$1.05 < \lvert\eta\rvert < 2.7$	2 – 6 mm $(R) \times 3$ – 7 mm (ϕ)
RPC	$\lvert\eta\rvert < 1.05$	10 mm (z) $\times$ 10 mm (ϕ)

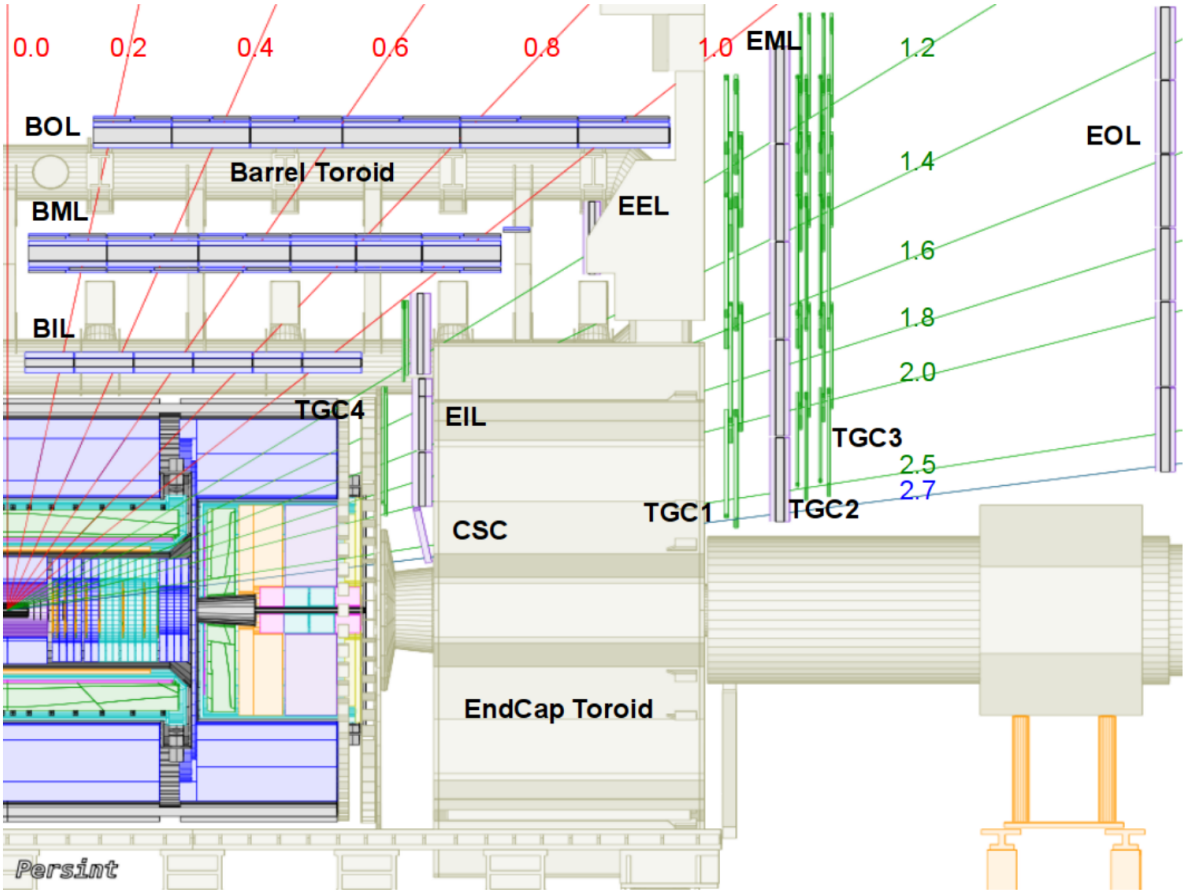

FIGURE 3.10: Illustration of the MS in the $y - z$-plane. The three layers in both barrel and end-caps are referred to as stations. The inner, middle and outer barrel (end-cap) stations are denoted BI (EI), BM (EM) and BO (EO), respectively [73].

3.6.1 Monitored Drift Tubes

The Monitored Drift Tubes (MDTs) are tailored to the task of precision tracking in all barrel and end-cap layers. One MDT tube consists of an aluminium cylinder of 30 mm diameter with a 50 μm tungsten-rhenium read-out wire positioned along its center. The MDTs are operated in proportional mode with an Ar/CO_2 (in the ratio 93/7) gas-mixture. The tubes are aligned perpendicular to the η-direction and hence only provides a measurement in this coordinate. The ϕ-coordinate is provided by the supplementary trigger chambers. Each MDT chamber in ATLAS is composed of three to eight layers of drift tubes, which combined provide a resolution of 35 μm in the η-direction. This composition is advantageous from an operational viewpoint since the loss of a single tube does not degrade the operation of others. The performance of the MDTs is highly dependent on the incoming flux of particles; at rates above 300 kHz/tube the hit efficiency is degraded by 35%. Due to this inefficiency, among other reasons, the Muon Spectrometer will undergo an upgrade in 2018,

which will replace the MDTs in the regions of ATLAS with the highest incoming particle rate. Details on this are given in [72].

3.6.2 Cathode Strip Chambers

Since the rate capability of the MDT technology is insufficient to operate at high η in the inner-most end-caps of the MS, Cathode Strip Chambers (CSC) are used in these regions instead. This technology offers excellent spatial resolution and can operate safely at counting rates up to 1 kHz/cm^2 [59]. The CSC is a permutation of the classical Multi-Wire Proportional Chamber (MWPC). It consists of parallel cathode planes with wires suspended in the η-direction in the gap. Strips in both the η and ϕ direction have been etched into the cathode planes, enabling the CSC to provide space-point measurements in both coordinates. The CSC is operated in proportional mode with an Ar/CO_2 gas-mixture (in the ratio 80/20). Under optimal signal-to-noise conditions the CSC provides a resolution of 60 μm per plane in the η-coordinate, and a resolution of 5 mm in the ϕ-coordinate. The particles encountering the CSC are measured in four consecutive planes. Because the spatial resolution provided by the CSC is sensitive to the angle of the trajectory, the CSC chambers are tilted by an angle of 12° such that particles originating from the IP on average are normal to the surface of the chambers.

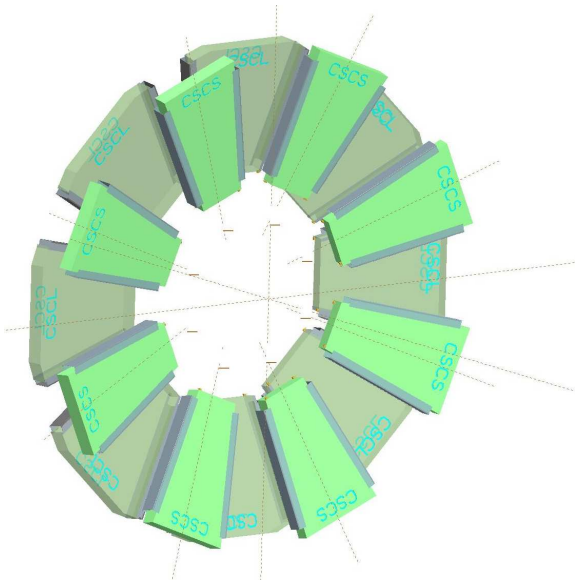

Figure 3.11: Layout of the CSC chambers [59].

3.6.3 Thin Gap Chambers

Thin Gap Chambers (TGCs) are used for triggering up to $|\eta| < 2.4$ and for measuring the ϕ-coordinate of particles in the end-cap regions. This technology is also based on the MWPC; wires are suspended in the η direction between two electrode planes, and strips are etched into one of the planes in order to read out the ϕ-coordinate. The η-coordinate is measured by groups of activated wires. The TGCs are operated with a highly quenching gas mixture of CO_2 and n-C_5H_{12} in a quasi-saturated mode, meaning that a gas gain of $\sim 3 \times 10^5$ is achievable. This type of operation allows for a fast response, which is needed to obtain functionality as a trigger detector. In the middle end-cap station of the MS, the MDT chambers are complemented by seven layers of TGCs: three in front of the MDT chambers and four behind. Combined, the TGC chambers in this station

measure the slope of the muon tracks with a precision of 2 – 3 mrad. This precision is needed in order to identify the trajectories pointing towards the primary vertex, which are used as a seed for the trigger. In the inner-most end-cap station of the MS, only two layers of TGCs are used. These do not provide a trigger, but offer a ϕ-coordinate measurement.

3.6.4 Resistive Plate Chambers

Resistive Plate Chambers (RPCs) are used for triggering in the barrel region of ATLAS. These detectors are wireless, parallel-plate detectors made with the highly resistive material Bakelite as electrodes. Metallic strips arranged in both the η- and ϕ-direction are mounted on the outer surface of the Bakelite plates. A signal is obtained in these metallic strips via a capacitive coupling with the Bakelite plates. The RPCs in ATLAS are operated in so-called saturated proportional mode with a gas-mixture consisting of $C_2H_2F_4$/Iso-C_4H_{10}/SF_6 (in the ratio 94.7/5/0.3). This operation enables the RPCs to deliver an extremely rapid signal with a rise time of ~5 ns and very small time jitter, which is needed for triggering. The RPCs are assembled together with MDT chambers of equal dimensions and integrated into a common mechanical structure. The trigger system in the barrel consists of three stations: two positioned around the MDTs in the middle barrel layer of the MS, and one mounted in the outer layer of the MS. The lever arm between the inner and outer RPCs permits the trigger to select high momentum tracks in the range 9 – 35 GeV, while the two inner chambers provide a low-p_T trigger on particles in the range 6 – 9 GeV.

3.6.5 Run-2 Updates

During the shutdown between Run-1 and -2, the initial design of the MS was completed by adding the last missing chambers in the transition region between the barrel and the end-caps ($1.0 < |\eta| < 1.4$), resulting in a 4% increase in the acceptance for muons at the level-1 trigger. In addition, four RPC-equipped MDT chambers were installed at the bottom of the ATLAS barrel between the middle and outer, and beyond the outer chamber layer of the MS, respectively, in order to improve efficiency in that region. A portion of the new MDT chambers contain tubes with a smaller radius compared to the ones used in the rest of the detector, allowing them to operate at higher rates [74].

3.6.6 Toroidal Magnets

The MS is able to measure the momentum of incident particles due to the application of a toroidal magnetic field bending particles in the η-plane. The toroidal magnet system consists of three individual magnets; a barrel toroid and two end-cap toroids. The barrel and end-cap toroids provide magnetic fields of 0.5 T and 1 T, respectively. For $|\eta| < 1.4$, the bending power is achieved solely through the use of the barrel toroid, while for$1.6 < |\eta| < 2.7$, the deflection comes from the end-cap toroid magnets. In the transition region covering $1.4 < |\eta| < 1.6$, the fields from both barrel and end-cap toroids contribute. All three toroidal components consist of eight coils arranged around the beam-pipe in ϕ, as illustrated in Figure 3.12. The magnetic fields are induced by windings of the NbTi/Cu superconductor cooled to 4.6 K. The coils in the barrel are air-core, span 25.3 m in length, and have inner and outer diameters of 9.4 m and 20.1 m, respectively. These coils are contained in individual cryogenic containers. The smaller end-cap coils are contained in a common cryogenic compartment in each end-cap.

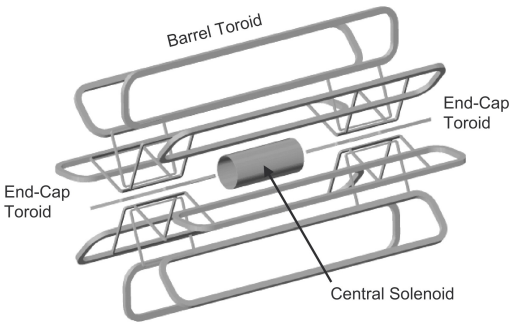

Figure 3.12: Schematic of the central solenoid and the three toroidal magnets [59].

3.7 Trigger and Data Acquisition

As explained earlier in this chapter, at peak luminosity, collisions will happen with bunch spacing of 25 ns resulting in a collision rate of 40 MHz. It is beyond the capabilities of existing technology to store the event information from all collisions. Therefore, ATLAS uses a sophisticated trigger system to make a harsh selection in which LHC collisions should be stored permanently and utilised for physics analysis. The multi-levelled trigger system consists of level-1 (L1), level-2 (L2) and the event-filter (EF), the latter two known as the High Level Trigger (HLT). Each trigger level refines the decisions made at the previous level and applies additional selection criteria. Events are stored for analysis if they pass all levels. As will be described below, upgrades were implemented between Run-1 and Run-2 to optimise the efficiency and bandwidth of the trigger system [75].

The hardware-based L1 trigger reduces the event rate significantly, in Run-1 to 75 kHz. This trigger level selects interesting objects such as high-p_T muons, electrons, photons, jets and τ-lepton decays, as well as large missing and total transverse energy. Muons are identified using the RPC and TGC detectors, as explained in Chapter 3.6, while the other objects are selected with the

calorimeter trigger (L1Calo) using information from all the calorimeter components mentioned in Chapter 3.5. All this information is used by the L1 trigger to define Regions of Interest (RoI), locations in η and ϕ containing interesting signatures. The output from the muon trigger chambers and L1Calo are processed by the Central Trigger Processor (CTP), which combines this information into triggers. Since the operating conditions of the LHC vary, it is possible to pre-scale the triggers such that bandwidth is used optimally as luminosity and background conditions change. The latency of the L1 trigger selection is up to 2.5 μs, during which the event data is buffered in memory located within the detector-specific front-end electronics.

In Run-1, the L2 and EF levels were separated. The L2 trigger selection was done on a processing farm using the RoI information provided by the L1 trigger as a seed. The L2 selection used all the available detector information within the RoIs with full granularity and precision, amounting to 2% of the total data from the event. After the L2 selection, the rate was reduced to ~3.5 kHz. The final stage of the event selection was carried out by the EF, which reduced the event rate to roughly 400 Hz using offline analysis procedures. Event passing all three levels were accepted for permanent storage.

The change in the LHC operating conditions happening between Run-1 and Run-2 described in Section 3 causes the trigger rates to grow by a factor of approximately 5. To maintain functionality and performance of the trigger and data acquisition system, a series of upgrades were implemented between the two operating periods. The L1 accept rate was increased to 100 kHz and a so-called topological trigger was implemented, allowing for more refined event characteristics to be taken into account in the L1 decision. Furthermore, the two HLT levels were merged into one level for simplification and dynamic resource sharing, the net effect being that the HLT output rate was elevated to 1 kHz at peak luminosity.

3.7.1 Minimum Bias Trigger Scintillators

Part of the ATLAS physics programme relies on the ability to trigger on charged particles in the forward region with minimal bias. For this purpose, ATLAS employs a dedicated set of detectors, the Minimum Bias Trigger Scintillators (MBTS). These detectors are integrated into the TileCal read-out chain, since they rely on the same physical principle and are placed in the same region.

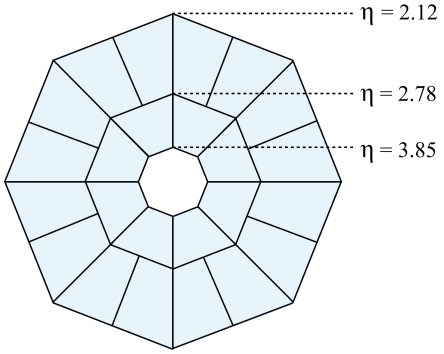

FIGURE 3.13: Layout of a Run-1 MBTS disk.

As the name indicates, the MBTS are scintillation detectors consisting of 2 cm thick scintillating plastic tiles of the

same type as deployed in the TileCal. They are installed in a ring around the beam-pipe on the face of the LAr Calorimeter end-cap cryostat at $z = \pm 3.6$ m. In Run-1, each counter contained two independent sectors; an inner sector at radial distance $14 \leq r \leq 43$ cm ($2.83 < |\eta| < 3.85$) and an outer sector at $43 \leq r \leq 88$ cm ($2.12 < |\eta| < 2.83$), the latter constructed from two individual parts. Both inner and outer sectors were trapezoidal in shape and covered $2\pi/8$ in ϕ. This layout is illustrated in Figure 3.13. Light from the sectors were collected by wave-length shifting optical fibers (WLS) embedded into grooves in the surface of the counter. Both the inner and outer sector was read out with 8 WLS, resulting in a total of 16 channels per MBTS counter. The light collected by the WLS was transported with clear optical fibers to the TileCal drawers and read out with TileCal photomultipliers and front-end electronics. In Run-1 the trigger readout was implemented by applying a leading-edge discriminator to the MBTS signal, which sent a signal to the Central Trigger Processor (CTP) for all modules over the given threshold, meaning that the MBTS served as a level-1 trigger. As will be described in Chapter 9, because of the very large radiation dose deposited during Run-1, the MBTS underwent a full replacement before the start of Run-2 [76, 77].

3.8 ATLAS Data Processing and Simulation

The data recorded by ATLAS passes through a complex processing chain before being ready for physics analysis. The output of the ATLAS detector, the RAW data, is composed of the events passing the final trigger level. This data has binary format and each event has a size of around 1.6 MB. In the Run-1 data processing chain, the RAW data is promptly processed with the ATHENA [78] software framework into data formats with object-oriented representation: at first into an Event Summary Data (ESD) format with an event size of 1 MB, and afterwards into an Analysis Object Data (AOD) format with an event size of 100 KB. The AODs are afterwards converted into Derived Physics Data files (D3PD), the format of which is well-suited for physics analysis because it easily can be accessed by standard tools such as ROOT [79]. The physics working groups in ATLAS define separate D3PDs containing the physics objects etc. relevant for the analysis in question. In Run-2, in order to harmonise the content of the D3PDs and reduce the manpower needed to produce the separate D3PDs, the data processing chain was redesigned such that the AOD and D3PD formats are replaced by a common format, the xAOD, which merges the two former formats. As a result, physics analysis in Run-2 is performed directly on the xAOD files [80, 81, 82, 83, 84].

A large portion of the ATLAS computing resources are dedicated to generating Monte Carlo (MC) samples. Five steps are needed to generate such samples. The first step, the event generation, consists of simulating particle production in the given collisions. This is done within the ATHENA framework and can be performed with most of the available event generators, an example being

PYTHIA [85]. Each generated event contains the particles emanating from a single interaction with the vertex located at the geometric origin. These generated events are afterwards passed on to the detector simulation. In this step, the response of the ATLAS detector components are simulated with the GEANT4 framework [86], which computes the interactions of the particles, including secondaries, with the detector material. Following the detector simulation, events are digitised. In the digitisation, the interaction of the particles are converted into detector signals. Furthermore, pile-up events are added. The output from this stage is equivalent to the RAW data coming from ATLAS. Following this step, the generated events are processed in the same way as the data.

CHAPTER 4

Overview of Heavy Higgs Boson Searches

4.1 Overview

The upcoming three chapters present searches for an additional, heavy Higgs boson in the $H \to ZZ^{(*)}$ decay channels. This Higgs boson is assumed to be heavier than the SM Higgs boson, CP-even and carrying no electric charge, and is such compatible with the 2HDM Higgs boson H described in Chapter 2. Despite targeting a resonance with great similarity to this particular 2HDM Higgs boson, the following searches aim at being as *model-independent*[1] as possible in order to broaden the sensitivity to a range of signals that is wider than described by 2HDM. In the context of this thesis, the model-independent approach entails that a minimum of assumptions are made about the signal. To facilitate this, the signal is modelled with the Narrow Width Approximation (NWA) described in Chapter 2, in which the signal has a very small width that is fixed over the full m_H range under consideration. By doing so, the dependency of Γ_H on m_H, which is present in for example the SM, is removed, meanwhile interference effects can be ignored. Furthermore, the model-independent approach is promoted by, whenever possible, avoiding assumptions about the relative rate of the ggF, VBF and VH production modes.

The three searches of this thesis are presented in chronological order. The first two analyses rely on data recorded during the Run-1 data-taking period, while the latter uses data recorded during Run-2.

The first analysis, the search for a heavy Higgs boson in the $H \to ZZ^{(*)} \to 4\ell$ decay channel using 20.3 fb^{-1} of data recorded at $\sqrt{s} = 8$ TeV, is presented in Chapter 5. The final results of this analysis are model-independent upper limits on the heavy Higgs boson production rate. The sensitivity of this analysis is enhanced by combining it with corresponding searches performed in

[1] The author acknowledges the inadequacy and self-contradiction of the phrase *model-independent*. However, in lack of a better expression, this term will be used throughout the thesis.

the three additional $H \to ZZ^{(*)}$ decay channels, $ZZ^{(*)} \to 2\ell 2\nu$, $2\ell 2q$ and $2\nu 2q$. This combination, which constitutes the second analysis of this thesis, is presented in Chapter 6. The combined results from these four searches include model-independent upper limits on the heavy Higgs boson production rate, among a 2HDM interpretation. The combination of these four searches improve on existing Run-1 searches conducted by ATLAS, which were performed in fewer decay channels and utilised the smaller data-set of 4.8 fb^{-1} recorded at the lower collision energy of $\sqrt{s} = 7$ TeV [87, 88, 89]. Furthermore, the previous searches did not perform a combination, meaning that the work presented in this thesis constitutes the first combination of the four $H \to ZZ^{(*)}$ decay channels performed by ATLAS. The work presented in Chapter 5 and Chapter 6 was finalised during Spring 2015 and published in EPJ C [90].

The third heavy Higgs boson search of this thesis is presented in Chapter 7. Here, a narrow resonance is targeted again and the $H \to ZZ^{(*)} \to 4\ell$ decay channel is used. This search is conducted with the very first portion of data recorded at $\sqrt{s} = 13$ TeV, and it is hence one of the first finalised searches performed with Run-2 data. The final results of this search are presented as model-independent upper limits on the heavy Higgs boson production rate. This latter analysis was performed during Fall 2015 and presented at the CERN Council meeting in December 2015.

Chapter 8 summarises the findings of the searches and discusses the projections for heavy Higgs boson searches at future LHC operation.

4.2 Author's Contribution

The author's contribution to the three upcoming chapters were:

- **Chapter 5**: Event selection optimisation studies (the double Z mass constraint presented in Section 5.3.5), signal modelling and production of results.
- **Chapter 6**: Implementation and execution of the combination, editor of internal documentation, as well as production of final results (both upper limits and the 2HDM interpretation).
- **Chapter 7**: Editor of the internal supporting documentation, workspace validation, production of results.

CHAPTER 5

Search for an Additional, Heavy Higgs Boson in the H →ZZ$^{(*)}$ →4l Decay Channel Using √s = 8 TeV Data

5.1 Introduction

This chapter presents the search for a heavy Higgs boson in the $H \to ZZ^{(*)} \to 4\ell$ channel with 20.3 fb^{-1} of pp collision data recorded at $\sqrt{s} = 8$ TeV. This particular decay of a Higgs boson into two Z bosons and subsequently to four leptons (either electrons or muons) is considered a benchmark process in experimental Higgs physics, since it is characterised by an excellent experimental resolution and has a highly favourable signal to background ratio. The $H \to ZZ^{(*)} \to 4\ell$ channel played a crucial role in the discovery of the SM Higgs boson in 2012 and in the subsequent measurements of its properties. However, as will be demonstrated in this chapter, this decay channel also holds great potential in the context of searches for additional Higgs bosons at masses above 125 GeV.

The following analysis searches for an additional, heavy, CP-even Higgs boson in the range $140 < m_H < 1000$ GeV, predicted by theories such as 2HDM, described in Chapter 2. In order to be sensitive to a wide range of signals, the following search aims at being as model-independent as possible, entailing minimal reliance on model-specific assumptions, as described in Chapter 4.

The following analysis employs a shape-based approach, meaning that it is conducted by searching for a signal that is located on top of a background distribution. The discriminant of the analysis, i.e. the variable that is used to distinguish signal and background events, is the invariant mass of the four leptons in the final-state, $m_{4\ell}$. The presence of a signal is quantified with the signal-strength μ, which is a scale factor on the yield (i.e. the number of events) of the signal, defined

with a pre-specified number of events as a reference. To determine the largest possible value of μ supported by data, the yields and shapes of the $m_{4\ell}$ distribution from the background and the hypothesised signal are combined into a statistical model, which is a likelihood function of the form:

$$\mathcal{L}(x_1, ..., x_n|\mu) = \text{Pois}(n|\mu S + B) \times \left[\prod_{e=1}^{n} \frac{\mu S f_S(x_e) + B f_B(x_e)}{\mu S + B}\right] \tag{5.1}$$

Here $x_i, ..., x_n$ are the n events observed in data, S and B are the predicted signal and background yields, while $f_S(x_e)$ and $f_B(x_e)$ are probability distribution functions (PDFs) describing the shape of the $m_{4\ell}$ distributions for the signal and background, respectively. The function above is used to derive upper limits on μ, which afterwards are translated into final results in the form of upper limits on the heavy Higgs boson production rate.

In order to go through the procedures listed above and thus perform the full analysis, a series of independent steps are needed. At first the event selection is defined, which is applied to the data-set and Monte Carlo samples in order to select events with four well-reconstructed leptons compatible with having originated from a decaying Higgs boson. This is described in Section 5.3. To construct the function in Equation 5.1, the shape and yield of the signal and backgrounds must be determined. The modelling of the signal is explained in Section 5.4, followed by the background estimation in Section 5.5. The systematic uncertainties of the search are described in Section 5.6. The statistical procedures used to extract results are described in Section 5.7. The final results in terms of upper limits on the heavy Higgs boson production rate are presented in Section 5.8.

5.2 The √s = 8 TeV Data-Set

The analysis of this chapter rely on the data-set recorded during Run-1, in which pp-collisions were delivered at $\sqrt{s} = 8$ TeV. Figure 5.1 shows the integrated luminosity delivered by the LHC and recorded by ATLAS throughout this period. The total amount of data recorded at $\sqrt{s} = 8$ TeV amounts to 21.3 fb^{-1}, however, given the data-taking efficiency of the ATLAS detector components listed in Table 5.1, only 20.3 fb^{-1} of the data is suited for usage in physics analysis.

Due to the intense operating conditions of the LHC described in Chapter 3, the phenomenon known as pile-up is inevitable. Two types of pile-up are distinguished; in-time and out-of-time pile-up. In-time pile-up is the occurrence of multiple pp interactions in one bunch crossing [91], resulting in multiple vertices being reconstructed per event. Out-of-time pile-up happens because

the read-out time of certain detector components (mainly the calorimeters) is longer than the time-span between the collisions, the result being that collisions from preceding/subsequent bunches distort the signal that is being read out. The distribution of the average number of pp interactions per bunch crossing, $\langle\mu\rangle$, during Run-1 is presented in Figure 5.1. As observed, the average number of interactions during the $\sqrt{s} = 8$ TeV data-taking is $\langle\mu\rangle = 20.7$, out of which the vast majority are caused by processes that are not related to the hard interaction that is of relevance to this search. Corrections for both types of pile-up are applied in the digitisation mentioned in Chapter 3.8.

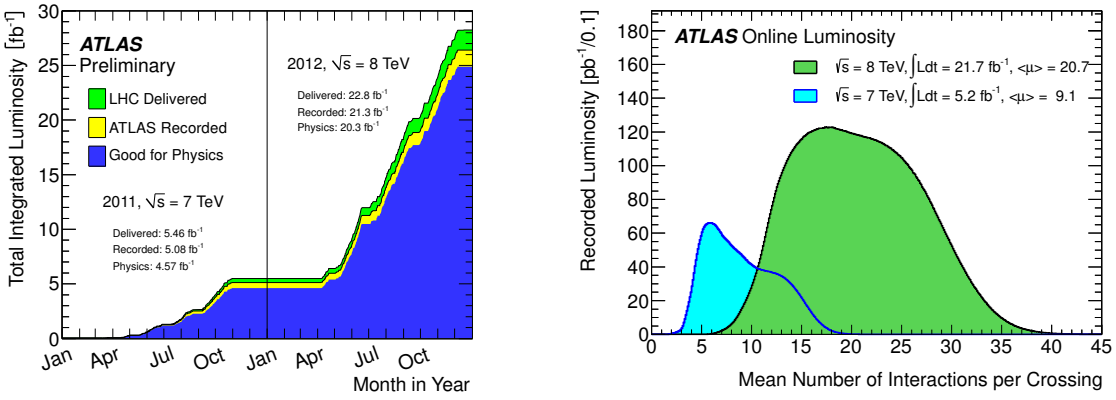

(A) (B)

Figure 5.1: Integrated luminosity versus time delivered by the LHC and recorded by ATLAS (A) among the distribution of $\langle\mu\rangle$ (B) [92].

Table 5.1: Percentage of data recorded during Run-1 by the ATLAS detector systems that is signified as suitable for physics analysis [93].

Inner Detector			**Calorimeters**		**Muon Spectrometer**				**Magnet Systems**	
Pixel	SCT	TRT	LAr	Tile	MDT	RPC	CSC	TGC	Solenoid	Toroids
99.9	99.1	99.8	99.1	99.6	99.6	99.8	100	99.6	99.8	99.5
All good for physics: 95.5%										

5.3 Event Selection

The event selection of this analysis consists of a sequence of requirements applied to the data-set and relevant Monte Carlo samples in order to pinpoint events that are compatible with originating

from the $H \to ZZ^{(*)} \to 4\ell$ decay, while simultaneously suppressing the contribution from backgrounds. The event selection is based on that of the $H \to ZZ^{(*)} \to 4\ell$ low-mass analysis, which was optimised towards a Higgs boson with a mass of 125 GeV. The event selection of this analysis differs in that it has been tailored to the high-mass regime, i.e. to values of m_H greater than 125 GeV. A major difference between the low- and high-mass regime is the changing kinematics of the $ZZ^{(*)}$ decay; if $m_H > 2 \times m_Z$, a condition which is satisfied over the majority of the mass range considered in this analysis, both Z bosons are on-shell, a fact that is exploited in the event selection. In this section, the triggering strategy and object reconstruction is covered, followed by a description of the event selection, which consists of lepton preselection, di-lepton and quadruplet selection, and lastly event categorisation.

5.3.1 Triggering

To identify events with a signature that is relevant for the targeted final-state, a series of triggers assuring the presence of one or more leptons is requested. The leptons must either match a single-lepton trigger requiring the presence of one lepton, or two leptons must match a di-lepton trigger requiring the presence of a lepton pair. The triggers used in this analysis are summarised in Table 5.2. The following naming convention applies [94]:

- `e` or `mu` refers to the trigger applying to electrons or muons, respectively.
- The number following `e` or `mu` denotes the threshold on the E_T (for electrons) or p_T (for muons) in the unit of GeV, which the object must pass.
- `v` indicates that the E_T or p_T threshold varies with η in order to account for the different amount of uninstrumented material in front of the calorimeters, which is not uniform in η.
- `i` indicates that an isolation requirement is added to the object.
- `h` indicates a requirement on the energy deposit in the hadronic calorimeter, which must be below a certain threshold, since this is an indication of the object being an electron.
- `T` signifies a higher E_T threshold on the level-1 trigger.
- `loose`, `medium` and `tight` refer to the stringency of the requirements applied in the object reconstruction.

The trigger efficiency is measured in data and Monte Carlo simulations using $Z \to \mu\mu$ and $Z \to ee$ events. For a Higgs boson at $m_H = 130$ GeV produced via the ggF production mechanism, the efficiency is found to be 97.6% for the 4μ final-state, 97.3% for the $2e2\mu/2\mu2e$ final-state and 99.7%

for the $4e$ final-state. The slightly lower number observed with the $2e2\mu$ and $2\mu2e$ final-state can be explained by differences in the di-lepton trigger efficiency. The probability of firing a di-lepton trigger is higher in the $4e$ and 4μ final-states since more leptons of the same flavour are present. Conversely, the probability of this is lower in the mixed final-states since fewer leptons of the same flavour are present. The uncertainties associated with the trigger efficiencies are calculated by checking the number of events that pass all the selection criteria with and without the trigger requirement. For both electron and muon triggers, this uncertainty is found to be less than 0.7%.

Table 5.2: Summary of the Run-1 triggers used in this analysis. When multiple trigger chains are indicated a logical OR is requested among them.

Channel	Single-lepton	Di-lepton
$4e$	e24vhi_medium1 e60_medium1	2e12Tvh_loose1 2e12Tvh_loose1_L2StarB
4μ	mu24i_tight mu36_tight	2mu13 mu18_mu8_EFFS
$2e2\mu$	4μ OR 4e OR e12Tvh_medium1_mu8 OR e24vhi_loose1_mu8	

5.3.2 Object Reconstruction

As explained above, this analysis searches for a heavy Higgs boson in the 4ℓ final-state, entailing that reconstructed electrons and muons are needed to perform the analysis. Furthermore, as explained in Chapter 2, a Higgs boson can be produced in association with up to several jets, originating as byproducts from the VBF production mechanism or as decay-products from a vector boson. As a result, jets are also needed in this analysis. A brief description of the reconstruction of these objects is provided in the following sections.

5.3.2.1 Electrons

Reconstructed electrons are composed of a track in the ID that points towards an electromagnetic (EM) cluster in the calorimeters. The EM clusters are built with the sliding window algorithm [95], which is a technique that sums calorimeter cells of size $\Delta\eta \times \Delta\phi = 0.025 \times 0.025$ longitudinally within a window of 3×5 cells (in $\eta \times \phi$) and adjusts the position of the window such that the contained transverse energy is at a local maximum. The tracks that are associated with EM clusters

are fitted with a Gaussian-Sum filter, which allows for energy losses caused by bremsstrahlung to be taken into account [96].

The electron identification is based on a set of discriminating variables that provide good separation between prompt electrons and fake electrons caused by jets. Two identification approaches are available; a cut-based approach and a maximum likelihood (LH) approach, both relying on the same variables. In the first approach, requirements are imposed sequentially to the discriminating variables. The second approach, which is employed in this analysis, makes use of PDFs of the discriminating variables for the signal and background. These PDFs are combined into a discriminant, $d\mathscr{L}$, onto which a cut is applied [97]. This discriminant is defined as:

$$d\mathscr{L} = \frac{\mathscr{L}_S}{\mathscr{L}_B + \mathscr{L}_S}, \qquad \mathscr{L}_S = \prod_{i=1}^{n} P_{s,\,i}(x_i), \qquad \mathscr{L}_B = \prod_{i=1}^{n} P_{b,\,i}(x_i) \tag{5.2}$$

Here $\bar{x}$ is the vector of discriminating variables, while $P_{s,\,i}(x_i)$ and $P_{b,\,i}(x_i)$ are the values of the PDF of the ith discriminating variable evaluated at x_i for the signal and background, respectively. These PDFs are obtained from data. Three working points are defined; LOOSE, MEDIUM and TIGHT, which differ in the level of purity and contamination specified by the requirement imposed to $d\mathscr{L}$. These three working points are not orthogonal, as electron candidates passing any of the tighter identification requirements also pass all of the looser requirements. In this analysis, LOOSE electrons are employed.

The discriminating variables used to identify the LOOSE electrons are summarised in Table 5.3. The LOOSE regime utilises variables that are particularly useful for discrimination against light-flavoured jets. These include the longitudinal and transverse shapes of the electromagnetic showers in the calorimeters, the properties of the tracks in the inner detector, the change in the momentum from the beginning to the end of the track due to brehmsstrahlung, and furthermore the matching between tracks and energy clusters. The variables $n_{hits}^{B-layer}$, n_{Pixel} and n_{Si} displayed in Table 5.3 are not used in the likelihood, however, requirements are applied to them directly regardless of the discriminant output in order to assure that each electron has a high-quality track associated. For LOOSE electrons it is required that $n_{Si} \geq 7$, and that either $n_{Pixel} \geq 2$ and $n_{hits}^{B-layer} = 1$ or $n_{Pixel} \geq 1$ and $n_{hits}^{B-layer} = 0$.

Table 5.3: The discriminating variables used in the LH electron identification approach for the LOOSE working point [95, 97].

Discriminating variable	Description
$R_{Had(1)}$	Ratio of E_T in first layer of hadronic calorimeter to E_T of the EM cluster (only used in range $\|\eta\| < 0.8$ and $\|\eta\| > 1.37$)
f_3	Ratio of energy in the third layer to the total energy
W_{η^2}	Lateral shower width
R_η	Ratio of energy in 3×7 cells over the energy in 7×7 cells centred at the electron cluster position
R_ϕ	Ratio of energy in 3×3 cells over the energy in 3×7 cells centred at the electron cluster position
W_{stot}	Total shower width
E_{ratio}	Ratio of energy difference between largest and second-largest energy deposit in the cluster over the sum of energies
f_1	Ratio of the energy in the strip layer to the total energy
$n_{hits}^{B-layer}$	Number of hits in the B-layer
n_{Pixel}	Number of hits in the pixel detector
n_{Si}	Number of hits in the pixel and SCT detectors combined
$\Delta p/p$	Momentum lost by the track between the perigee and the last measurement point divided by original momentum
n_{TRT}	Total number of hits in the TRT
r_{TRT}	Ratio of the number of high-threshold hits to the total number of hits in the TRT
$\Delta\eta_1$	$\Delta\eta$ between the cluster position in the strip layer and the extrapolated track
$\Delta\phi_{Res}$	$\Delta\phi$ between the cluster position in the middle layer and the extrapolated track

5.3.2.2 Muons

The muon track reconstruction is performed independently in the ID and MS and afterwards combined into the muon objects that are used in physics analyses. Four types of muon objects are defined:

- **Stand-Alone (SA) / Extrapolated (ME):** the muon trajectory is reconstructed solely from MS information. The track parameters near the IP are obtained by extrapolating the trajectory back to the point of closest approach to the beam-axis, while taking the estimated energy loss in the calorimeters into account. This muon type is mainly used to extend the muon acceptance into the range $2.5 < |\eta| < 2.7$, which is not covered by the ID. The inclusion of SA muons into this analysis (and several other ATLAS analyses, such as the SM ZZ analysis) relied on a dedicated effort performed within the $H \to ZZ^{(*)} \to 4\ell$ analysis group to demonstrate the quality of this muon type [73].

- **Combined (CB):** the muon trajectory is reconstructed independently in the ID and MS and afterwards combined with a global fit. The measured space-points from the MS may be added to or removed from the track in order to improve the fit quality. The CB muon type is the most common muon object.

- **Segment-tagged (ST):** a track from the ID is classified as a muon if it can be associated with at least one local track segment in the MDT or CSC chambers. ST muons can be used to increase the acceptance in cases where a muon only crossed a single layer of MS chambers, either because of low p_T or because it falls in regions outside the MS acceptance.

- **Calorimeter-tagged (CaloTag):** a track in the ID is identified as a muon if it can be associated to an energy deposit in the calorimeter compatible with a minimum ionising particle. This muon object can be used to recover acceptance in the uninstrumented regions of the MS. The identification criteria of this muon type are optimised for a region of $|\eta| < 0.1$ and a momentum range of $25 \leq p_T \leq 100$ GeV.

Two different muon reconstruction strategies are used in Run-1: STACO and MUID. These are able to reconstruct the same type of muon objects, but differ in how the information from the ID and MS is combined. STACO relies on a statistical combination of tracks reconstructed independently in the ID and MS, whereas MUID upon identifying track patterns in the ID and MS performs a global refit of the full trajectory. Furthermore, these two algorithms have different performance in terms of reconstruction efficiency and rejection of fakes. More details are given in [98, 99, 100].

The analysis presented in this chapter uses STACO muons, as does the vast majority of physics analyses on ATLAS.

5.3.2.3 Jets

In this analysis, jets are used as indicator of the underlying production mechanism of each event, i.e. whether an event appears to be VBF-like, VH-like or ggF-like. Jets are reconstructed from topological clusters [96], which are formed by iteratively adding neighbouring cells to a seed, provided that the energy in the cell is above a threshold that is defined as a function of the noise level. This particular cluster-type is able to accommodate non-uniform showers with a variety of shapes and sizes, which makes it well-suited for the purpose of jet reconstruction since jets do not have a definite shower shape. The jet reconstruction is done with the anti-k_T algorithm [101] using a distance parameter of $\Delta R = 0.4$. After forming a jet, the topological clusters are corrected from the electromagnetic scale to the hadronic energy scale using a p_T and η-dependent jet energy scale (JES) calibration. Furthermore, a correction is applied that adjusts the energy of the jets in order to remove the contribution from both in-time and out-of-time pile-up. In addition, jets originating from pile-up are suppressed by imposing a requirement on the jet vertex fraction (JVF) [102]. The JVF is defined as the ratio of the sum of p_T for all tracks matched to a given jet and associated with the primary vertex, relative to the total sum of p_T for all tracks matched to the jet. A requirement on JVF results in improved stability of the reconstructed jet multiplicity against pile-up. In this analysis, it is therefore required that $|\text{JVF}| > 0.5$. Lastly, in order to reject jets that are not associated to real energy deposits in the calorimeters, the selected jets are required to pass the standard "looser" working point as defined in [103].

5.3.3 Lepton Pre-Selection

The lepton pre-selection is summarised in Table 5.4. The $H \to ZZ^{(*)} \to 4\ell$ event selection aims at selecting four leptons in either of the final-states $4e$, 4μ, $2e2\mu$ or $2\mu2e$, with the following sequence of requirements. Muons are allowed to be either the CB or ST type if satisfying $p_T > 6$ GeV and $|\eta| < 2.7$. One muon of the type CaloTag or SA is allowed in each event. A CaloTag muon is accepted if satisfying $p_T > 15$ GeV and $|\eta| < 0.1$, while a SA muon must pass $p_T > 6$ GeV, $|\eta| < 2.7$ and have a distance of $\Delta R > 0.2$ to the nearest ST type muon. Electrons are required to be identified with the likelihood approach, of LOOSE quality, and must satisfy $E_T > 7$ GeV and $|\eta| < 2.47$. The three highest-p_T leptons must in descending order pass thresholds of $p_T > 20$ GeV, 15 GeV and 10 GeV. Additionally, the four leptons must be separated by a distance of $\Delta R > 0.1$ for identical flavours and $\Delta R > 0.2$ for different flavours.

A requirement is imposed on the transverse impact parameter significance, which is defined as the ratio of the transverse impact parameter d_0 (measured with respect to the primary vertex) and its associated error, σ_{d_0}. This is done in order to suppress contamination from leptons originating from secondary, displaced vertices, which could happen via processes such as heavy-flavoured quark decays and photon conversion. Furthermore, this requirement rejects tracks that for other reasons do not point towards the primary vertex. This quantity is required to be < 3.5 for muons and < 6.5 for electrons.

In addition to the above, the leptons in each event are required to be well-isolated, since the opposite can be an indication of the lepton originating from processes such as heavy-flavoured quark decays where the lepton is surrounded by jet activity, or of the lepton being faked by a jet. Two types of isolation, based on information from the ID and calorimeters, are defined. The normalised track isolation relies on information from the ID and is for both electrons and muons defined as the sum of the transverse momenta of tracks, $\sum p_T$, inside a cone of $\Delta R < 0.2$ around the lepton, excluding the lepton track itself, normalised by the lepton p_T. All leptons are required to have a normalised track isolation of < 0.15. A similar approach is used for the normalised calorimetric isolation. For muons, this second type of isolation is defined as the sum of energy, $\sum E_T$, deposited in calorimeter cells within a cone of $\Delta R < 0.20$ around the muon, normalised with the muon p_T. Before normalising, the muon ionisation energy is subtracted, which is obtained as the sum cells in a smaller cone around the muon [104, 105]. This quantity is required to be < 0.30. For electrons, this type of isolation is computed as the sum of energy in the topological clusters within a cone of $\Delta R < 0.2$ around the electron cluster, divided by the electron p_T. To remove the contribution from the electron itself, the core of the electron cluster is subtracted from the sum. The value of this type of isolation is required to be < 0.20. For both types of isolation, any contribution from another lepton in the quadruplet within $\Delta R < 0.2$ is subtracted. For the calorimetric isolation, the contribution of any electron in the quadruplet within $\Delta R < 0.18$ is subtracted.

5.3.4 Di-lepton Pairing and Quadruplet Selection

The di-lepton pairing and quadruplet selection is summarised in Table 5.5. Upon selecting at least four good leptons, the four-vectors of the two Z bosons can be constructed. This happens by forming di-lepton pairs by matching oppositely-charged, same-flavoured leptons. The pair with the invariant mass closest to the Z pole, m_{12}, is named the leading pair, while the second pair with invariant mass m_{34} is called the sub-leading pair. The leading pair is enforced to be on-shell by requiring $50 < m_{12} < 106$ GeV. At m_H values smaller than twice the Z boson mass, the sub-leading di-lepton pair is expected to be off-shell. Therefore, the mass-window requirement applied

to m_{34} depends on the value of $m_{4\ell}$. For $m_{4\ell} < 140$ GeV, the sub-leading di-lepton pair must satisfy $m_{34} > 12$ GeV. This lower threshold rises linearly to 50 GeV in the interval $140 < m_{4\ell} < 190$ GeV. If more than one quadruplet exists, the one with m_{12} closest to the Z pole is retained. In the rare event of multiple quadruplets having the same m_{12}, the one with the highest m_{34} is selected. To avoid overlap with the low-mass analysis, only events satisfying $m_{4\ell} > 135$ GeV are used. The search reaches up to $m_{4\ell} < 1200$ GeV – above this value, the sensitivity to a potential signal from a heavy Higgs boson is expected to be negligible.

A final state radiation (FSR) correction is applied, where the fully reconstructed low-E_T FSR photons emitted by the leptons are added to the four-momenta of the parent di-lepton system. This technique improves the experimental resolution and recuperates a portion of the events failing the selection due to the requirement on the invariant mass of either di-lepton system. The procedure is applied to leptons originating from an on-shell Z boson. Hence, for $m_{4\ell} < 190$ GeV, the correction is only applied to the leading di-lepton pair, while for $m_{4\ell} > 190$ GeV, it can be applied to either of the pairs. Two types of FSR photons are considered; collinear and non-collinear, distinguished by an angular distance of $\Delta R > 0.15$ and $\Delta R < 0.15$, respectively, to the parent lepton. The fraction of events corrected with a collinear and non-collinear FSR photon is 4% and 1%, respectively.

5.3.5 Double Z Mass Constraint Studies

The precision with which the Z peak can be reconstructed is constrained by experimental effects related to the lepton momentum measurement. To improve the experimental resolution, a correction is added to the di-lepton system, which recomputes the four-momenta of the leptons with a kinematic fit that exploits the knowledge of the Z boson line-shape and the uncertainties on the lepton momentum measurement. This Z mass constraint (ZMC) uses a fit consisting of a convolution of a Breit-Wigner distribution with a Gaussian. The Breit-Wigner models the line-shape of the Z boson and the Gaussian represents the lepton momentum response by having a width equal to the experimental resolution. Since the natural width of the Z boson is of the same order as the experimental di-lepton resolution, an improvement in the latter is expected. For a narrow Higgs boson, which is the target of this search, the ZMC has been found to improve the $m_{4\ell}$ resolution by about 15%. For widths much larger than the experimental resolution, the improvement is expected to be insignificant.

Given that the ZMC models the Z boson line-shape with a Breit-Wigner, the constraint can only be applied to di-lepton pairs originating from on-shell Z bosons. Therefore, in the low-mass analysis the constraint was only applied to the leading di-lepton pair. In this search however, both

TABLE 5.4: Summary of the lepton pre-selection requirements.

Lepton Pre-selection	
Electrons	LOOSE LH quality electrons with $p_T > 7$ GeV and $\|\eta\| < 2.47$
Muons	CB or ST muons with $p_T > 6$ GeV and $\|\eta\| < 2.7$ Maximum one CT or SA muon CT muons with $p_T > 15$ GeV and $\|\eta\| < 0.1$ SA muons with $p_T > 6$ GeV, $2.5 < \|\eta\| < 2.7$ and $\Delta R > 0.2$ from closest ST

TABLE 5.5: Summary of the requirements imposed in the di-lepton pairing and quadruplet selection.

Di-lepton pairing and quadruplet selection	
Kinematics	At least one quadruplet consisting of two same-flavoured di-lepton pairs Leading leptons must satisfy $p_T > 20$ GeV, 15 GeV and 10 GeV Leading di-lepton pair must satisfy $50 < m_{12} < 106$ GeV Sub-leading di-lepton must satisfy $m_{threshold} < m_{34} < 115$ GeV Remove quadruplet if alternative di-lepton pair yields $m_{\ell\ell} < 5$ GeV $\Delta R(\ell, \ell') > 0.10$ (0.20) for all same (different) flavoured leptons in quadruplet.
Isolation	Isolation requirement applied to all leptons in quadruplet Contribution from the other leptons of the quadruplet is subtracted Lepton track isolation ($\Delta R < 0.20$): $\Sigma p_T / p_T < 0.15$ Electron calorimeter isolation ($\Delta R < 0.20$) : $\Sigma E_T / E_T < 0.20$ Muon calorimeter isolation ($\Delta R < 0.20$) : $\Sigma E_T / E_T < 0.30$
Impact parameter	Impact parameter significance requirement applied to all leptons in quadruplet For electrons : $d_0/\sigma_{d_0} < 6.5$ For muons : $d_0/\sigma_{d_0} < 3.5$

Z bosons are on-shell provided that $m_H > 2 \times m_Z$, meaning that the ZMC can be applied to both if the value of $m_{4\ell}$ is above the threshold for the ZZ^* to ZZ transition.

As will be explained in Section 5.5, the major backgrounds to this search originate from the irreducible di-boson continuum processes $q\bar{q} \to ZZ^{(*)}$ and $gg \to ZZ^{(*)}$. In the first attempts to apply the double ZMC, it was observed that the $m_{4\ell}$ distributions from these backgrounds were artificially shaped, such that a dip in the $m_{4\ell}$ spectrum was sculpted around the threshold for applying the double ZMC. Such an effect would be problematic in the limit-setting procedure, since an artificial, downward fluctuation in the background modelling could cause a fake excess to appear in the data. The dip was believed to happen as a result of the high probability of performing incorrect pairing of the di-lepton pairs near the ZZ^* and ZZ transition region. In order to test this hypothesis, two $q\bar{q} \to ZZ^{(*)}$ Monte Carlo samples were generated with the POWHEG and PYTHIA generators with different thresholds for applying the double ZMC. These thresholds were $m_{4\ell} \geq 190$ GeV and $m_{4\ell} \geq 210$ GeV, respectively, the rationale being that all events at the higher threshold exclusively would originate from on-shell Z bosons. The $m_{4\ell}$ distributions from these two samples, after applying the event selection described in Section 5.3.3 and 5.3.4, are presented in Figure 5.2. As observed, the dip appears when either threshold is applied and is shifted according to the value, suggesting that the occurrence of the dip is not related to the $ZZ^{(*)}$ to ZZ transition region.

To investigate further, the invariant mass distributions of the di-lepton pairs, $m_{\ell\ell}$, are examined. The distribution of this parameter is presented in Figure 5.3 for both the leading and sub-leading pairs, and is shown with and without the ZMC applied, along with the unconstrained distribution (i.e.where no ZMC is applied) at generator (truth) level. From Figure 5.3 it is confirmed that the ZMC works as intended on the leading di-lepton pair; the distribution becomes more compatible with the distribution at generator level after the constraint is applied. However, this is not the case for the sub-leading pair; a distinct dip is present in the centre of the unconstrained peaks on both the reconstructed and generated level. This occurs because the di-lepton pair closest to the Z pole per definition is assigned to be the leading pair, meaning that its $m_{\ell\ell}$ distribution does not follow the Z boson line-shape. Hence, applying the ZMC is senseless. This miscorrection can also explain the artificial sculpting of the $m_{4\ell}$ distribution. In Figure 5.2, the $m_{4\ell}$ distribution is presented with the constraint applied exclusively to the leading pair. As observed, there is no issue with artificial shaping of the background. Since the ZMC is unable to accommodate the line-shape of the sub-leading di-lepton pair, it is not sensible to apply the constraint to both pairs. Therefore, in this analysis, the ZMC is only applied to the leading di-lepton pair, regardless of the $m_{4\ell}$ value.

The experimental resolution obtained after applying the ZMC varies with final-state and the Higgs boson mass. For the 4μ final-state, the experimental resolution varies from 1.5% at $m_H =$

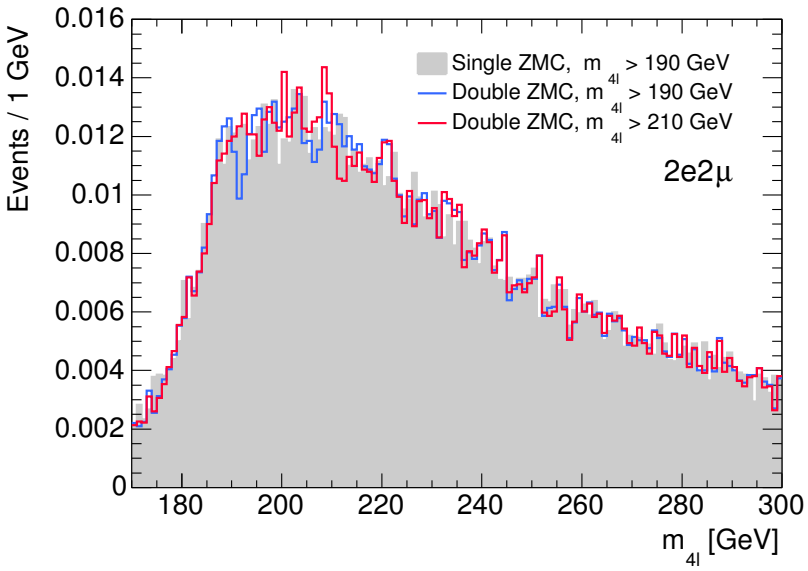

FIGURE 5.2: The $m_{4\ell}$ distribution in the $2e2\mu$ final-state after having applied the ZMC to either (grey) or both di-lepton pairs at two different thresholds of $m_{4\ell} \geq 190$ GeV (blue) and $m_{4\ell} \geq 210$ GeV (red). All distributions are normalised to unity.

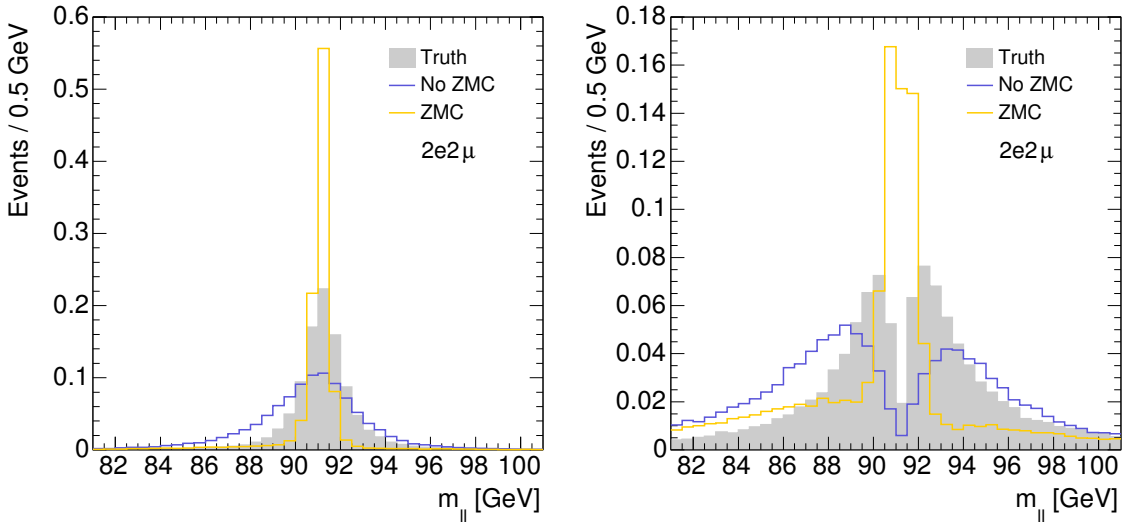

(A) (B)

FIGURE 5.3: The $m_{\ell\ell}$ distribution of the leading (A) and sub-leading (B) di-lepton pair in the $2e2\mu$ final-state for $m_H = 190$ GeV before and after applying the ZMC at a threshold of $m_{4\ell} \geq 190$ GeV. The distribution on generator (truth) level is shown for comparison. All distributions are normalised to unity.

200 GeV to 3.5% at $m_H = 1$ TeV, while for $4e$ events, it ranges from 2% at $m_H = 200$ GeV to below 1% at $m_H = 1$ TeV.

5.3.6 Event Categorisation

As described in Chapter 2, a heavy Higgs boson is predicted to be produced via the gluon-fusion (ggF) mechanism, the vector boson-fusion (VBF) mechanism, or via associated production (VH), where the Higgs boson is produced in association with a Z or W boson. In order to measure the rates for these processes separately, events passing the event selection described in the previous section are classified according to six orthogonal categories, as either VBF-like, VH-like or ggF-like, where the latter is segmented into four additional categories depending on the final-state. All six event categories use the four-lepton invariant mass, $m_{4\ell}$, as discriminant. The classification of events into these event categories is illustrated in Figure 5.4, while the selection efficiency of each event category is shown in Figure 5.5[1].

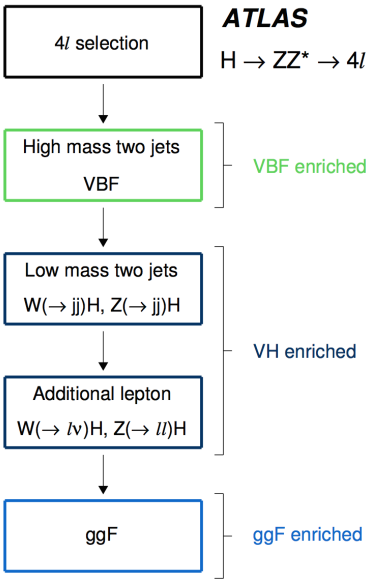

Figure 5.4: Schematic of the sequential event categorisation employed in this analysis.

In this analysis, initially it is tested whether an event carries the distinct VBF signature of two high-p_T jets produced in opposite hemispheres. VBF-like events are selected by requiring at least two jets with $p_T > 25$ GeV and $|\eta| < 2.5$ or $p_T > 30$ GeV and $2.5 < |\eta| < 4.5$, and with the leading two jets together having an invariant mass of $m_{jj} > 130$ GeV. As seen in Figure 5.5, the selection efficiency of events originating from the VBF production mechanism in the VBF-like event category is approximately 55% and nearly constant as a function of m_H. Also seen from Figure 5.5 is the fact that the VBF event category has considerable contamination of events originating from the ggF production mechanism, ranging between 10% at low mass and 30% at high mass[2]. The increase in ggF contamination occurring as a function of m_H happens due to larger jet multiplicities and because of increasing p_T of the leading jet. Assuming SM couplings for the Higgs boson, the purity of the VBF event category, defined as the number of true VBF events divided by the number of events originating from all production mechanisms, varies between 20% at low mass and 60% at high mass. The large

[1] In this figure, the Complex Pole Scheme (CPS) appears, in which the Higgs boson has the natural width from the SM. CPS samples were generated in the early phases of the current analysis, but was not used after the decision to model the signal with the Narrow Width Approximation had been taken.

[2] In order to suppress the contamination to the VBF event category from the ggF production mechanisms, the earlier versions of this analysis employed a BDT discriminant that was trained on the kinematic properties of the final-state objects of the VBF mechanism, including $\Delta\eta$ between the two jets. However, due to unreasonably long processing times for all statistical procedures, this discriminant was removed from the present version of the analysis.

variation of this number is due to the change in the relative rate of VBF and ggF production, and due to the variation of the ggF contamination.

If an event fails the selection of the VBF event category, it is tested whether it possesses the VH signature, i.e. the signature of a Higgs boson accompanied by two jets originating from the $W \to qq'$ or $Z \to q\bar{q}$ decay, or by one or two leptons from either the $W \to \ell\nu$ or $Z \to \ell\ell$ decay. An event is thus classified as VH-like if a jet-pair is present that satisfies the same p_T and η requirement as for the VBF event category, and furthermore $40 < m_{jj} < 130$ GeV. A VH-like event must also pass the selection on a multivariate discriminant used to separate the VH signal from the ggF signal. This discriminant is the output of a boosted decision tree (BDT) making use of m_{jj}, $\Delta\eta_{jj}$, the p_T of the two jets, and the value of η of the leading jet. Events are required to have a VH BDT score of at least -0.393, the value of which has been optimised for the low-mass analysis. For a $m_H = 125$ GeV Higgs boson, this requirement yields a signal efficiency of 75% and background rejection of 60%, while for a $m_H = 300$ GeV Higgs boson, the signal efficiency and background rejection is equal to 72% and 68%, respectively. In order to account for leptonic decays of the W or Z boson, events failing this selection may still be classified as VH-like if an additional lepton with $p_T > 8$ GeV is present.

If an event fails the requirements for the VH event category, it falls into the ggF event category. Events in the ggF event category are segmented according to the exact final-state, i.e. $4e$, $2e2\mu$, $2\mu2e$ or 4μ, which is possible due to the plentiful statistics.

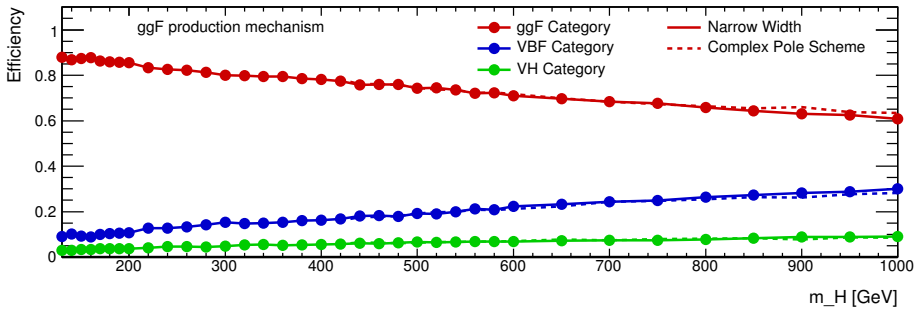

(A)

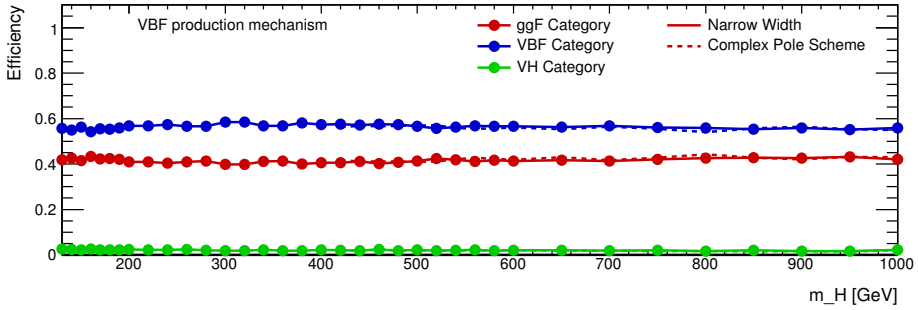

(B)

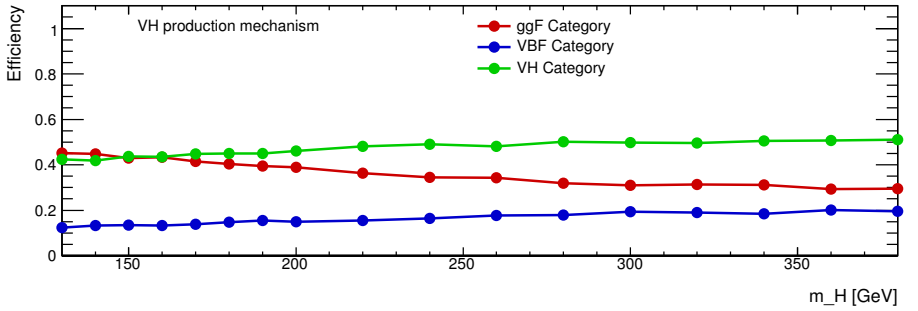

(C)

Figure 5.5: Selection efficiency for the ggF (inclusive), VBF and VH event categories as a function of m_H for a Higgs boson originating from the ggF (A), VBF (B) and VH (C) production mechanisms. For the ggF and VBF production mechanisms, the efficiency using the Complex Pole Scheme (CPS) samples is compared with the efficiency using the NWA samples.

5.4 Signal Modelling

This section describes the modelling of the signal. Ultimately, to perform the likelihood fit with Equation 5.1, the signal PDF $f_S(x_e)$ is required. In this analysis, it is desirable to perform the fit at a sufficiently large number of m_H values, thereby obtaining a spacing that is small enough to benefit fully from the excellent mass resolution of this decay channel. This requires that the PDF $f_S(x_e)$ is constructed for a spectrum of m_H values. As will be described below, this is achieved by applying a smoothing algorithm to fully simulated Monte Carlo (MC) samples.

5.4.1 The Narrow Width Approximation

The search presented in this chapter relies on the hypothesis that the width of the additional, heavy Higgs boson, Γ_H, is very narrow. The signal is modelled with the Narrow Width Approximation (NWA), where it follows the line-shape of a Breit-Wigner with a width of 4.07 MeV, which is the value of the width of the SM Higgs boson at $m_h = 125$ GeV. However, the specific choice of Γ_H is subordinate as long as it is significantly below the experimental resolution. As explained in Chapter 2 and Chapter 4, the NWA is useful within the contexts of both a model-independent and 2HDM interpretation; in the model-independent scenario, the fixed width removes the model-specific relation between m_H and Γ_H, while in 2HDM, the use of the NWA makes the search valid over a large portion of the 2HDM parameter space. Furthermore, the assumption of a narrow width is convenient since the two types of interference related to heavy Higgs boson production safely can be ignored; the interference between the heavy Higgs boson and the light Higgs boson ($H - h$ interference), and the interference between the heavy Higgs boson and the ZZ continuum ($H - ZZ$ interference).

5.4.2 Monte Carlo Samples

The $H \to ZZ^{(*)}$ process is modelled using the POWHEG [106, 107] Monte Carlo (MC) event generator, which separately calculates ggF and VBF production up to next-to-leading order (NLO). Afterwards, the generated samples are interfaced to PYTHIA [85], which decays the Z bosons and hadronizes the events. The Higgs boson p_T spectrum in the ggF process is reweighted to include QCD corrections up to NLO and QCD soft-gluon resummations up to next-to-next-to-leading logarithm (NNLL) [108]. PHOTOS [109] is used for quantum electrodynamics (QED) radiative corrections in the final-state. The simulation of a Higgs boson produced in association with a W or Z boson is done with PYTHIA.

For the ggF production mode, samples are generated with a step-size of 10 GeV in the range $140 \leq m_H \leq 200$ GeV, 20 GeV for $200 \leq m_H \leq 600$ GeV, and 50 GeV for $600 \leq m_H \leq 1000$ GeV. The same intervals are used for the VBF mode, except that a step-size of 25 GeV is used in the range $300 \leq m_H \leq 600$ GeV. The VH samples are only produced for $m_H \leq 400$ GeV since the contribution beyond this point is expected to be negligible and hence is ignored. The VH samples are generated with a step-size of 5 GeV for $m_H \leq 200$ GeV and 20 GeV for $200 \leq m_H \leq 400$ GeV.

5.4.3 Shape Parametrisation

A smoothing procedure is applied to the signal MC samples in order to remove statistical fluctuations and in order to construct the PDF $f_S(x_e)$ in Equation 5.1. Given that the spacing of m_H between these MC samples is significantly larger than the experimental resolution of the 4ℓ decay channel, the benefits of its excellent resolution are not fully exploited. Therefore, an interpolation technique is integrated into the smoothing procedure, which produces signal shapes at the m_H points where fully simulated samples are not available.

The smoothing is done with the Kernel Estimating Your Shape (KEYS) algorithm [110]. This procedure models the shape of an input data-set by replacing each entry of the data with a Gaussian kernel function and summing these up, thereby obtaining a non-parametric, smooth description of the input distribution. The parameter ρ acts as a scale factor on the kernel width and hence controls the degree of smoothing. In this analysis, KEYS is used with an adaptive binning approach, resulting in more bins in the important region under the peak, and less bins in the tails where the yield is close to zero. The adaptive width can be interpreted as the natural precision with which any given input data-set can be modelled. Examples of $f_S(x_e)$ obtained at $m_H = 300$ GeV in the six event categories are presented in Figure 5.6. As seen from this figure, good agreement between the smoothed shapes and the MC is observed in the ggF and VBF event categories. A minor inconsistency around the center of the peak is observed in the VH event category, which leaves room for optimisation in future studies.

At the m_H values where no simulated samples are available, signal shapes are obtained by morphing two shapes obtained from the MC samples on either side of m_H. This method is implemented with the `RooStarMomentMorph` class, which is part of the `RooFit` framework [111]. The result of this procedure is a set of signal shapes available over the full m_H range in a step-size of 5 GeV. Excerpts of these are presented in Figure 5.7. The shapes presented in this figure are normalised to unity, and hence constitute the final PDFs $f_S(x_e)$ used in the construction of the likelihood function.

When using KEYS, the uncertainty arising from limited statistics in the MC must be taken into account. This is done by evaluating the uncertainty per bin and afterwards stitching these together, resulting in an uncertainty band on the obtained signal shape. This uncertainty is implemented with the `RooStarMomentMorph` [112] class. As will be explained in Section 5.6, these MC statistical uncertainties are included as nuisance parameters in the final fit.

5.4.4 Acceptance and Yield

In order to obtain the final yields of the signal, the acceptance, defined as the fraction of signal events passing the full event selection, must be taken into account. This quantity is estimated with the Monte Carlo samples used to generate the signal shapes for each event category of the analysis. The acceptance at the mass points intermediate to the fully simulated points is obtained with interpolation. The statistical uncertainty on the acceptance arising from the limited size of the MC samples is evaluated by varying the acceptance up and down by its statistical uncertainty and re-evaluating the interpolation – the band spanned by these operations is taken as the uncertainty on the acceptance, which is included as a normalisation uncertainty in the final fit. The obtained acceptance is presented in Figure 5.8 for the VBF, VH and inclusive ggF event categories.

As mentioned in the introduction to this chapter, the signal-strength μ is defined in reference to a predefined number of events. For this purpose, the SM Higgs boson cross-sections and $H \to ZZ^{(*)}$ branching ratios are used. These are obtained from the LHC Higgs Cross Section Working Group [36]. Given that the final results of this search are presented as upper limits on the Higgs boson production cross-section times $H \to ZZ^{(*)}$ branching ratio, the reference cross-section and branching ratios factor out and hence have no impact on the final results.

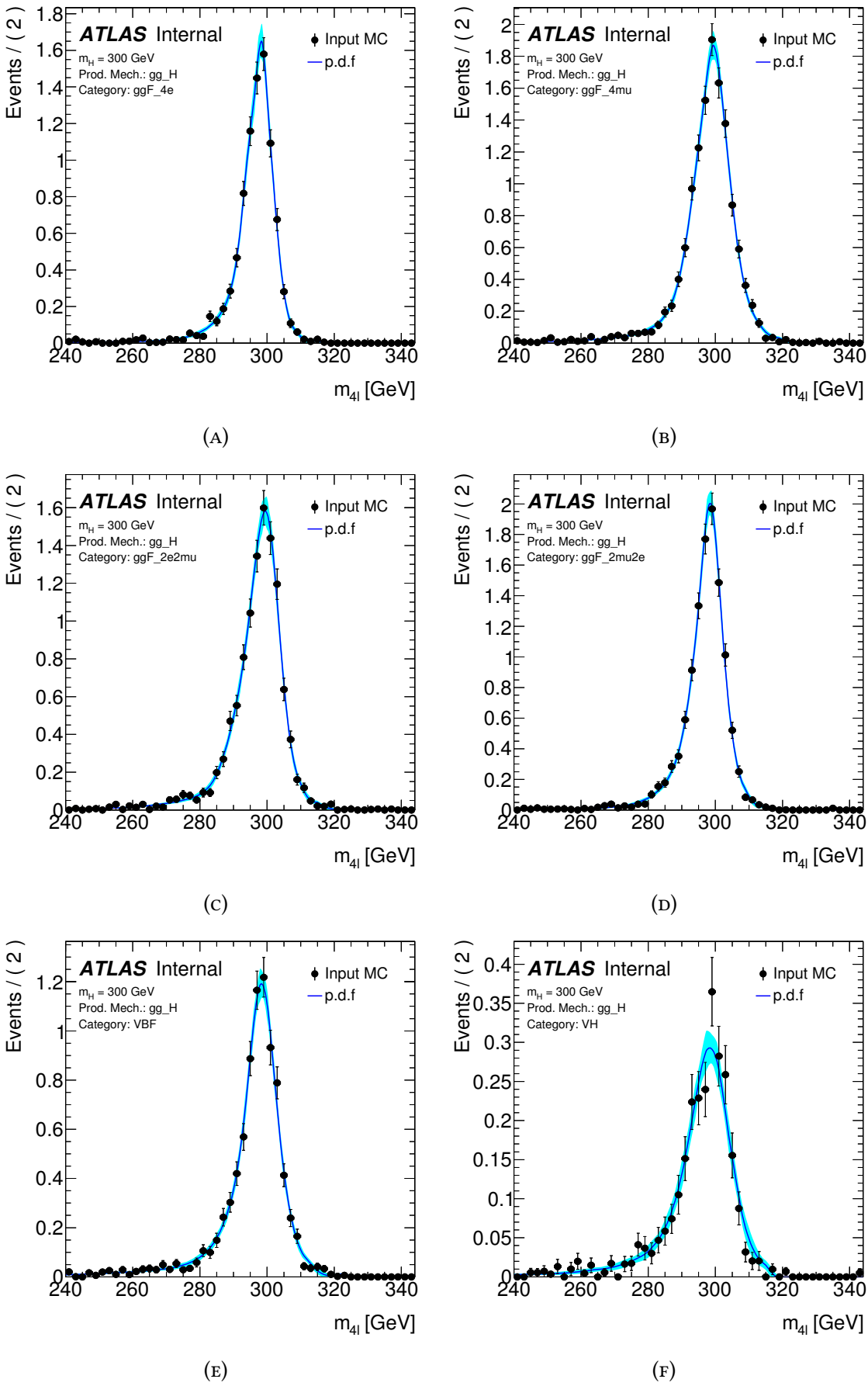

Figure 5.6: Signal shapes obtained with KEYS in the six event categories overlaid with the generated MC events at $m_H = 300$ GeV. The signal originates from the ggF production mechanism. The cyan band represents the MC statistical uncertainties.

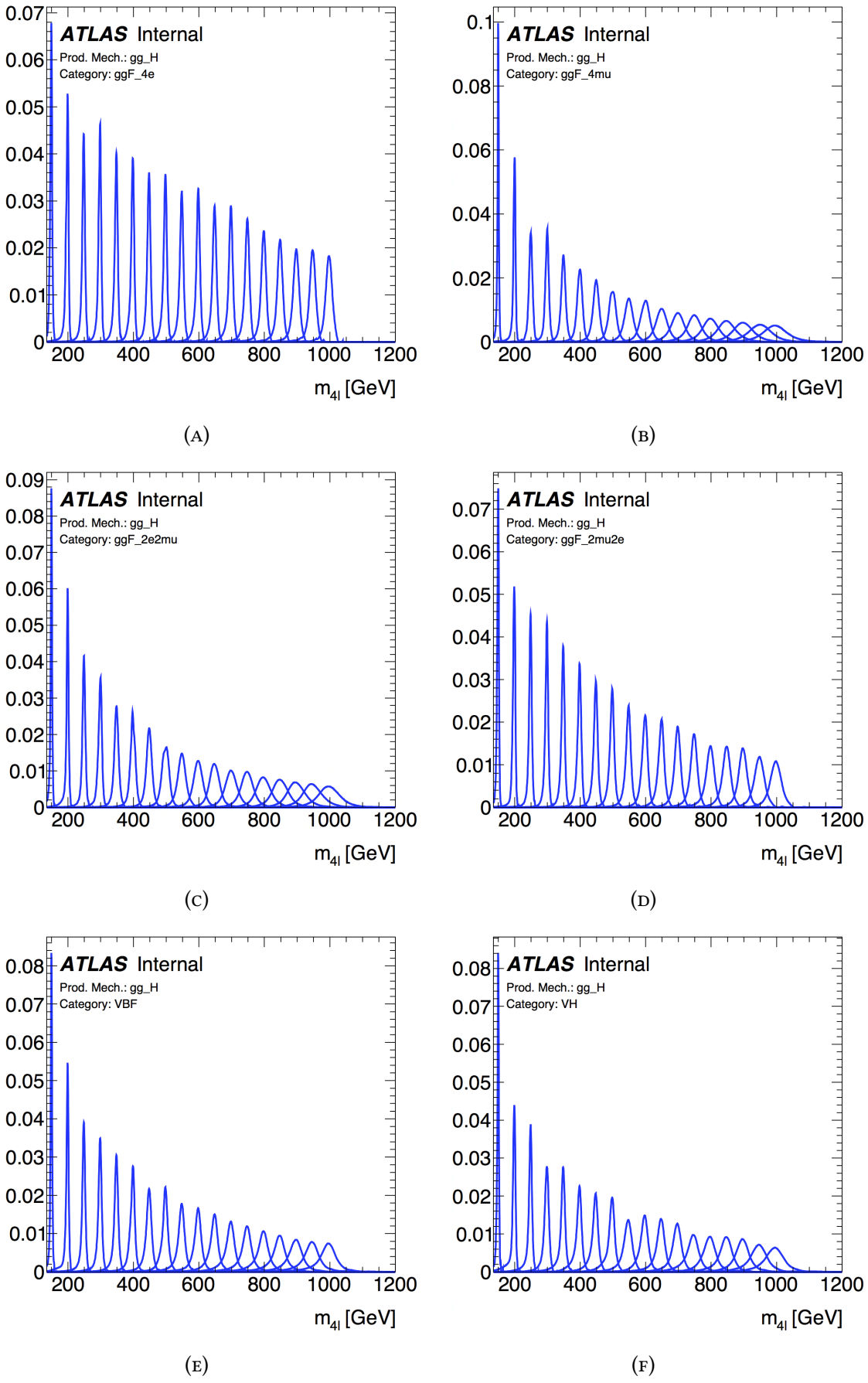

FIGURE 5.7: Signal PDFs ($f_S(x_e)$) presented at select m_H values in the six event categories with the signal originating from the ggF production mechanism.

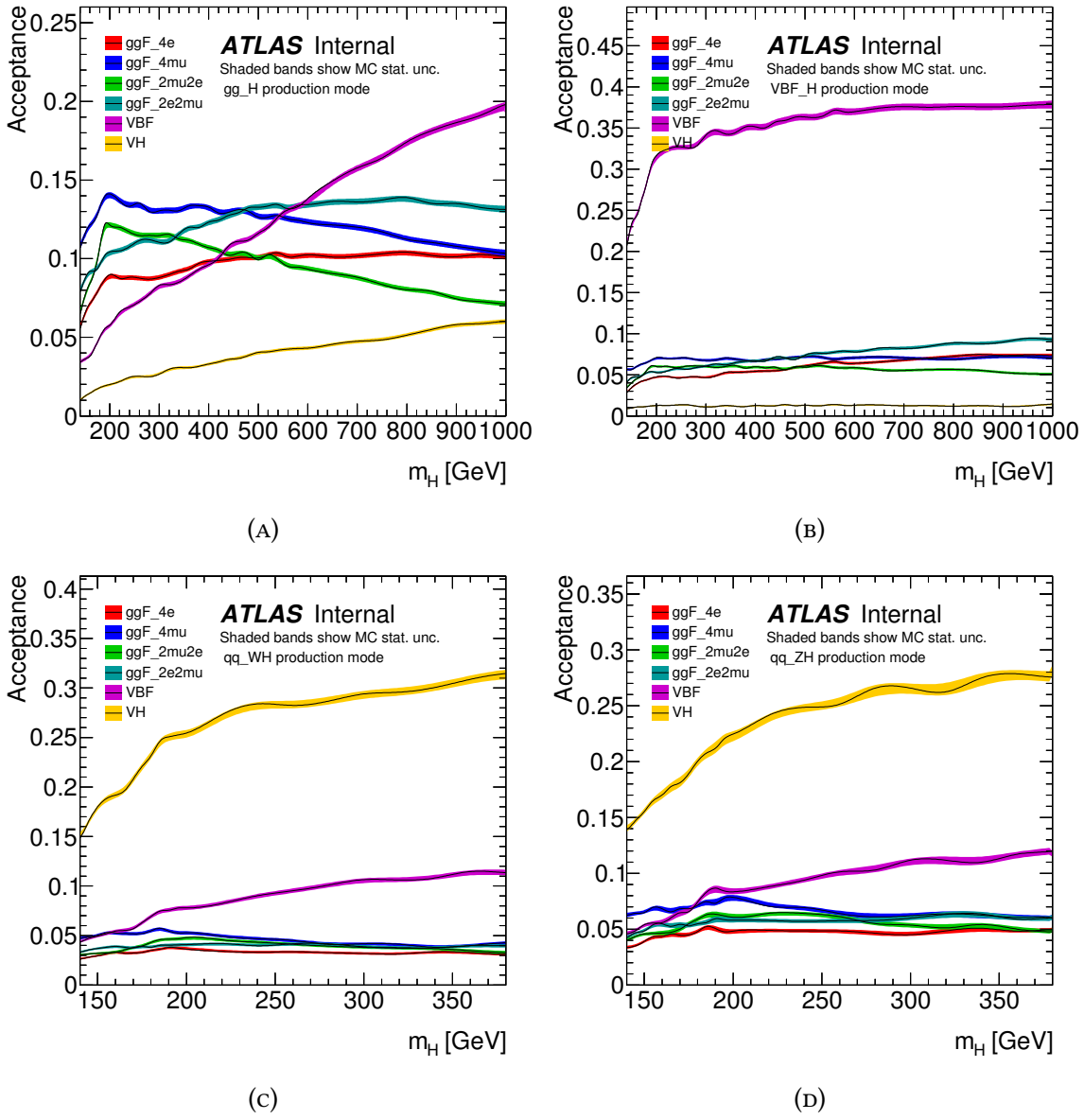

(A) (B)

(C) (D)

Figure 5.8: The signal acceptance in the six event categories segmented according to production mechanism. The acceptance is obtained from MC and defined as the fraction of events passing the selection with respect to the total number of events. The shaded band indicates the MC statistical uncertainty on the acceptance.

5.5 Background Modelling

The background processes in this analysis that can give rise to a final-state with four leptons are classified as either reducible or irreducible. Reducible backgrounds refers to processes that fake the signature of the signal, for example when jets are misidentified as leptons, or where additional leptons originating from photon conversion or heavy-flavoured quark decays are present. Irreducible backgrounds refers to processes that give rise to signatures that are almost identical to that of the signal and thereby more difficult to suppress. The former type of background is estimated with a combination of data-driven methods and simulation, while the latter relies exclusively on simulation. A description of the estimation of both is given below.

5.5.1 Irreducible Backgrounds

The dominant irreducible backgrounds to this search originate from the non-resonant ZZ production, which happens via the processes $q\bar{q} \to ZZ^{(*)}$ and $gg \to ZZ^{(*)}$. The first contributes with 90% to the total irreducible yield and the latter with the remaining 10%. The Feynman diagrams of these processes are shown in Figure 5.9 and Figure 5.10. In this analysis, the contribution to the total yield from the irreducible backgrounds is determined from simulation exclusively. Since the lepton kinematics and theoretical uncertainties in the two processes are different, they are simulated independently. Upon generating the relevant MC samples, the KEYS procedure with adaptive binning as described in Section 5.4 is used to smooth the distributions and construct $f_B(x_e)$, which is needed to build the likelihood function in Equation 5.1.

5.5.1.1 Quark-induced ZZ Continuum

To simulate the $q\bar{q} \to ZZ^{(*)}$ process, the POWHEG event generator is used. The renormalisation and factorisation scale are set to m_{ZZ} and the CT10 NLO PDF set is used [113]. The events generated with POWHEG are interfaced to PYTHIA for hadronization and showering. In order to normalise to the NNLO QCD cross-section [114], a m_{ZZ}-differential k-factor is applied, the net effect being a cross-section increase in the high-mass region of approximately 4%. A correction for NLO EW effects following the calculations of [115, 116] is taken into account with the reweighting procedure described in [117]. The higher-order EW corrections reduce the inclusive ZZ production cross-section by a few percent. Since

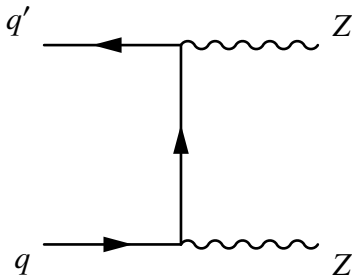

FIGURE 5.9: Leading-order diagram for the non-resonant process $q\bar{q} \to ZZ^{(*)}$.

the impact of the EW effects is of the same order as the NNLO QCD corrections, but in opposite direction, either both of the corrections or none of them should be taken into account [118].

The EW production of $q\bar{q} \to ZZ^{(*)} + 2$ jets is generated using MADGRAPH5 interfaced to PYTHIA. The interference and contribution from the light Higgs boson produced via the VBF mechanism is included in this simulation.

The $m_{4\ell}$ distributions obtained from the simulated $q\bar{q} \to ZZ^{(*)}$ samples among with the smoothed KEYS shapes are presented in Figure 5.11.

5.5.1.2 Gluon-induced ZZ Continuum

The $gg \to ZZ^{(*)}$ background is modelled using the MCFM generator [119], which generates events to LO accuracy. The interference between this background component and the light Higgs boson, described in Chapter 2, is taken into account by MCFM automatically. The events are afterwards interfaced to PYTHIA for hadronization and showering with the CT10 NNLO PDF set. Full NLO and NNLO QCD calculations are not available for the $gg \to ZZ^{(*)}$ process, but have instead been performed for the $gg \to h \to ZZ^{(*)}$ process. Furthermore, it has been demonstrated that the QCD radiative corrections for the $gg \to WW$ process are similar to those of the $gg \to h \to WW$ process [120]. Therefore, the generated $gg \to ZZ^{(*)}$ MCFM samples are scaled with the m_{ZZ}-differential k-factor calculated with the $gg \to h \to ZZ^{(*)}$ process. Since the MCFM generator only works up to LO accuracy its modelling of the jet activity is not considered terribly realistic. The SHERPA generator is known to provide a better description of the jet kinematics because it is able to include up to one jet in the matrix element. Given that the event categories are highly sensitive to the jet kinematics, the SHERPA estimate of the fraction of events in each category is preferred. Therefore, the fraction of events falling into the ggF, VBF and VH categories obtained with MCFM are scaled according to the values obtained with SHERPA.

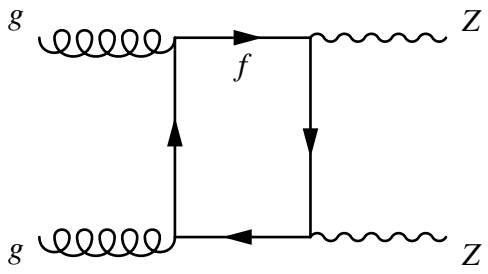

Figure 5.10: Leading-order diagram for the non-resonant process $gg \to ZZ^{(*)}$.

The $m_{4\ell}$ distributions obtained from the $gg \to ZZ^{(*)}$ samples among the smoothed KEYS shapes are presented in Figure 5.12.

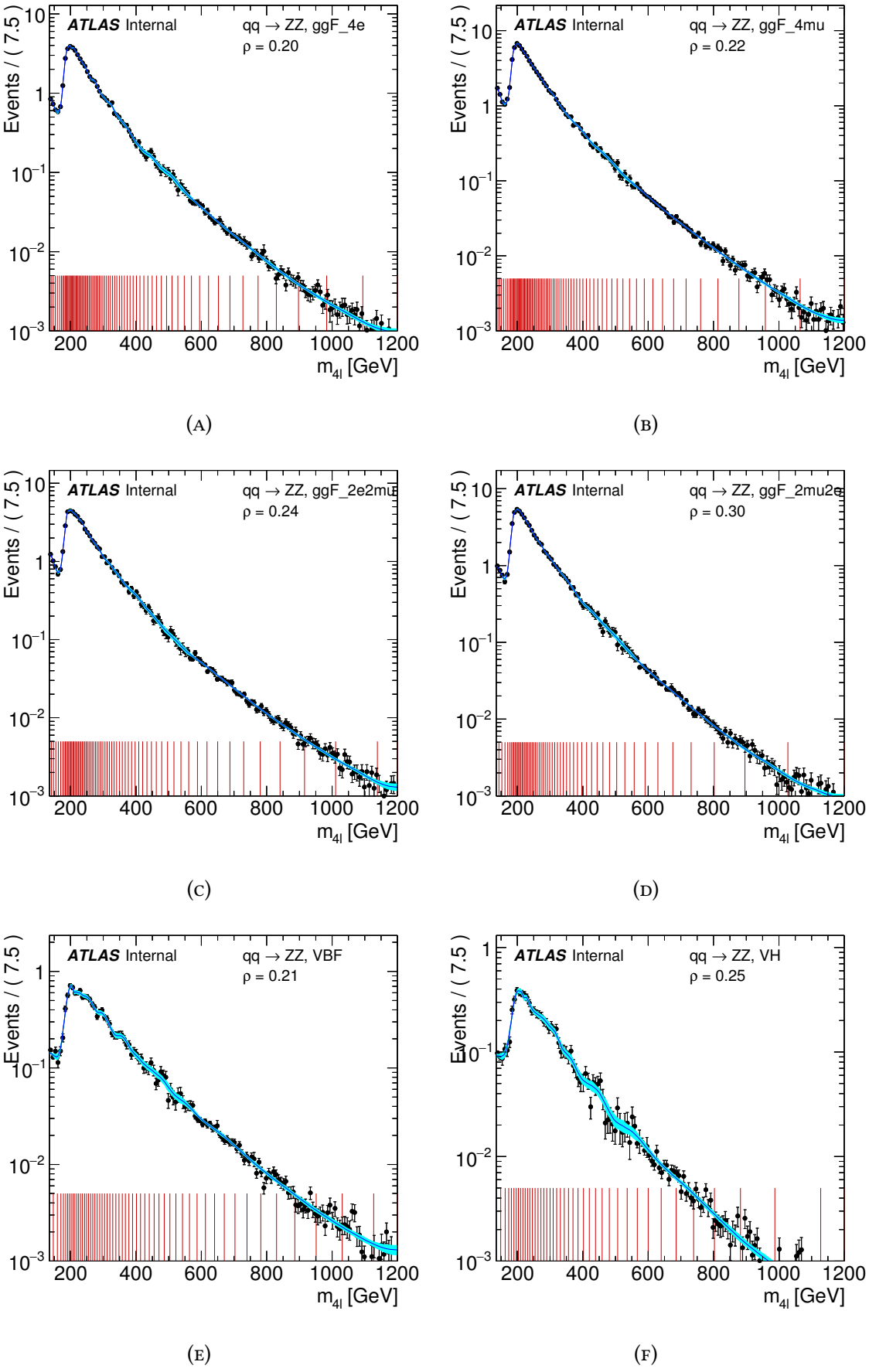

FIGURE 5.11: The background shapes obtained with the KEYS procedure for the $q\bar{q} \to ZZ^{(*)}$ process in the six event categories, overlaid with the generated MC events. The cyan band indicates the MC statistical uncertainty. The red lines show the boundaries of the bins used in the adaptive binning procedure.

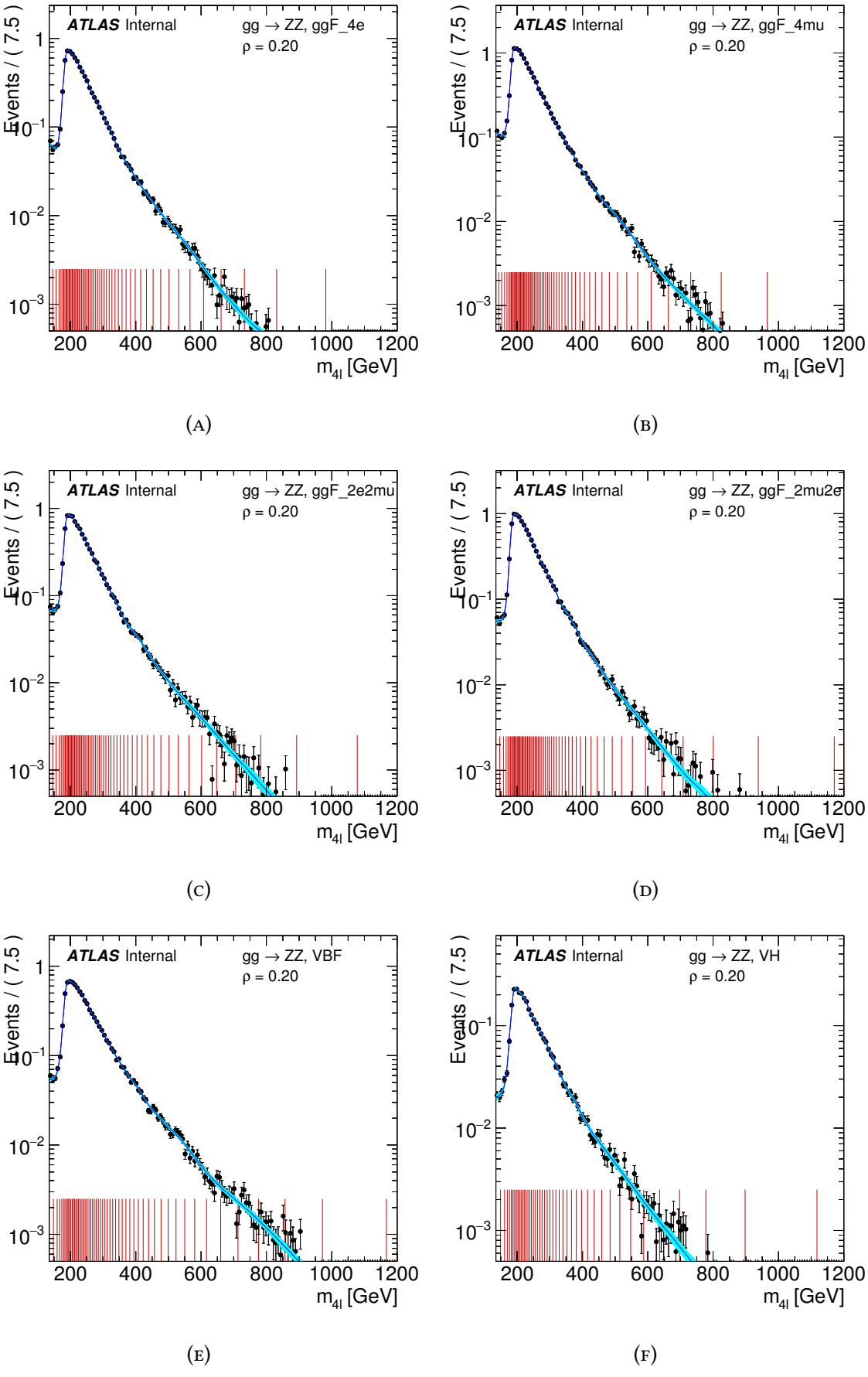

Figure 5.12: The background shapes obtained with the KEYS procedure for the $gg \to ZZ^{(*)}$ process in the six different event categories, overlaid with the generated MC events. The cyan band indicates the MC statistical uncertainty. The red lines show the boundaries of the bins used in the adaptive binning procedure.

5.5.2 Reducible Backgrounds

The reducible backgrounds to the 4ℓ decay channels originate from Z+jets processes and $t\bar{t}$ events, where jets from light-flavoured quarks are misidentified as leptons, or where additional leptons are present from heavy-flavoured quark decays or from photon conversion. A small contribution from WZ production is also present. As will be shown, the composition of the reducible backgrounds depends on the flavour of the subleading di-lepton pair. Therefore, different approaches are used for deriving the shape and the normalisation of the backgrounds, which are segmented into the categories $\ell\ell\mu\mu$ and $\ell\ell ee$. Upon estimating the shape and normalisation of the backgrounds, the obtained $m_{4\ell}$ distributions are again smoothed with the KEYS algorithm to obtain $f_B(x_e)$ from Equation 5.1.

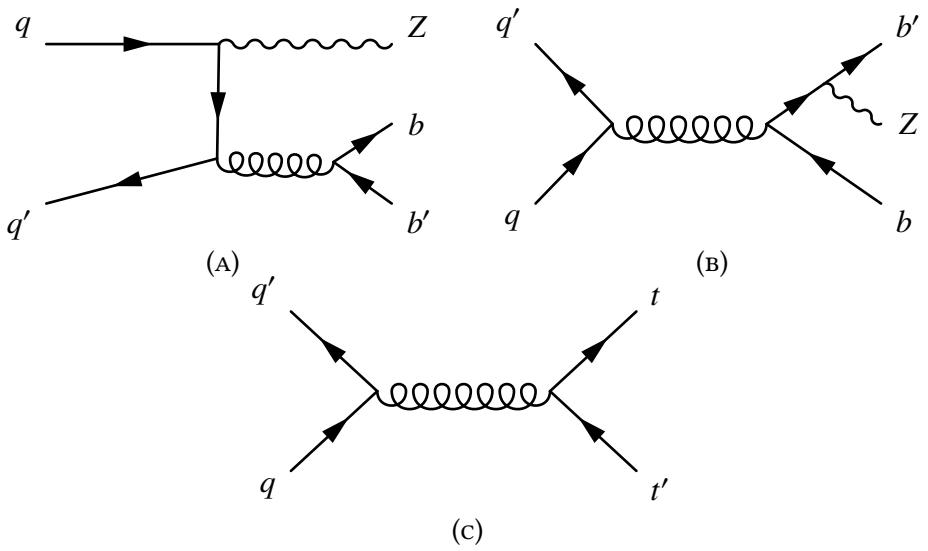

FIGURE 5.13: Examples of lowest-order Feynman diagrams contributing to Z+jets ((A) and (B)) and $t\bar{t}$ production (C).

5.5.2.1 Monte Carlo Samples

The Z+jets MC samples are generated with ALPGEN [121] and interfaced to PYTHIA for hadronisation. The $t\bar{t}$ MC samples are generated with POWHEG interfaced to PYTHIA for hadronisation, to PHOTOS for QED radiative corrections, and to TAUOLA [122, 123] for tau-decay simulation. The WZ samples are generated with SHERPA.

5.5.2.2 $\ell\ell\mu\mu$

The $\ell\ell\mu\mu$ background has three main components – two from Z+jets processes, where heavy-flavoured ($b\bar{b}$) and light-flavoured quarks are distinguished, and the third from $t\bar{t}$ events. The latter component can easily be distinguished from the former two with the m_{12} variable defined in Section 5.3 – the distribution of this variable has a distinct peak around the Z pole for the former two components, but is approximately flat for the latter. To estimate the yield from these processes, an unbinned maximum likelihood fit is performed on data to four different control regions (CR) simultaneously. These CR are defined such that each is enriched in one or more of the background processes:

- **Inverted impact parameter significance CR**. The nominal event selection is applied to the leading di-lepton pair. On the subleading di-lepton pair, the impact parameter significance selection is inverted for at least one lepton in the pair and the isolation requirements is not applied. This particular control region has a large contribution from the $Z + b\bar{b}$ and $t\bar{t}$ processes, since leptons originating from heavy-flavoured quark decays have a larger impact parameter due to the displaced vertex.

- **Inverted isolation CR**. The nominal event selection is applied to the leading di-lepton pair. The subleading di-lepton pair has the standard impact parameter significance selection applied and the isolation selection is inverted for at least one lepton in the pair. By loosening the isolation requirement, the contribution from the Z+light jets component is increased.

- **Same-charge CR**. The nominal event selection is applied to the leading di-lepton pair. The subleading di-lepton pair has neither the impact parameter significance requirement, nor the isolation selection requirements applied. The two leptons in the subleading di-lepton pair are required to have the same charge. All reducible background components have a significant contribution to this CR.

- $e\mu$ **CR**. In this CR, the leading di-lepton pair is required to consist of two leptons with opposite charge and different flavour. For the subleading di-lepton pair, neither of the impact parameter significance or isolation requirements are applied, and leptons with both same and opposite charge are accepted. By doing so, events from the Z+jets processes are suppressed, and contribution from the $t\bar{t}$ process is enhanced.

The above definitions imply that the four regions are orthogonal to each other. Their m_{12} distributions are presented in Figure 5.14. A fifth control region containing all of the above background components is also defined, and used to normalise all the $\ell\ell\mu\mu$ background components in the

maximum likelihood fit. The fit results are thus expressed in terms of number of events in this particular control region. Although the total yield is extracted from a fit to data, the relative ratio of events in the four regions is determined from simulation and hence kept fixed in the fit. The number of $\ell\ell\mu\mu$ background events in the signal region (SR) is obtained by extrapolating the obtained yields with transfer factors. These transfer factors are calculated from MC, and are defined from the per-event probability for each type of background component to satisfy the specific selection criteria of the individual control regions. The obtained transfer factors are presented in Table 5.6.

The small contribution from WZ decays is estimated entirely from simulation.

TABLE 5.6: Probability for the $Z + b\bar{b}$, Z+light jets and $t\bar{t}$ background components to pass the additional isolation and impact parameter requirements of the nominal event selection. The quoted errors correspond to the statistical error arising from the limited size of the MC samples, and a systematic error defined as the difference observed in the 3ℓ final-state in data and MC.

Background component	**Transfer factor** [%]
$Z + b\bar{b}$	3.10 ± 0.19
Z+ light jets	3.0 ± 1.8
$t\bar{t}$	0.55 ± 0.09

5.5.2.3 $\ell\ell ee$

The background in the $\ell\ell ee$ final-state mainly arises from objects mistakenly identified as prompt electrons, which can happen via jets from light-flavoured quarks being misidentified as electrons, via photon conversions, and via non-isolated electrons from heavy-flavoured quark decays. Both the shape and normalisation of the $\ell\ell ee$ background is estimated with a data-driven method, where a "$3\ell + X$" control region is defined. This consists of three leptons with tight selection criteria applied, and one electron with looser selection requirements applied, the latter being denoted X. This method has the advantage that one only has to consider the background composition of the final lepton, X. The three highest-p_T leptons in the event must satisfy the nominal selection, and the two lowest-p_T leptons are required to be electrons. The impact parameter and isolation requirements are removed for the latter electron, among with a loosening of its likelihood ID requirement. Furthermore, the two latter electrons are required to have same charge, as to minimise the contribution from the $ZZ^{(*)}$ continuum.

As stated above, the X component is expected to have three subcomponents; one consisting of jets from light-flavoured quarks faking an electron (f), one consisting of photon conversion and FSR contribution (γ), and a third of electrons originating from the semi-leptonic decays of heavy-flavoured quarks (q). The yield of these subcomponents are extracted with a simultaneous fit on data to the number of hits in the B-layer ($n_{hits}^{B-layer}$) and the number of high- to low-threshold hits in the TRT (r_{TRT}). This approach works because most electrons originating from a converted photon do not have a B-layer hit, and because the TRT threshold can distinguish the hadrons misidentified as electrons from the electrons originating from photon-conversion and heavy-flavoured quark decays. Due to the low contribution of the heavy-flavour component in the $3\ell + X$ CR, the fit is constrained to the yield predicted from MC with a Gaussian constraint allowing a variation of 20%.

The result of the fit is shown in Figure 5.15 for the $2\mu 2e$ and $4e$ channels combined. As for the $\ell\ell\mu\mu$ background, the yields from the CR are extrapolated to the SR with transfer factors. For the f and γ subcomponents, a transfer factor is applied that takes the p_T dependent efficiencies into account, corrected with a data/MC scale factor. Since the heavy-flavour component is small, the p_T bin weights from the fit suffer from large statistical fluctuations. Therefore, the extrapolation of this subcomponent to the signal region is done with an inclusive transfer factor, which is defined as the ratio of events observed in the SR and CR. The efficiencies used to calculate the transfer factors are presented in Table 5.7.

Table 5.7: Probability for the three $\ell\ell ee$ background components to pass the nominal event selection in the $4e$ and $2\mu 2e$ final-states. These three components originate from light-flavoured quarks faking an electron (f), photon conversion and FSR contribution (γ), and the semi-leptonic decays of heavy-flavoured quarks (q). The quoted errors include systematic uncertainties and the statistical uncertainty arising from the MC estimation.

Background component	**Transfer factor** [%]	
	$4e$	$2\mu 2e$
f	3.4 ± 0.04	3.4 ± 0.04
γ	2.4 ± 0.4	2.4 ± 0.4
q	11 ± 2	9 ± 2

5.5.2.4 Reducible Background Shapes

The $m_{4\ell}$ distributions of the reducible backgrounds are needed in order to derive the shape and hence produce the PDF $f_B(x_e)$, which is required to construct the likelihood function. The shape

of the distribution for the $\ell\ell\mu\mu$ background is taken from simulation, where the uncertainty is estimated by varying the selection on the track isolation and impact parameter significance. The corresponding distribution for the $\ell\ell ee$ background originates from the $3\ell + X$ sample, after reweighting with the transfer factor in order to match the kinematics of the signal region. The uncertainty on the shape of the $\ell\ell ee$ background is taken as the difference between those obtained with the method described above and corresponding shapes obtained with two separate methods used as a cross-check.

Upon obtaining $m_{4\ell}$ distributions for the various background components, these are smoothed with the KEYS algorithm. The obtained PDFs $f_B(x_e)$ along with the systematic variations are shown in Figure 5.16.

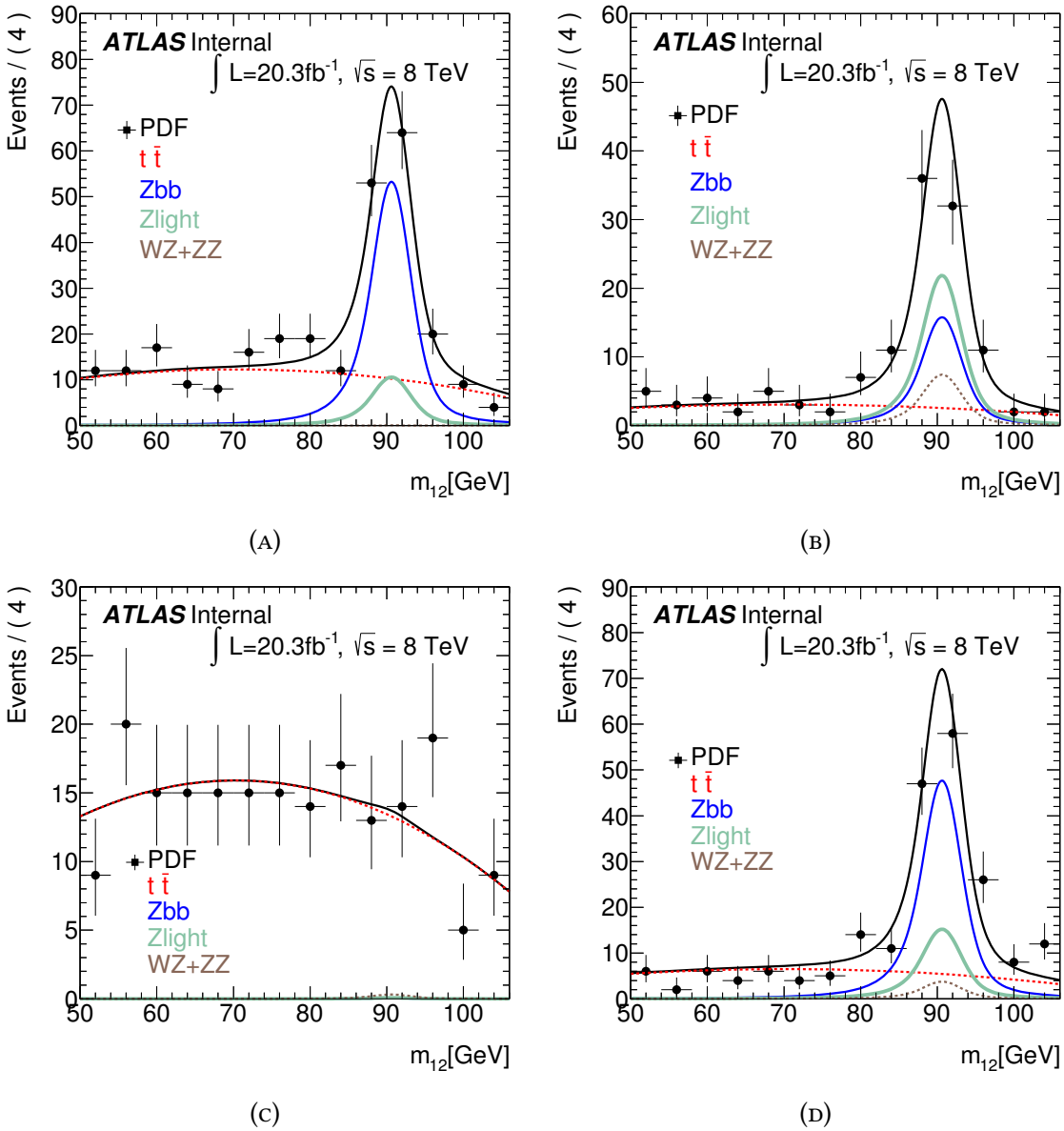

Figure 5.14: The observed m_{12} distributions in data and the results of the maximum likelihood fit imposed to the four control regions described in the text. The fit results are shown for the total background as well as the individual components. The WZ and ZZ contamination is estimated entirely from simulation.

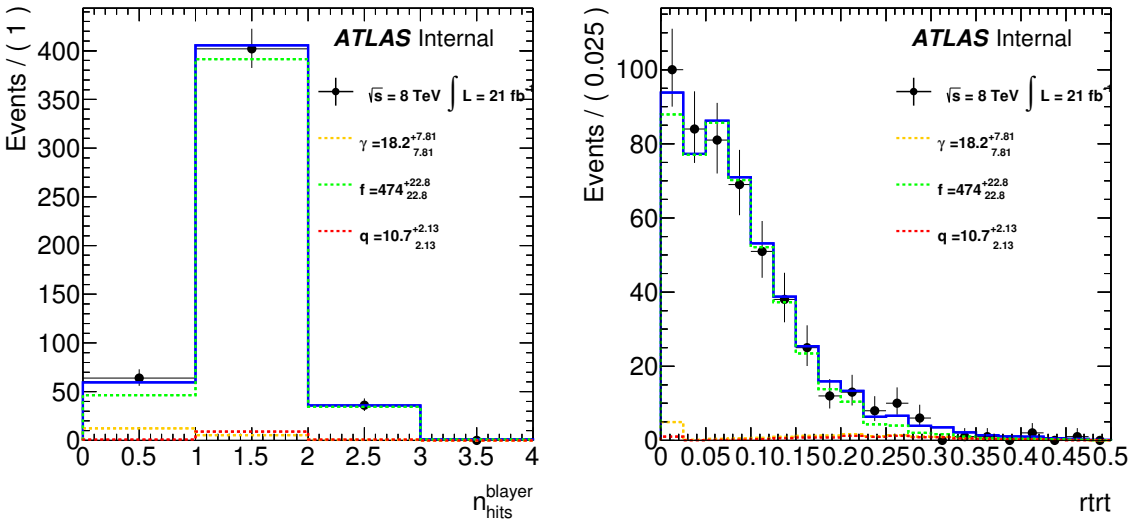

(A) (B)

FIGURE 5.15: Fits applied to $n_{hits}^{B-layer}$ (A), the number of hits in the innermost pixel detector layer, and r_{TRT} (B), the ratio of the number of high-threshold to low-threshold hits in the TRT, for the $2e2\mu$ final-state. The histograms show the light-flavoured jets mistakenly identified as an electron (f), electrons from photon-conversion (γ) and electrons from heavy-flavoured decays (q).

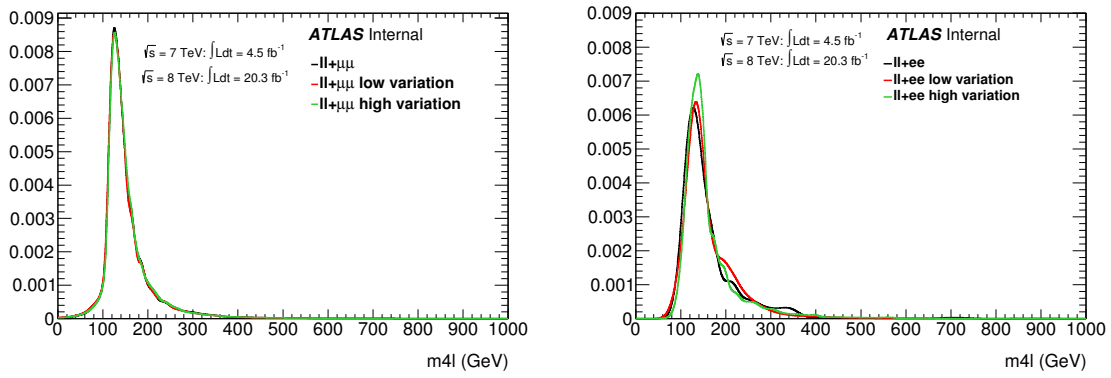

(A) (B)

FIGURE 5.16: $f_B(x_e)$ for the $\ell\ell\mu\mu$ (A) and $\ell\ell ee$ (B) background in the signal region, overlaid with systematic variations. The presented shapes were produced with both $\sqrt{s} = 7$ TeV and $\sqrt{s} = 8$ TeV data, however, only the latter is used in the present analysis.

5.6 Systematic Uncertainties

This section describes the dominant systematic uncertainties. The full set is described in [124]. The systematic uncertainties are divided according to their source, and therefore into experimental and theoretical. Generally, the systematic uncertainties can affect the normalisation of a distribution, its shape, or both. All systematic uncertainties presented in the following are incorporated into the likelihood function in Equation 5.1 as nuisance parameters (NPs), the details of which are explained in Section 5.7.

5.6.1 Experimental Uncertainties

The dominant experimental uncertainties affecting this search arise from the uncertainty on the integrated luminosity, from the lepton reconstruction and identification, and from the jet energy scale (JES). These sources of uncertainty are described separately below. The effect of the experimental uncertainties on the yield of a Higgs boson signal with $m_H = 400$ GeV is shown in Table 5.8.

Table 5.8: Experimental systematic uncertainties on the signal yield per event category at $m_H = 400$ GeV. Only uncertainties resulting in a variation of at least 0.5% for at least one m_H value are shown. The combined uncertainty for the four ggF event categories, folded in quadrature, is 6.81%.

Nuisance parameter	ggF $4e$	ggF 4μ	ggF $2e2\mu$	ggF $2\mu2e$	VBF	VH
Electron reconstruction, identification and trigger efficiencies						
ATLAS_EL_2012_ST_10	0.13%	-	0.04%	0.07%	0.04%	0.07%
ATLAS_EL_2012_ST_15	0.20%	-	0.07%	0.10%	0.08%	0.05%
ATLAS_EL_2012_ID_low	0.34%	-	0.11%	0.18%	0.13%	0.11%
ATLAS_EL_2012_REC_low	0.36%	-	0.11%	0.18%	0.13%	0.22%
ATLAS_EL_2012_REC_high	0.42%	-	0.18%	0.21%	0.18%	0.15%
ATLAS_EL_2012_IDST_high	2.90%	-	1.38%	1.45%	1.25%	1.20%
ATLAS_EL_TRIG	0.01%	-	0.02%	0.03%	0.01%	0.01%
ATLAS_H4l_EL_EFF_ISOIP	0.13%	-	0.04%	0.07%	0.05%	0.09%
Muon reconstruction, identification and trigger efficiencies						
ATLAS_MU_EFF	-	1.63%	0.82%	0.82%	0.91%	0.96%
ATLAS_MU_TRIG	-	0.14%	0.01%	0.02%	0.05%	0.05%

Continued on next page

Nuisance parameter	ggF $4e$	ggF 4μ	ggF $2e2\mu$	ggF $2\mu2e$	VBF	VH
Electron energy scale and resolution						
ATLAS_EM_LArElecUnconv_Barrel	0.10%	-	-0.10%	0.07%	-0.01%	-0.43%
ATLAS_EM_mRes_CT	0.06%	-	0.41%	-0.39%	-0.04%	0.42%
ATLAS_EM_LArCalib_Barrel	0.07%	-	0.06%	-0.07%	0.00%	0.00%
ATLAS_EM_mRes_MAT	0.04%	-	-0.34%	0.31%	0.03%	-0.41%
ATLAS_EM_PS_Barrel	0.05%	-	-0.14%	0.14%	-0.00%	0.00%
ATLAS_EM_MatCryo_Barrel	0.15%	-	0.05%	-0.05%	-0.01%	0.49%
ATLAS_EM_ES_Z	0.14%	-	0.15%	-0.13%	-0.01%	0.51%
ATLAS_EM_mRes_ST	0.11%	-	-0.20%	0.21%	0.01%	0.49%
ATLAS_EM_L2Gain	0.07%	-	0.16%	-0.16%	0.00%	0.07%
Muon momentum scale						
ATLAS_MU_MS	-	-0.07%	-0.32%	0.31%	0.02%	-0.01%
ATLAS_MU_MS_RES_ID	-	0.10%	0.50%	-0.54%	0.04%	-0.16%
ATLAS_MU_MS_RES_MS	-	-0.05%	0.43%	-0.49%	-0.14%	-0.06%
Jet energy scale						
ATLAS_JES_2012_Eta_StatMethod	0.37%	0.25%	0.19%	0.16%	0.77%	0.80%
ATLAS_JES_2012_Mixed2	0.14%	0.12%	0.05%	0.04%	0.26%	0.53%
ATLAS_JES_2012_PilePt	0.12%	0.14%	0.10%	0.09%	0.15%	0.75%
ATLAS_JES_2012_PileRho_ANA_BG	0.81%	0.44%	0.62%	0.50%	1.61%	2.20%
ATLAS_JES_Eta_Modelling	0.91%	1.24%	1.05%	1.18%	3.93%	1.78%
ATLAS_JES_NPV	0.29%	0.24%	0.28%	0.33%	0.72%	1.17%
ATLAS_JES_Mu	0.23%	0.23%	0.26%	0.15%	0.68%	0.76%
ATLAS_JES_FlavComp_ANA_BG	1.90%	1.81%	1.70%	1.64%	5.40%	5.08%
ATLAS_JES_FlavResp	0.87%	0.96%	1.00%	1.04%	2.92%	3.04%
ATLAS_JES_BASE1	0.23%	0.21%	0.24%	0.18%	0.80%	1.17%
ATLAS_JES_BASE2	0.35%	0.40%	0.50%	0.53%	1.90%	2.06%
ATLAS_JES_BASE3	0.33%	0.36%	0.42%	0.42%	1.54%	2.02%
ATLAS_JES_BASE4	0.14%	0.14%	0.19%	0.17%	0.49%	1.22%
ATLAS_JES_BASE5	0.04%	0.06%	0.05%	0.06%	0.17%	0.43%
ATLAS_JES_BASE6	0.09%	0.09%	0.12%	0.12%	0.33%	0.78%

Continued on next page

Nuisance parameter	ggF $4e$	ggF 4μ	ggF $2e2\mu$	ggF $2\mu2e$	VBF	VH
Total	4.06%	3.10%	3.18%	3.19%	8.26%	7.77%

5.6.1.1 Lepton Trigger, Reconstruction and Identification

The following list of systematic uncertainties apply to the lepton trigger, reconstruction and identification:

- Seven NPs describe the uncertainties on the electron reconstruction and identification efficiency (all designated with ATLAS_EL_2012 in Table 5.8). These are based on components that are correlated or uncorrelated across different bins of E_T.
- One NP on the isolation and IP significance cut-efficiency is applied for electrons with $E_T <$ 15 GeV (H4l_EL_EFF_ISOIP).
- One NP represents the reconstruction and identification uncertainty for muons (MU_EFF).
- One NP represents the uncertainty on the signal yield originating from the electron trigger efficiency uncertainty (EL_TRIG) and the muon trigger efficiency uncertainty (MU_TRIG).

5.6.1.2 Lepton Scale and Resolution

An implication of the uncertainty on the lepton scale is the swapping of the leading and sub-leading Z boson, the consequence being that events migrate between the $2e2\mu$ and $2\mu2e$ final-states. However, this normalisation uncertainty is anti-correlated between the two categories and therefore largely cancels out, leaving no noticeable impact on the overall yield. Another implication of the scale uncertainty is a shift of the peak position of the signal. In this search, the following systematic uncertainties apply to the lepton scale and resolution:

- 25 NPs describe the uncertainties on the electron energy scale, and one NP describe the uncertainty on the electron momentum scale. The impact from the former on the peak position of the signal was found to be less than 0.5% over the full m_H spectrum.
- Four NPs describe the electron and photon energy resolution uncertainties. The leading electron resolution uncertainties on the signal are binned in $m_{4\ell}$ and has a maximum uncertainty of 15% occurring near the peak region of a given m_H value.

- One NP describes the muon momentum scale uncertainty (`MU_MS`), while two NPs represent the muon momentum resolution uncertainty in the MS (`MU_MS_RES_MS`) and ID (`MU_MS_RES_ID`). The impact from the former on the peak position of the signal was found to be less than 0.15% over the full m_H spectrum. The resolution uncertainties on the signal are segmented in $m_{4\ell}$ and peaks with a value of 10% in the peak region of a given m_H value.

5.6.1.3 Jet Scale and Resolution

A total of 15 NPs are used in this search to describe the different sources of JES uncertainty, each of which has associated variations depending on the jet p_T and η. These NPs (all carrying a name starting with `ATLAS_JES`) and their effect on the normalisation of a signal at $m_H = 400$ GeV are shown in Table 5.8. The JES uncertainties most relevant to this search are associated to the *in situ* calibration techniques. These are techniques which assess differences in the jet energy measurement between data and MC by exploiting variables such as the p_T balance between a jet and a well-measured reference object, the flavour composition, the difference in response between quark-initiated jets and gluon-initiated jets, and uncertainties due to pile-up [125]. A detailed description of all sources of JES uncertainties is given in [124].

5.6.1.4 Reducible Background Uncertainties

As described in Section 5.5, the reducible background is estimated with data-driven techniques. Uncertainties arise from differences between the nominal method described in this thesis and the supplementing methods described in [124], uncertainties on the transfer factors used to extrapolate from the control region to the signal region, and limited statistics in the control regions. The following NPs are included in the final fit:

- Two NPs (`ATLAS_norm_SF_H4l_Z_llee_2012` and `ATLAS_norm_SF_H4l_Zbb_llmumu_2012`) describe the normalisation uncertainty for he $\ell\ell ee$ and $\ell\ell\mu\mu$ backgrounds.

- Two NPs (`ATLAS_shape_SF_H4l_Z_llee_2012` and `ATLAS_shape_SF_H4l_Z_llee_2012`) describe the difference in the shape of the $m_{4\ell}$ distribution obtained using the different background estimation techniques. These are illustrated in Figure 5.16.

5.6.2 Theoretical Uncertainties

Theoretical uncertainties affect the modelling of the signal and also the irreducible backgrounds, since these are estimated entirely from simulation. For the signal, besides the uncertainties arising

from the limited MC statistics described in Section 5.4, uncertainties on the acceptance of the event selection and the categorisation are taken into account. Since the final results of the analysis are expressed as limits on the production cross-section, uncertainties on the reference cross-section are not needed.

5.6.2.1 Signal

As described in Section 5.4, the modelling of the signal relies on fully simulated samples generated with POWHEG and PYTHIA. The main uncertainty on this modelling is related to the signal acceptance, which is highly sensitive to underlying theoretical parameters. This uncertainty is therefore evaluated by varying the parameters of POWHEG and PYTHIA and comparing the results when applying the full selection of the analysis at generator (truth) level. The following variations are considered and included in the final fit as NPs:

- One NP describes the QCD scale uncertainty, which is derived from varying the renormalisation (μ_R) and factorisation (μ_F) scales. The μ_F and μ_R variations are found to have a small effect on the acceptance, less than 1.5%. Furthermore, no clear trend as a function of m_H is observed.

- One NP describes the uncertainty from increasing and decreasing the initial state radiation (ISR) and final state radiation (FSR) in the simulation. The ISR and FSR variations cause an effect of up to 10%, which is anti-correlated between the ggF-like and VBF/VH-like event categories. The ISR/FSR acceptance uncertainties are summed in quadrature and parametrised as a function of m_H with a linear fit.

- One NP describes the uncertainty from replacing the nominal PDF. The PDF variations give rise to minor changes in acceptance, maximum 3%, with no clear trend as a function of m_H.

The above acceptance uncertainties are summarised in Table 5.9, segmented according to three event categories; inclusive ggF, VBF and VH. In order to harmonise and facilitate the combination of the heavy Higgs search in this channel with those performed in the three additional $H \to ZZ^{(*)}$ channels, each of the three acceptance uncertainties are split from a single component into two. These two components separately describe the uncertainties on ggF and VBF production. More details on this will be given in Chapter 6, where the combination of the four searches in the $H \to ZZ^{(*)}$ decay channels is documented.

TABLE 5.9: Uncertainties on the acceptance of the signal arising from variations in the underlying theoretical parameters used in the generation of the signal samples. The uncertainties are presented for a signal originating from both the ggF and VBF production mode, and its effect on the inclusive ggF, VBF and VH event categories is shown. The uncertainty arising from the ISR/FSR variation varies as a function of m_H.

Source of uncertainty	**ggF production**			**VBF production**		
	ggF	VBF	VH	ggF	VBF	VH
QCD scale	0.7%	1%	1%	1%	1%	2%
PDF	2%	2%	2.5%	1%	0.5%	2%
ISR/FSR	2 − 5%	7 − 10%	4 − 7%	1 − 2%	0.5 − 2%	1 − 5%

5.6.2.2 Backgrounds

The theoretical uncertainties affecting the $q\bar{q} \to ZZ^{(*)}$ background are:

- One NP describe the QCD scale uncertainties, which are evaluated by varying μ_R and μ_F. This method provides an uncertainty parametrised in $m_{4\ell}$ and is therefore both a shape and a normalisation uncertainty of 4%.

- One NP describe the acceptance uncertainties. These are obtained in a similar way as for the signal, by evaluating the difference in the observed yields at generator level when varying μ_R and μ_F. This uncertainty is found to be 8% for the VBF category, 3% for the VH category, and 4% for the ggF categories.

- Two NPs are included which take the uncertainties on the NLO EW corrections into account. The first is a systematic uncertainty of 100%, which is applied to the NLO EW weight (as described in [126]) in order to account for the inaccuracy arising from the calculation being performed at LO QCD. A second uncertainty of 100% is applied to the weights to account for the fact that the EW NLO corrections only are valid in the regime where both Z bosons are on-shell. This results in an uncertainty of 2.6%, 1.9% and 0.5% in the VBF, VH, and ggF event categories, respectively.

- One NP describing the uncertainty on the PDF and α_s, which is parametrised as function of $m_{4\ell}$ and therefore result in a shape uncertainty and in an overall normalisation uncertainty. For the $q\bar{q} \to ZZ^{(*)}$ background this leads to a normalisation uncertainty of 3%.

For the $gg \to ZZ^{(*)}$ background, the following theoretical uncertainties are taken into account:

- One NP describing the uncertainty on the k-factor. An uncertainty of 30% is attributed to the interference and an additional 100% is added due to the unknown validity of applying the k-factor derived with the $gg \to h \to ZZ^{(*)}$ processes to the $gg \to ZZ^{(*)}$ processes. This is applied in addition to the uncertainty on the k-factor arising from varying the QCD scale.

- One NP describing the uncertainty on the acceptance. These are assessed by comparing the acceptance of the SHERPA samples to the samples showered with PYTHIA, since these two generators have different parton showering models. Differences of 92%, 91% and 14% are observed for the VBF, VH and ggF categories, respectively.

- One NP describing the uncertainty on the PDF and α_s, which is parametrised as function of $m_{4\ell}$ and therefore result in a shape uncertainty and in an overall normalisation uncertainty. For the $gg \to ZZ^{(*)}$ background this leads to a normalisation uncertainty of 8%.

Table 5.10: Uncertainties on the backgrounds arising from variations in the underlying theoretical parameters used in the generation of the background samples. The uncertainties are presented for both the $q\bar{q} \to ZZ$ and $gg \to ZZ$ processes, and their effect on the inclusive ggF, VBF and VH event categories is shown.

Source of uncertainty	$q\bar{q} \to ZZ$			$gg \to ZZ$		
	ggF	VBF	VH	ggF	VBF	VH
QCD scale	4%	4%	4%	100%	100%	100%
PDF+α_S	3%	3%	3%	8%	8%	8%
Acceptance	4%	8%	3%	14%	92%	91%
NLO EW correction	0.5%	2.6%	1.9%	–	–	–

5.6.2.3 MC Statistical Uncertainties

The uncertainties on the shape of $f_S(x_e)$ and $f_B(x_e)$ arising due to limits MC statistics are included as systematic uncertainties. These are computed with the method described in Section 5.4.3 and included for both the signal and the $ZZ^{(*)}$ backgrounds.

5.7 Statistical Procedures

This section describes the statistical procedures employed in this search in order to obtain final results in the form of upper limits on the heavy Higgs boson production rate.

5.7.1 Including Nuisance Parameters

As mentioned in the previous section, each systematic uncertainty of this search is incorporated into the likelihood function as a NP, θ. A NP is constrained about its nominal expectation value, $\tilde{\theta}$, by the distribution $N(\tilde{\theta}|\theta)$, which is determined from some auxiliary measurement. In this analysis, the constraint on θ is a unit Gaussian, i.e. it has the form:

$$G(\tilde{\theta}|\theta, 1) = \frac{1}{\sqrt{2\pi}} e^{-\frac{(\tilde{\theta}-\theta)^2}{2}} \tag{5.3}$$

Both the signal and the backgrounds are parametrised in terms of the NPs such that the response of the signal and background to each θ is factorised from the nominal value of the expected rate. This implies that both the yield and shape depends on the value of the NPs, and the following expression, where n_0 is the nominal expectation of either the signal or background yield (i.e. S or B in Equation 5.1), therefore holds:

$$n = n_0 \times \prod_{i=1}^{N_\theta} \nu(\theta_i) \tag{5.4}$$

The form of $\nu(\theta_i)$ depends on the source of the systematic uncertainty. In this search, the systematic uncertainties can affect either the normalisation of a distribution, its shape, or both. For systematic uncertainties affecting the normalisation, $\nu(\theta_i)$ takes the form $\nu(\theta) = \kappa^\theta$. Since θ is constrained by a unit Gaussian, κ^θ is log-normally distributed. If a NP affects the shape of the signal or background distributions, the NP is separated into a normalisation component and a shape component, such that the variation of the shape does not affect the expected rate. The variation of the shape component is done with vertical interpolation [127, 128].

Using the above convention, the NPs are added to the likelihood function as constraint terms (or penalty terms), and the likelihood function therefore takes the form:

$$\mathcal{L}(x_1, ..., x_n|\mu, \boldsymbol{\theta}) = \text{Pois}(n|\mu S + B) \times \left[\prod_{e=1}^{n} \frac{\mu S f_S(x_e) + B f_B(x_e)}{\mu S + B} \right] \times \prod_{i=1}^{N_\theta} N(\tilde{\theta}|\theta) \tag{5.5}$$

Here $\boldsymbol{\theta}$ denotes the full set of the total number nuisance parameters, N_θ. By incorporating the NPs into the likelihood function as constraint terms, the value of the likelihood increases when a NP is shifted from its nominal value. When maximising the likelihood function, the presence of

NPs broadens the likelihood curve, reflecting the loss of information that including the systematic uncertainties corresponds to. As will be explained in the following section, the value and constraint of the NPs can be determined from data by conditioning them in the likelihood fit, meaning that they are fitted to data in order to identify the values that maximise the likelihood. Given that the signal and background distributions have this dependence on the NPs, the distribution of these quantities is presented post-fit, i.e. after the fit in which the NPs are conditioned to the data.

5.7.2 The Fitting Model

The final step of the analysis is conducted with the likelihood function in the form of Equation 5.5. A fit with this is performed simultaneously to the six event categories described in Section 5.3.6. For each event category, the likelihood function contains several terms describing the contribution from both the signal and the backgrounds. The likelihood function for the VBF and VH event categories both contain six terms; two terms representing the signal contribution from the ggF and VBF production modes, and four terms describing the contribution from the $q\bar{q} \to ZZ^{(*)}$, $gg \to ZZ^{(*)}$, $\ell\ell ee$ and $\ell\ell\mu\mu$ backgrounds. Each of the likelihood functions for the four ggF categories contain the contribution from the ggF and VBF production modes, from the $q\bar{q} \to ZZ^{(*)}$ and $gg \to ZZ^{(*)}$ backgrounds, among the contribution from either the $\ell\ell ee$ or $\ell\ell\mu\mu$ background, depending on the final-state. As a result, the complete likelihood function contains 32 terms.

The likelihood terms representing the contribution from the signal are scaled with the the signal-strength μ, which is defined as:

$$\mu = \frac{\sigma \times BR}{\sigma_{\text{SM}} \times BR_{\text{SM}}} \tag{5.6}$$

Here σ_{SM} is the total SM Higgs boson production cross-section and BR_{SM} the SM Higgs boson branching ratios. With this convention, μ represents the scale factor on the yield of signal, which can be used to turn the signal on and off in the likelihood function. The absence of a signal, i.e. background-only conditions, corresponds to $\mu = 0$, while $\mu = 1$ signifies absolute compliance with the signal prediction from the reference model. In order to facilitate the model-independent search strategy, two additional signal-strengths are defined:

$$\mu_{\text{ggF}} = \frac{\sigma \times BR}{\sigma_{\text{SM, ggF}} \times BR_{\text{SM}}} \qquad \mu_{\text{VBF}} = \frac{\sigma \times BR}{\sigma_{\text{SM, VBF}} \times BR_{\text{SM}}} \tag{5.7}$$

Here $\sigma_{\text{SM,ggF}}$ and $\sigma_{\text{SM, VBF}}$ denote the SM values for the ggF and VBF production cross-sections. These two additional signal-strengths are required in order to disentangle the contribution from the different production modes and thereby estimate their rates separately. μ_{ggF} acts on all the likelihood terms describing the ggF contribution, while μ_{VBF} acts on all the terms describing the VBF and VH contribution. The μ_{VBF} scale factor is applied to the VH event category as well, since the yield from this production mechanism is expected to be very small, and furthermore because the rates of the VBF and VH production modes scale with the same couplings.

5.7.3 The CL_S Technique

The results of this chapter will be presented as upper limits on the Higgs boson production cross-section times $H \to ZZ$ branching ratio. These upper limits (or exclusion limits) signify the maximum production rate that the data can support at a given statistical confidence level. The limits are derived with the modified confidence interval method (CL_S) [129, 130], in which the background-only hypothesis, $\mu = 0$, is tested against a signal plus background hypothesis where $\mu > 0$. In practise, the limits are set on μ and afterwards translated into units of fb.

To perform the statistical procedures, the likelihood function in Equation 5.5 is used to construct the profile likelihood ratio defined as:

$$\lambda(\mu) = \frac{\mathcal{L}\left(\mu, \hat{\hat{\boldsymbol{\theta}}}(\mu)\right)}{\mathcal{L}\left(\hat{\mu}, \hat{\boldsymbol{\theta}}\right)} \tag{5.8}$$

The denominator contains the unconditional maximum-likelihood fit, where the parameter of interest, μ, and the full set of NPs, $\boldsymbol{\theta}$, accommodate to the values that maximise the likelihood function, $\hat{\mu}$ and $\hat{\boldsymbol{\theta}}$. The numerator contains the conditional maximum-likelihood fit, where the NPs take on the values that maximise the likelihood for a specified hypothesis of μ, $\hat{\hat{\boldsymbol{\theta}}}$. With these definitions, the profile likelihood ratio measures the compatibility of a given μ hypothesis with the value favoured by data, $\hat{\mu}$: $\lambda(\mu) \to 1$ implies good agreement and $\lambda(\mu) \to 0$ poor agreement.

The profile likelihood ratio in Equation 5.8 is used to define the test-statistic:

$$\tilde{q}_\mu = \begin{cases} -2\ln\lambda(\mu) & \text{if } \hat{\mu} \leq \mu, \\ 0 & \text{if } \hat{\mu} \geq \mu, \end{cases} \tag{5.9}$$

The presence of a signal is assumed to manifest as a positive contribution on top of the background, i.e. as an excess of events. Hence, this procedure exclusively tests μ hypotheses with values greater than what is observed in data. Therefore, in instance of $\hat{\mu} \geq \mu$, the test-statistic is set equal to 0. For a given data-set and μ hypothesis, the observed value of the test-statistic $\tilde{q}_{\mu,\,obs}$ is returned. The value of the test-statistic as function of μ follows the probability distribution $f(\tilde{q}_\mu|\mu')$. In practise, the computation of $f(\tilde{q}_\mu|\mu')$ distributions is done with asymptotic approximations, the details of which are given in [130].

With the definitions above, the $\mathrm{CL_S}$ limit is defined as [131]:

$$\mathrm{CL_S}(\mu) = \frac{\mathrm{CL_{s+b}}(\mu)}{\mathrm{CL_b}(\mu)} \tag{5.10}$$

$$\mathrm{CL_{s+b}}(\mu) = \int_{\tilde{q}_{\mu,\,obs}}^{\infty} f(\tilde{q}_\mu|\mu) d\tilde{q}_\mu \tag{5.11}$$

$$\mathrm{CL_b}(\mu) = \int_{\tilde{q}_{\mu,\,obs}}^{\infty} f(\tilde{q}_\mu|\mu = 0) d\tilde{q}_\mu \tag{5.12}$$

The 95% $\mathrm{CL_S}$ upper limit on μ is obtained by finding the maximum value of μ that yields a $\mathrm{CL_S}$ of 0.05.

Two sets of limits are computed; the expected and the observed. The expected limit represents the sensitivity of the given analysis. It is calculated from Equation 5.10, but instead of integrating from $\tilde{q}_{\mu,\,obs}$, the integration happens from the median significance $\mathrm{med}[Z_\mu] = \sqrt{\tilde{q}_{\mu,\,A}}$ [130], where $\tilde{q}_{\mu,\,A}$ is given by:

$$\tilde{q}_{\mu,\,A} = -2 \ln \left[\frac{\mathcal{L}\left(\mu, \hat{\hat{\boldsymbol{\theta}}}\right)}{\mathcal{L}\left(\mu', \boldsymbol{\theta}\right)} \right] \tag{5.13}$$

The value of $\tilde{q}_{\mu,\,A}$ is obtained from the Asimov data-set, which is pseudo-data-set that in this instance is generated under the background-only hypothesis. This particular data-set is defined such that all statistical fluctuations are suppressed, meaning that when using it to evaluate the estimators for all parameters, the true parameter values are obtained, i.e. $\hat{\theta}_{\mathrm{Asimov}} = \theta$, and in this instance $\hat{\mu} = \mu' = 0$.

5.7.4 Nuisance Parameter Rankings and Pulls

In order to validate the behaviour of the fit described above and assess the importance of the individual systematic uncertainties, their pull, their impact on the parameter of interest (POI), among their relative ranking in terms of impact are derived. These quantities are summarised in Figure 5.17 to Figure 5.20. For a NP constrained by a unit Gaussian, these quantities are defined as follows:

- The **pull** indicates the level of consistency between the nominal value of a NP (θ_0) and the value it obtains in the unconditional fit ($\hat{\theta}$), and is defined as the distance between these two numbers normalised with the nominal constraint ($\Delta\theta$), i.e. as $(\hat{\theta}-\theta_0)/\Delta\theta$. When calculating the pull, the signal-strength for the production mechanism not under test is profiled in the unconditional fit. The constraint on the NP is calculated as well, and this quantity is used to assess whether a NP is over-constrained by the fit. Since the pull is normalised with $\Delta\theta$, the constraint is allowed to take on values between ± 1. In Figure 5.17 to Figure 5.20, the pull and constraint is visualised with the black points, the values of which should be read from the lower horizontal axis.

- The **pre-fit impact** is found by holding the NP constant at its value obtained in the unconditional fit while shifting the value by ± 1 and redoing the fit. The change in the fitted value of the POI, which in this analysis is denoted either $\Delta\mu_{\text{ggF}}$ or $\Delta\mu_{\text{VBF}}$, happening as a result of the ± 1 variation of each individual NP is taken as the impact. In Figure 5.17 to Figure 5.20, the pre-fit impact is represented by the yellow area and is measured in units of $\Delta\mu_{\text{ggF}}$ or $\Delta\mu_{\text{VBF}}$ shown on the upper horizontal axis.

- The **post-fit impact** is found by holding the NP constant at its value obtained in the unconditional fit, but this time assessing its impact on the POI when shifting its value $\pm 1\sigma$. In Figure 5.17 to Figure 5.20 the post-fit impact is represented by the grey, cross-hatched area.

- The **ranking** lists the NPs in terms of post-fit impact in descending order.

The above quantities are computed at discrete m_H values separately for both μ_{ggF} and μ_{VBF}. The procedures are performed on data and also on an Asimov data-set, where a pre-defined value of μ_{ggF} and μ_{VBF} are injected. In this analysis, Asimov data-sets with $\mu_{\text{ggF}} = \mu_{\text{VBF}} = 0$ and 0.1 are used. However, since the fitted value of μ_{ggF} and μ_{VBF} in the data and in the Asimov data-set with $\mu_{\text{ggF}} = \mu_{\text{VBF}} = 0$ is very close to 0, the change in the POI observed from varying the individual NPs is smaller than the tolerance of the fit, meaning that the change in the POI cannot be determined

reliably. As a result, only the ranking calculated with the $\mu_{\text{ggF}} = \mu_{\text{VBF}} = 0.1$ Asimov data-set is considered in this analysis.

Figure 5.17 to Figure 5.20 show the systematic ranking performed on this Asimov data-set at $m_H = 200$ GeV and $m_H = 900$ GeV. At both low and high mass, the dominant uncertainties on μ_{ggF} and μ_{VBF} are the ZZ theory systematic uncertainties. For ggF, the dominant experimental uncertainty is on the integrated luminosity, while for VBF the dominant experimental uncertainties are on the JES.

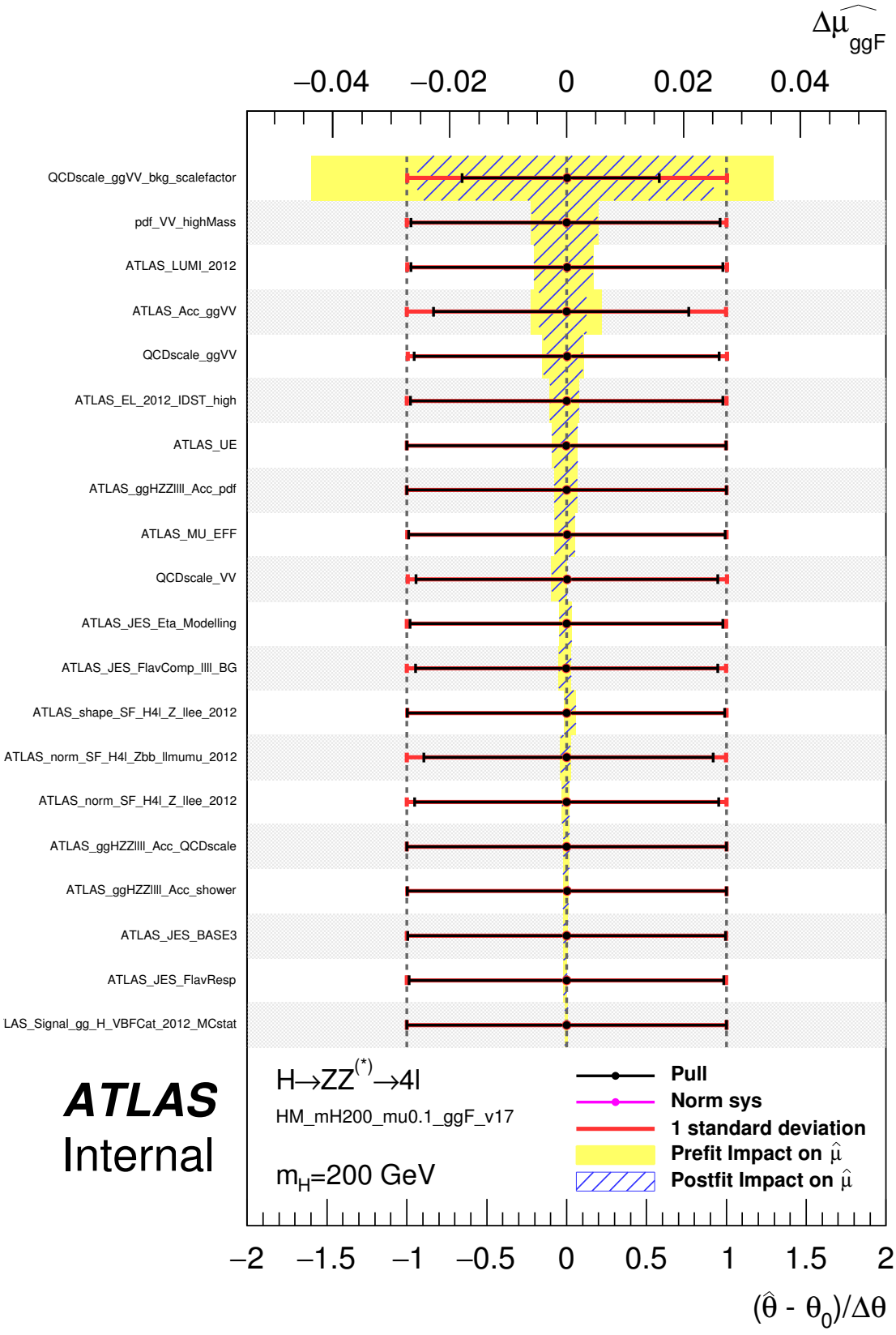

FIGURE 5.17: Nuisance parameter ranking performed with μ_{ggF}. The ranking was performed at $m_H = 200$ GeV with an Asimov data-set generated with $\mu = 0.1$.

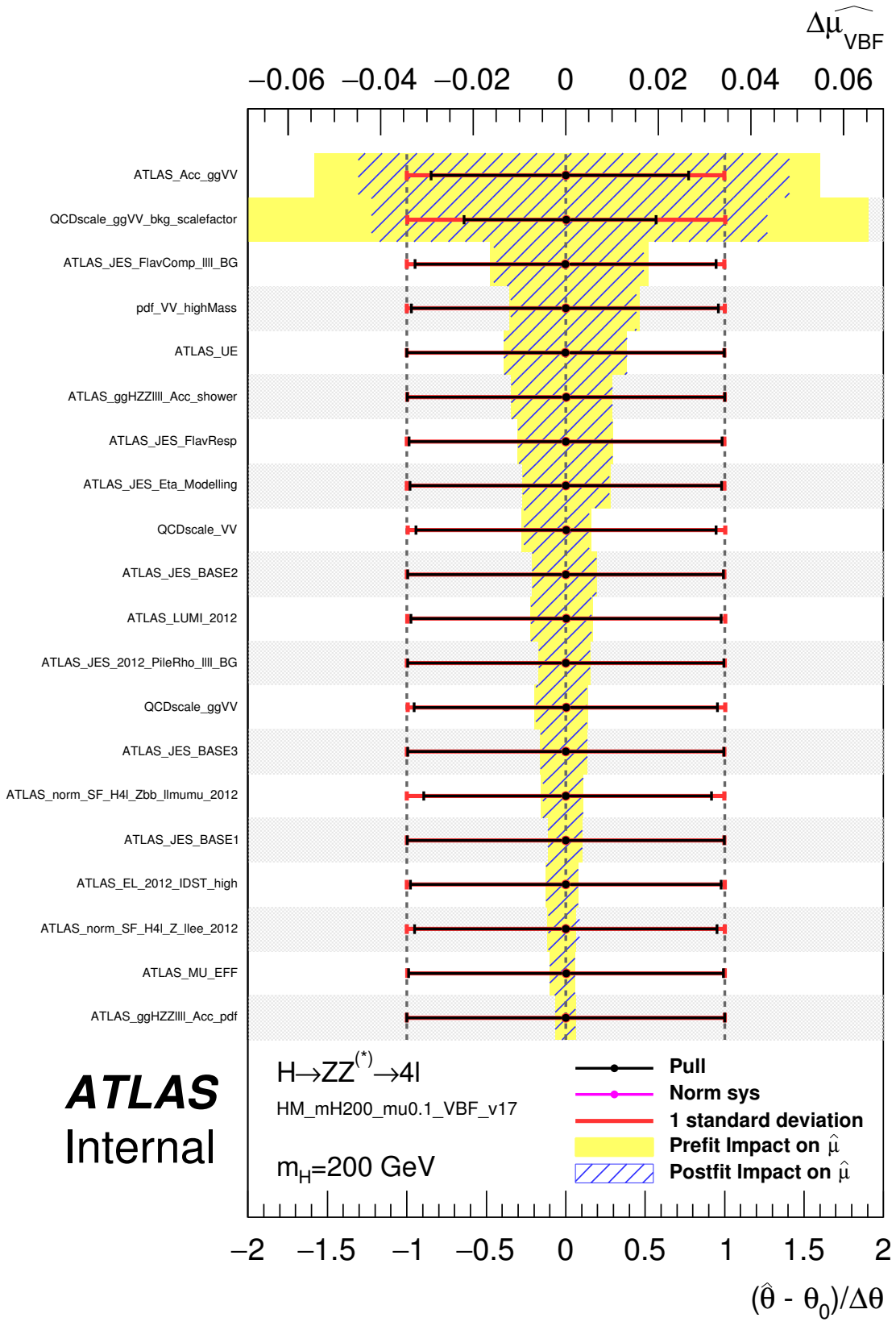

Figure 5.18: Nuisance parameter ranking performed with μ_{VBF}. The ranking was performed at $m_H = 200$ GeV with an Asimov data-set generated with $\mu = 0.1$.

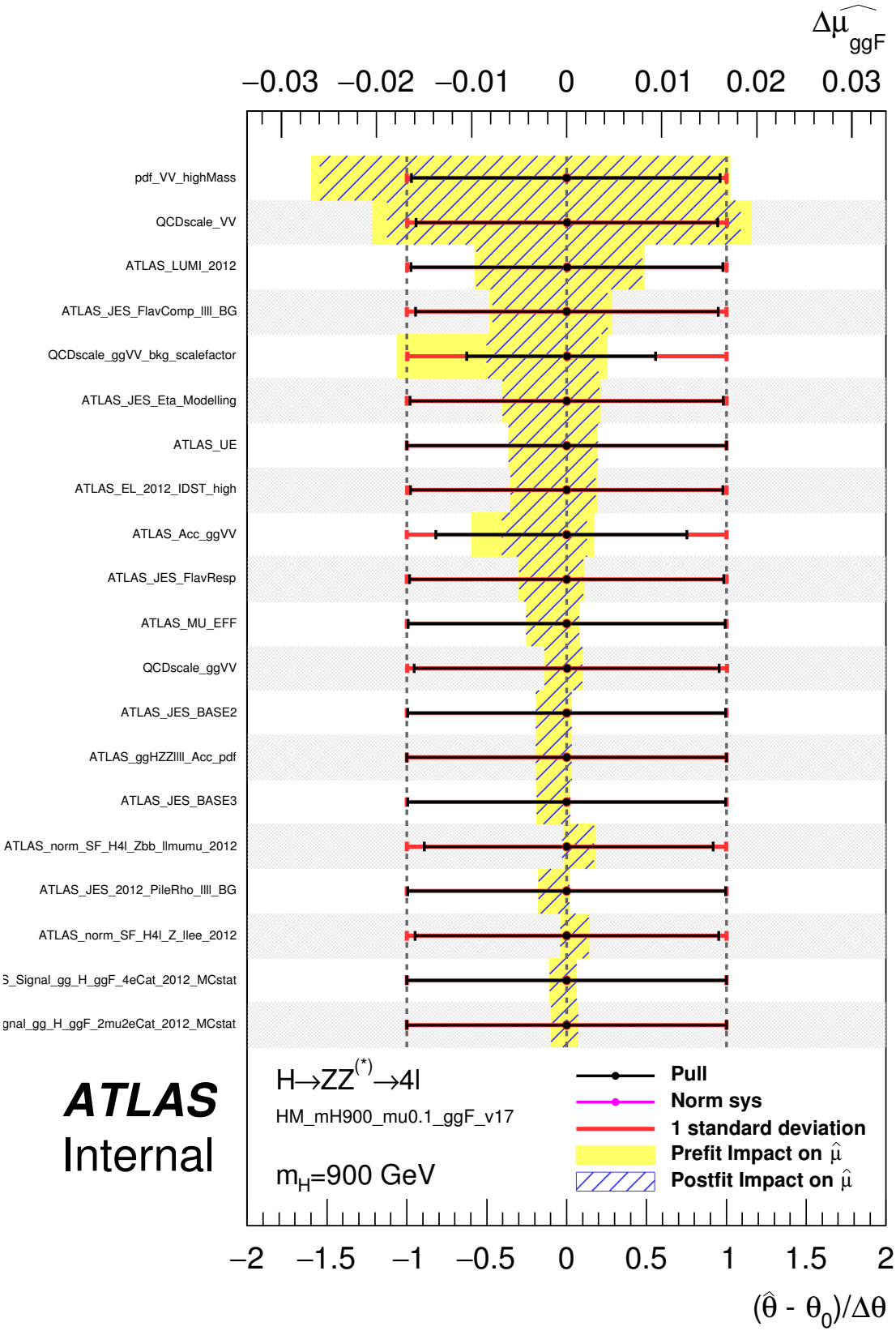

FIGURE 5.19: Nuisance parameter ranking performed with μ_{ggF}. The ranking was performed at $m_H = 900$ GeV with an Asimov data-set generated with $\mu = 0.1$.

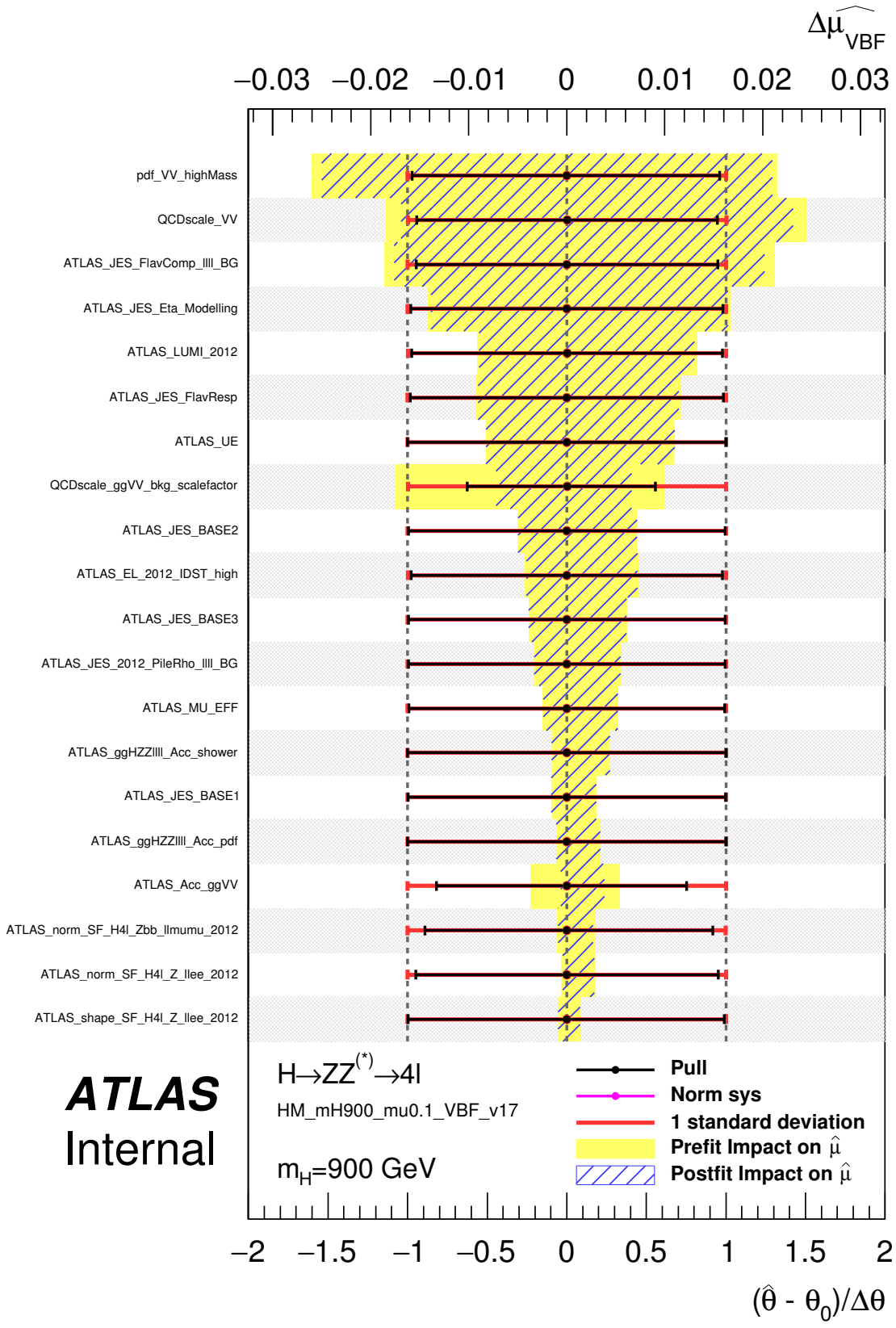

Figure 5.20: Nuisance parameter ranking performed with μ_{VBF}. The ranking was performed at $m_H = 900$ GeV with an Asimov data-set generated with $\mu = 0.1$.

5.8 Results

This section presents the final results of the search in terms of model-independent upper limits on the heavy Higgs boson production cross-section times $H \to ZZ^{(*)}$ branching ratio.

5.8.1 Post-fit Yields and Distributions

The post-fit $m_{4\ell}$ distributions are shown in Figure 5.21 to Figure 5.24. Figure 5.21 presents the inclusive $m_{4\ell}$ distribution, while Figure 5.22, Figure 5.23 and Figure 5.24 show the distributions segmented into the individual event categories. The yields before and after the likelihood fit are presented in Table 5.11, among the observed number of events in data. In this fit, the signal-strengths μ_{ggF} and μ_{VBF} are set to zero as to mimic background-only conditions, which is necessary since the post-fit background expectation depends on the m_H hypothesis. When comparing the pre-fit and post-fit yields from Table 5.11, a slight deficit is observed in the ggF event categories post-fit, although the yields are consistent within the 1σ uncertainties on the expectations. Post-fit, the expected background yield is reduced by ~4%, while the uncertainty on the yield is reduced from 13% to 5%, which is due to reasonably large uncertainties on the $ZZ^{(*)}$ backgrounds are constrained by the fit. A few excesses above the background expectation are observed in the distributions in the inclusive ggF event category: one at around 200 GeV, and two at around 900 GeV. The first is driven by an excess in the ggF $2\mu 2e$ and $2e2\mu$ event categories and the latter by the ggF $2\mu 2e$ and ggF 4μ event categories. These excesses are all within 2σ of the background expectation.

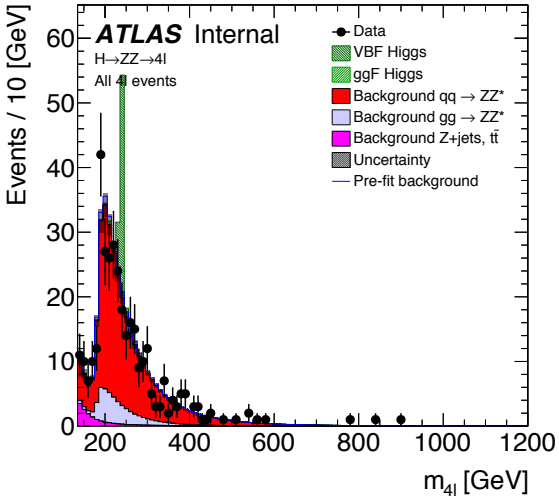

Figure 5.21: Post-fit $m_{4\ell}$ distributions for all event categories. The expected VBF signal for $m_H = 240$ GeV is shown, normalised to a cross-section corresponding to five times the observed VBF limit. The ggF signal is normalised to the best-fit value from a fit where the ggF signal floats freely and the VBF signal is set to zero. The hashed band on the MC distributions shows the systematic uncertainty on the expectation. The blue line indicates the pre-fit background distribution.

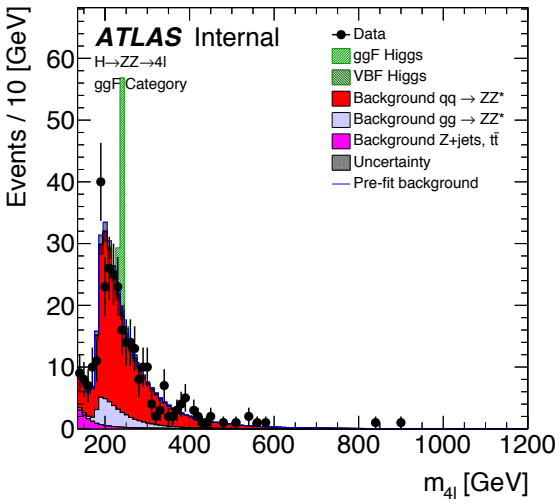

Figure 5.22: Post-fit $m_{4\ell}$ distributions for the four ggF event categories (inclusively). The expected ggF signal for $m_H = 240$ GeV is shown, normalised to a cross-section corresponding to five times the observed ggF limit. The VBF signal is normalised to the best-fit value from a fit where the VBF signal floats freely and the ggF signal is set to zero. The hashed band on the MC distributions shows the systematic uncertainty on the expectation. The blue line indicates the pre-fit background distribution.

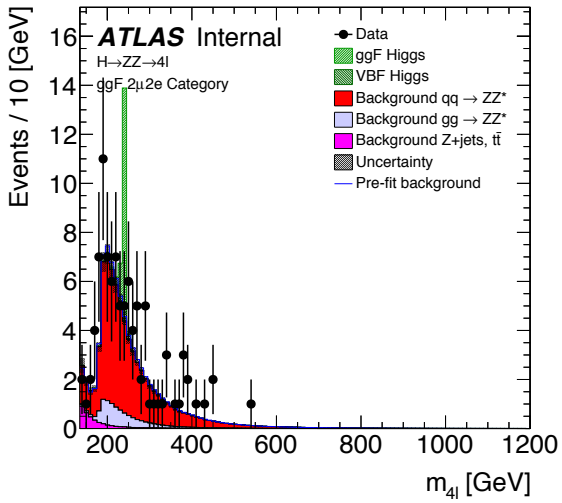

(A) ggF $2e2\mu$

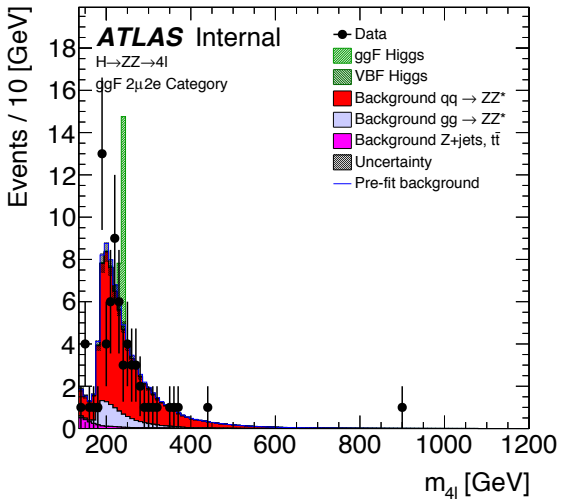

(B) ggF $2\mu2e$

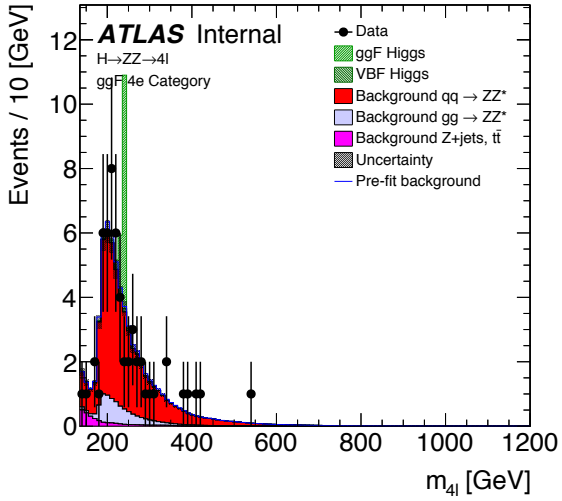

(C) ggF $4e$

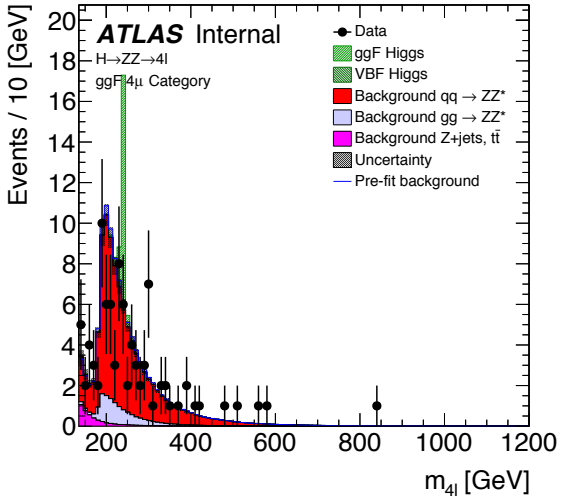

(D) ggF 4μ

FIGURE 5.23: Post-fit $m_{4\ell}$ distributions for the ggF event categories. The expected ggF signal for $m_H = 240$ GeV is shown, normalised to a cross-section corresponding to five times the observed ggF limit. The VBF signal is normalised to the best-fit value from a fit where the VBF signal floats freely and the ggF signal is set to zero. The hashed band on the MC distributions shows the systematic uncertainty on the expectation. The blue line indicates the pre-fit background distribution.

Table 5.11: Expected and observed background yields pre- and post-fit. Since the post-fit background expectation depends on the m_H hypothesis, for the results shown in this table, μ_{ggF} and μ_{VBF} are set to zero. Only the systematic uncertainties on the yields are presented, since the statistical uncertainties on the expected yields are negligible.

Pre-fit

Event category	$q\bar{q} \to ZZ^{(*)}$	$gg \to ZZ^{(*)}$	Reducible	Total	Observed
ggF $4e$	52.5 ± 3.8	9.6 ± 8.1	2.5 ± 0.6	64.6 ± 8.6	56
ggF 4μ	88.1 ± 6.0	14.9 ± 12.5	3.6 ± 1.2	106.6 ± 13.2	92
ggF $2e2\mu$	64.9 ± 4.4	11.3 ± 9.6	3.1 ± 1.0	79.3 ± 10.0	98
ggF $2\mu2e$	69.6 ± 4.7	12.5 ± 10.5	2.6 ± 0.6	84.6 ± 11.0	70
VBF	14.6 ± 1.9	4.9 ± 5.4	1.1 ± 0.8	20.7 ± 5.9	22
VH	7.38 ± 1.04	1.6 ± 1.7	0.5 ± 0.3	9.4 ± 2.1	9
All ggF	275 ± 18.8	48.3 ± 40.7	11.8 ± 2.5	335.1 ± 42.5	316
All 4ℓ	297 ± 19.8	54.8 ± 45.6	13.3 ± 3.5	365.2 ± 47.2	347

Post-fit

Event category	$q\bar{q} \to ZZ^{(*)}$	$gg \to ZZ^{(*)}$	Reducible	Total	Observed
ggF $4e$	51.2 ± 3.1	7.9 ± 3.5	2.6 ± 0.5	61.7 ± 3.3	56
ggF 4μ	85.8 ± 4.8	12.2 ± 5.4	4.3 ± 1.4	102.4 ± 5.0	92
ggF $2e2\mu$	63.3 ± 3.5	9.3 ± 4.1	3.7 ± 1.1	76.3 ± 3.7	98
ggF $2\mu2e$	67.9 ± 3.8	10.3 ± 4.5	2.7 ± 0.5	80.8 ± 4.0	70
VBF	14.1 ± 1.6	5.1 ± 3.3	1.5 ± 0.9	20.7 ± 3.3	22
VH	7.1 ± 0.9	1.6 ± 1.0	0.6 ± 0.3	9.3 ± 1.2	9
All ggF	268.2 ± 14.9	39.8 ± 17.4	13.3 ± 2.6	321.2 ± 15.3	316
All 4ℓ	289.3 ± 16.0	46.5 ± 19.4	15.4 ± 3.7	351.2 ± 16.6	347

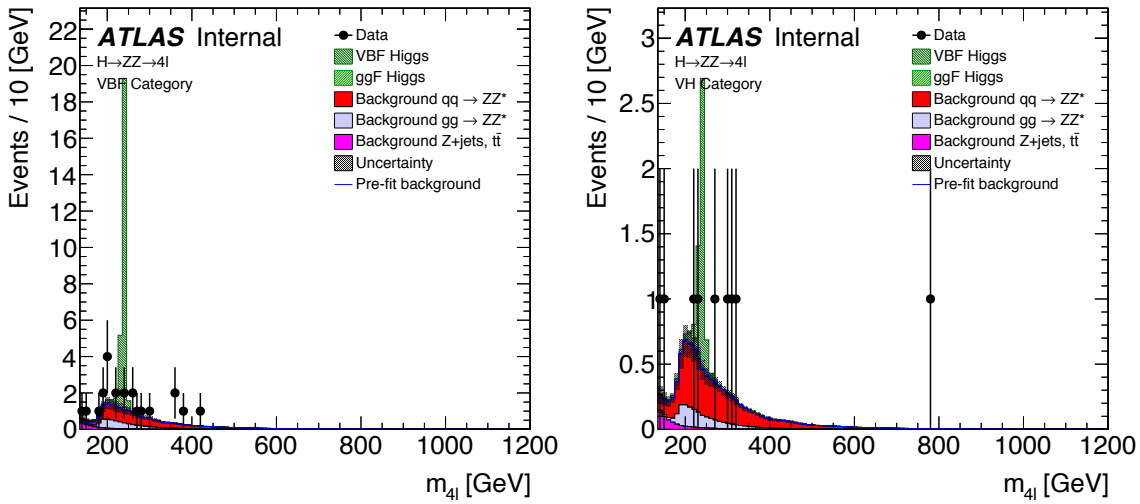

(A) VBF (B) VH

FIGURE 5.24: Post-fit $m_{4\ell}$ distributions for the VBF and VH categories. The expected VBF signal for $m_H = 240$ GeV for is shown, normalised to a cross-section corresponding to five times the observed VBF limit. The ggF signal is normalised to the best-fit value from a fit where the ggF signal floats freely and the VBF signal is set to zero. The hashed band shows the systematic uncertainty on the expectation. The blue line indicates the pre-fit background distribution.

5.8.2 Upper Limits on Heavy Higgs Boson Production Rate

The results of this analysis, upper limits on the heavy Higgs boson production cross-section times $H \to ZZ^{(*)}$ branching ratio using the NWA, are obtained as a function of m_H with the CL_S procedure. Figure 5.25 presents the observed and expected 95% upper limits on $\sigma \times BR(H \to ZZ^{(*)})$ for the ggF and VBF production modes. In this figure, the dashed, black line represents the expected limit, while the solid black dots show the observed limits. The uncertainty on the expected limit is represented with the green and the yellow bands, which show the $\pm 1\sigma$ and $\pm 2\sigma$ deviation. With these conventions, a signal would manifest as an excess above the expected limits. The numerical values for the limits can be found in Table 5.12 to Table 5.15. In the production of these limits, the parameter of interest not under test is profiled to data.

As seen in Figure 5.25, the observed limits are well within the 2σ bands over the full considered m_H range. A few excursions into the 2σ band are observed at the mass points where excesses are observed in the $m_{4\ell}$ distributions, but no deviations outside the 2σ bands are observed. In the ggF event category, a 95% CL_S upper limit on $\sigma \times BR(H \to ZZ^{(*)})$ of 330 fb is set at $m_H = 200$ GeV and of 38 fb at $m_H = 1$ TeV. The corresponding limits obtained in the VBF event category are 277 fb at $m_H = 200$ GeV and 35 fb at $m_H = 1$ TeV.

5.9 Conclusion and Further Work

A search for an additional, heavy Higgs boson in the $H \to ZZ^{(*)} \to 4\ell$ decay channel was conducted in the interval $140 < m_H < 1000$ GeV using the Narrow Width Approximation. The search employed separate event categories to distinguish ggF, VBF and VH events, in order to set upper limits on the cross-section times branching ratio for ggF and VBF production. The observed event rates were compatible with the background predictions and no excess was observed. In the ggF event category, a 95% CL_S limit on $\sigma \times BR(H \to ZZ^{(*)})$ of 330 fb (38 fb) is set at $m_H = 200$ GeV ($m_H = 1$ TeV) with an expected limit of 329 fb (43 fb). The corresponding limits obtained in the VBF event category on $\sigma \times BR(H \to ZZ^{(*)})$ are 277 fb (35 fb) at $m_H = 200$ GeV ($m_H = 1$ TeV) with expected limits of 179 fb (41 fb).

The results from this analysis will be developed further in Chapter 6, where they are combined with the additional three heavy Higgs boson searches in the $H \to ZZ^{(*)}$ channels, resulting in more powerful exclusion limits. In addition, a 2HDM interpretation will be performed. The results from this search are compared to the corresponding search with Run-2 data in Chapter 8.

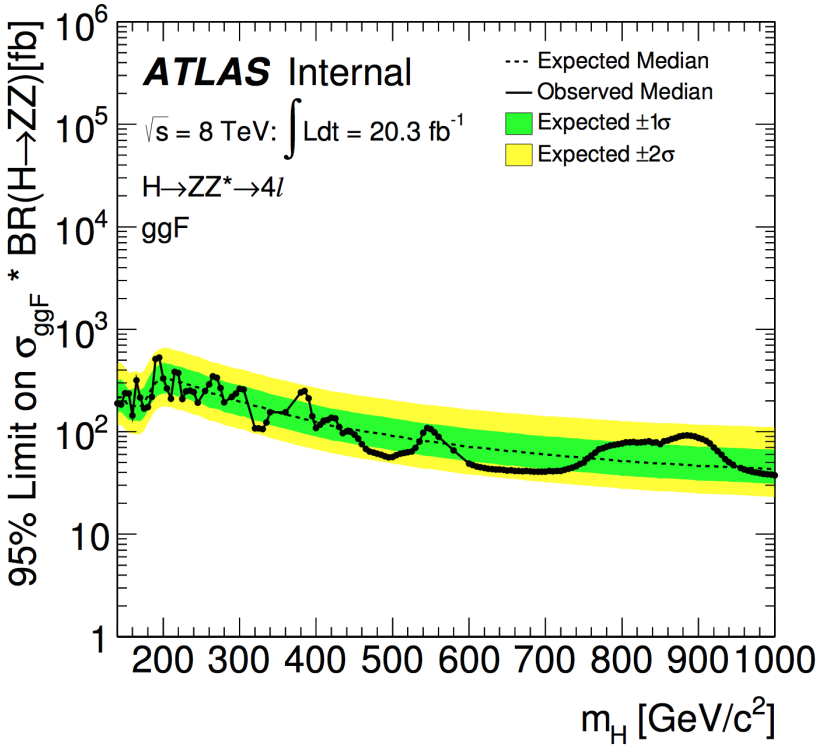

(A)

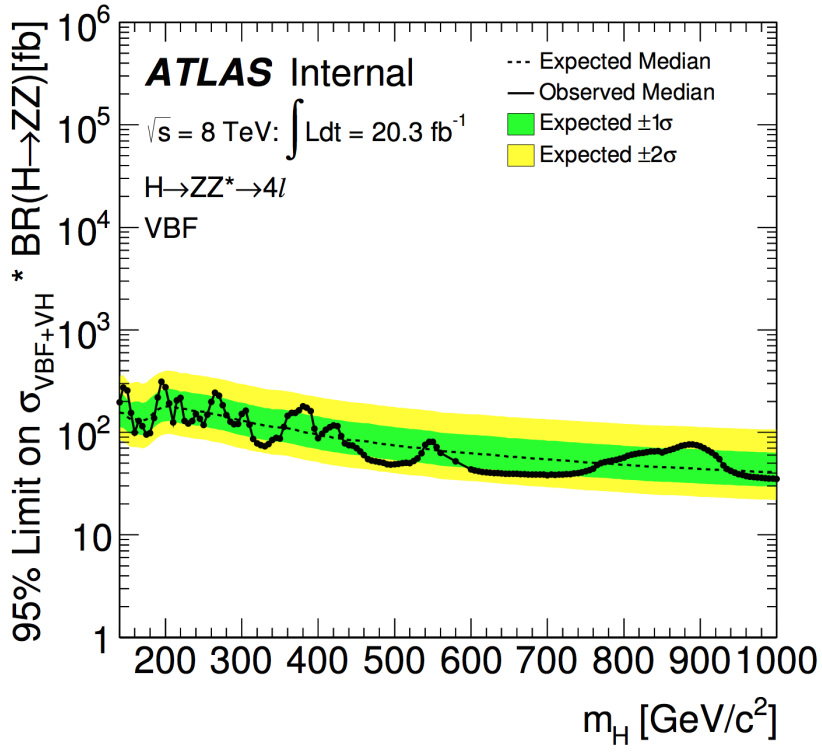

(B)

FIGURE 5.25: 95% CL_S upper limits on $\sigma \times BR(H \to ZZ^{(*)})$ as a function of m_H in the ggF (A) and VBF (B) event categories. The solid black line and points indicate the observed limit. The dashed black line indicates the expected limit, while the yellow and green the bands represent the 1σ and 2σ uncertainty on the expected limit.

Table 5.12: Expected and observed limits on $\sigma \times BR(H \to ZZ^{(*)})$ obtained in the ggF event category

m_H	Limit on $\sigma \times BR(H \to ZZ^{(*)})$ [fb]					
[GeV]	Obs.	Exp.	$+2\sigma$	$+1\sigma$	-1σ	-2σ
140	188	215	459	315	155	115
145	184	217	472	325	157	117
150	239	197	425	291	142	106
155	236	181	374	255	131	97
160	144	178	385	262	128	96
165	317	178	389	265	128	95
170	215	175	370	253	126	94
175	169	192	397	273	138	103
180	174	225	469	328	162	121
185	219	267	545	384	192	143
190	514	300	603	427	216	161
195	529	319	633	448	230	171
200	330	329	660	470	237	176
205	265	328	654	464	236	176
210	210	323	643	455	233	174
215	385	314	626	442	227	169
220	375	304	613	434	219	163
225	209	302	606	429	218	162
230	248	292	582	411	210	156
235	252	285	569	402	205	153
240	244	273	551	389	197	146
245	192	271	545	384	195	145
250	186	258	518	364	186	138
255	249	251	507	356	181	135
260	289	238	486	341	171	128
265	349	236	477	334	170	127
270	338	231	469	328	167	124
275	268	226	458	321	163	121
280	194	216	444	310	155	116
285	192	213	435	304	153	114
290	219	207	424	295	149	111
295	236	202	415	289	146	109
300	264	197	409	285	142	106
305	257	196	403	280	141	105
310	178	190	391	272	137	102
315	119	185	381	265	133	99
320	108	178	373	259	128	96
325	108	176	366	253	127	95
330	106	172	358	248	124	92
335	123	167	349	241	121	90
340	154	162	340	235	117	87
345	140	159	334	230	114	85
350	120	155	326	225	112	83

m_H	Limit on $\sigma \times BR(H \to ZZ^{(*)})$ [fb]					
[GeV]	Obs.	Exp.	$+2\sigma$	$+1\sigma$	-1σ	-2σ
355	131	152	320	220	109	81
360	155	148	314	216	107	79
365	158	145	307	211	105	78
375	208	139	295	202	100	75
380	242	135	290	198	98	73
385	250	133	283	193	96	71
390	212	130	278	190	94	70
395	141	127	273	186	92	68
400	109	125	270	183	90	67
405	117	122	262	178	88	66
410	128	120	258	175	87	65
415	130	118	254	172	85	63
420	137	114	249	168	82	61
425	135	113	247	166	82	61
430	111	112	244	164	80	60
435	97	110	240	162	79	59
440	101	108	237	160	78	58
445	100	107	233	157	77	57
450	94	105	229	154	75	56
455	86	103	226	152	74	55
460	75	102	224	150	73	55
465	68	101	221	148	72	54
470	64	99	219	146	72	53
475	63	98	216	144	71	53
480	61	97	215	143	70	52
485	60	96	212	141	69	51
490	58	94	209	139	68	51
495	56	93	206	137	67	50
500	57	91	203	135	65	49
505	59	90	201	133	65	48
510	61	89	199	132	64	48
515	62	88	197	130	63	47
520	63	86	194	128	62	46
525	64	85	192	126	61	46
530	70	84	189	125	60	45
535	80	83	187	123	60	44
540	98	81	184	121	58	44
545	109	81	183	120	58	43
550	106	80	182	119	58	43
555	98	80	181	118	57	43
560	89	78	179	117	56	42
580	66	75	172	112	54	40
600	49	71	164	107	51	38

TABLE 5.13: Expected and observed limits on $\sigma \times BR(H \rightarrow ZZ^{(*)})$ obtained in the ggF event category

m_H	Limit on $\sigma \times BR(H \rightarrow ZZ^{(*)})$ [fb]					
[GeV]	Obs.	Exp.	$+2\sigma$	$+1\sigma$	-1σ	-2σ
605	47	71	164	106	51	38
610	46	70	163	105	51	38
615	45	70	162	105	50	37
620	44	69	160	103	50	37
625	44	68	159	103	49	37
630	43	68	158	102	49	36
635	43	67	156	101	48	36
640	43	66	155	100	48	36
645	42	66	154	99	47	35
650	42	65	152	98	47	35
655	42	65	152	97	47	35
660	41	64	151	97	46	35
665	42	64	150	96	46	34
670	41	63	149	95	46	34
675	41	63	147	94	45	34
680	41	62	146	93	45	33
685	41	61	145	92	44	33
690	41	61	144	92	44	33
695	41	61	143	91	44	33
700	41	59	141	90	43	32
705	41	60	142	90	43	32
710	41	59	141	90	43	32
715	41	59	140	89	42	32
720	42	58	139	88	42	31
725	43	58	139	88	42	31
730	43	57	138	87	41	31
735	45	57	137	87	41	31
740	46	56	136	86	41	30
745	48	56	136	86	40	30
750	50	55	134	84	40	30
755	55	55	134	84	40	30
760	58	55	133	84	40	30
765	63	55	132	83	39	29
770	67	54	132	83	39	29
775	69	54	131	82	39	29
780	71	54	130	82	39	29
785	73	53	130	81	38	29
790	74	53	129	81	38	28
795	76	52	128	80	38	28
800	77	51	126	79	37	28

m_H	Limit on $\sigma \times BR(H \rightarrow ZZ^{(*)})$					
[GeV]	Obs.	Exp.	$+2\sigma$	$+1\sigma$	-1σ	-2σ
805	79	52	127	79	37	28
810	79	51	126	78	37	28
815	79	51	125	78	37	27
820	78	51	125	77	36	27
825	79	50	124	77	36	27
830	79	50	124	77	36	27
835	81	50	123	76	36	27
840	78	49	123	76	36	27
845	79	49	122	76	35	26
850	76	49	121	74	35	26
855	81	49	122	75	35	26
860	82	49	122	75	35	26
865	85	48	121	74	35	26
870	87	48	121	74	35	26
875	90	48	120	74	35	26
880	91	48	120	73	34	26
885	92	47	119	73	34	25
890	91	47	119	73	34	25
895	90	47	118	72	34	25
900	87	46	116	71	33	25
905	85	46	117	72	33	25
910	81	46	117	71	33	25
915	77	46	116	71	33	25
920	70	46	116	71	33	25
925	65	46	116	71	33	25
930	59	46	116	70	33	25
935	54	46	115	70	33	24
940	50	45	115	70	33	24
945	48	45	114	70	32	24
950	44	44	112	68	32	24
955	44	45	114	69	32	24
960	43	45	114	69	32	24
965	42	44	113	69	32	24
970	41	44	113	68	32	24
975	40	44	112	68	32	24
980	39	44	112	68	32	23
985	39	44	112	68	31	23
990	39	43	111	67	31	23
995	38	43	111	67	31	23
1000	38	43	109	66	31	23

Table 5.14: Expected and observed limits on $\sigma \times BR(H \rightarrow ZZ^{(*)})$ obtained in the VBF event category

m_H	Limit on $\sigma \times BR(H \rightarrow ZZ^{(*)})$ [fb]					
[GeV]	Obs.	Exp.	$+2\sigma$	$+1\sigma$	-1σ	-2σ
140	196	156	353	230	112	84
145	273	154	362	234	111	82
150	256	141	321	209	102	76
155	155	134	299	195	96	72
160	99	134	309	201	97	72
165	129	133	309	201	96	71
170	115	130	297	193	94	70
175	95	134	304	199	97	72
180	99	143	330	215	103	77
185	138	156	354	233	112	84
190	219	167	373	247	120	89
195	311	174	389	258	126	94
200	277	179	399	265	129	96
205	192	180	401	266	130	96
210	125	178	397	264	128	95
215	206	174	391	259	126	94
220	217	170	377	250	122	91
225	130	169	380	251	122	91
230	122	167	373	247	120	89
235	130	163	367	242	118	88
240	151	161	363	240	116	86
245	136	161	360	238	116	86
250	118	158	354	234	114	85
255	148	156	350	231	113	84
260	198	152	342	226	110	82
265	243	151	339	224	109	81
270	228	148	333	220	106	79
275	185	145	329	217	105	78
280	148	142	322	212	102	76
285	127	139	315	207	100	75
290	120	136	308	202	98	73
295	121	132	301	197	95	71
300	151	130	297	195	94	70
305	162	128	293	192	92	69
310	119	125	286	186	90	67
315	87	123	282	184	89	66
320	78	120	277	180	87	65
325	75	119	272	177	86	64
330	73	116	266	173	84	63
335	77	115	264	172	83	62
340	84	113	260	169	81	61
345	88	113	259	169	81	60
350	87	112	257	168	81	60

m_H	Limit on $\sigma \times BR(H \rightarrow ZZ^{(*)})$					
[GeV]	Obs.	Exp.	$+2\sigma$	$+1\sigma$	-1σ	-2σ
355	114	111	255	166	80	60
360	145	110	252	164	79	59
365	155	108	248	161	78	58
370	155	106	244	159	76	57
375	165	104	240	156	75	56
380	179	101	234	152	73	54
385	174	99	231	149	72	53
390	162	98	228	148	71	53
395	109	97	225	146	70	52
400	88	95	222	143	69	51
405	97	93	217	140	67	50
410	106	92	215	138	66	49
415	113	90	212	136	65	49
420	117	89	208	134	64	48
425	115	88	206	133	63	47
430	92	87	204	131	63	47
435	78	86	202	129	62	46
440	75	84	198	127	61	45
445	74	84	197	126	61	45
450	70	83	195	125	60	45
455	65	83	194	125	60	44
460	60	82	192	123	59	44
465	55	81	191	123	58	44
470	53	80	189	121	58	43
475	52	79	186	119	57	42
480	51	78	183	117	56	42
485	50	77	182	117	56	41
490	49	76	180	115	55	41
495	48	75	179	114	54	41
500	49	74	176	113	54	40
505	49	74	175	112	53	40
510	50	73	173	111	53	39
515	51	72	172	110	52	39
520	50	71	169	108	51	38
525	52	71	169	108	51	38
530	56	71	168	107	51	38
535	62	70	167	106	51	38
540	76	69	165	105	50	37
545	81	69	164	104	49	37
550	81	68	162	103	49	36
555	72	67	160	101	48	36
560	63	66	157	99	47	35
580	52	64	154	97	46	34

TABLE 5.15: Expected and observed limits on $\sigma \times BR(H \rightarrow ZZ^{(*)})$ obtained in the VBF event category

m_H	Limit on $\sigma \times BR(H \rightarrow ZZ^{(*)})$					
[GeV]	Obs.	Exp.	+2σ	+1σ	-1σ	-2σ
600	43	62	150	95	45	33
605	42	62	150	95	45	33
610	42	62	149	94	44	33
615	41	61	149	93	44	33
620	41	61	148	93	44	33
625	40	60	147	92	43	32
630	40	60	145	91	43	32
635	40	59	144	90	43	32
640	40	59	143	90	42	32
645	40	58	142	89	42	31
650	39	58	140	88	42	31
655	39	58	141	88	42	31
660	39	57	140	88	41	31
665	39	57	140	87	41	31
670	39	57	139	86	41	30
675	39	56	138	86	40	30
680	39	56	137	85	40	30
685	39	55	136	85	40	30
690	39	55	136	84	40	30
695	39	55	135	84	40	29
700	38	54	134	83	39	29
705	39	54	134	83	39	29
710	39	54	133	83	39	29
715	39	54	133	82	39	29
720	39	53	132	82	38	29
725	39	53	131	81	38	28
730	39	52	130	80	38	28
735	40	52	130	80	38	28
740	40	52	129	79	37	28
745	41	51	128	79	37	28
750	42	51	127	78	37	27
755	43	51	127	78	37	27
760	44	51	126	78	36	27
765	48	50	126	77	36	27
770	50	50	125	77	36	27
775	51	50	125	76	36	27
780	52	50	124	76	36	27
785	53	49	123	76	35	26
790	54	49	123	75	35	26
795	55	49	122	75	35	26
800	57	48	121	74	35	26
805	59	48	121	74	35	26
810	61	48	120	73	34	26
815	62	47	120	73	34	25
820	63	47	119	73	34	25
825	63	47	118	72	34	25
830	64	47	118	72	34	25
835	65	46	117	71	33	25
840	65	46	117	71	33	25
845	66	46	117	71	33	25
850	64	46	116	70	33	25
855	66	46	116	70	33	25
860	67	46	116	70	33	24
865	69	45	116	70	33	24
870	71	45	116	70	33	24
875	74	45	115	70	32	24
880	75	45	115	69	32	24
885	76	45	114	69	32	24
890	76	44	114	69	32	24
895	75	44	113	68	32	24
900	73	44	112	68	32	24
905	70	44	113	68	32	24
910	67	44	112	68	31	23
915	64	43	112	67	31	23
920	60	43	111	67	31	23
925	55	43	111	67	31	23
930	48	43	111	67	31	23
935	44	43	110	66	31	23
940	42	43	110	66	31	23
945	41	42	109	66	30	23
950	39	42	109	65	30	23
955	38	42	109	65	30	23
960	38	42	109	65	30	22
965	37	42	108	65	30	22
970	37	42	108	65	30	22
975	36	41	108	64	30	22
980	36	41	107	64	30	22
985	36	41	107	64	30	22
990	36	41	107	64	30	22
995	35	41	107	64	30	22
1000	35	41	107	63	29	22

CHAPTER 6

Combination of Heavy Higgs Boson Searches in the $H \to ZZ^{(*)}$ Decay Channels Using $\sqrt{s} = 8$ TeV Data

6.1 Introduction

This chapter describes the combination of heavy Higgs boson searches performed by ATLAS in four $H \to ZZ^{(*)}$ decay channels: $ZZ^{(*)} \to 4\ell$, $ZZ^{(*)} \to 2\ell 2\nu$, $ZZ^{(*)} \to 2\ell 2q$ and $ZZ^{(*)} \to 2\nu 2q$. These four analyses search for a neutral, CP-even, heavy Higgs boson using 20.3 fb^{-1} of pp-collision data recorded at $\sqrt{s} = 8$ TeV. As in the $ZZ^{(*)} \to 4\ell$ analysis, the additional searches employ a model-independent, shape-based search strategy by using the NWA, and by segmenting events into ggF- and VBF-like event categories for the $2\ell 2\nu$ and $2\ell 2q$ analyses. Individually, all channels set upper limits on the heavy Higgs boson production cross-section times $H \to ZZ^{(*)}$ branching ratio, while the $2\ell 2\nu$ and $2\ell 2q$ decay channels in addition impose limits on the 2HDM parameter space. By performing a combination, the sensitivity of the four searches is combined, which allows for stronger limits to be set on either type of limits. The four decay channels supplement each other nicely in the combination since they have sensitivity in different mass regimes, a fact which is partially is driven by the difference in the branching ratio to the final-states, shown in Table 6.1. Two types of results are produced after the combination: upper limits on the heavy Higgs boson production rate and a 2HDM interpretation, where limits are imposed on $\tan(\beta)$ as function of both $\cos(\beta - \alpha)$ and m_H.

The chapter is segmented as follows; Section 6.2 to Section 6.4 presents an overview of the three searches performed in the $ZZ^{(*)} \to 2\ell 2\nu$, $ZZ^{(*)} \to 2\ell 2q$ and $ZZ^{(*)} \to 2\nu 2q$ decay channels. This includes an overview of the event categorisation, statistical modelling and a short description

of the background estimation, which is of high relevance when understanding the nuisance parameters of the individual and combined searches. Section 6.5 presents the implementation of the combination of the four searches. The combination is performed by merging the likelihood functions of the individual searches such that a simultaneous fit across all signal and control regions can be performed. Before doing so, a correlation scheme is defined, which specifies the nuisance parameters that are common across multiple searches. Following a description of the combination, Section 6.7 presents the results of the analysis. Section 6.8 concludes the chapter.

TABLE 6.1: Branching ratios for a SM Higgs boson in the four decay modes considered in this combination at selected m_h values. In this table $\ell = e, \mu$, $\nu = \nu_e, \nu_\mu, \nu_\tau$ and $q = u, d, c, s, b$ [36].

Branching Ratio	$m_h = 200$ GeV	$m_h = 500$ GeV	$m_h = 900$ GeV
$BR(H \to ZZ) \times BR(ZZ \to 4\ell)$	1.15×10^{-3}	1.18×10^{-3}	1.38×10^{-3}
$BR(H \to ZZ) \times BR(ZZ \to 2\ell 2\nu)$	2.40×10^{-2}	2.52×10^{-2}	2.86×10^{-2}
$BR(H \to ZZ) \times BR(ZZ \to 2\ell 2q)$	4.18×10^{-2}	3.47×10^{-2}	3.71×10^{-2}
$BR(H \to ZZ) \times BR(ZZ \to 2\nu 2q)$	7.16×10^{-2}	7.54×10^{-2}	8.53×10^{-2}

6.2 The H→ZZ$^{(*)}$→2l2v Decay Channel

The final-state of the search in the $H \to ZZ^{(*)} \to 2\ell 2\nu$ decay channel carries the experimental signature of a di-lepton pair from a $Z \to \ell\ell$ decay and missing transverse energy, E_T^{miss}, originating from the $Z \to \nu\nu$ decay. In Run-1, in addition to the important contribution to the heavy Higgs boson search presented in this chapter, this particular final-state played an important role in the analyses constraining the width of the SM Higgs boson documented by ATLAS in [37] and CMS in [132]. The search presented in the following uses two event categories, ggF and VBF, and is performed in the interval $240 \leq m_H \leq 1000$ GeV. The expected sensitivity of the $ZZ^{(*)} \to 2\ell 2\nu$ decay channel is competitive with that of the $ZZ^{(*)} \to 2\ell 2q$ and $ZZ^{(*)} \to 2\nu 2q$ decay channels at intermediate and high Higgs boson masses because of the relatively large value of the branching ratio of the decay, shown in Table 6.1. A brief description of this analysis is presented in the following – more rigorous reviews can be found in [90, 133].

6.2.1 Missing Transverse Energy Reconstruction

Both the $2\ell 2\nu$ analysis and the $2\nu 2q$ analysis presented in Section 6.4 rely on the reconstruction of missing transverse energy, E_T^{miss}. This quantity is determined from the energy collected by the

electromagnetic and hadronic calorimeters and by muons measured by the muon spectrometer and inner detector. The missing energy components in the transverse directions, $E^{miss}_{x(y)}$, are calculated as [134]:

$$E^{miss}_{x(y)} = E^{miss,\,e}_{x(y)} + E^{miss,\,\gamma}_{x(y)} + E^{miss,\,\tau}_{x(y)} + E^{miss,\,jets}_{x(y)} + E^{miss,\,\mu}_{x(y)} + E^{miss,\,soft}_{x(y)} \tag{6.1}$$

Here the individual terms represent the contribution from calibrated electrons (e), photons (γ), hadronically decaying τ-leptons, jets and muons (μ). The soft term is reconstructed from detector signals not associated with any object passing the above selection cuts, which can be ID tracks or calorimeter signals. Given the large geometrical acceptance of the calorimeters, nearly all activity in a given event can be recorded. From $E^{miss}_{x(y)}$, the azimuthal angle ϕ^{miss} and the magnitude E^{miss}_T can be calculated as:

$$E^{miss}_T = \sqrt{(E^{miss}_x)^2 + (E^{miss}_y)^2} \tag{6.2}$$

$$\phi^{miss} = \arctan\left(E^{miss}_y / E^{miss}_x\right) \tag{6.3}$$

The quantity E^{miss}_T will be used in the event selection of the following analysis.

6.2.2 Event Categorisation

A di-lepton pair originating from a Z boson is identified by selecting two same-flavoured, oppositely charged leptons, which together have an invariant mass in the range $76 < m_{\ell\ell} < 106$ GeV. The presence of two neutrinos is enforced by requiring $E^{miss}_T > 70$ GeV. The selected events are classified as either ggF- or VBF-like. The VBF event category requires at least two high-p_T jets reconstructed in opposite hemispheres of the detector. If these criteria are not met, but the event contains zero or one high-p_T jet, the event is classified as ggF-like. These two event categories are segmented further according to the final-state, meaning that $ee\nu\nu$ and $\mu\mu\nu\nu$ events are distinguished. The selection efficiency for the ggF and VBF event categories is in the range of ~5% to 15% and ~1% to 11%, respectively.

Because the z component of the momentum of both neutrinos cannot be measured, the four-vectors of all the individual final-state objects cannot be reconstructed. Therefore, the analysis employs the transverse mass, m_T, as discriminant in all event categories. This quantity is constructed from the di-lepton system and E^{miss}_T, and is defined as:

$$(m^{ZZ}_T)^2 \equiv \left(\sqrt{m^2_Z + |p^{\ell\ell}_T|^2} + \sqrt{m^2_Z + |E^{miss}_T|^2}\right)^2 - |\vec{p}^{\,\ell\ell}_T + \vec{E}^{miss}_T|^2 \tag{6.4}$$

The resolution of m_T varies with m_H and ranges from 7% at $m_H = 240$ GeV to 15% at $m_H = 1$ TeV. The distribution of the m_T discriminant (post-fit) is presented in Figure 6.1.

6.2.3 Backgrounds

The dominant irreducible backgrounds to this search originate from the non-resonant $q\bar{q} \to ZZ^{(*)}$ and $gg \to ZZ^{(*)}$ continuum, while a smaller portion originates from WZ production, the diagram of which is shown Figure 6.2. The contribution from these processes are estimated with simulated POWHEG MC samples.

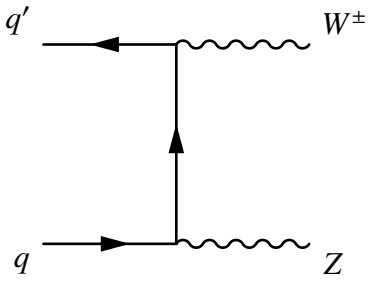

FIGURE 6.2: Leading-order diagram of WZ production.

Other background processes giving rise to final-states with a mix of both same-flavoured (ee, $\mu\mu$) and different-flavoured ($e\mu$, μe) di-lepton pairs include WW, $t\bar{t}$, Wt and $Z \to \tau\tau$. These backgrounds are determined collectively with a data-driven method that estimates the contamination from the $e\mu$ control region in the ee and $\mu\mu$ signal region.

Z+jets processes contribute significantly to the signal region. The contribution of this process is derived with a data-driven sideband method similar to that employed for the reducible backgrounds in the $H \to ZZ^{(*)} \to 4\ell$ decay channel, in which data from the the signal region is compared to regions where one or more of the requirements of the selection are reversed. This background suffers from large systematic uncertainties related to the high sensitivity of E_T^{miss} to MC mis-modelling. As will be seen in Section 6.5, this systematic is dominant after the combination with the additional three decay channels.

Additional processes are expected to contribute very modestly to the total background. These processes include W+jets production and multi-jet production with jets misidentified as leptons. These backgrounds are estimated from data using a sample with a loosened requirement on E_T^{miss}. The background in the signal region is afterwards derived using a transfer factor obtained from simulation. A small contribution from the off-shell production of the SM Higgs boson is also anticipated.

The estimated background yields (post-fit) from the $2\ell 2\nu$ search are presented in Table 6.2 in conjunction with the total number of events observed in data.

6.2.4 Statistical Modelling

The heavy Higgs boson search in the $2\ell 2\nu$ channel uses a binned likelihood function on the form:

$$\mathcal{L}(b_1, ..., b_n|\mu, \boldsymbol{\theta}) = \text{Pois}(n|\mu S + B) \times \left[\prod_{i \in \text{bins}}^{n} \frac{\mu S_i + B_i}{\mu S + B} \right] \tag{6.5}$$

In this equation, the events are segmented into n bins of the discriminant m_T, S_i and B_i are the expected signal and background yields in the ith bin, while S and B are the total number of expected events integrated over all bins. The four event categories, ggF and VBF segmented according to the final-states $\ell\ell = \mu\mu$ and $\ell\ell = ee$, are fitted simultaneously. Because of limited statistics, instead of using a shape-based approach, a counting-experiment is performed in the VBF event category, meaning that a single bin is used. As in the analysis in the 4ℓ decay channel, the systematic uncertainties are incorporated into the likelihood function as nuisance parameters. In this analysis, the dominant uncertainties are related to the estimation of the Z+jets background, the theoretical uncertainties on the $ZZ^{(*)}$ background (similar to those obtained in the 4ℓ analysis) and the theoretical uncertainty on the signal acceptance, the latter being up to 4.5% in ggF event category and up to 7% in VBF event category [133].

TABLE 6.2: Expected background yields and observed number of events in data after the full selection of the ggF and VBF event categories of the $H \to ZZ^{(*)} \to 2\ell 2\nu$ search. The first and second uncertainty corresponds to the statistical and systematic component, respectively.

Component	**Event category**		
	ggF		VBF
$q\bar{q} \to ZZ$	110	± 1 ± 10	$0.13 \pm 0.04 \pm 0.02$
$gg \to ZZ$	11	± 0.1 ± 5	$0.12 \pm 0.01 \pm 0.05$
WZ	47	± 1 ± 5	$0.10 \pm 0.05 \pm 0.1$
$WW/t\bar{t}/Wt/$Ztt	58	± 6 ± 5	$0.41 \pm 0.01 \pm 0.08$
$Z(\to e^+e^-, \mu^+\mu^-)$+jets	74	± 7 ± 20	$0.8 \pm 0.3 \pm 0.3$
Other backgrounds	4.5	± 0.7 ± 0.5	—
Total background	310	± 9 ± 40	$1.6 \pm 0.3 \pm 0.5$
Observed	309		4

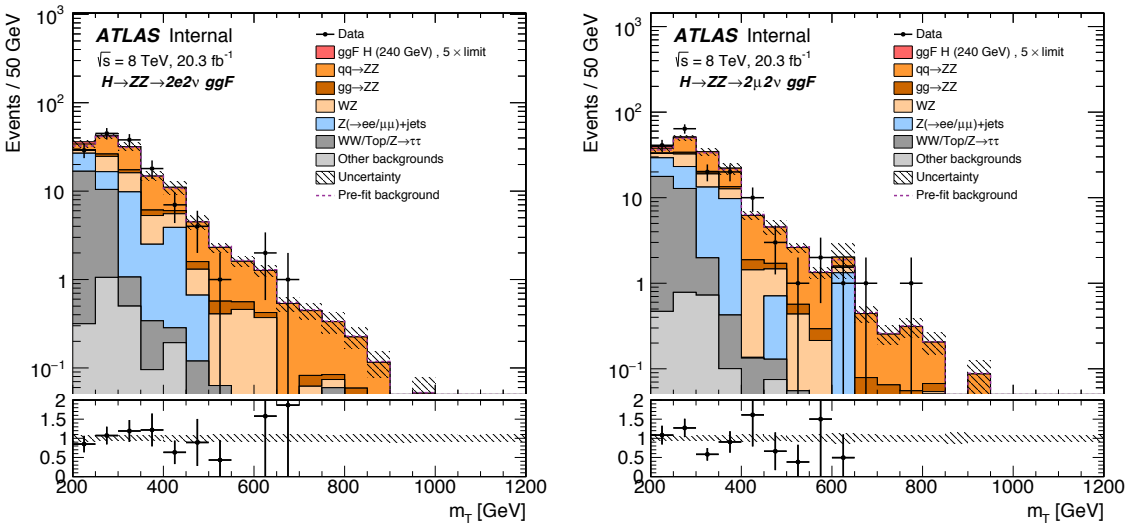

(A) ggF $ee\nu\nu$ (B) ggF $\mu\mu\nu\nu$

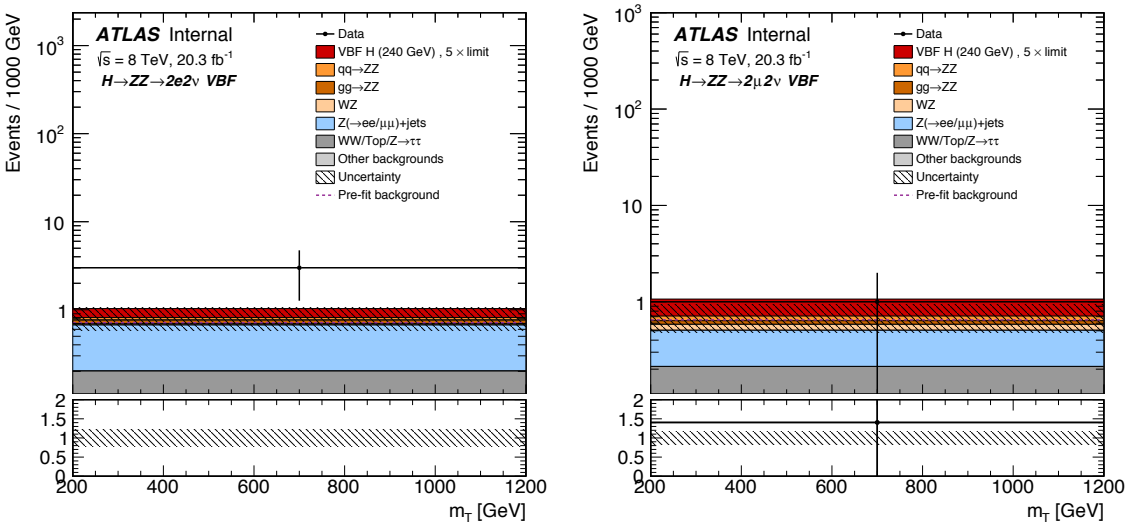

(C) VBF $ee\nu\nu$ (D) VBF $\mu\mu\nu\nu$

FIGURE 6.1: The distribution of m_T for the $H \to ZZ^{(*)} \to 2\ell 2\nu$ search in the ggF event category ((A) and (B)) and the VBF event category ((C) and (D)). A signal at $m_H = 240$ GeV is injected, normalized to a cross-section corresponding to five times the observed limit presented in Section 6.7. A counting experiment is performed in the VBF event category due to limited statistics.

6.3 The H→ZZ$^{(*)}$→2l2q Decay Channel

The experimental signature targeted in the search in the $ZZ^{(*)} \to 2\ell 2q$ decay channel is a final-state containing two leptons and either one or two jets. The analysis employs four event categories in the signal region, three for ggF and one for VBF, and five control regions used to constrain the background, some of which are shared with the $2\nu 2q$ analysis. Taking all event categories into account, the $2\ell 2q$ search is conducted in the range $200 \leq m_H \leq 1000$ GeV. This search is particularly sensitive at high mass, due to the reasonably large branching ratio of the $ZZ^{(*)} \to 2\ell 2q$ decay, and due to an experimental resolution that is comparable to that of the $H \to ZZ^{(*)} \to 4\ell$ search. The analysis is outlined below – more details can be found in [90, 135].

6.3.1 b-tagging

Of great importance to this particular analysis are the techniques used to distinguish b-quark decays, so-called b-tagging. The basic b-tagging algorithms use charged particle tracks to produce a set of variables that discriminate between different jet flavours. ATLAS uses three b-tagging algorithms providing complementary information: an algorithm based on the impact parameter, another based on a secondary vertex reconstruction, and a third relying on decay chain multi-vertex reconstruction. The latter approach uses the topology of weak b- and c-hadron decays to search for a common line connecting the primary vertex to decay vertices. The output of these three b-tagging algorithms are combined into a multivariate discriminant. The MV1c algorithm, used in this analysis, combines the information from these three taggers with a neural network that is trained on b-jets as a signal and c-jets as background. The performance of the MV1c algorithm has been calibrated at working points corresponding to efficiencies between 60% to 80% [136, 137]. In this analysis, the sum of the MV1c algorithm for the two leading jets, MV1cSum, will be used as discriminant.

6.3.2 Event Categorisation

The event selection is initiated by identifying a pair of oppositely charged, same-flavoured leptons from the $Z \to \ell\ell$ decay with an invariant mass of $83 \leq m_{\ell\ell} \leq 99$ GeV. Afterwards, events are divided into several event categories: resolved ggF, merged-jet ggF, and VBF.

The resolved ggF event category is defined for $m_H < 700$ GeV and requires the presence of two jets from the $Z \to qq$ decay with an invariant mass of $70 < m_{jj} < 105$ GeV. The sensitivity is optimised by further segmenting events as either tagged or untagged, distinguished by the b-jet multiplicity; the first label requires exactly two b-tagged jets, and the latter 0 or 1. The final

selection efficiency for these two event categories is around 6% for 0+1 tag and 2% for 2-tag for a NWA signal with $m_H = 900$ GeV. The event selection efficiency is slightly higher at lower mass, and peaks around 12% for 0+1 tag and around 3% for 2-tag. The discriminant of the resolved ggF event category is the invariant mass of the four final-state objects, $m_{\ell\ell jj}$. The experimental resolution is similar in both event categories, at the order of 2 – 3%, and is independent of m_H. The distribution of $m_{\ell\ell jj}$ for both tagged and untagged events is presented in Figure 6.3.

The merged-jet ggF event category is defined for $m_H \geq 700$ GeV and is instantiated because the jets from the $Z \to qq$ decay start to overlap due to the high boost of the Z bosons, causing the resolved ggF event category to lose efficiency. The merged-jet analysis is performed when events do not pass the definition of the other event categories, namely when the selected di-jet system has an invariant mass that is outside of both the signal region and the m_{jj} sidebands used in the definition of the control regions, or if the event contains a single high-p_T jet in addition to the di-lepton pair. As such, the merged-jet ggF event category is explicitly orthogonal to the resolved. This event category requires the invariant mass of the leading jet to be within the range 70 – 105 GeV. If two jets are selected, the jet with the highest p_T is chosen as the $Z \to qq$ candidate. The discriminating variable for this channel is the three-body invariant mass of the two leptons plus the leading jet, $m_{\ell\ell j}$. This event category is treated inclusively in b-tag multiplicity due to limited statistics. The overall efficiency of the merged selection is 5.3% on a NWA signal at $m_H = 900$ GeV, considering only contribution from a ggF signal. The resulting resolution corresponds to 2.5% for a signal with $m_H = 900$ GeV. The distribution of $m_{\ell\ell j}$ obtained in this analysis is presented in Figure 6.3.

To qualify for the VBF event category, an event must contain at least four jets, two of them, the VBF-jets, being non-b-tagged and located in opposite hemispheres of the detector. As with the previous event category, the VBF events are treated inclusively in b-tag multiplicity due to limited statistics. As in the resolved ggF event category, the discriminant is the invariant mass of the four final-state objects originating from the ZZ decay, i.e. $m_{\ell\ell jj}$. This results in an experimental resolution of 2 – 3% over the full m_H range. The discriminant for the VBF event category is shown in Figure 6.3 as well.

6.3.3 Backgrounds

The main background to the $2\ell 2q$ search is the production of Z+jets. In addition, there are significant contributions from top-quark and di-boson production in the resolved ggF event category, as well as a small contribution from multi-jet production.

For the Z+jets background, the shape is obtained from simulation, however, the MC samples are constrained with control regions defined from the sidebands of the m_{jj} distribution (m_j in

the case of the merged event category). The Z control region (ZCR) is defined from the nominal selection, except it is required that m_{jj} lies outside of the signal region. This is defined as $105 < m_{jj} < 150$ GeV and $50 < m_{jj} < 70$ GeV for the resolved event categories, and $30 < m_{jj} < 70$ GeV for the merged.

In the resolved ggF event category, the Z+jets control region is divided according to jet multiplicity, and the Z+jets sample is divided according to the flavour of the jet; $Z + jj$ (light-flavoured jets coming from u, d, s or g), $Z + cj$ (c-jets), $Z + bj$ (b-jets) and Z+hf (heavy-flavour jets, namely b- and c-jets). The normalisations for each of these components are determined in the final likelihood fit, and are constrained with separate normalisation factors using the MV1c variable described in Section 6.3.1. In the VBF and merged-jet ggF event categories, the normalisation of the Z+jets background is done inclusively in b-jet multiplicity, and there is no breakdown according to flavour. Since these two event categories probe very different regions of phase space, each has a separate normalisation factor in the fit, using either $m_{\ell\ell jj}$ or $m_{\ell\ell j}$ as discriminant. The distributions of the discriminants used to constrain the Z+jets backgrounds are shown in Appendix A.

The tagged, resolved ggF event category has a significant contribution coming from $t\bar{t}$ and single-top processes. As for the Z+jets background, the normalisation of the top-component is determined from a control region defined from the nominal selection, but where it is required that an event must contain a $e\mu$ di-lepton pair. The variable $m_{\ell\ell jj}$ is used as discriminant in this control region. The statistics for this control region in the VBF and merged ggF event categories are small, and therefore, the normalisation is assumed to be the same across all event categories.

The small multi-jet background in the $2\ell 2q$ final-state is estimated from data. The di-boson background, composed of $ZZ/WZ \to \ell\ell jj$ processes, and the SM $Zh \to \ell\ell bb$ background are estimated from simulation. The $gg \to ZZ^{(*)}$ background is not estimated by itself, instead the $q\bar{q} \to ZZ^{(*)}$ cross-section is scaled to include its contribution.

The estimated background yields (post-fit) obtained in the $2\ell 2q$ decay channel are presented in Table 6.3 in conjunction with the total number of events observed in data.

6.3.4 Statistical Modelling

The heavy Higgs search in the $2\ell 2q$ decay channel uses a likelihood function on the same form as the $2\ell 2\nu$ channel, i.e. on the form of Equation 6.5, binned in either of the discriminants. The fit is imposed simultaneously to all event categories in the signal region and to the control regions, all summarised in Table 6.4. As in the other analyses, the systematic uncertainties of this search are incorporated as nuisance parameters. The dominant uncertainties in this search are on the Z+jets background modelling, the jet systematics, and the uncertainty on the diboson background

modelling at high m_H [135]. The background normalisation factors are also included as nuisance parameters in the fit and hence conditioned to data.

TABLE 6.3: Number of events observed in data compared to the fitted background predictions for the $H \to ZZ^{(*)} \to 2\ell 2q$ search in the untagged, tagged, and merged-jet ggF event categories, along with the VBF event category.

Component	**Event category**			
	ggF untagged	ggF tagged	ggF merged	VBF
$Z + jj$	35 300 ± 700	14 ± 3	—	—
$Z + cj$	5210 ± 730	34 ± 3	—	—
$Z + bj$	2310 ± 110	59 ± 6	—	—
Z+hf	1610 ± 130	1100 ± 30	—	—
Z+jets	—	—	62 ± 6	600 ± 30
$t\bar{t}/Wt$	332 ± 14	200 ± 9	0.32 ± 0.05	34 ± 4
Diboson	1040 ± 70	140 ± 10	5.0 ± 0.5	18 ± 4
Multijet	152 ± 1	9 ± 5	—	—
$Zh \to \ell\ell bb$	10.4 ± 0.3	9 ± 4	—	—
SM background	46 000 ± 210	1600 ± 30	67 ± 6	650 ± 30
Data	46014	1542	73	644

TABLE 6.4: Summary of the signal- and control-regions among the discriminants entering the likelihood fit in the $2\ell 2q$ decay channel in the signal region (SR) and control regions (CR). The MV1cSum variable is the sum of the of the MV1c b-tagging algorithm output for the two leading jets. Rows with "–" indicate that the given region is not included in the fit. The m_{jj} CR and $e\mu$ CR for the resolved ggF are shared with the $2\nu 2q$ analysis.

N_{b-tag}	**ggF resolved**			**ggF merged**		**VBF**	
	m_{jj} SR	m_{jj} CR	$e\mu$ CR	m_j SR	m_j CR	m_{jj} SR	m_{jj} CR
0 b-tag	$m_{\ell\ell jj}$	MV1cSum	–	$m_{\ell\ell j}$	$m_{\ell\ell jj}$	$m_{\ell\ell jj}$	$m_{\ell\ell jj}$
1 b-tag							
2 b-tag	$m_{\ell\ell jj}$	MV1cSum	$m_{\ell\ell jj}$				

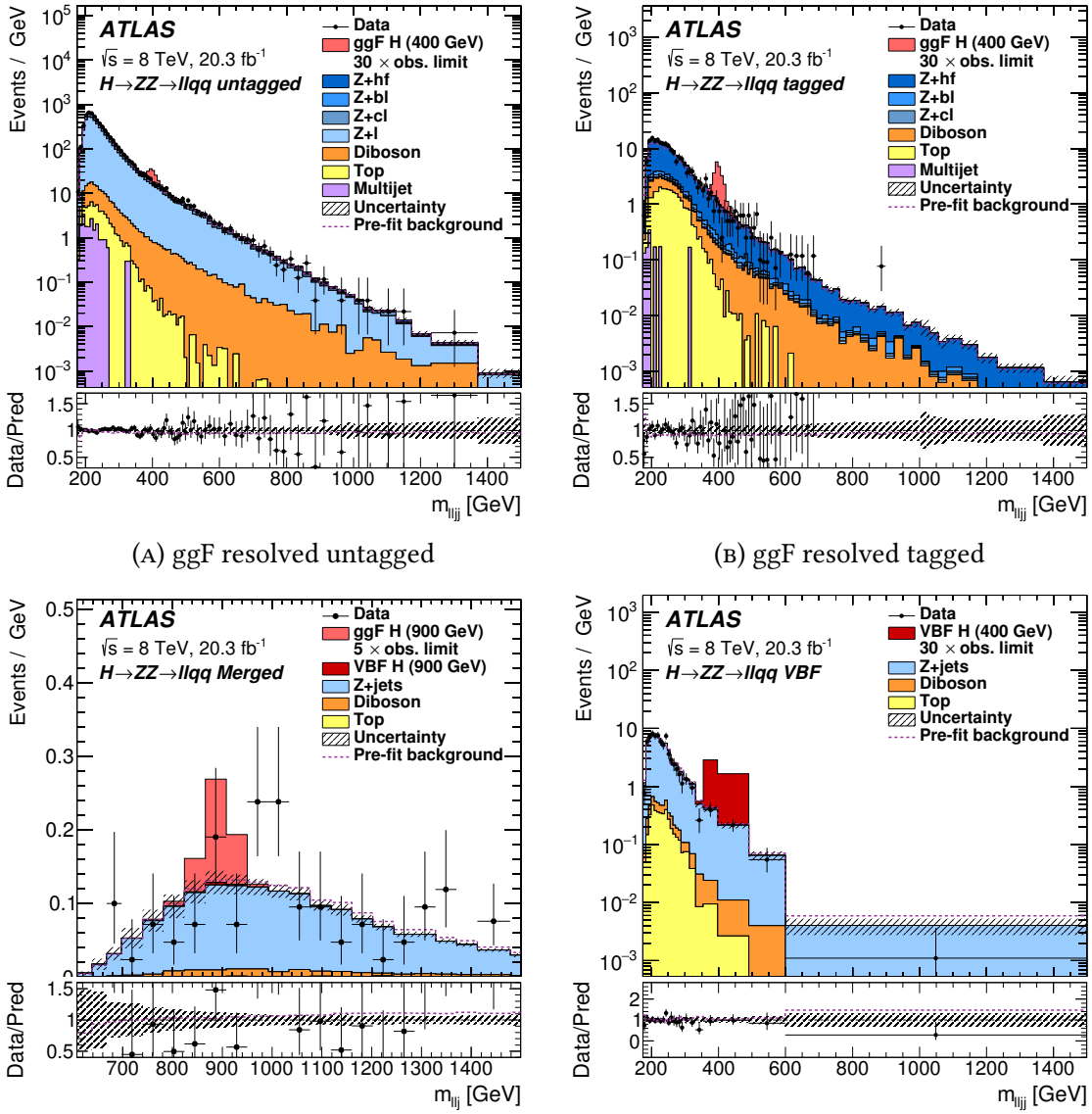

(A) ggF resolved untagged

(B) ggF resolved tagged

(C) ggF merged

(D) VBF

Figure 6.3: Distribution of the discriminating variables in the four signal regions; $m_{\ell\ell jj}$ ((A), (B) and (D)) and $m_{\ell\ell j}$ ((C)). The distributions are presented post-fit, i.e. after the combined likelihood fit described in Section 6.5. Overall, good agreement between data and MC is observed, except for a few excesses in the ggF resolved, tagged event category around $m_H = 900$ GeV and in the ggF merged event category around $m_H = 950$ GeV. Although the range of the discriminants extend up to 1.5 TeV, combined search results are not produced for m_H >1 TeV.

6.4 The H→ZZ$^{(*)}$→2ν2q Decay Channel

The heavy Higgs boson search in the $2\nu 2q$ decay channel targets a final-state containing two jets and E_T^{miss}. As in the search conducted with the $2\ell 2q$ decay channel, this analysis includes several control regions in the fit, some of which are shared among the two channels. Compared to the other three channels, the sensitivity of the $2\nu 2q$ channel at lower Higgs boson mass is expected to be low, for which reason the search is conducted in the interval $400 \leq m_H \leq 1000$ GeV. A brief overview of the analysis is given in the following sections. More details are available in [138].

6.4.1 Event Selection and Categorisation

The targeted final-state of the $H \to ZZ^{(*)} \to 2\nu 2q$ search contains a significant portion of missing transverse energy, $E_T^{miss} > 160$ GeV, and two jets with an invariant mass of $70 < m_{jj} < 105$ GeV. As opposed to the other channels, this analysis only employs a ggF-like event category. As in the resolved ggF event category of the $2\ell 2q$ analysis, the ggF event category is divided according to b-jet multiplicity with the same requirements applying. Events with more than two b-jets are rejected.

The sensitivity of the $2\nu 2q$ search is improved by adding a mass dependent requirement on the jet transverse momenta. Instead of having a single requirement on the jet transverse energy which is a function of the measured mass of the di-boson system, a set of requirements based on the generated m_H are applied. The background is estimated separately for each of these separate jet requirements. The specific requirement is found by rounding the generated m_H to the nearest 100 GeV, the value of which is denoted m_H^{bin}. Then, the sub-leading jet must satisfy $p_T > 0.1 \times m_H^{bin}$ in events without any b-tagged jets, and $p_T > 0.1 \times m_H^{bin} - 10$ GeV in events with at least one b-tagged jet.

The discriminating variable used in this search is the transverse mass m_T as defined in Equation 6.4, but with the $\ell\ell$-system exchanged with the qq-system. The m_T resolution is better at low mass, ranging from about 9% at $m_H = 400$ GeV to 14% at $m_H = 1$ TeV. The distribution of this variable in the tagged and untagged event categories is shown in Figure 6.4.

6.4.2 Backgrounds

The dominant backgrounds for the $2\nu 2q$ search are Z+jets, W+jets and $t\bar{t}$. The shape of these backgrounds are estimated with simulation, and the normalisation of these simulated samples are constrained by the fit to data. The estimation of the Z+jets background is overlapping with that in the $2\ell 2q$ analysis, meaning that the two channels share a control region and normalisation

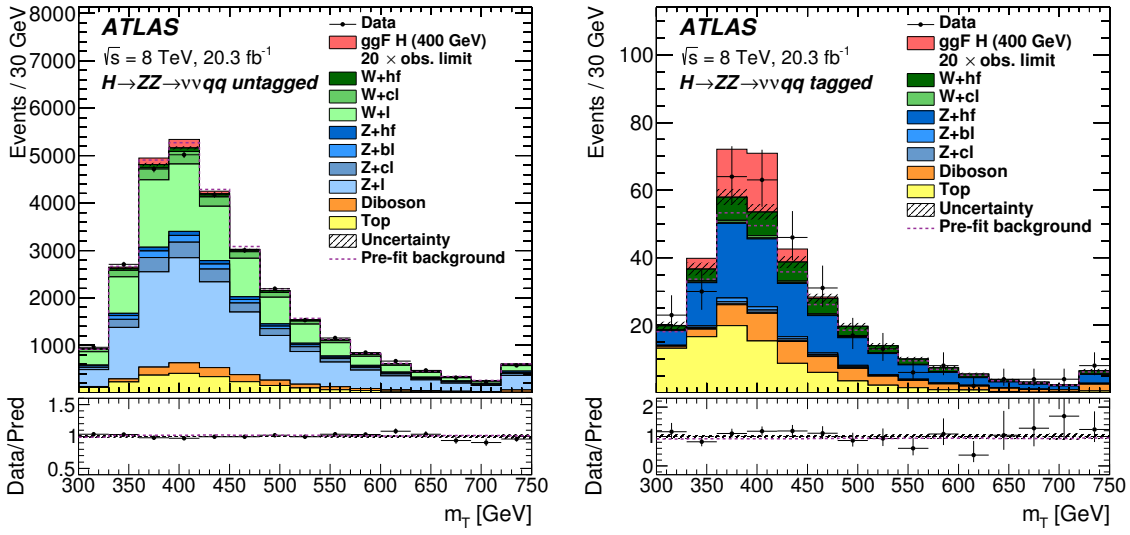

(A) (B)

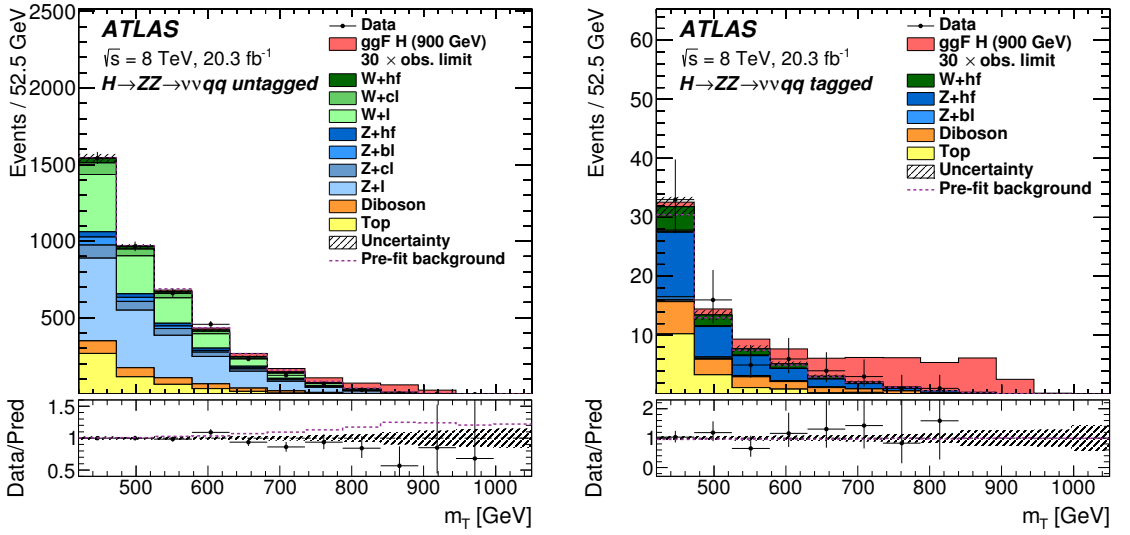

(C) (D)

FIGURE 6.4: The distributions of m_T used in the $H \to ZZ^{(*)} \to 2\nu 2q$ search in the untagged ((A), (C)) and tagged ((B), (D)) event categories for a Higgs boson signal at $m_H = 400$ GeV ((A), (B)) and $m_H = 900$ GeV ((C), (D)). The dashed line shows the total background used as input to the fit. For $m_H = 400$ GeV, the signal is normalised to a cross-section corresponding to 20 times the observed limit presented in Section 6.7, while for $m_H = 900$ GeV, it is normalised to 30 times the observed limit.

factors. The W+jets background estimation also relies on a control region, which is defined from the same selection as the signal, except that exactly one muon must be present. As for the Z+jets background, the normalisation of the individual flavour components of the W+jets background are determined from the fit by using the MV1c discriminant in the tagged and untagged control regions. The flavour components are broken down into $W + jj$ (light-flavoured jets), $W + cj$ (a light-flavoured and a c-jet) and W+hf (heavy-flavour jets, which can be either cc, bj, bc and bb). In addition to the above, the $2\nu 2q$ channel shares a control region with the $2\ell 2q$ analysis for the estimation of the $t\bar{t}$ background, and the normalisation of this component is thus constrained with the $m_{\ell\ell jj}$ discriminant.

Backgrounds from di-boson and single-top production are estimated entirely from simulation. The minor multi-jet background is estimated with a data-driven sideband method, similar to that used to estimate the Z+jets background in the $2\ell 2\nu$ search.

The estimated background yields from the $2\nu 2q$ search are presented in Table 6.5 in conjunction with the total number of events observed in data.

TABLE 6.5: Number of observed events in data compared to the fitted background predictions for the $H \to ZZ^{(*)} \to 2\nu 2q$ search in the untagged and tagged ggF event categories for the $m_H = 400$ GeV and $m_H = 900$ GeV selection.

Component	**Mass and event category**			
	$m_H =$ 400 GeV selection		$m_H =$ 900 GeV selection	
	Untagged	Tagged	Untagged	Tagged
$Z + jj$	12 400 ± 400	1.7 ± 0.3	1590 ± 70	0.26 ± 0.06
$Z + cj$	1800 ± 300	3.8 ± 0.4	250 ± 40	0.65 ± 0.08
$Z + bj$	790 ± 50	5.1 ± 0.7	121 ± 8	0.9 ± 0.2
Z+hf	580 ± 50	120 ± 7	120 ± 10	25 ± 2
$W + jj$	7800 ± 300	1.6 ± 0.1	990 ± 50	0.19 ± 0.03
$W + cj$	1200 ± 100	2.9 ± 0.4	160 ± 20	0.44 ± 0.05
W+hf	450 ± 100	40 ± 10	76 ± 20	9 ± 3
$t\bar{t}/Wt$	2100 ± 100	90 ± 6	520 ± 50	16 ± 1
Diboson	1200 ± 200	44 ± 5	270 ± 40	14 ± 2
$Zh \to \nu\nu bb$	6.8 ± 0.2	5 ± 2	1.4 ± 0.04	1.1 ± 0.5
SM Background	28 400 ± 300	310 ± 10	4090 ± 70	66 ± 4
Data	28573	323	4096	69

6.4.3 Statistical Modelling

The binned likelihood function of the $2\nu 2q$ decay channel has the form:

$$\mathcal{L}(\mu,\theta) = P(n|\mu S + B_{SR}) \times P(m|B_{CR}) \tag{6.6}$$

Here B_{SR} and B_{CR} are the number of expected background events in the signal and control region, while S is the signal yield. The event categories and the discriminants entering this fit are summarised in Table 6.6. As in the other searches, the systematic uncertainties are included as nuisance parameters, the dominant ones being the uncertainties on the background modelling (related to normalisation and flavour composition, or modelling of the shapes), and on the jet energy scale [138].

TABLE 6.6: Summary of the regions and input distributions entering the likelihood fit in the $2\nu 2q$ channel. The MV1cSum variable is the sum of the of the MV1c b-tagging algorithm output for the two leading jets. The $t\bar{t}$ and Z+jets CR are shared with the control regions of the merged-jet ggF event category of the $2\ell 2q$ analysis (named $e\mu$ CR and m_{jj} CR, respectively, in Table 6.4).

Channel	**SR**	**CR**, Z+jets	**CR**, $t\bar{t}$	**CR**, W+jets
0-tag 1-tag	m_T	MV1cSum	-	MV1cSum
2-tag	m_T	MV1cSum	$m_{\ell\ell jj}$	-

6.5 Combination

In the combination of the four $H \to ZZ^{(*)}$ channels, the individual likelihood functions are merged such that a combined fit is performed simultaneously to the signal and control regions of all four searches, which effectively means that the combined likelihood function consist of the product of the four individual functions. The discriminants and event categories from all four channels entering the combined fit are summarised in Table 6.7.

An essential part of the combination lies in defining a correlation scheme, described in Section 6.5.2, which specifies the parameters of interests and nuisance parameters that are correlated between the various channels. The impact and the pull of these are calculated in order to validate the compatibility of the combined likelihood function with the individual likelihood functions, and done as a sanity check to validate the behaviour of the fit.

TABLE 6.7: Summary of the distributions entering the likelihood fit for each event category of the four searches.The control regions shared between the $2\ell 2q$ and $2\nu 2q$ decay channels are marked with grey.

Channel	Event category		SR	Z+jets CR	W+jets CR	$t\bar{t}$ CR
4ℓ	ggF	$4e$	m_{4e}			
		$2e2\mu$	$m_{2e2\mu}$			
		$2\mu 2e$	$m_{2\mu 2e}$			
		4μ	$m_{4\mu}$			
	VBF		$m_{4\ell}$			
	VH		$m_{4\ell}$			
$2\ell 2\nu$	ggF		m_T^{ee}			
			$m_T^{\mu\mu}$			
	VBF		N_{evt}^{ee}			
			$N_{\text{evt}}^{\mu\mu}$			
$2\ell 2q$	ggF	untagged	$m_{\ell\ell jj}$	MV1cSum		
		tagged	$m_{\ell\ell jj}$	MV1cSum		$m_{\ell\ell jj}$
		merged-jet	$m_{\ell\ell j}$	$m_{\ell\ell j}$		
	VBF		$m_{\ell\ell jj}$	$m_{\ell\ell jj}$		
$2\nu 2q$	ggF	untagged	m_T	MV1cSum	MV1cSum (0 b-tag)	
				MV1cSum	MV1cSum (1 b-tag)	
		tagged	m_T			$m_{\ell\ell jj}$

6.5.1 Input

The combination is implemented with a common likelihood combination tool developed within an ATLAS physics working group [139]. The analyses in the individual $H \to ZZ^{(*)}$ decay channels provide a `RooFit` [111] workspace as input to the combination. Given that a single workspace is provided per m_H point, the combination is exclusively performed at the points that overlap between multiple channels. Due to an overlap in control regions, the $2\ell 2q$ and $2\nu 2q$ channels provide a common input to the combination. An overview of the contribution to the combination from the various channels as a function of m_H is given in Table 6.8.

Table 6.8: Overview of the input to the combination from the four decay channels as a function of m_H. The m_H spacing specifies the distance between the m_H values where input is available.

Search range	**Channel(s)**	**m_H spacing**
$140 \leq m_H \leq 195$ GeV	4ℓ	5 GeV
$200 \leq m_H \leq 220$ GeV	4ℓ, $2\ell 2q$	20 GeV
$240 \leq m_H \leq 380$ GeV	4ℓ, $2\ell 2q$, $2\ell 2\nu$	20 GeV
$400 \leq m_H \leq 1000$ GeV	4ℓ, $2\ell 2q$ $2\ell 2\nu$, $2\nu 2q$	20 GeV for $m_H < 600$ GeV 50 GeV for $m_H > 600$ GeV

6.5.2 Correlation Scheme

Parameters are correlated if they arise from the same physical effect and/or if representing the same quantity, and a correlation of 100% is therefore assumed. In practise, for a given correlated NP, this is implemented by using a common NP in all decay channels. The correlation of NPs between the four decay channels is reported in Table 6.9. The parameter of interest in the likelihood functions of all channels are the signal-strength parameters μ_{ggF} and μ_{VBF}, which are assumed to be correlated between all channels.

To reduce the processing time needed to perform the statistical procedures, a subset of the NPs belonging to the individual channels are removed, or pruned, before the combination. The pruning is performed by removing the NPs that cause a shift smaller than a threshold value on the normalisation. Details on this can be found in the separate supporting documentation [124, 133, 135, 138]. No pruning is performed post-combination.

The groups of NPs that are sensible to correlate among the searches are the theoretical uncertainties on the signal and the background, among the jet energy scale (JES) systematics. The motivation for correlating these nuisance parameters, among the reason for not combining others, is described below.

Table 6.9: Correlation of NPs between the four channels. NPs denoted with × are correlated. Parameters denoted with "–" are removed by the pruning procedure in the respective channel at all m_H values. A subset of the NPs are pruned for a subset of m_H values for the individual channels. ∘ signifies that the NP is only correlated across the $2\ell 2q$ and $2\nu 2q$ decay channels.

Nuisance parameter	**Channel(s)**				**Source of uncertainty**
	4ℓ	$2\ell 2\nu$	$2\ell 2q$	$2\nu 2q$	
ATLAS_SigPDF_VBF	–	×	×	×	VBF signal pdf
ATLAS_SigPDF_ggF	×	×	×	×	ggF signal pdf
ATLAS_SigQCD_VBF	–	×	×	×	VBF signal QCD scale
ATLAS_SigQCD_ggF	×	×	×	×	ggF signal QCD scale
ATLAS_SigISRFSR_VBF	–	×	∘	∘	VBF signal ISR/FSR
ATLAS_SigISRFSR_ggF	×	×	∘	∘	ggF signal ISR/FSR
QCDscale_VV	×	×	∘	∘	$q\bar{q} \to ZZ^{(*)}$ QCD scale
QCDscale_ggVV	×	×	∘	∘	$gg \to ZZ^{(*)}$ QCD scale
pdf_VV	×	×	∘	∘	$q\bar{q} \to ZZ^{(*)}$ pdf
QCDscale_ggVV_kfactor	×	×	∘	∘	$gg \to ZZ^{(*)}$ NNLO k-factor
ATLAS_LUMI_2012	×	×	×	×	Integrated luminosity
ATLAS_JES_BASE1	×	×	∘	∘	Baseline in-situ JES
ATLAS_JES_BASE2	×	×	∘	∘	Baseline in-situ JES
ATLAS_JES_BASE3	×	×	∘	∘	Baseline in-situ JES
ATLAS_JES_BASE4	–	×	∘	∘	Baseline in-situ JES
ATLAS_JES_BASE5	–	×	∘	∘	Baseline in-situ JES
ATLAS_JES_BASE6	–	×	∘	∘	Baseline in-situ JES
ATLAS_JES_EtaModelling	–	×	∘	∘	Jet η inter-calibration
ATLAS_JES_EtaStatMethod	–	×	∘	∘	Jet η inter-calibration
ATLAS_JES_HightPt	–	–	∘	∘	High p_T jet modelling
ATLAS_JES_NPV	–	×	∘	∘	JES pile-up dependence
ATLAS_JES_Mu	–	×	∘	∘	JES pile-up dependence
ATLAS_JES_PilePt	×	×	∘	∘	JES pile-up dependence
ATLAS_JES_PileRho	×	×	∘	∘	JES pile-up dependence
ATLAS_JES_FlavComp	×	×	∘	∘	Jet flavour composition (q/g)
ATLAS_JES_FlavRes	×	×	∘	∘	Flavour-dependent jet response

6.5.2.1 Jet Systematics

The $2\ell 2q$ and $2\nu 2q$ searches contain jets in the final-state from the $Z \to qq$ decay, while the 4ℓ and $2\ell 2\nu$ searches exclusively use jets to segment the data into to the various event categories. The former two channels have a considerable amount of statistics in both the signal and control regions, and therefore have the potential to constrain and pull the NPs related to jets across all four decay channels. However, since the origin of the jets in the final-state of the various event categories of the four searches differ, these jets probe very different parts of the kinematic phase space. As a result, the constraints on the jet NPs imposed by the $2\ell 2q$ and $2\nu 2q$ searches are unlikely to provide the best description of the jets appearing in the other two searches. Therefore, in this combination, the jet NPs are not correlated between the $2\ell 2q$ and $2\nu 2q$ decay channels and the remaining two.

Despite not correlating the JES systematics between all channels, the impact on the final limits on μ when correlating them is studied. This study is performed at three m_H points, and is conducted with a comparison of the upper limits on μ computed with the CL_S technique explained in Chapter 5 using the combined likelihood function. The limits in two different scenarios are compared; when using the default correlation scheme in Table 6.9, and when correlating the JES systematics between all channels. The impact is studied separately for ggF and VBF by fitting either μ_{ggF} or μ_{VBF} and letting the other float in the fit. The impact is summarised in Table 6.10 and Table 6.11, where an increment indicates that the limit decreased in value. As seen, the impact on the ggF limits is <0.7% in all instances, and is therefore considered negligible. The largest impact on the VBF limits is 2.5%, which is observed in a single instance. However, at the remaining points the effect is 1.5% at maximum, and the impact is hence considered negligible for the VBF event category as well.

TABLE 6.10: Percentage change in the ggF limits when correlating JES systematics between all channels. An increment indicates that the limit decreased in value.

m_H [GeV]	Expected [%]	Observed [%]	+2σ [%]	+1σ [%]	-1σ [%]	-2σ [%]
240	0.55	0.66	0.58	0.55	0.55	0.55
400	0.71	0.72	0.71	0.71	0.71	0.71
900	0.18	0.16	0.16	0.17	0.18	0.18

Table 6.11: Percentage change in the VBF limits when correlating JES systematics between all channels. An increment indicates that the limit decreased in value.

m_H [GeV]	Expected [%]	Observed [%]	$+2\sigma$ [%]	$+1\sigma$ [%]	-1σ [%]	-2σ [%]
240	-1.6	-2.5	-1.4	-1.5	-1.6	-1.6
400	-1.5	-1.8	-1.4	-1.4	-1.5	-1.5
900	0.013	0.033	0.005	0.011	0.013	0.013

6.5.2.2 Theory Systematics

The theoretical systematic uncertainties affecting the ZZ backgrounds are correlated between the 4ℓ and $2\ell 2\nu$ channels, but not to the $2\ell 2q$ and $2\nu 2q$ decay channels. The reason for not doing so is that the two groups of decay channels assess these particular systematic uncertainties with different methods, and because the background estimation of the $2\ell 2q$ analysis does not include the $gg \to ZZ^{(*)}$ background.

The theoretical uncertainty on the signal acceptance from the PDF and QCD scale are correlated between all four channels. The ISR/FSR signal acceptance uncertainty is correlated between 4ℓ and $2\ell 2\nu$, and between $2\nu 2q$ and $2\ell 2q$, but not across all search channels. The reason for not doing so is that the ISR/FSR signal acceptance uncertainties are represented by a single NP, and that the ISR and FSR effects have different impact on the acceptance of the four channels; the uncertainty on the former two channels is dominated by ISR effects, while the uncertainty on the latter two channels is dominated by FSR.

6.5.2.3 Lepton Systematics

Uncertainties in the lepton energy scale and resolution are treated as uncorrelated between all four searches because different lepton objects are used, and due to differences in the selection. A check is performed to estimate the impact from correlating the lepton scale and resolution systematics between the $2\ell 2\nu$, $2\ell 2q$ and $2\nu 2q$ decay channels. Since a subset of these nuisance parameters are removed by the pruning, only `ATLAS_MU_MS_RES_MS` and `ATLAS_EL_RES` are correlated in this test. The impact is assessed with the same procedure as for the JES systematics described in Section 6.5.2.1, by comparing the obtained limits before and after combining these two nuisance parameters. The study is performed at the two mass points 400 GeV and 900 GeV for ggF and VBF. The change in the limits for ggF and VBF at both mass points is found to be <0.1% and thus considered negligible.

6.6 Nuisance Parameter Rankings and Pulls

The NP rankings and pulls defined in Section 5.7 are computed to assess the behaviour of the combined fit and the compatibility of the combined NPs to that of the individual analyses. As was the case with the 4ℓ analysis, only Asimov data generated with $\mu_{\text{ggF}} = \mu_{\text{VBF}} = 0.1$ is used.

Figure 6.5 to Figure 6.8 present the top 20 ranked systematic uncertainties obtained with the combined fit at $m_H = 200$ GeV and $m_H = 900$ GeV. Figure 6.9 to Figure 6.12 summarise the 20 NPs that are pulled and constrained the most by the data at $m_H = 200$ GeV and $m_H = 900$ GeV, respectively. The NPs appearing in these figures are summarised and explained in Table 6.12. A description of the behaviour of the NPs segmented according to their parent analysis is given below. As a general trend, the NPs from the 4ℓ and $2\ell 2\nu$ decay channels rank highest at low mass, where these analyses are the most sensitive. At high mass, the uncertainties from the $2\ell 2q$ and $2\nu 2q$ decay channels dominate. Overall, no anomalies are observed, and the behaviour of the NPs is consistent with what is observed in the individual channels.

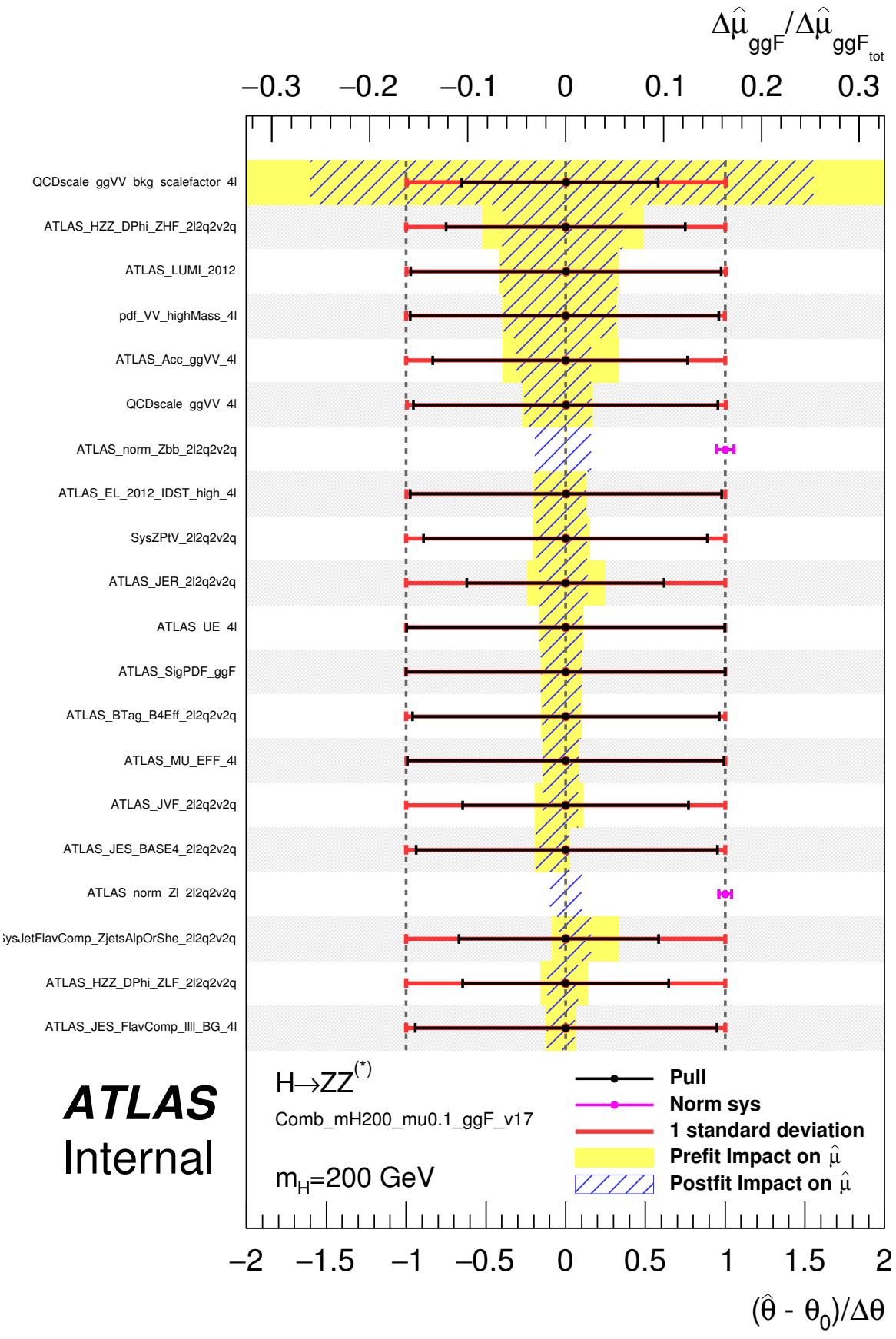

Figure 6.5: Nuisance parameter ranking for the combined fit performed at $m_H = 200$ GeV with Asimov data generated with $\mu_{ggF} = 0.1$.

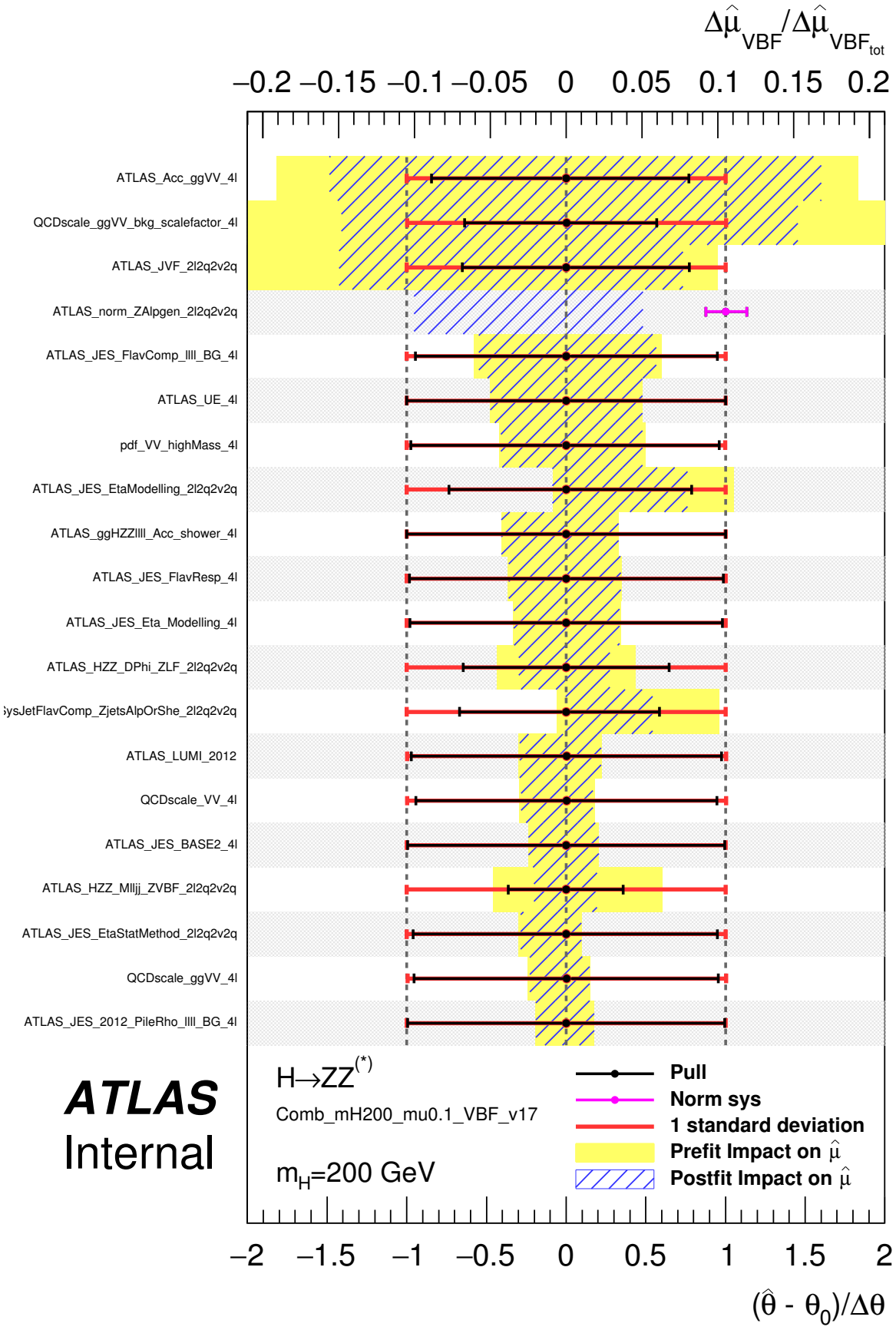

FIGURE 6.6: Nuisance parameter ranking for the combined fit performed at $m_H = 200$ GeV with Asimov data generated with $\mu_{\text{VBF}} = 0.1$.

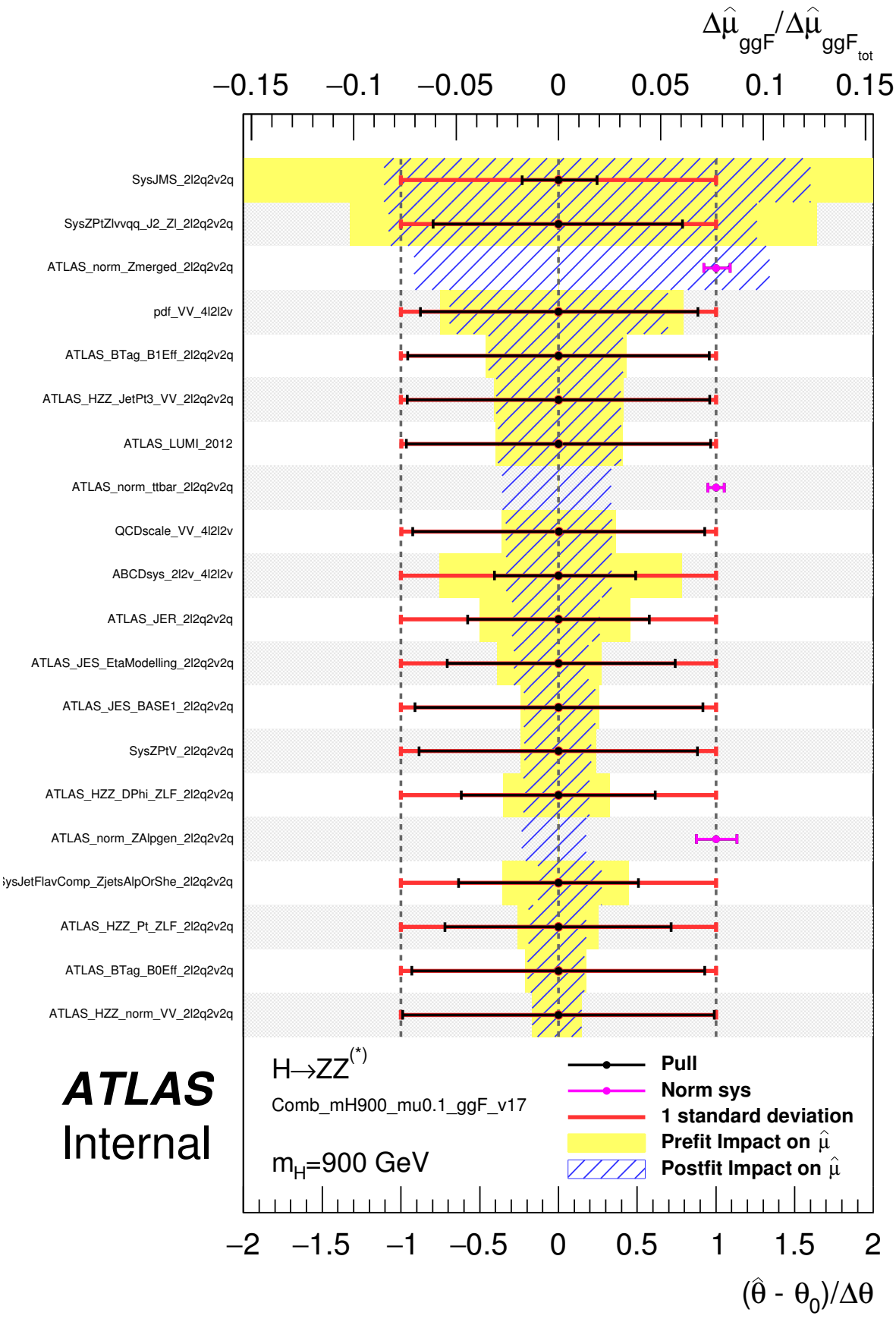

FIGURE 6.7: Nuisance parameter ranking for the combined fit performed at $m_H = 900$ GeV with Asimov data generated with $\mu_{ggF} = 0.1$.

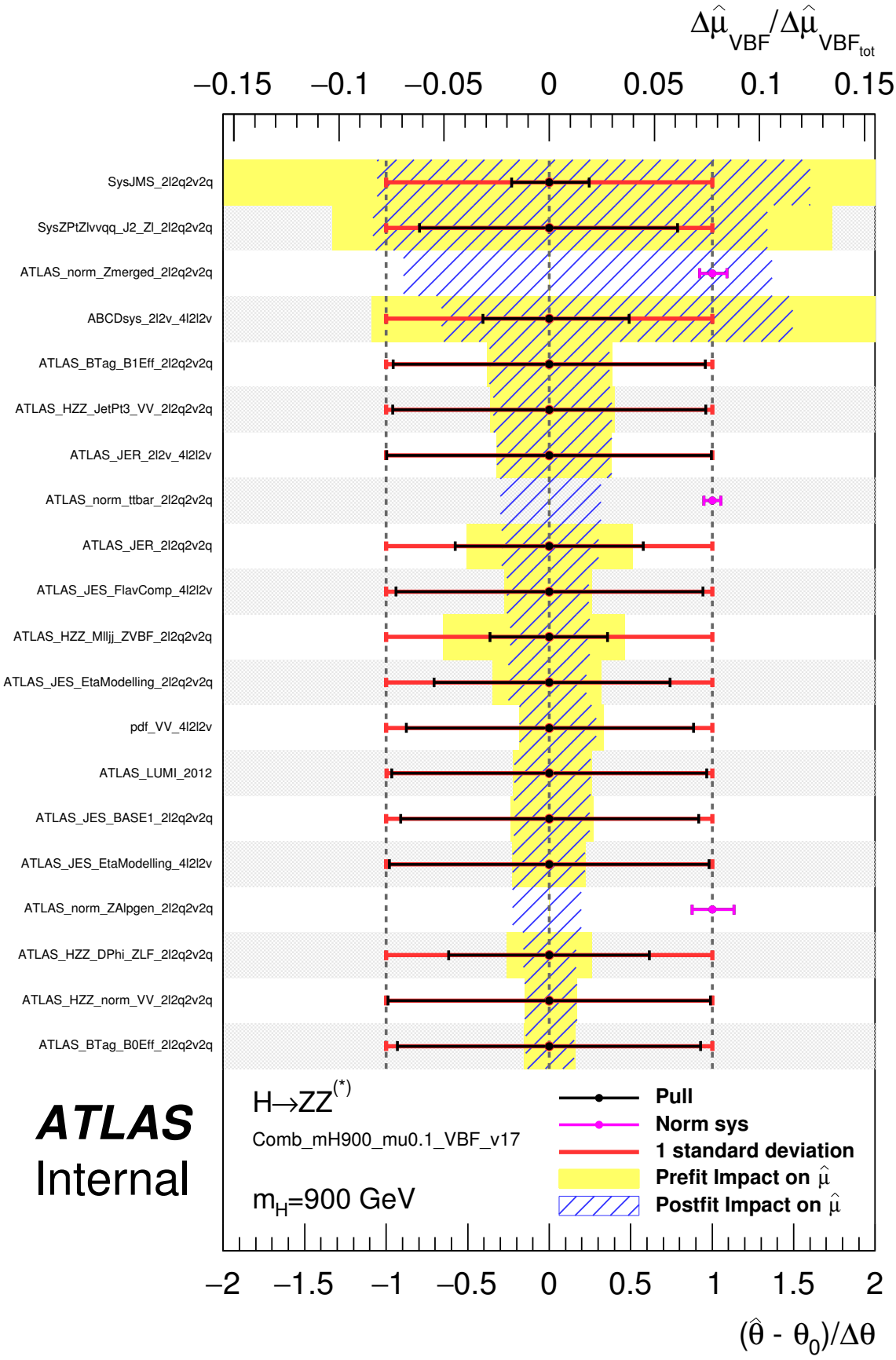

FIGURE 6.8: Nuisance parameter ranking for the combined fit performed at $m_H = 900$ GeV with Asimov data generated with $\mu_{\text{VBF}} = 0.1$.

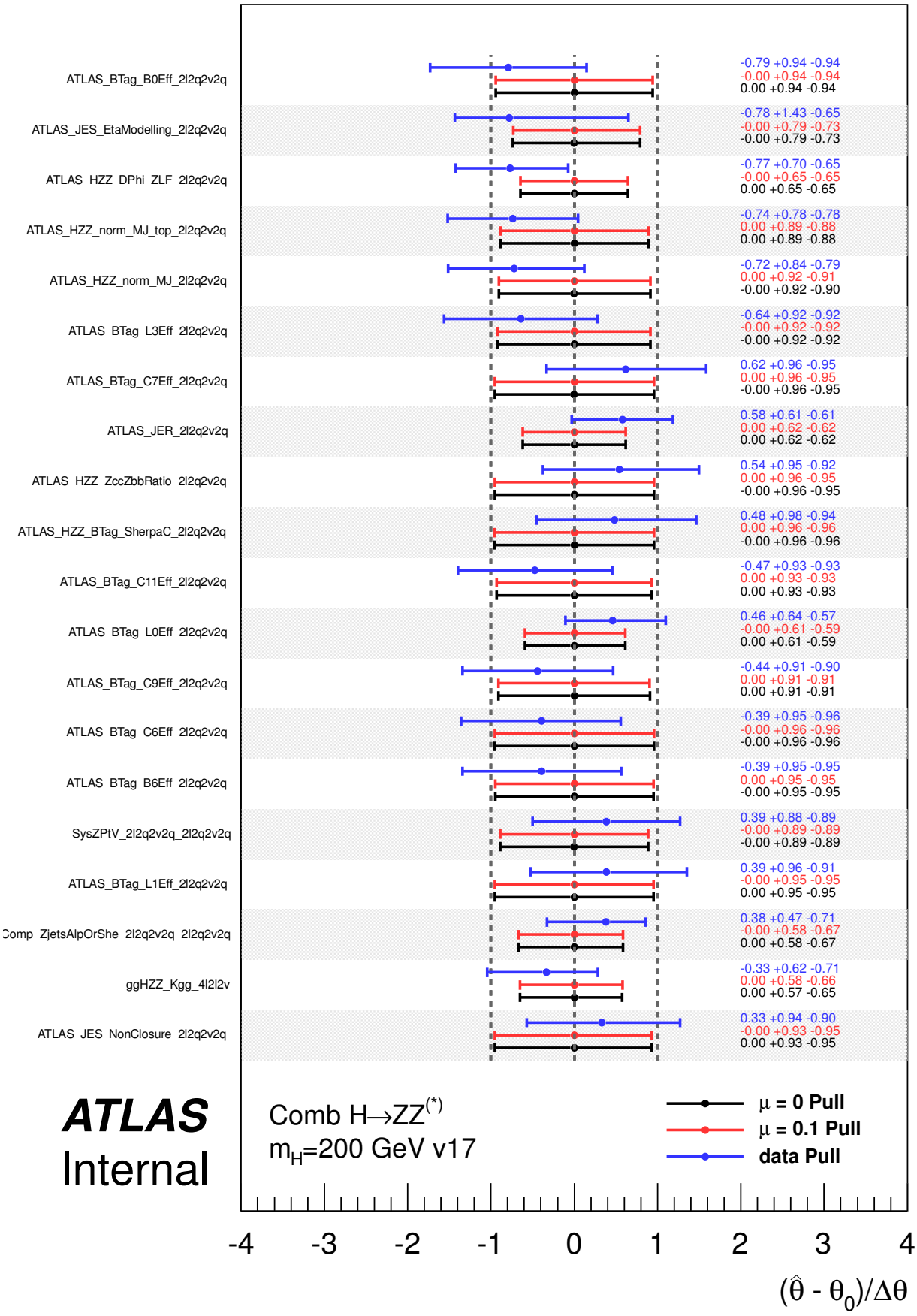

Figure 6.9: Ranking of the 20 most pulled NPs performed with the combined likelihood function on data for $m_H = 200$ GeV.

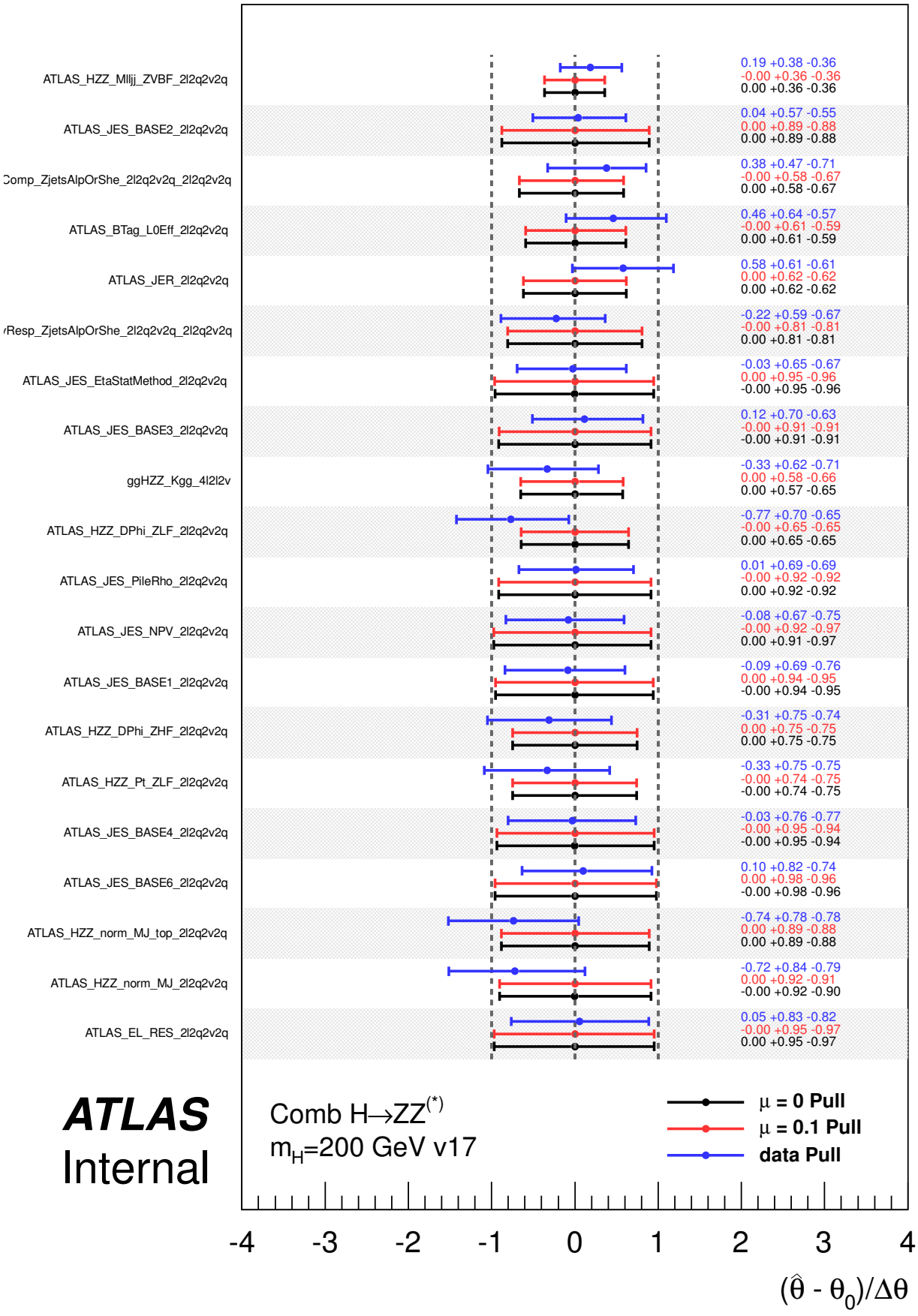

FIGURE 6.10: Ranking of the 20 most constrained NPs performed with the combined likelihood function on data for $m_H = 200$ GeV.

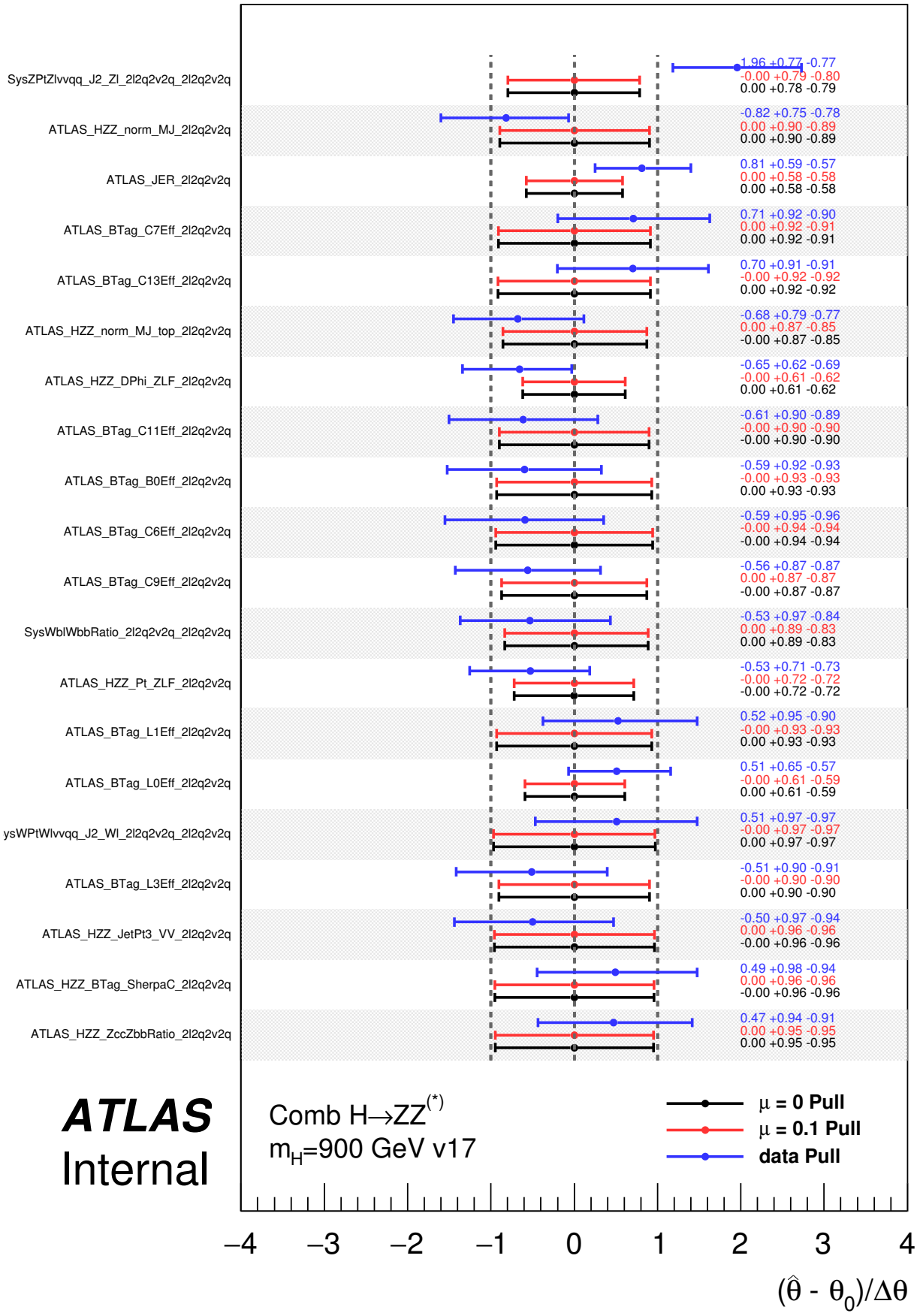

Figure 6.11: Ranking of the 20 most pulled NPs performed with the combined likelihood function on data for $m_H = 900$ GeV.

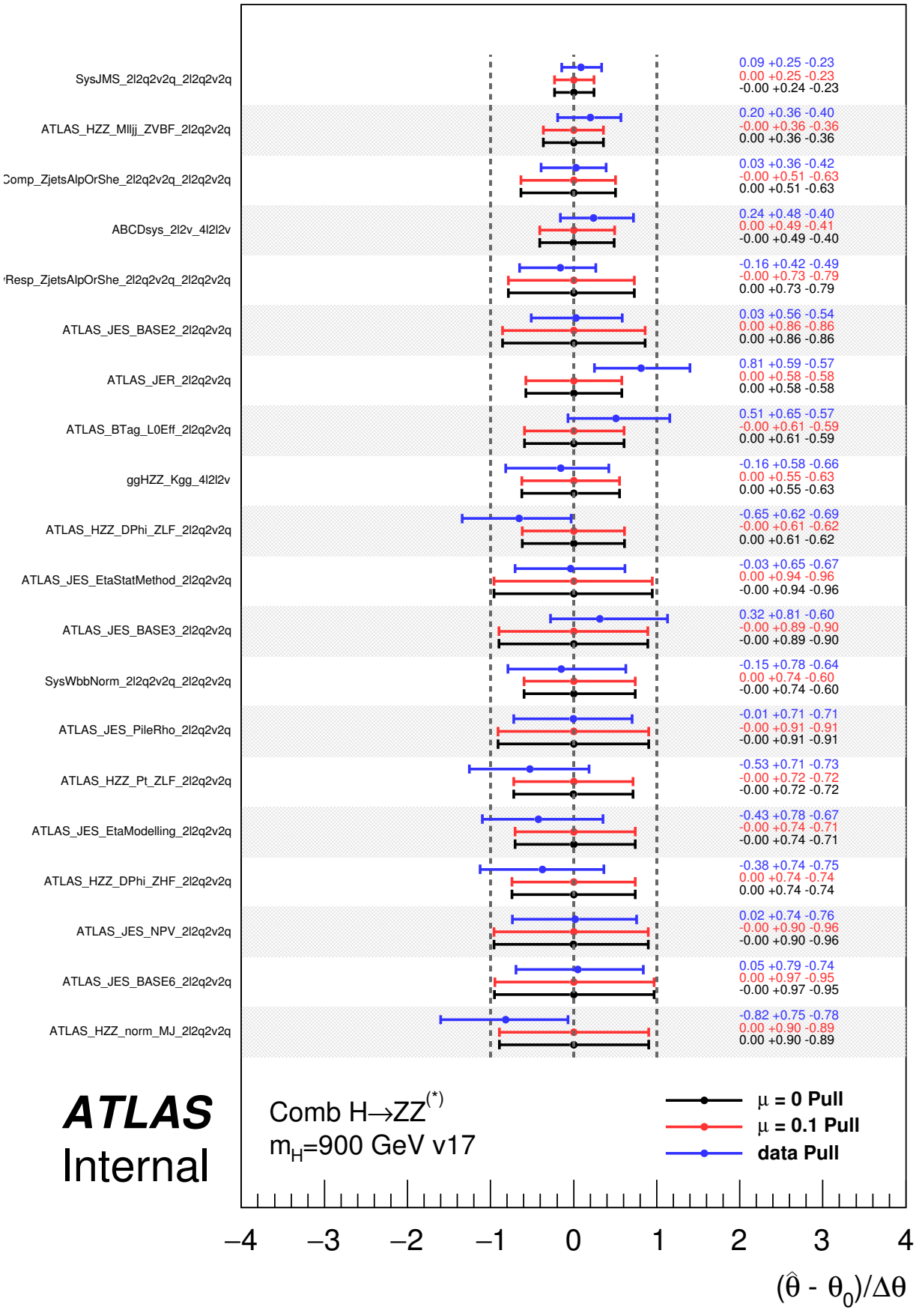

FIGURE 6.12: Ranking of the 20 most constrained NPs performed with the combined likelihood function on data for $m_H = 900$ GeV.

Table 6.12: Overview of the nuisance parameters appearing in Figure 6.5 to Figure 6.12 listed in alphabetical order. The symbol "×" signifies which decay channel(s) the NP is affiliated to. A subset of the NPs appearing in Table 6.9 have been assigned a new name in the combination. When an NP appears more than once for more than one decay channel, the reason is that the NP was not combined between the respective channels, which could be due to the NP being pruned of the channel not contributing at the respective m_H point.

Nuisance parameter	**Channel(s)**				**Source of uncertainty**
	4ℓ	$2\ell 2\nu$	$2\ell 2q$	$2\nu 2q$	
ABCDsys_2l2v_4l2l2v		×			Z+jets background estimation
ATLAS_Acc_ggVV_4l	×				$gg \to ZZ^{(*)}$ theory acceptance
ATLAS_BTag_BnEff_2l2q2v2q			×	×	b-jet identification (n = 1 − 10)
ATLAS_BTag_CnEff_2l2q2v2q			×	×	c-jet identification (n = 1 − 15)
ATLAS_BTag_LnEff_2l2q2v2q			×	×	Light-jet identification (n = 1 − 15)
ATLAS_EL_2012_IDST_high_4l	×				Electron ID efficiency
ATLAS_EL_RES_2l2q			×	×	Electron resolution correction
ATLAS_ggHZZllll_Acc_shower_4l	×				ggF signal ISR/FSR
ATLAS_HZZ_BTag_SherpaC_2l2q2v2q			×	×	Generator-dependent b-jet identification
ATLAS_HZZ_DPhi_ZHF_2l2q(2v2q)			×	×	$\Delta\phi$ shape for heavy-flavour
ATLAS_HZZ_DPhi_ZLF_2l2q			×	×	$\Delta\phi$ for light-flavour
ATLAS_HZZ_Mlljj_ZVBF_2l2q(2v2q)			×	×	Z $m_{\ell\ell jj}$ shape for VBF
ATLAS_HZZ_norm_VV_2l2q2v2q			×	×	Background normalisation
ATLAS_HZZ_norm_MJ_2l2q(2v2q)			×	×	Background normalisation
ATLAS_HZZ_norm_MJ_top_2l2q(2v2q)			×	×	Background normalisation
ATLAS_HZZ_ZccZbbRatio_2l2q2v2q			×	×	$Z \to cc/Z \to bb$ ratio
ATLAS_JER_2l2q(2v2q)			×	×	Jet energy resolution
ATLAS_JER_2l2v_4l2l2v		×			Jet energy resolution

Continued on next page

Nuisance parameter	Channel(s)				Source of uncertainty
	4ℓ	$2\ell 2\nu$	$2\ell 2q$	$2\nu 2q$	
ATLAS_JES_2012_PileRho_llll_BG_4l	×				Jet energy scale pile-up dependence
ATLAS_JES_BASEn_2l2q(2v2q)			×	×	Jet energy calibration uncertainty (n = 1 − 6)
ATLAS_JES_Eta(_)Modelling_4l(2l2v)	×	×			Jet energy scale η inter-calibration
ATLAS_JES_EtaModelling_2l2q2v2q			×	×	Jet energy scale η inter-calibration
ATLAS_JES_EtaStatMethod_2l2q(2v2q)			×	×	Statistical error on η inter-calibration
ATLAS_JES_FlavComp_llll_BG_4l	×				Jet flavour composition (q/g)
ATLAS_JES_FlavComp_4l2l2v	×	×			Jet flavour composition (q/g)
ATLAS_JES_FlavResp_4l	×				Flavour-dependent jet response
ATLAS_JES_NPV_2l2q(2v2q)			×	×	Jet energy scale pile-up dependence
ATLAS_JES_PileRho_2l2q(2v2q)			×	×	Jet energy scale pile-up dependence
ATLAS_JVF_2l2q2v2q			×	×	Jet vertex fraction efficiency
ATLAS_LUMI_2012	×	×	×	×	Integrated luminosity
ATLAS_MU_EFF_4l	×				Muon reconstruction and ID
ATLAS_norm_ttbar_2l2q2v2q			×	×	Background normalisation
ATLAS_norm_Zl_2l2q2v2q			×	×	Background normalisation
ATLAS_norm_Zbb_2l2q2v2q			×	×	Background normalisation
ATLAS_norm_ZAlpgen_2l2q2v2q			×	×	Background normalisation
ATLAS_norm_Zmerged_2l2q2v2q			×	×	Background normalisation
ATLAS_SigPDF_ggF	×	×	×	×	ggF signal pdf
ATLAS_UE_4l	×				Underlying event impact on signal acceptance
ggHZZ_Kgg_4l2l2v	×	×			$gg \to ZZ^{(*)}$ NNLO k-factor
pdf_VV_highMass_4l	×				$q\bar{q} \to ZZ^{(*)}$ pdf

Continued on next page

Nuisance parameter	Channel(s)				Source of uncertainty
	4ℓ	$2\ell 2\nu$	$2\ell 2q$	$2\nu 2q$	
pdf_VV_4l2l2v	×	×			$q\bar{q} \to ZZ^{(*)}$ pdf
QCDscale_ggVV_bkg_scalefactor_4l	×				$gg \to ZZ^{(*)}$ NNLO k-factor
QCDscale_ggVV_4l	×				$gg \to ZZ^{(*)}$ QCD scale
QCDscale_VV_4l(2l2v)	×	×			$q\bar{q} \to ZZ^{(*)}$ QCD scale
SysJetFlavComp_ZjetsAlpOrShe_2l2q(2v2q)			×	×	Flavour composition (g/q) for Z+jets SHERPA+ALPGEN samples
SysJetFlavResp_ZjetsAlpOrShe_2l2q2v2q			×	×	Flavour response (g/q) for Z+jets SHERPA+ALPGEN samples
SysJMS_2l2q2v2q			×	×	Jet mass scale uncertainty
SysZPtV_2l2q2v2q			×	×	Z p_T shape
SysZPtZlvvqq_J2_Zl_2l2q2v2q			×	×	Z boson p_T shape
SysWbbNorm_2l2q2v2q			×	×	Background normalisation (W+jets)
SysWblWbbRatio_2l2q2v2q			×	×	$W \to bl/W \to bb$ ratio
SysWPtWlvvqq_J2_Wl_2l2q2v2q			×	×	W p_T shape

6.6.1 Nuisance Parameters From the 4l and 2l2v Decay Channels

As seen in Figure 6.5 to Figure 6.6, at low mass the ZZ theory systematic uncertainties from the 4ℓ channel propagate to the combined model, a behaviour that is consistent with what was observed for this particular channel in Chapter 5. Furthermore, the pulls and constraints of the following, specific NPs are noticed:

- In the 4ℓ and $2\ell 2\nu$ decay channels, the correlated theory uncertainties on the ZZ background are pulled down slightly to compensate for the fact that slightly less events than expected are observed in the ggF categories of both channels. As observed from Figure 6.9, Figure 6.10 and Figure 6.12, the combined NP ggHZZ_Kgg_4l2l2v is pulled down to -0.3σ at low mass and to -0.2σ at high mass. Furthermore, this NP is constrained by the data to about +0.6σ, -0.7σ at low mass and to ±0.6σ at high mass.

- From Figure 6.7 and Figure 6.8 it is seen that the NP `ABCDsys_2l2v_4l2l2v`, representing the uncertainty on the Z+jets background estimation, is the highest ranked uncertainty from the $2\ell 2\nu$ analysis. This is compatible with the individual $2\ell 2\nu$ analysis, where this systematic dominated. Furthermore, from Figure 6.12 it is seen that this NP is constrained by the fit at high mass, which could happen as a result of the initial uncertainty being too conservative.

6.6.2 Nuisance Parameters From the 2l2q and 2v2q Decay Channels

As mentioned above, the $2\ell 2q$ and $2\nu 2q$ decay channels have a plentiful data-sample in the control regions, which allows them to pull and constrain a large number of the jet-related uncertainties. In particular, the following NPs are noticed:

- The jet energy resolution NP, `ATLAS_JER_2l2q2v2q` is known to be overestimated. From Figure 6.9 to Figure 6.12 it is seen that this NP is both pulled (to +0.6σ at $m_H = 200$ GeV and +0.8σ at $m_H = 900$ GeV) and constrained considerably (±0.6σ at $m_H = 200$ GeV, 900 GeV).

- The jet flavour composition NP from the Z+jets background, named `Comp_ZjetsAlpOrShe-_2l2q2v2q_2l2q2v2q`, is conservatively taken to be 50% with a 100% uncertainty. Consequently, as seen in Figure 6.9 to Figure 6.12, the data has the power to pull (+0.4σ at $m_H = 200$ GeV) and constrain it (+0.4σ, -0.7σ at $m_H = 200$ GeV, ±0.4σ at $m_H = 400$ GeV).

- The jet η modelling NP, `ATLAS_JES_EtaModelling_2l2q2v2q`, is pulled (-0.8σ at $m_H = 200$ GeV, -0.4σ at $m_H = 900$ GeV) by the large statistics in the VBF channels, such as to better describe the jets in the VBF event category.

- The uncertainty on the jet mass scale `SysJMS_2l2q2v2q` is conservatively taken to be 14%. As seen in Figure 6.12, this NP is consequently constrained by the fit at high mass, which is the only region where this NP is relevant.

- The modelling of the Z+jet backgrounds in the $2\ell 2q$ and $2\nu 2q$ decay channels is improved by applying several corrections to kinematic distributions, such as p_Z and $\Delta\phi_{jj}$ for the ggF event categories and $m_{\ell\ell jj}$ for the VBF event categories. A conservative uncertainty of 50% or 100% is applied to these corrections. As observed, these uncertainties are constrained by the fit.

In addition to the above, a large number of b-tagging parameters are pulled or constrained, which is expected since the b-tagging MV1c-based discriminant in the Z+jets CRs is used as input to the fit. For both the jet and b-tagging NPs, the pulls and constraints are similar to those observed in the published SM VH $H \to bb$ analysis [140].

6.7 Results

The following sections present the results of the combination of the four searches: model-independent upper limits on the heavy Higgs boson production rate and a 2HDM interpretation.

6.7.1 Upper Limits on Heavy Higgs Boson Production Rate

Upper limits on the heavy Higgs boson cross-section times $H \to ZZ^{(*)}$ branching ratio obtained with the combination of all four channels are presented in Figure 6.13 (in units of pb) and Table 6.13 (in units of fb). These results were produced with the CL_S procedure described in Section 5.7.3 and as well computed separately for the ggF and VBF production modes. The expected limits from the individual channels are shown as well for comparison.

As seen from the expected limits in Figure 6.13, the 4ℓ search has the better sensitivity at low mass. At high mass, the sensitivity of the combined $2\ell 2q$ *and* $2\nu 2q$ searches is greatest, with the sensitivity of the $2\ell 2\nu$ channel being only slightly inferior. Only the 4ℓ channel contributes in the range $m_H < 200$ GeV, and the limits in this regime are hence the same as those obtained in the individual 4ℓ analysis. Compared to the corresponding results produced with the 4ℓ channel alone, a significant increase is observed in the sensitivity after the combination. For example, at $m_H = 200$ GeV, 400 GeV and 700 GeV, the expected ggF limits from the 4ℓ channel alone decrease from 329 fb to 324 fb, from 125 fb to 84 fb, and from 59 fb to 22 fb. For VBF, the improvement at the same mass points are from 179 fb to 135 fb, from 95 fb to 55 fb, and from 54 fb to 18 fb.

A few excursions into the 2σ bands are present in the observed limits, which are driven by the local deviations in the input distributions. For example, the excess occurring around 200 GeV and the deficit occurring around 300 GeV have propagated from the 4ℓ search, while the deficits at higher mass are driven by fluctuations in the $2\ell 2q$ search. No excursions outside the 2σ band are observed in the considered mass range between 140 GeV and 1 TeV. The observed limits on the production cross-section times branching ratio for heavy Higgs boson range from 359 fb at $m_H = 200$ GeV to 10 fb at $m_H = 1$ TeV for the ggF event category, and from 214 fb at $m_H = 200$ GeV to 13 fb at $m_H = 1$ TeV for the VBF event category.

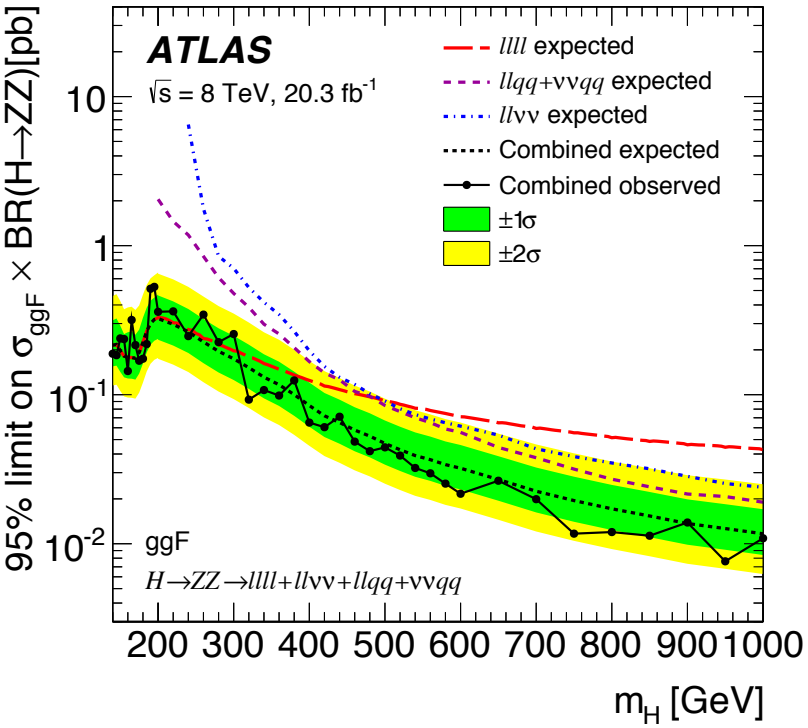

(A)

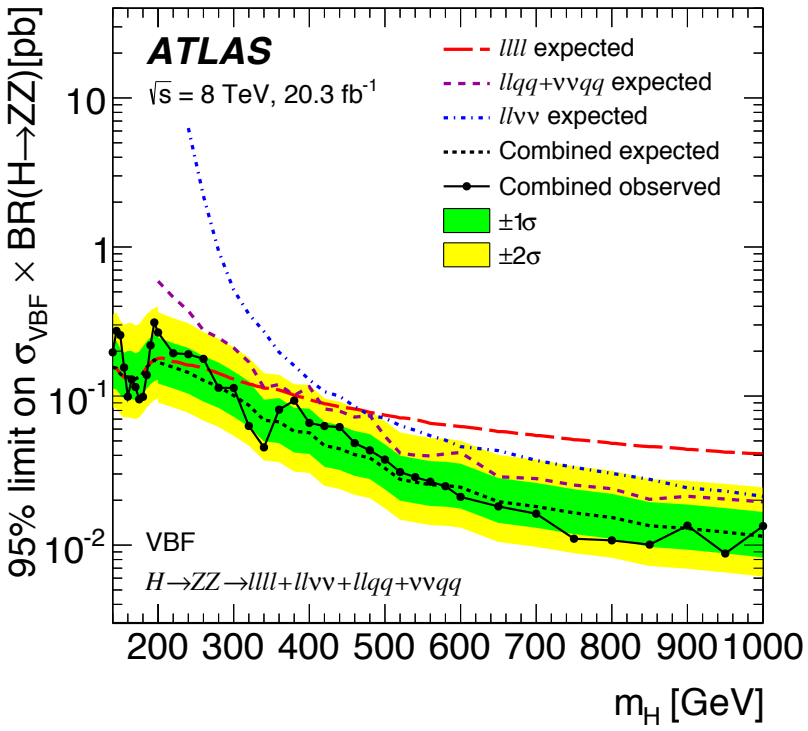

(B)

FIGURE 6.13: 95% CL_S upper limits on $\sigma \times \mathrm{BR}(H \rightarrow ZZ)$ as a function of m_H, resulting from the combination of all four searches in the ggF (A) and VBF (B) event categories. The solid black line and points indicate the observed limit. The dashed black line indicates the expected limit, while the yellow and green the bands represent the 1σ and 2σ uncertainty on the expected limit. The dashed, coloured lines indicate the expected limits obtained from the individual searches.

Table 6.13: Expected and observed limits on $\sigma \times BR(H \to ZZ^{(*)})$ obtained in the ggF event category (left) and the VBF event category (right).

m_H	Limit on $\sigma \times BR(H \to ZZ^{(*)})$ [fb]					
[GeV]	Obs.	Exp.	$+2\sigma$	$+1\sigma$	-1σ	-2σ
140	188	215	459	315	155	115
145	184	217	472	325	157	117
150	239	197	425	291	142	106
155	236	181	374	255	131	97
160	144	178	385	262	128	96
165	317	178	389	265	128	95
170	215	175	370	253	126	94
175	169	192	397	273	138	103
180	174	225	469	328	162	121
185	219	267	545	384	192	143
190	514	300	603	427	216	161
195	529	319	633	448	230	171
200	359	324	648	463	233	174
220	362	296	593	422	213	159
240	247	264	528	375	190	141
260	344	225	455	322	162	121
280	225	195	393	278	140	104
300	255	174	350	248	125	93
320	92	151	304	216	109	81
340	107	131	262	186	94	70
360	98	116	233	166	84	62
380	124	100	200	142	72	53
400	64	84	168	120	60	45
420	60	72	143	102	51	38
440	71	65	129	92	46	34
460	48	57	115	82	41	31
480	41	52	105	75	37	28
500	44	47	94	67	33	25
520	39	42	85	60	30	22
540	32	39	78	55	28	20
560	29	36	73	52	26	19
580	25	33	68	48	24	18
600	21	32	65	45	23	17
650	26	26	54	38	19	14
700	19	22	46	32	16	12
750	11	19	40	28	14	10
800	11	17	35	24	12	9
850	11	15	32	22	11	8
900	13	13	28	19	9	7
950	7	12	26	18	9	6
1000	10	11	25	17	8	6

m_H	Limit on $\sigma \times BR(H \to ZZ)$ [fb]					
[GeV]	Obs.	Exp.	$+2\sigma$	$+1\sigma$	-1σ	-2σ
140	196	156	353	230	112	84
145	273	154	362	234	111	82
150	256	141	321	209	102	76
155	155	134	299	195	96	72
160	99	134	309	201	97	72
165	129	133	309	201	96	71
170	115	130	297	193	94	70
175	95	134	304	199	97	72
180	99	143	330	215	103	77
185	138	156	354	233	112	84
190	219	167	373	247	120	89
195	311	174	389	258	126	94
200	214	135	292	198	97	72
220	161	130	278	189	94	70
240	164	124	265	181	89	66
260	156	112	237	163	80	60
280	102	103	217	150	74	55
300	103	91	193	133	66	49
320	58	79	167	115	57	42
340	42	64	132	88	46	34
360	76	63	130	91	45	33
380	88	54	113	79	39	29
400	64	55	116	80	40	29
420	62	46	96	67	33	24
440	61	44	91	63	31	23
460	48	40	83	58	29	21
480	43	38	79	55	27	20
500	37	32	67	47	23	17
520	30	27	57	39	19	14
540	28	26	54	38	19	14
560	26	25	52	36	18	13
580	24	25	51	36	18	13
600	21	24	50	35	17	13
650	18	19	40	28	14	10
700	16	18	37	26	13	9
750	11	16	33	23	11	8
800	10	15	31	22	11	8
850	10	13	27	19	9	7
900	13	12	26	18	9	6
950	8	12	25	17	8	6
1000	13	11	24	16	8	6

6.7.2 2HDM Interpretation

As explained in Chapter 2, within the context of 2HDM, the ratio of ggF to VBF production depends on the 2HDM parameter space. Reversely, given that the analyses of this chapter segment the data according to ggF and VBF production, the measured ratio of the two can be used to impose limits on the 2HDM parameter space, which is the approach that is employed in this work. Two types of interpretations are performed; direct limits on the $\tan(\beta)$ vs $\cos(\beta-\alpha)$ space, and limits on $\tan(\beta)$ as function of m_H.

The following 2HDM interpretation is limited to the part of the 2HDM parameter space where the NWA is valid. As explained in Chapter 2, the 2HDM Higgs boson H only acquires a narrow width in a subset of the 2HDM parameter space, and furthermore only at certain m_H values. Since the natural width of the heavy Higgs boson in these studies is disguised by the experimental resolution of the four search channels, the maximum allowed width will be determined by the analyses with the best resolution, i.e. the 4ℓ and $2\ell 2q$ decay channels. A threshold of $\Gamma_H = 0.5\%$ of m_H is used as the maximum allowed width at any given point in the 2HDM parameter space – beneath this threshold, the width of the heavy Higgs boson is below the experimental resolution of all decay channels.

Figure 6.14 shows exclusion limits in the $\cos(\beta-\alpha)$ versus $\tan(\beta)$ plane for Type-1 and Type-2 2HDM assuming a heavy Higgs boson with a mass of $m_H = 200$ GeV. This m_H value is chosen such that the assumption of a narrow-width Higgs boson is valid over most of the parameter space, while maintaining the experimental sensitivity at a maximum. When calculating the limits at a given point in the $\cos(\beta-\alpha)$ vs $\tan(\beta)$ space, the relative rate of ggF and VBF production in the fit is set according to the prediction of the 2HDM for that parameter choice. In Figure 6.14, the white regions indicate regions of parameter space not excluded by the present analysis; here, the cross-section predicted by the 2HDM is below the experimental sensitivity. The red hashed area shows the observed exclusion limit, with the solid red line denoting the edge of the excluded region. The dashed, blue line represents the expected exclusion contour, and the shaded bands the 1σ and 2σ uncertainties on the expectation.

Figure 6.15 presents exclusion limits on $\tan(\beta)$ as a function of m_H for both Type-1 and Type-2 2HDM. In this scenario, it is assumed that $\cos(\beta-\alpha) = \pm 0.1$. This point in the 2HDM parameter space is reasonably close to the alignment limit, given that the light Higgs couplings are not changed from their SM values by more than a factor of two. In this figure, the grey area masks regions where the width of the boson is larger than the threshold value and hence theoretically inaccessible.

The results presented above are discussed further in Chapter 8, which summarises the experimental searches of this thesis.

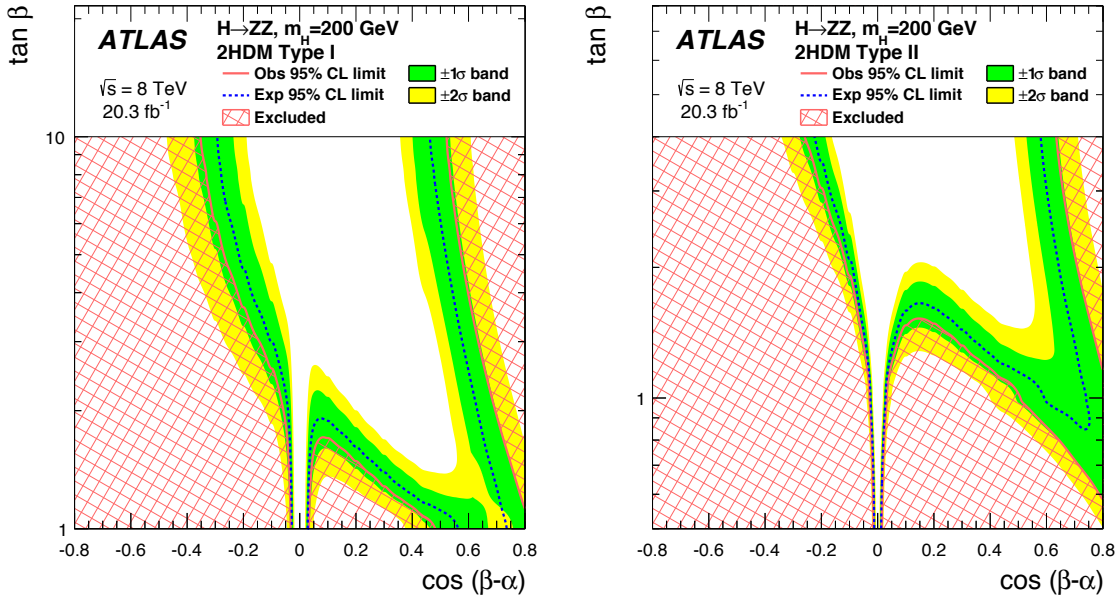

(A) (B)

Figure 6.14: 95% CL_S exclusion contours in the 2HDM Type-1 (A) and Type-2 (B) models for $m_H = 200$ GeV, shown as a function of the parameters $\cos(\beta-\alpha)$ and $\tan(\beta)$. The red, hashed area shows the observed exclusion limit, with the solid red line denoting the edge of the excluded region. The dashed, blue line represents the expected exclusion contour, and the shaded bands the 1σ and 2σ uncertainties on the expectation. The vertical axis range is set such that regions where the light Higgs couplings are enhanced by more than a factor of three from their SM values are avoided.

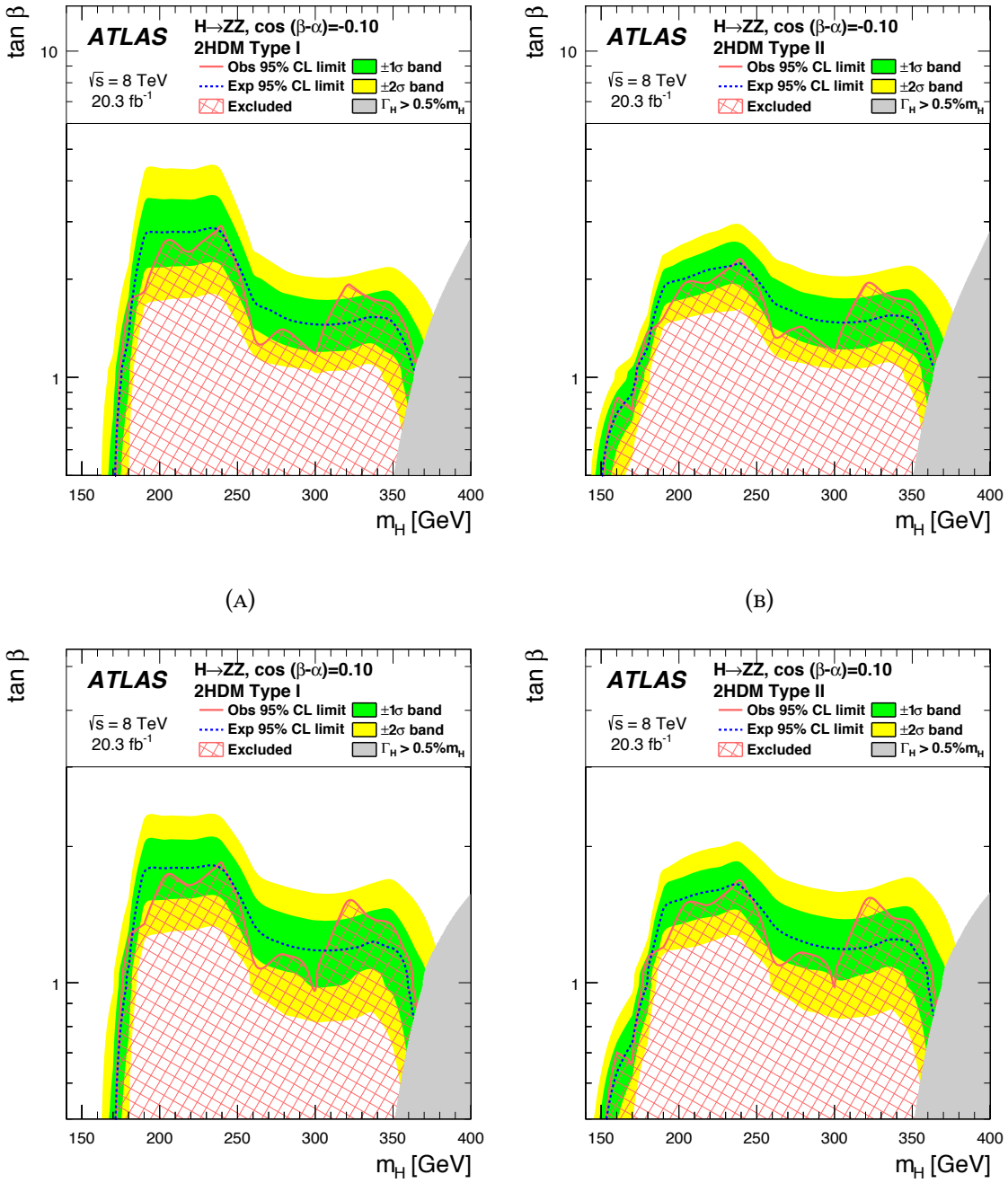

FIGURE 6.15: 95% CL_S exclusion contours in the 2HDM Type-1 (A) and Type-2 (B) models for $\cos(\beta-\alpha)$ = -0.1 and $\cos(\beta-\alpha)$ = 0.1 (C) and (D), shown as a function of m_H and the parameter $\tan(\beta)$. The shaded area shows the observed exclusion, with the black line denoting the edge of the excluded region. The blue line represents the expected exclusion contour and the shaded bands the 1σ and 2σ uncertainties on the expectation. The grey area masks regions where the width of the boson is greater than 0.5% of m_H.

6.8 Conclusion

This chapter presented the combination of heavy Higgs boson searches conducted in the $H \to ZZ^{(*)} \to 4\ell$, $2\ell 2\nu$, $2\ell 2q$ and $2\nu 2q$ decay channels using 20.3 fb^{-1} of pp collision data recorded at $\sqrt{s} = 8$ TeV.

The results of these searches are interpreted in the model-independent scenario of a heavy Higgs boson with a narrow width. In these results, the considered Higgs boson mass range extends up to 1 TeV for all four decay modes and down to as low as 140 GeV with the 4ℓ channel alone. Limits on production and decay of a heavy Higgs boson to two Z bosons are set separately for ggF and VBF production mechanisms. No significant excess of events over the SM prediction is found in either scenario. For the combination of all decay modes, 95% CL_S upper limits range from 359 fb at $m_H = 200$ GeV to 10 fb at $m_H = 1$ TeV for the ggF event category, and from 214 fb at $m_H = 200$ GeV to 13 fb at $m_H = 1$ TeV for the VBF event category.

The results of this search are also interpreted in the context of Type-1 and Type-2 2HDM, with exclusion contours imposed to the $\cos(\beta - \alpha)$ versus $\tan(\beta)$ and m_H versus $\tan(\beta)$ planes for $m_H = 200$ GeV. A discussion of these results within the context of similar searches is given in Chapter 8.

CHAPTER 7

Search for an Additional, Heavy Higgs Boson in the $H \to ZZ^{(*)} \to 4l$ Decay Channel Using $\sqrt{s} = 13$ TeV Data

7.1 Introduction

This chapter presents the continued search for a heavy Higgs boson using the first portions of LHC Run-2 data, more specifically 3.2 fb^{-1} of pp collision data recorded at $\sqrt{s} = 13$ TeV. The following search is a direct continuation of the Run-1 analysis presented in Chapter 5, and thus searches for a heavy, CP-even, Higgs boson with a narrow width in the interval $200 \leq m_H \leq 1000$ GeV, using the $H \to ZZ^{(*)} \to 4\ell$ decay channel. As in Run-1, the analysis consists of applying a sequence of requirements to the data in order to select events compatible with originating from the $H \to ZZ^{(*)} \to 4\ell$ decay, using the four-lepton invariant mass, $m_{4\ell}$ as a discriminant. The final results of this search are presented as upper limits on the heavy Higgs boson production cross-section times $H \to ZZ^{(*)} \to 4\ell$ branching ratio. The analysis strategy from Run-1, including the event selection, background estimation and statistical methodology, is reused in this search. Therefore, only the differences with respect to the Run-1 analysis presented in Chapter 5 will be described here. The changes to this analysis include:

- A new data-set is utilised and different MC generators are used to simulate the signal and backgrounds, as described in Section 7.2 and Section 7.3.
- Updates on the requirements for object reconstruction are implemented in order to accommodate the presence of the IBL, which as described in Chapter 3 was installed before Run-2. This is mentioned in Section 7.4.1

- Updates are implemented in the muon object reconstruction and identification: a "third" muon chain, which employs new reconstruction algorithms and improvements to the existing ones, is integrated, and a new variable, "the $1/p$ significance", is introduced in the identification. Both are described in Section 7.4.2.
- A new set of triggers, including asymmetric di-lepton and tri-lepton triggers, are introduced. These are described in Section 7.4.3.
- The impact parameter significance and isolation requirements are optimised as to yield the highest signal efficiency for the Run-2 operating conditions. This optimisation is described in Section 7.4.4.
- The categorisation of events according to production mechanism is omitted, as described in Section 7.4.5.
- A new method to compute the signal shapes, $f_S(x_e)$, relying on analytical parametrisation, is implemented. This method is described in Section 7.4.6.
- In the modelling of the reducible backgrounds, fewer control regions are used in the estimation of the $\ell\ell\mu\mu$ subcomponents, and a new TRT variable is used to estimate the $\ell\ell ee$ subcomponents. These are described in Section 7.4.8.

7.2 The $\sqrt{s} = 13$ TeV Data-Set

In the first part of the Run-2 period spanning from August 2015 to November 2015 the LHC delivered 4.2 fb^{-1} of pp collision data at $\sqrt{s} = 13$ TeV with 25 ns bunch-spacing. The progress of the LHC data delivery and ATLAS data recording throughout this period is shown in Figure 7.1. As seen, the data-set recorded by ATLAS in this period amounts to 3.9 fb^{-1}. Given the data-taking efficiency of the ATLAS detector systems presented in Table 7.1, 3.2 fb^{-1} is usable for physics analysis. Figure 7.1 also presents the mean number of interactions per bunch-crossing, $\langle\mu\rangle$, in the first portion of Run-2. As observed, this quantity was reduced from $\langle\mu\rangle = 20.7$ in Run-1 to 13.7 in Run-2, happening as a result of decreasing bunch intensity in the latter data-taking period. This difference is taken into account by the pile-up correction procedures implemented in the ATLAS simulation chain, which have been tailored to the new conditions of the Run-2 operating environment.

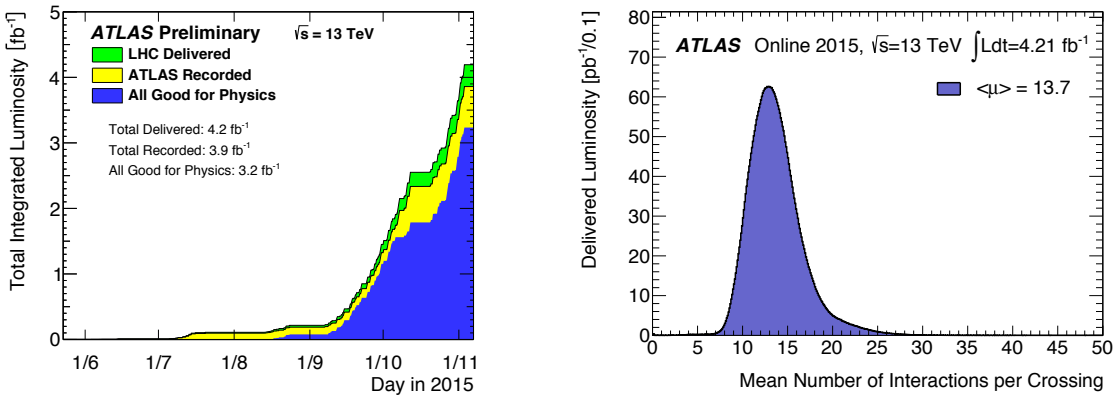

(A) (B)

Figure 7.1: Integrated luminosity versus time delivered by the LHC and recorded by ATLAS (A) among the distribution of $\langle\mu\rangle$ (B) in LHC Run-2 [141].

Table 7.1: Percentage of data recorded during Run-2 by the ATLAS detector systems that is signified as suitable for physics analysis [93]. The lower efficiency for the Pixel detector is related to the IBL being turned off for a period corresponding to 0.2 fb^{-1}.

Inner Detector			**Calorimeters**		**Muon Spectrometer**				**Magnet Systems**	
Pixel	SCT	TRT	LAr	Tile	MDT	RPC	CSC	TGC	Solenoid	Toroids
93.5	99.4	98.3	99.4	100	100	100	100	100	100	97.8
All good for physics: 87.1%										

7.3 Monte Carlo Samples

The generators used to simulate the signal and the background have been changed with respect to Run-1. For the signal, as in Run-1, the simulation of events is done with POWHEG interfaced to PYTHIA and PHOTOS. Now, for both the signal and the backgrounds, the simulated events are interfaced to EVTGEN [142] for the simulation of B-hadron decays. For part of the backgrounds, new event generators are used. This is described in more details in Section 7.4.8.

7.4 Analysis Changes Since Run-1

This section describes the changes implemented to the core of the analysis.

7.4.1 Impact of IBL

The space-point measurements from the newly-installed IBL are integrated into this analysis, a procedure which has the biggest impact on the electron reconstruction. As was the case in Run-1, this analysis employs LOOSE LH electrons. In Run-2, it is required that these electrons have one hit in the IBL in addition to the requirements imposed in Run-1. The IBL improves the precision of the track parameters, specifically it is expected to reduce the error on the transverse impact parameter (d_0), which leads to an improvement in the background rejection since the discriminating power of this variable increases [143]. Furthermore, the presence of the extra detector material from the IBL is accounted for in this analysis by integrating it into the jet calibration procedure.

7.4.2 Muon Reconstruction and Identification

The reconstructed muon types used in this analysis are the same as those in the Run-1 analysis described in Section 5.3.2. A new muon reconstruction chain is utilised, which combines the most advantageous features of the STACO and MUID algorithms mentioned in Chapter 5. In this new reconstruction chain, Hough transforms are used to identify the hit patterns for seeding the segment-finding algorithm, and the calculation of the energy loss in the calorimeter has been updated [144, 145]. When assigning a primary muon type, the new reconstruction chain gives preference to the CB muon type.

Several changes are implemented in the muon identification with respect to Run-1. In this analysis, the acceptance for ST muons is constrained from $|\eta| < 2.7$ to $|\eta| < 0.1$. For CB muons, an additional requirement on a new variable is added to improve the rejection of fakes. These muon candidates, originating from in-flight decays of charged hadrons, often have a kink in their reconstructed track. The direct consequence of this is a poor compatibility between the measured momentum in the ID and the MS, and a poor chi-squared quality of the fit of the combined ID-MS track. These muons can be suppressed with the "$1/p$ significance", which is defined as:

$$\frac{|1/p_{ID} - 1/p_{MS}|}{\sqrt{\sigma_{ID}^2 + \sigma_{ME}^2}} \tag{7.1}$$

Here p_{ID} and p_{MS} is the momentum measured in the ID or MS, respectively, while σ_{ID} and σ_{ME} are the corresponding uncertainties on the momentum measurement. To suppress the number of hadrons misidentified as muons, this variable is required to be < 7.

7.4.3 Triggers

The triggers used in the online selection of this analysis include single-, di- and tri-lepton signatures, the latter being a new feature introduced in Run-2. At low luminosities ($\leq 1{\times}10^{34}$ cm^{-2}s^{-1}), the p_T threshold for single-lepton triggers can be kept at the reasonably low value of ≤ 24 GeV. However, at higher luminosities, increased p_T thresholds are required in order to accommodate the L1 trigger limits, meaning that the trigger selection efficiency for 4ℓ events drops to below 99%. This drop in efficiency can be recuperated by using the tri-lepton ($3e$, $2e1\mu$, $1e2\mu$ and 3μ) triggers. A summary of the triggers used in this analysis is presented in Table 7.2, with the naming conventions from Chapter 5 applying. The trigger efficiencies are $99.4 \pm 0.3\%$ for the $4e$ final-state, $99.2 \pm 0.2\%$ for the 4μ final-state, $99.9 \pm 0.03\%$ for the $2e2\mu$ final-state and $98.9 \pm 0.4\%$ for the $2\mu2e$ final-state.

Table 7.2: Summary of the triggers used during the 2015 data-taking for $4e$, 4μ and mixed final-state, $2e2\mu$. When multiple chains are indicated a logical OR is requested among them. The naming convention follows that of Chapter 5.

Channel	Single-lepton	Di-lepton	Tri-lepton
$4e$	e24_lhmedium_L1EM18VH e24_lhmedium_L1EM20VH e60_lhmedium e120_lhloose	2e12_lhloose_L12EM10VH	e17_lhloose_2e9_lhloose
4μ	mu20_iloose_L1MU15 mu40 mu60_0eta105_msonly	2mu10 mu18_mu8noL1	3mu6 3mu6_msonly mu18_2mu4noL1
$2e2\mu$	$4e$ OR 4μ	$4e$ OR 4μ OR e17_lhloose_mu14 e24_medium_L1EM20VHI_mu8noL1 e7_medium_mu24	$4e$ OR 4μ OR 2e12_lhloose_mu10 e12_lhloose_2mu10

7.4.4 Optimization of Isolation and d_0 Significance

The requirements on lepton isolation and impact parameter (d_0) significance are effective tools to suppress fake muons and electrons. Since fakes appear more frequently in the low-p_T regime, in the Run-2 version of this analysis, the requirements on these variables have been optimised as to maximise the significance in the low-mass region (in the range $120 \leq m_H \leq 130$ GeV) where the contamination is expected to be most severe.

In Run-2, the definition of the calorimetric isolation has been redefined. In Run-1, the calorimetric isolation was defined as the sum of E_T in the calorimeter cells within a cone centred around the lepton direction – a definition which proved very poor pile-up resilience. In Run-2, to improve on this, the definition of the calorimetric isolation instead relies on summing the E_T in the topological cluster surrounding a lepton within a cone of a predefined size [145]. As described in Section 5.3.2.3, since topological clusters already have a minimum requirement imposed on the noise level in the individual calorimeter cells, noise suppression is effectively applied when using topological clusters. This isolation energy is corrected for the contribution from pile-up and the core energy of the lepton is subtracted. When the core energy is subtracted, some remaining electron energy is leaking into the isolation cone – this is subtracted as well. The basic calculation of the track isolation is performed as in Run-1, but with a p_T-dependent cone-size [144].

For muons, for track isolation at a cone-size of $\Delta R < 0.3$, the highest significance is obtained for values smaller than 0.15. The optimal requirement for calorimetric isolation on muons is found to be the same as in Run-1 (less than 0.30), when using a cone-size of $\Delta R < 0.2$. For electrons, using a cone-size of $\Delta R < 0.2$ for both types of isolation, the optimal requirements are found to be less than 0.15 and 0.30 for track and calorimetric isolation, respectively.

The requirements on the impact parameter significance, d_0/σ_{d_0}, for muons and electrons are optimized on the sub-leading di-lepton pair after applying the optimised isolation requirements. The new impact parameter significance requirement is defined as the smallest value that maximises the signal efficiency. For both electrons and muons, the optimal value is found to be $d_0/\sigma_{d_0} < 3.5$. However, as the significance does not vary greatly with the exact value of the requirement, the recommendations provided by the ATLAS combined performance groups are used. Hence, in this analysis, the requirement on d_0/σ_{d_0} is lowered from < 3.5 to < 3.0 for muons and from < 6.5 to < 5 for electrons.

7.4.5 Event Categorisation

Besides the changes in object reconstruction and event selection mentioned above, the baseline selection is kept the same as in Run-1. However, due to limited statistics, the event categorisation does not segment events according to production mechanism. Hence, the results of this search are not presented separately for ggF and VBF, but instead inclusively.

7.4.6 Signal Shape Parametrisation

A major change with respect to the Run-1 analysis is the method used to derive the signal shapes, $f_S(x_e)$. Instead of smoothing MC distributions with the KEYS algorithm and afterwards interpolating these to obtain shapes continuously in m_H, the signal shape is parametrised with an analytical function. This method is advantageous since the shape of the signal template is controlled better than with KEYS (which is highly sensitive to statistical fluctuations in the MC), and because the statistical uncertainties arising due to limited MC statistics can be avoided.

The shape of the narrow signal in the four-lepton final-state is parametrised as the sum of a Crystal Ball line-shape (CB) and a Gaussian (G). The expression for this model is thus given by:

$$f_S(m_{4\ell}) = f_{\mathrm{CB}} \cdot \mathrm{CB}(m_{4\ell};\ \mu,\ \sigma_{\mathrm{CB}},\ \alpha_{\mathrm{CB}},\ n_{\mathrm{CB}}) + (1 - f_{\mathrm{CB}}) \cdot \mathrm{G}(m_{4\ell};\ \mu,\ \sigma_{\mathrm{G}}) \tag{7.2}$$

In this expression, the parameters σ_{CB} and σ_{G} represent the experimental resolution in the individual final-states. The mean value of the distributions, μ, is shared among the two distributions, while the parameter f_{CB} specifies their relative normalisation. The parameters n_{CB} and α_{CB} regulate the shape and position of the non-Gaussian tail of the CB function. The parameters of Equation 7.2 are determined by fitting to fully simulated MC samples at a set of discrete m_H values. This fit is illustrated in Figure 7.2, which shows the signal templates at $m_H = 200$ GeV and 900 GeV in the $4e$, 4μ and $2e2\mu$ final-states. In order to construct shapes that are continuous in m_H, the six free parameters of Equation 7.2 are interpolated between the discrete m_H points as to obtain continuous values. This is done for each individual parameter by imposing a fit to the the values obtained at the discrete m_H points. Examples of the final signal shapes at a spectrum of m_H points are presented in Figure 7.3.

During the development of this method, it was validated that no significant bias is introduced in the signal yield and in the position of the peak. The impact on the yield was investigated with a closure test, which was performed by comparing the signal yield extracted from the integral of the fit and from a simple count of the events going into the fit. This bias was found to be below 3% in all final-states and is hence considered negligible. A second study of this bias was performed by comparing the signal yield obtained with the interpolated values of the parameters with respect to the best-fit values of the parameters at a given mass point. This bias was found to be minor, less than 1%, 2% and 3.5% in the 4μ, $4e$ and $2\mu2e$+$2e2\mu$ final-states, respectively. Correspondingly, the bias on the position of the peak (i.e. the fitted value of m_H) was found to be less than 0.7%, 1% and 0.8% in the 4μ, $4e$ and $2\mu2e$+$2e2\mu$ final-states, respectively, and hence also considered safe to

ignore.

7.4.7 Signal Acceptance

The signal acceptance is estimated using the same MC samples used for the signal shapes, and is defined as the fraction of generated $H \to ZZ^{(*)} \to 4\ell$ events passing the event selection for each final-state. To obtain values for the acceptance continuous in m_H, it is parametrised as a function of m_H with a 2nd order polynomial, separately for each production mechanism and final-state. The acceptance functions for ggF and VBF production are shown in Figure 7.4. As seen in Figure 7.4, the obtained acceptances are very similar for ggF and VBF production. Hence, the acceptance values obtained from the ggF production mechanism will be used in the following.

7.4.8 Background Modelling

This analysis considers the same backgrounds as in Run-1, and the estimation of these is done with the same methods: data-driven techniques are used to estimate the reducible backgrounds separately for the $\ell\ell\mu\mu$ and $\ell\ell ee$ component, while the estimation of the irreducible ZZ continuum is estimated entirely from simulation. The obtained distributions are smoothed with the KEYS algorithm to obtain $f_B(x_e)$. The changes with respect to Run-1 in the background estimation are:

- The estimation of the $\ell\ell\mu\mu$ background is simplified with respect to Run-1 by utilising fewer control regions (CR). At first, to determine the yields from the Z+heavy jets and $t\bar{t}$ components, the inverted impact parameter significance CR and $e\mu$ CR are fitted. Afterwards, in order to estimate the Z+light jets component, the inverted isolation CR is fitted with the yields obtained from the other two CR kept constant. The fit imposed to these three CRs is presented in Figure 7.5. Afterwards, as in Run-1, the yields are extrapolated to the signal region (SR) with transfer factors.

- As in Run-1, the estimation of the $\ell\ell ee$ background component relies on the "3ℓ+X" CR. The three subcomponents of this background, the contribution from photon conversion or FSR photons (γ), from light jets faking an electron (f) and from electrons from heavy-flavoured quark decays (q), are estimated with a template fit to observables from the ID. To do so, the number of B-layer hits, $n_{hits}^{B-layer}$, and the *TRT electron probability*, p_{TRT}^{e}, are used. This latter variable is calculated from the number of high-threshold hits, and replaces the ratio of high-threshold to low-threshold hits (r_{TRT}), which was used in Run-1. The variable $n_{hits}^{B-layer}$ provides discrimination between the γ and f components, as photons populate

$n_{hits}^{B-layer} = 0$ in the distribution, while the p_{TRT}^{e} variable separates γ and q from f. The fits to these variables is presented in Figure 7.6.

- Different generators are used for a subset of the backgrounds. Firstly, the $gg \to ZZ^{(*)}$ background is in this analysis simulated with SHERPA. The Z+jets background is simulated with SHERPA, with alternative samples generated with POWHEG or MADGRAPH interfaced to PYTHIA. Diboson samples are generated with POWHEG interfaced to PYTHIA. The minor contribution from backgrounds originating from tri-boson processes VVV among $t\bar{t}Z$ processes are now included, and estimated entirely from simulation using the SHERPA generator and MADGRAPH interfaced to PYTHIA, respectively. The remaining backgrounds are generated as in Run-1.

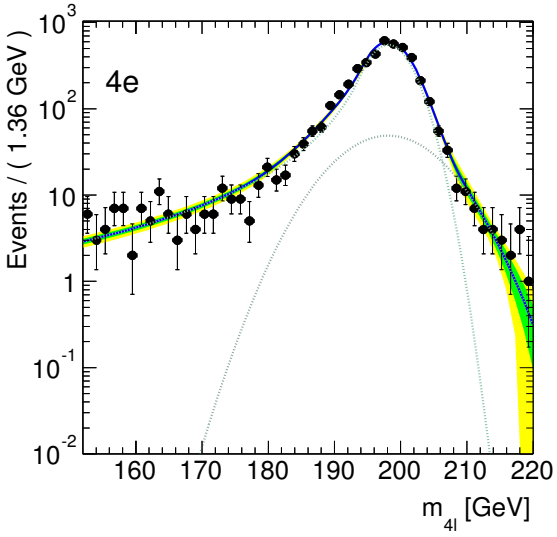

(A) $4e$, $m_H = 200$ GeV

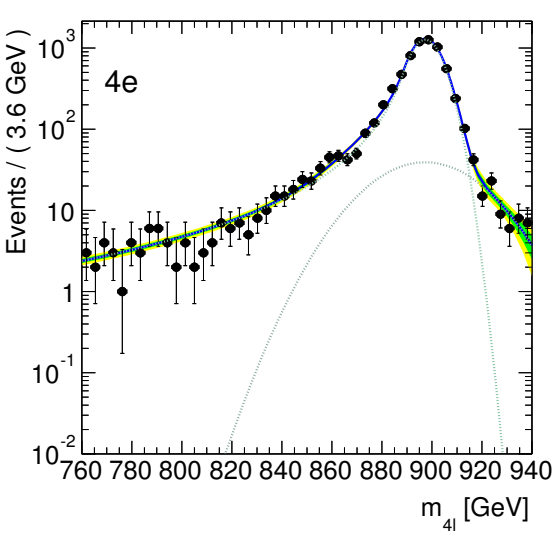

(B) $4e$, $m_H = 900$ GeV

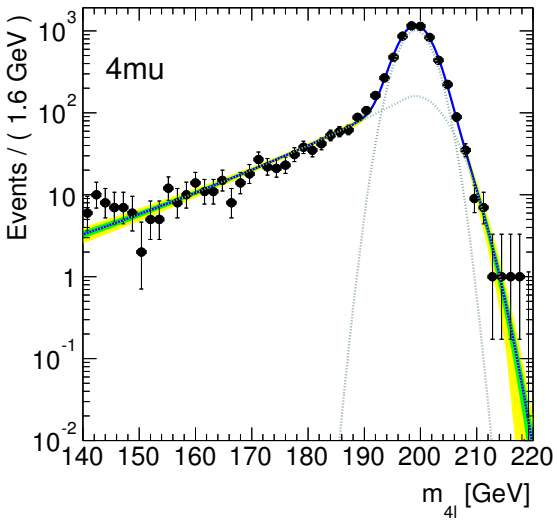

(C) 4μ, $m_H = 200$ GeV

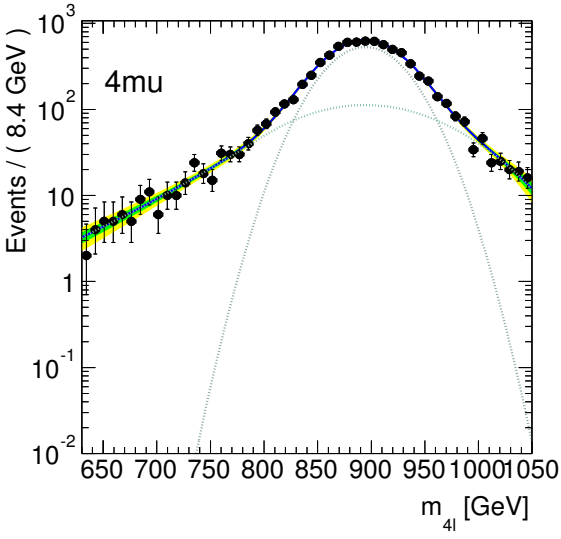

(D) 4μ, $m_H = 900$ GeV

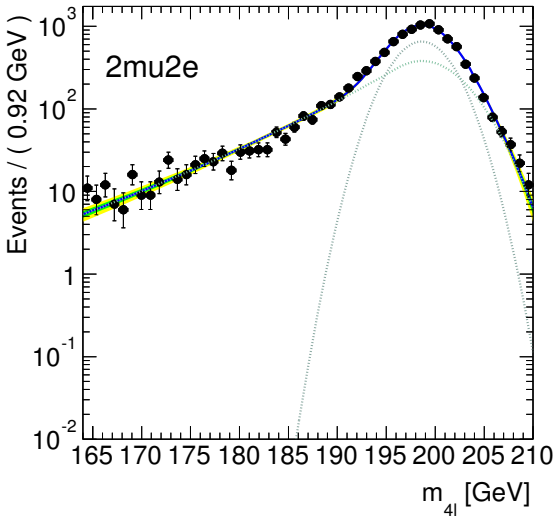

(E) $2e2\mu$, $m_H = 200$ GeV

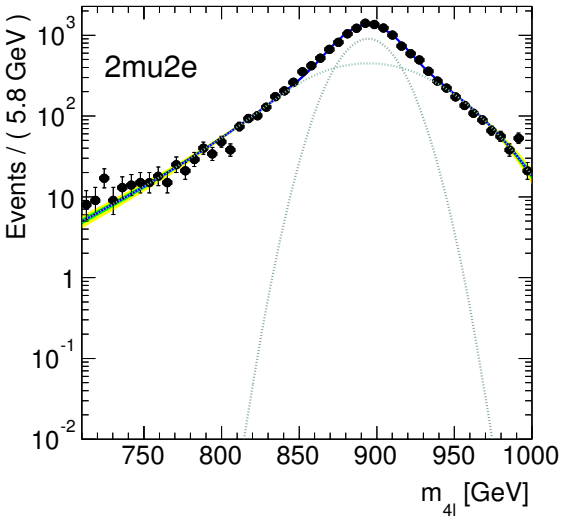

(F) $2e2\mu$, $m_H = 900$ GeV

FIGURE 7.2: The function in Equation 7.2 (blue curve) fitted to MC samples for the $4e$, 4μ and $2e2\mu$ final-states at $m_H = 200$ GeV and 900 GeV. Both the Crystal Ball (dashed green) and Gaussian components (dashed grey) of the fit are shown.

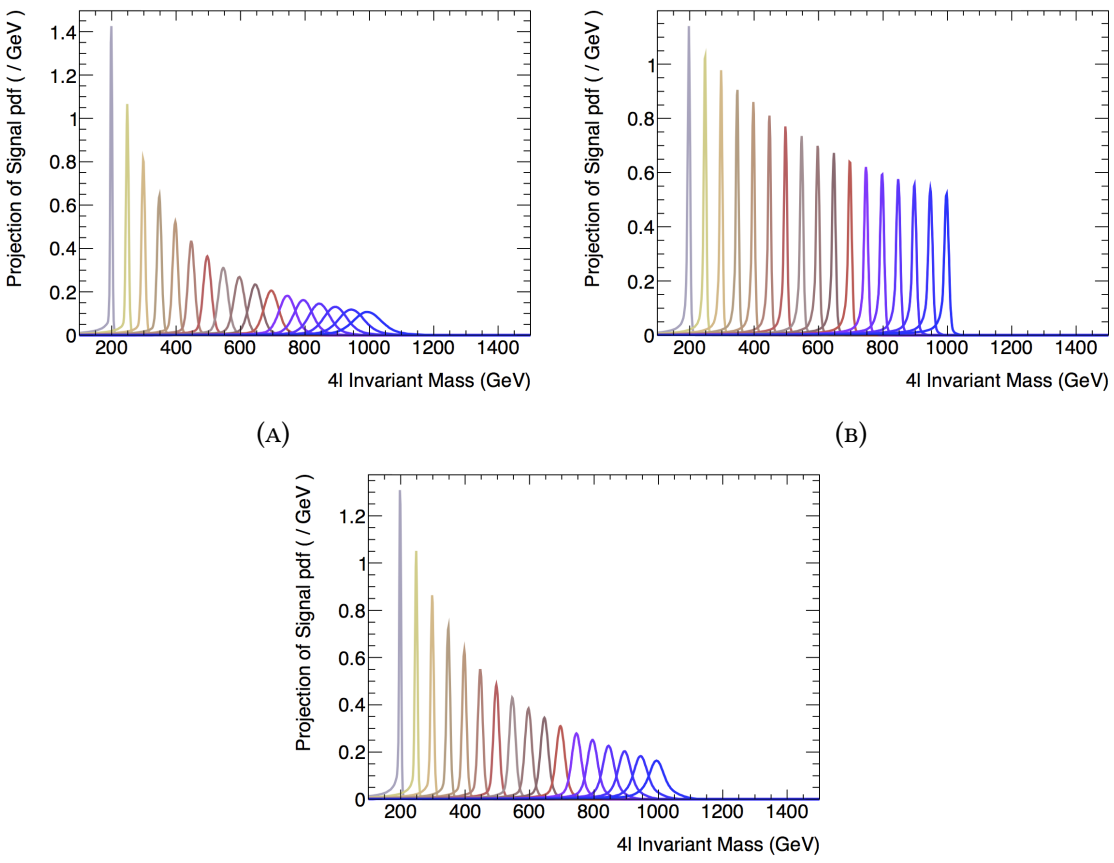

Figure 7.3: Examples of signal shapes $f_S(x_e)$ obtained with the analytical parametrisation at select m_H values for the 4μ final-state (A), the $4e$ final-state (B) and the mixed final-states $2\mu 2e$+$2e2\mu$ (C).

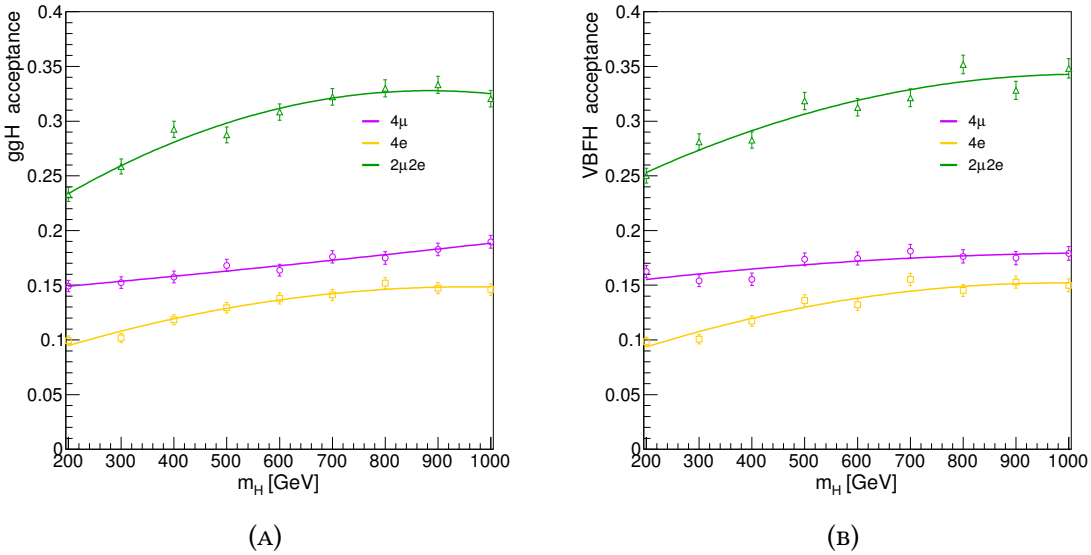

Figure 7.4: The signal acceptance as a function of m_H for ggF (A) and VBF (B) production. For each production mechanism, the acceptance of the final-states is determined separately.

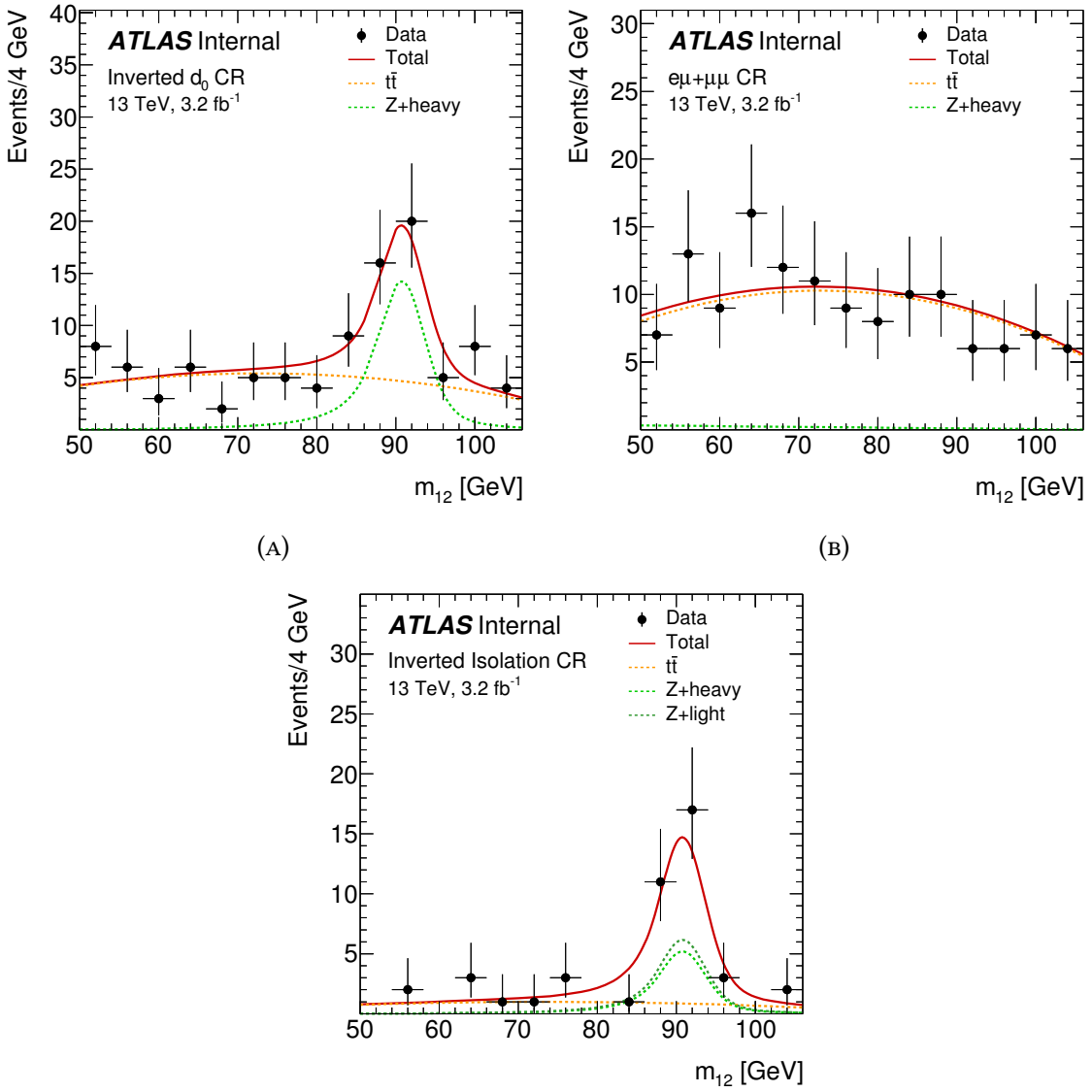

FIGURE 7.5: The observed m_{12} distributions in data in the three control regions described above. The data is fitted simultaneously in the the inverted d_0 (A) and the $e\mu$+$\mu\mu$ (B) CRs. The dashed lines correspond to the Z+heavy jets and $t\bar{t}$ components of the fit. The fitted Z+heavy jets yield is fixed when fitting the inverted isolation CR (C) to extract the yield of the Z+light jets component.

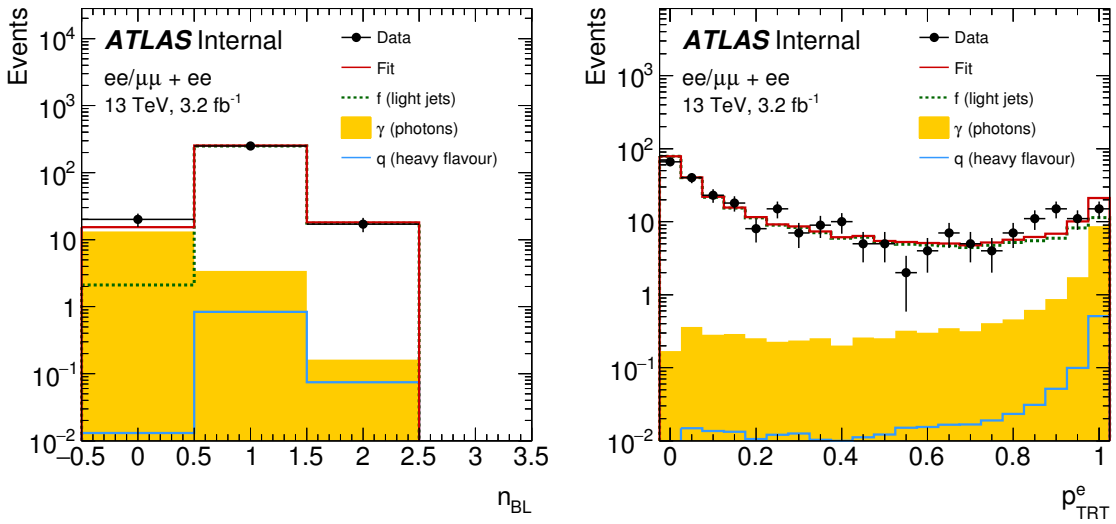

(A) (B)

Figure 7.6: Fits applied to the number of hits in the B-layers, $n_{hits}^{B-layer}$, (A) and the TRT electron probability, p_{TRT}^{e}, (B) for the $4e$ and $2\mu 2e$ final-states. The histograms show the light-flavoured jets mistakenly identified as an electron (f), electrons from photon conversion of from FSR (γ) and electrons from heavy-flavoured quark decays (f).

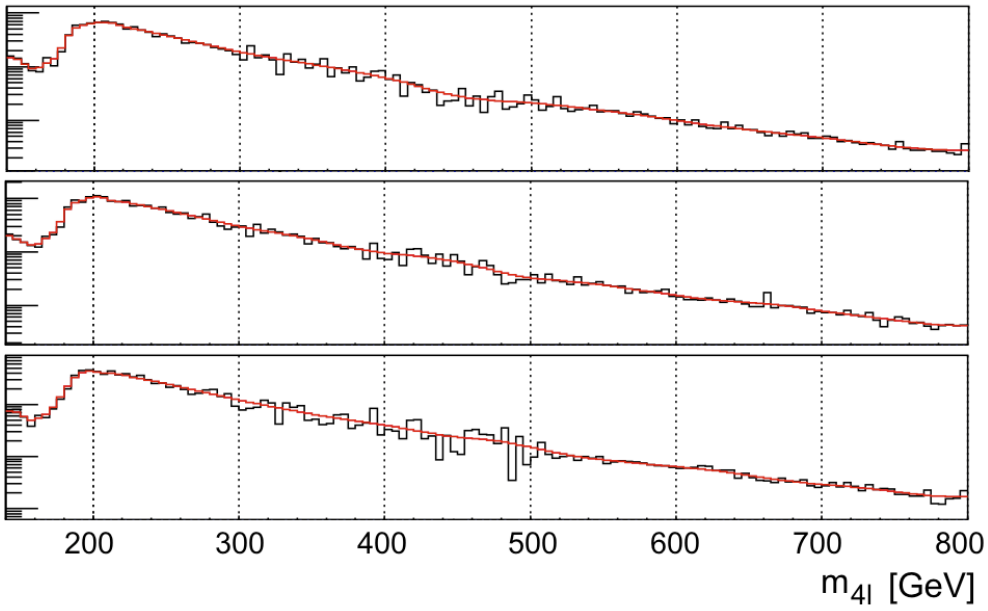

Figure 7.7: Distribution of $m_{4\ell}$ obtained from the irreducible ZZ background for the 4μ (top), $2e2\mu$+$2\mu 2e$ (middle) and $4e$ (bottom) final-states. The red line represents the smoothed shape obtained with KEYS.

7.4.9 Systematic Uncertainties

Given the great similarity with the Run-1 analysis, the vast majority of the included experimental and theoretical uncertainties are the same as in Run-1. The few that differ are described below.

7.4.9.1 Signal Shape Uncertainties

In the analytical signal shape parametrisation, uncertainties are assigned to the individual parameters of the analytical function. These systematic uncertainties are determined by re-doing the fit with Equation 7.2 on the MC samples containing systematic variations, meaning that each systematic variation gives rise to an uncertainty on each of the parameters in Equation 7.2. In addition to this, the impact on the signal yield and peak position from each of these variations is derived as well. The impact on the number of signal events is found to be 3.5% at maximum, while the impact on the position of the peak reaches maximum at 1%. A summary of the effect from the experimental systematic uncertainties on these two quantities is provided in Table 7.3. These numbers are cross checked with a second approach, in which the fits are imposed to the MC samples containing the systematic variations, but where all the parameters of $f_S(x_e)$ are kept constant, except the number of signal events and the mean of the distributions. The second approach yielded variations comparable to the first method.

7.4.10 Systematic Rankings

Figures 7.8 to Figure 7.10 present the ranking of the 10 dominant systematic uncertainties performed with Asimov data. These figures follow the same principles and conventions as those presented in Section 5.7. The ranking is performed with Asimov data generated with $\mu = 0$ at $m_H = 300$ GeV, 600 GeV and 900 GeV. At these three mass points, the uncertainty on the integrated luminosity (`ATLAS_lumi_2015`) is the dominant source of uncertainty, followed closely by the theoretical uncertainties on the background, such as the uncertainty on the $gg \to ZZ^{(*)}$ k-factor (`QCDscale_ggVV`) and PDF uncertainty on the $q\bar{q} \to ZZ^{(*)}$ background (`pdf_qq`). At all three mass points, no anomalies in terms of pulls or over-constraints are observed. As was the case in the Run-1 analysis, due to μ obtaining a very small value in the fit to data, the ranking on data is not included here.

Table 7.3: Summary of the effects of the experimental systematic uncertainties on the signal yield and on the peak position, expressed in %, on the 4μ, $4e$ and $2\mu 2e$ final-states. MUON_MS, MUON_MS_RES_ID and MUON_MS_RES_MS denote the muon momentum scale uncertainty and the momentum resolution uncertainty in the ID and MS, respectively. EG_SCALE and EG_RESOLUTION denote the uncertainty on the electron energy scale and on the electron energy resolution, respectively.

	4μ	
Uncertainty	Impact on yield (%)	Impact on peak position (%)
MUON_MS_RES_ID	2.5	0.2
MUON_MS_RES_MS	0.6	0.1
MUON_MS	0.2	0.1
	$4e$	
Uncertainty	Impact on yield (%)	Impact on peak position (%)
EG_SCALE	0.5	0.6
EG_RESOLUTION	0.3	0.1
	$2\mu 2e$	
Uncertainty	Impact on yield (%)	Impact on peak position (%)
EG_SCALE	0.2	0.3
EG_RESOLUTION	0.1	0.1
MUON_MS_RES_ID	1.5	0.1
MUON_MS_RES_MS	0.5	0.1
MUON_MS	0.1	0.1

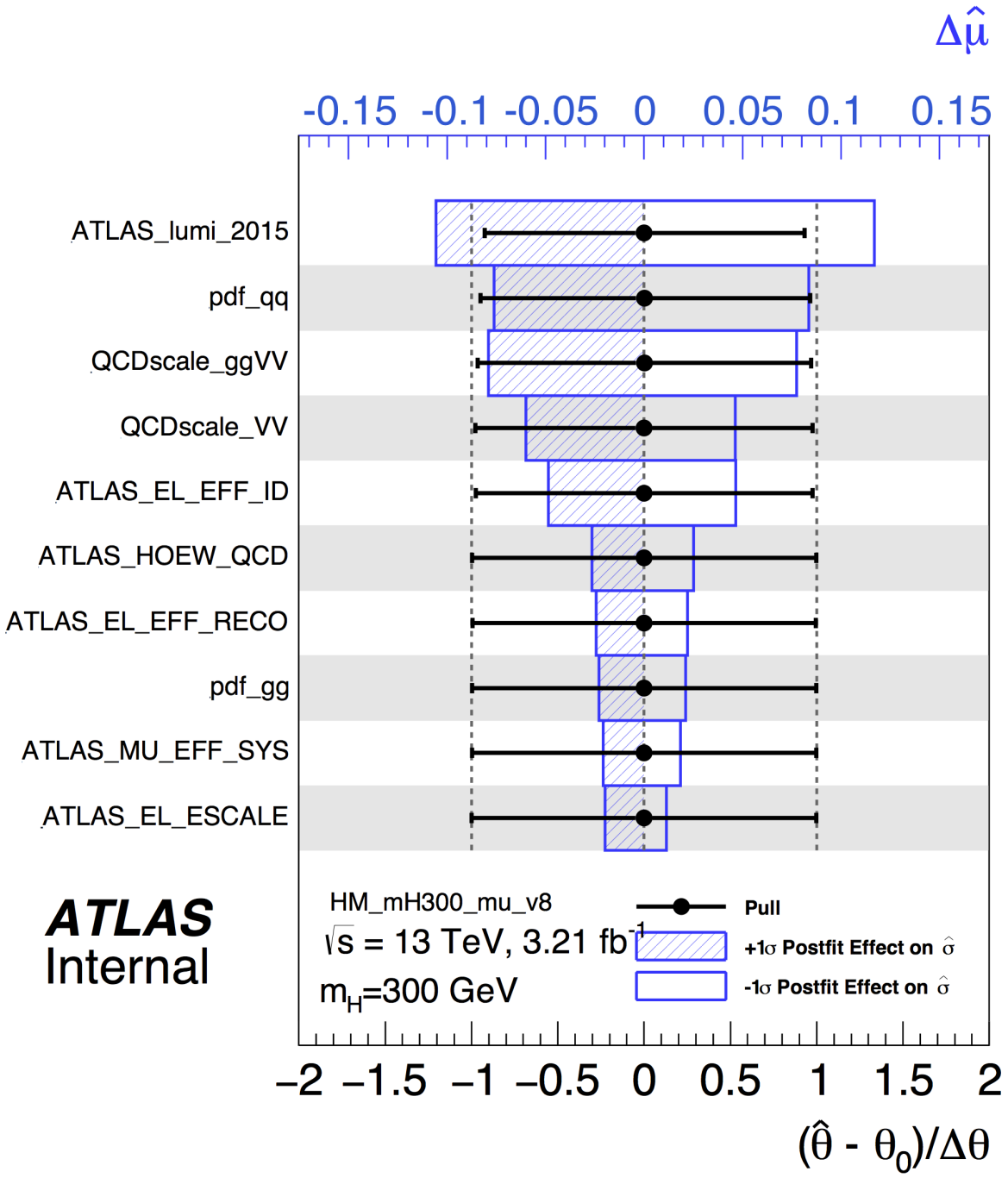

FIGURE 7.8: Nuisance parameter ranking performed with Asimov data generated at $\mu = 0$ at $m_H = 300$ GeV.

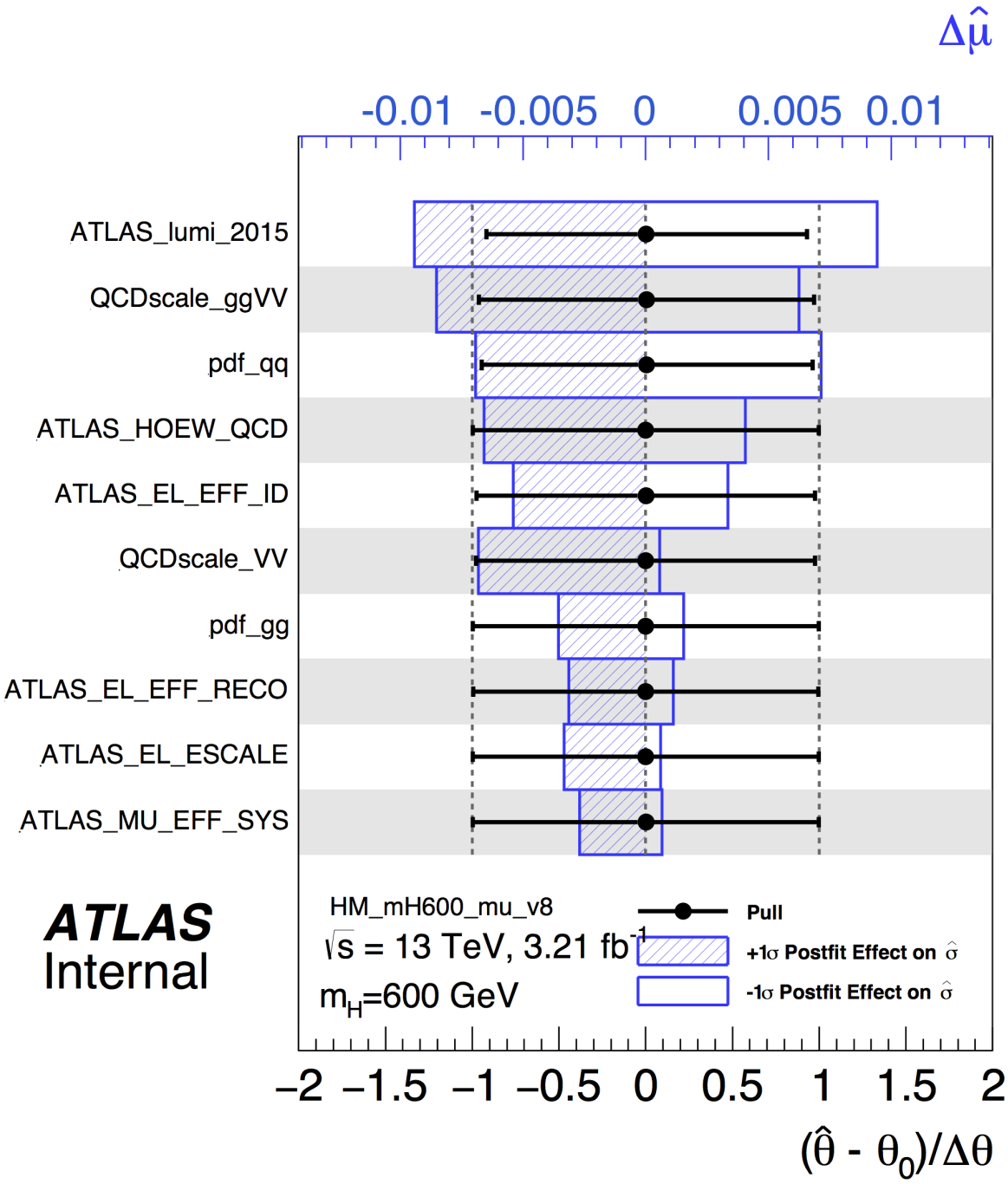

Figure 7.9: Nuisance parameter ranking performed with Asimov data generated at $\mu = 0$ at $m_H = 600$ GeV.

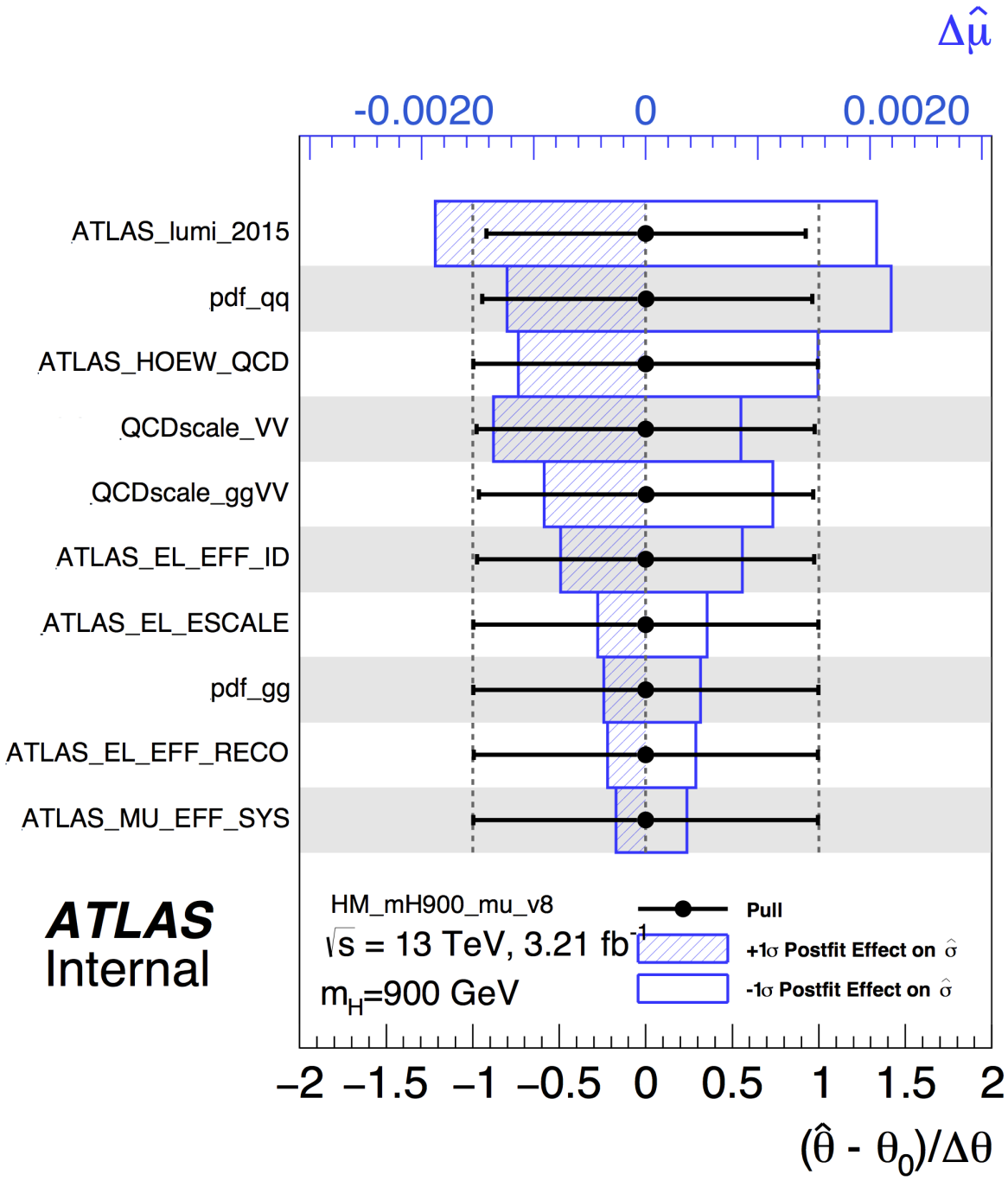

FIGURE 7.10: Nuisance parameter ranking performed with Asimov data generated at $\mu = 0$ at $m_H = 900$ GeV.

7.5 Results

This section presents the results of the search, in terms of upper limits on the heavy Higgs boson production cross-section times $H \to ZZ^{(*)} \to 4\ell$ branching ratio.

7.5.1 Post-fit Yields and Distributions

Figure 7.11 presents the post-fit $m_{4\ell}$ distributions obtained with data and MC for the individual final-states and inclusively. The obtained post-fit yields are presented in Table 7.11. A few noticeable excesses are present: around $m_H = 450$ GeV in the $4e$, $2e2\mu$ and $2\mu2e$ final-state, and around $m_H = 600$ GeV and 700 GeV in the $4e$ and $2\mu2e$ final-states, respectively. Deficits occur at low mass, $m_H < 300$ GeV, in all final-states. Overall deficits are observed in the yields of the $4e$ and $2\mu2e$ final-states, which propagate to the inclusive event count for all final-states.

Table 7.4: Expected and observed events yields for the four-lepton final-states obtained in this search over the full considered mass range. The expected yields are shown post-fit for an integrated luminosity of 3.2 fb^{-1} at $\sqrt{s} = 13$ TeV.

Channel	$ZZ^{(*)}$	Z+jets, $t\bar{t}$, WZ	ttV,VVV	Total	Observed
4μ	22.1 ± 2.2	0.05 ± 0.02	0.23 ± 0.01	22.4 ± 2.2	20
$2e2\mu$	16.9 ± 1.6	0.05 ± 0.02	0.21 ± 0.01	17.2 ± 1.6	17
$2\mu2e$	18.1 ± 2.6	0.06 ± 0.02	0.19 ± 0.01	18.3 ± 2.6	13
$4e$	13.9 ± 2.1	0.06 ± 0.02	0.18 ± 0.01	14.1 ± 2.1	12
Total	71.0 ± 7.7	0.23 ± 0.04	0.81 ± 0.04	72.1 ± 7.7	62

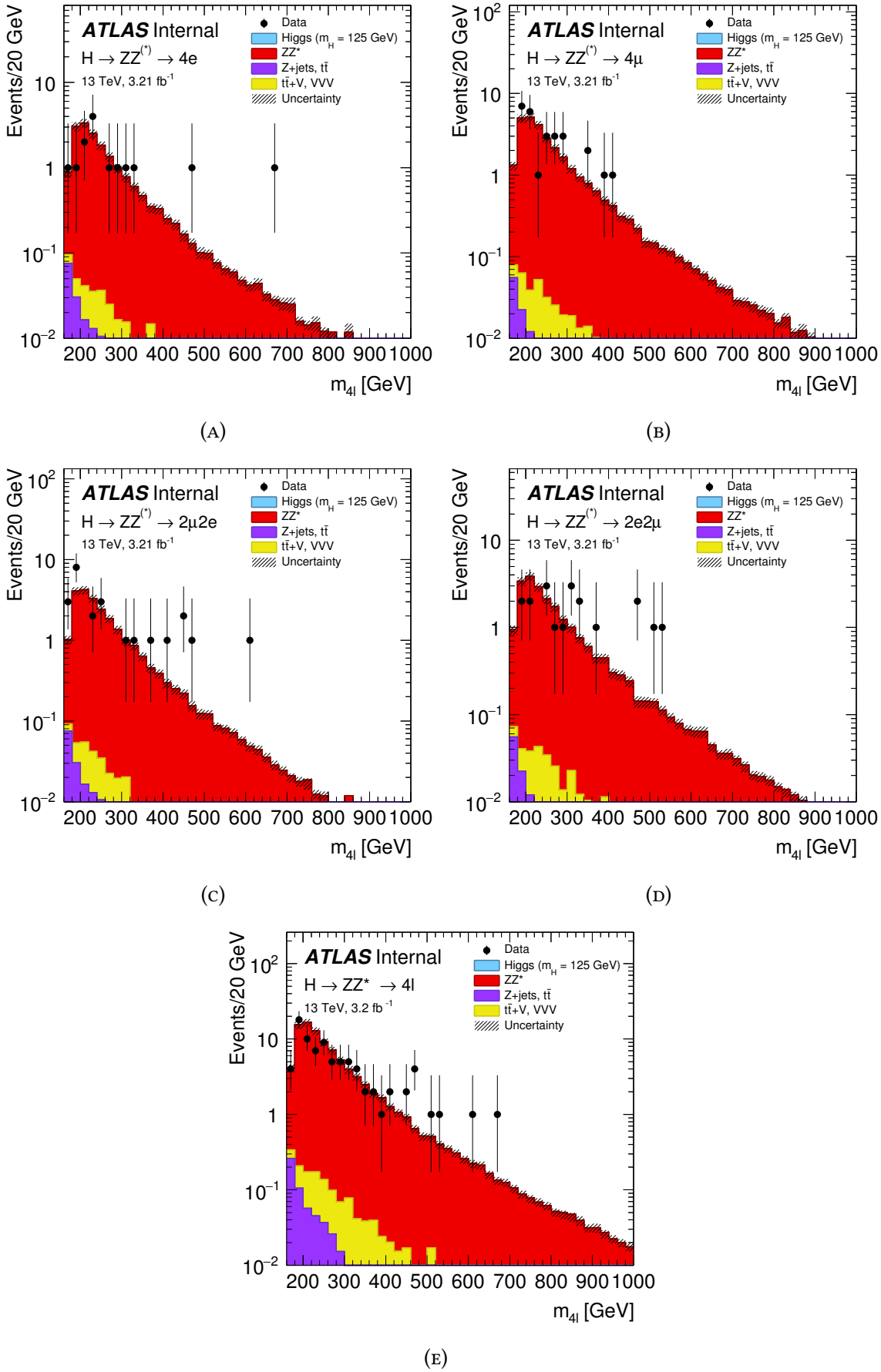

FIGURE 7.11: Post-fit $m_{4\ell}$ distributions broken down according to final-state: $4e$ (A), 4μ (B), $2\mu 2e$ (C), $2e2\mu$ (D) and inclusively (E). The hashed band on the MC distributions represent the systematic uncertainty on the expectation.

7.5.2 Upper Limits on Heavy Higgs Boson Production Rate

The results of this analysis are expressed as upper limits on the heavy Higgs boson production cross-section times the $H \to ZZ^{(*)} \to 4\ell$ branching ratio. The limits are computed with the CL_S procedure described in Section 5.7. Since this analysis does not include dedicated ggF and VBF event categories, only one POI, μ, is present in the fit. Figure 7.12 presents the obtained limits produced with a m_H step-size of 5 GeV, while Table 7.5 and Table 7.6 presents the numerical limits.

As seen from Figure 7.12, over the majority of the mass range, the observed limit is well within the 1σ bands. Around $m_H = 450$ GeV an excursion into the 2σ band is present, which is driven by the excess observed at this mass points in the $4e$, $2e2\mu$ and $2\mu2e$ final-states. Furthermore, deficits are seen in the observed limit at masses below 300 GeV, which are driven by the slight deficits observed in Figure 7.11. The 95% CL_S upper limits range from 4.6 fb at $m_H = 200$ GeV to 1.0 fb at $m_H = 1$ TeV. The results are discussed further in Chapter 8.

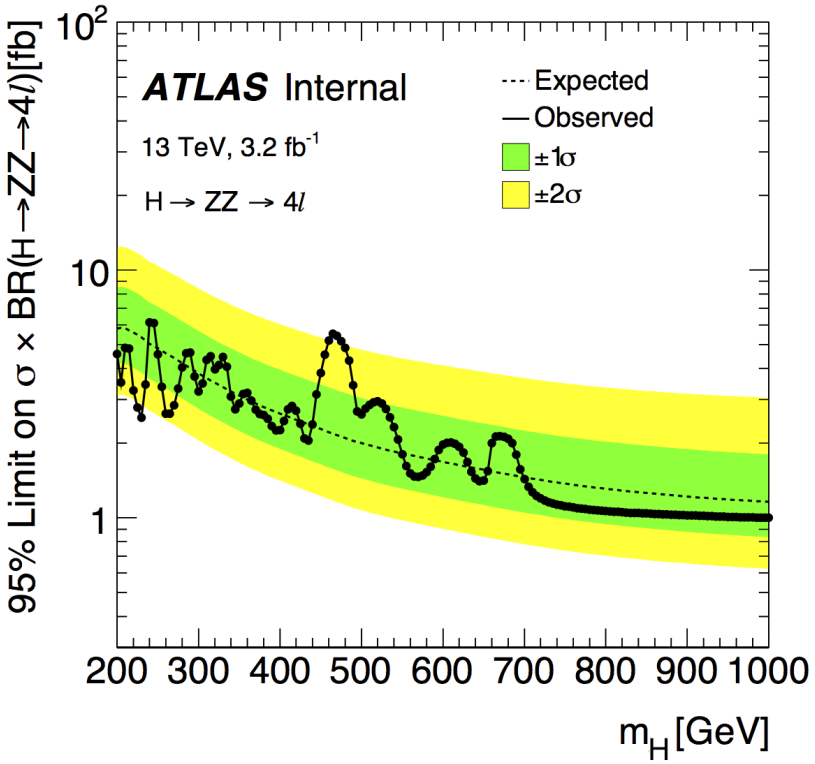

Figure 7.12: 95% CL_S upper limits on $\sigma \times BR(H \to ZZ^{(*)} \to 4\ell)$ as a function of m_H. The solid black line and points indicate the observed limit. The dashed black line indicates the expected limit and the bands the 1σ and 2σ uncertainty ranges about the expected limit.

TABLE 7.5: Expected and observed limits on $\sigma \times BR(H \to ZZ^{(*)} \to 4\ell)$ in fb.

m_H	Limit on $\sigma \times BR(H \to ZZ^{(*)} \to 4\ell)$ [fb]					
[GeV]	Obs.	Exp.	$+2\sigma$	$+1\sigma$	-1σ	-2σ
200	4.59	5.81	12.32	8.50	4.18	3.12
205	3.52	5.85	12.41	8.56	4.21	3.14
210	4.85	5.81	12.35	8.51	4.19	3.12
215	4.82	5.71	12.14	8.36	4.11	3.06
220	3.26	5.60	11.92	8.20	4.03	3.00
225	2.78	5.48	11.70	8.04	3.95	2.94
230	2.54	5.35	11.43	7.85	3.85	2.87
235	3.45	5.19	11.11	7.61	3.74	2.78
240	6.15	5.04	10.82	7.40	3.63	2.71
245	6.10	4.93	10.60	7.25	3.55	2.65
250	4.56	4.83	10.40	7.10	3.48	2.59
255	3.38	4.72	10.18	6.95	3.40	2.53
260	2.63	4.62	9.97	6.80	3.33	2.48
265	2.63	4.51	9.77	6.65	3.25	2.42
270	2.84	4.41	9.56	6.50	3.18	2.37
275	3.32	4.31	9.36	6.36	3.10	2.31
280	4.04	4.21	9.17	6.22	3.03	2.26
285	4.60	4.11	8.97	6.08	2.96	2.21
290	4.64	4.02	8.78	5.94	2.89	2.16
295	3.71	3.92	8.60	5.81	2.83	2.11
300	3.23	3.83	8.42	5.68	2.76	2.06
305	3.48	3.75	8.25	5.55	2.70	2.01
310	4.34	3.66	8.09	5.43	2.64	1.97
315	4.49	3.58	7.93	5.32	2.58	1.92
320	3.98	3.51	7.78	5.21	2.53	1.88
325	4.14	3.44	7.64	5.11	2.48	1.84
330	4.46	3.37	7.50	5.01	2.43	1.81
335	4.07	3.30	7.37	4.91	2.38	1.77
340	3.09	3.24	7.24	4.82	2.33	1.74
345	2.74	3.17	7.12	4.73	2.29	1.70
350	2.89	3.11	7.00	4.65	2.24	1.67
355	3.16	3.05	6.88	4.56	2.20	1.64
360	3.19	3.00	6.77	4.48	2.16	1.61
365	2.97	2.95	6.66	4.40	2.12	1.58
370	2.73	2.89	6.56	4.33	2.09	1.55
375	2.63	2.85	6.47	4.26	2.05	1.53
380	2.60	2.80	6.37	4.20	2.02	1.50
385	2.51	2.76	6.29	4.13	1.99	1.48
390	2.35	2.71	6.20	4.07	1.96	1.46
395	2.25	2.67	6.12	4.01	1.93	1.43

m_H	Limit on $\sigma \times BR(H \to ZZ^{(*)} \to 4\ell)$ [fb]					
[GeV]	Obs.	Exp.	$+2\sigma$	$+1\sigma$	-1σ	-2σ
400	2.26	2.63	6.04	3.96	1.90	1.41
405	2.46	2.60	5.96	3.90	1.87	1.39
410	2.75	2.56	5.89	3.85	1.84	1.37
415	2.82	2.52	5.82	3.79	1.82	1.35
420	2.70	2.49	5.74	3.74	1.79	1.33
425	2.39	2.45	5.67	3.69	1.77	1.31
430	2.09	2.42	5.60	3.64	1.74	1.30
435	2.05	2.38	5.53	3.59	1.72	1.28
440	2.38	2.35	5.47	3.55	1.69	1.26
445	3.15	2.31	5.40	3.50	1.67	1.24
450	3.85	2.28	5.33	3.45	1.64	1.22
455	4.55	2.25	5.27	3.40	1.62	1.21
460	5.19	2.22	5.21	3.36	1.60	1.19
465	5.54	2.19	5.14	3.31	1.57	1.17
470	5.42	2.16	5.08	3.27	1.55	1.16
475	5.16	2.13	5.02	3.23	1.53	1.14
480	4.85	2.10	4.97	3.19	1.51	1.13
485	4.32	2.07	4.91	3.15	1.49	1.11
490	3.42	2.05	4.86	3.11	1.47	1.10
495	2.69	2.02	4.81	3.08	1.46	1.09
500	2.61	2.00	4.77	3.04	1.44	1.07
505	2.76	1.98	4.73	3.01	1.43	1.06
510	2.85	1.96	4.69	2.98	1.41	1.05
515	2.92	1.94	4.65	2.96	1.40	1.04
520	2.95	1.92	4.61	2.93	1.38	1.03
525	2.89	1.90	4.57	2.90	1.37	1.02
530	2.75	1.89	4.53	2.88	1.36	1.01
535	2.54	1.87	4.50	2.85	1.35	1.00
540	2.32	1.85	4.47	2.83	1.33	0.99
545	2.07	1.83	4.43	2.80	1.32	0.98
550	1.80	1.82	4.40	2.78	1.31	0.98
555	1.62	1.81	4.37	2.76	1.30	0.97
560	1.51	1.79	4.34	2.74	1.29	0.96
565	1.47	1.78	4.31	2.72	1.28	0.95
570	1.46	1.76	4.29	2.70	1.27	0.95
575	1.48	1.75	4.26	2.68	1.26	0.94
580	1.53	1.74	4.23	2.66	1.25	0.93
585	1.61	1.72	4.20	2.64	1.24	0.92
590	1.73	1.71	4.17	2.62	1.23	0.92
595	1.88	1.69	4.15	2.60	1.22	0.91

Table 7.6: Expected and observed limits on $\sigma \times BR(H \to ZZ^{(*)} \to 4\ell)$ in fb.

m_H	Limit on $\sigma \times BR(H \to ZZ^{(*)} \to 4\ell)$ [fb]					
[GeV]	Obs.	Exp.	$+2\sigma$	$+1\sigma$	-1σ	-2σ
600	1.98	1.68	4.12	2.58	1.21	0.90
605	2.01	1.67	4.09	2.56	1.20	0.90
610	2.02	1.66	4.07	2.54	1.19	0.89
615	1.99	1.64	4.05	2.52	1.18	0.88
620	1.93	1.63	4.02	2.51	1.18	0.88
625	1.83	1.62	4.00	2.49	1.17	0.87
630	1.68	1.61	3.97	2.47	1.16	0.86
635	1.54	1.60	3.95	2.45	1.15	0.86
640	1.44	1.58	3.92	2.44	1.14	0.85
645	1.40	1.57	3.90	2.42	1.13	0.84
650	1.41	1.56	3.88	2.40	1.13	0.84
655	1.54	1.55	3.85	2.39	1.12	0.83
660	2.00	1.54	3.83	2.37	1.11	0.83
665	2.13	1.53	3.81	2.35	1.10	0.82
670	2.14	1.52	3.79	2.34	1.09	0.81
675	2.12	1.51	3.76	2.32	1.09	0.81
680	2.09	1.50	3.74	2.31	1.08	0.80
685	2.00	1.49	3.72	2.29	1.07	0.80
690	1.80	1.48	3.70	2.28	1.06	0.79
695	1.57	1.47	3.68	2.26	1.06	0.79
700	1.43	1.46	3.66	2.25	1.05	0.78
705	1.34	1.45	3.64	2.23	1.04	0.78
710	1.27	1.44	3.62	2.22	1.04	0.77
715	1.23	1.43	3.60	2.21	1.03	0.77
720	1.20	1.42	3.59	2.19	1.02	0.76
725	1.17	1.41	3.57	2.18	1.02	0.76
730	1.16	1.40	3.55	2.17	1.01	0.75
735	1.14	1.40	3.53	2.16	1.01	0.75
740	1.13	1.39	3.52	2.15	1.00	0.75
745	1.12	1.38	3.50	2.13	1.00	0.74
750	1.11	1.37	3.49	2.12	0.99	0.74
755	1.11	1.37	3.47	2.11	0.98	0.73
760	1.10	1.36	3.46	2.10	0.98	0.73
765	1.09	1.35	3.44	2.09	0.97	0.73
770	1.09	1.35	3.43	2.08	0.97	0.72
775	1.08	1.34	3.42	2.07	0.97	0.72
780	1.08	1.33	3.40	2.06	0.96	0.72
785	1.08	1.33	3.39	2.05	0.96	0.71
790	1.07	1.32	3.38	2.04	0.95	0.71
795	1.07	1.32	3.37	2.04	0.95	0.71
800	1.07	1.31	3.35	2.03	0.94	0.70
805	1.06	1.30	3.34	2.02	0.94	0.70
810	1.06	1.30	3.33	2.01	0.94	0.70
815	1.06	1.29	3.32	2.01	0.93	0.69
820	1.05	1.29	3.31	2.00	0.93	0.69
825	1.05	1.28	3.30	1.99	0.92	0.69
830	1.05	1.28	3.29	1.98	0.92	0.69
835	1.05	1.27	3.28	1.98	0.92	0.68
840	1.04	1.27	3.27	1.97	0.91	0.68
845	1.04	1.26	3.26	1.96	0.91	0.68
850	1.04	1.26	3.25	1.95	0.91	0.68
855	1.04	1.25	3.24	1.95	0.90	0.67
860	1.04	1.25	3.23	1.94	0.90	0.67
865	1.04	1.25	3.22	1.94	0.90	0.67
870	1.03	1.24	3.21	1.93	0.89	0.67
875	1.03	1.24	3.21	1.92	0.89	0.66
880	1.03	1.23	3.20	1.92	0.89	0.66
885	1.03	1.23	3.19	1.91	0.89	0.66
890	1.03	1.23	3.18	1.91	0.88	0.66
895	1.03	1.22	3.17	1.90	0.88	0.66
900	1.02	1.22	3.17	1.89	0.88	0.65
905	1.02	1.21	3.16	1.89	0.88	0.65
910	1.02	1.21	3.15	1.88	0.87	0.65
915	1.02	1.21	3.15	1.88	0.87	0.65
920	1.02	1.20	3.14	1.87	0.87	0.65
925	1.02	1.20	3.13	1.87	0.87	0.64
930	1.01	1.20	3.13	1.86	0.86	0.64
935	1.01	1.19	3.12	1.85	0.86	0.64
940	1.01	1.19	3.11	1.85	0.86	0.64
945	1.01	1.19	3.11	1.85	0.86	0.64
950	1.01	1.19	3.10	1.84	0.85	0.64
955	1.01	1.18	3.10	1.84	0.85	0.63
960	1.01	1.18	3.09	1.83	0.85	0.63
965	1.01	1.18	3.09	1.83	0.85	0.63
970	1.01	1.18	3.08	1.83	0.85	0.63
975	1.00	1.17	3.08	1.82	0.84	0.63
980	1.00	1.17	3.07	1.82	0.84	0.63
985	1.00	1.17	3.07	1.81	0.84	0.63
990	1.00	1.17	3.06	1.81	0.84	0.63
995	1.00	1.16	3.06	1.81	0.84	0.62
1000	1.00	1.16	3.05	1.80	0.84	0.62

7.6 Conclusion and Further Work

A search for an additional heavy Higgs boson in the $H \rightarrow ZZ^{(*)} \rightarrow 4\ell$ decay channel was conducted in the interval $140 < m_H < 1000$ GeV using the Narrow Width Approximation. This analysis employed 3.2 fb^{-1} of pp collision data recorded at $\sqrt{s} = 13$ TeV, and is such one of the first completed analyses conducted by ATLAS with Run-2 data. The final results of this search were expressed as model-independent upper limits on the heavy Higgs boson production cross-section times branching ratio. No indications of a heavy Higgs boson was observed, and 95% CL_S limits were set on $\sigma \times BR(H \rightarrow ZZ^{(*)} \rightarrow 4\ell)$ ranging from 4.6 fb at $m_H = 200$ GeV to 1.0 fb at $m_H = 1$ TeV.

The results from this search, among a projection using additional Run-2 data, are discussed in Chapter 8.

CHAPTER 8

Conclusion of Heavy Higgs Boson Searches

8.1 Summary

The three previous chapters presented searches for a heavy, CP-even, electrically neutral Higgs boson in the interval $140 < m_H < 1000$. Despite targeting a resonance with close resemblance to the 2HDM Higgs boson H, the presented analyses employed a model-independent search strategy. This was enforced by using the Narrow Width Approximation (NWA), and by, as far as possible, segmenting the data into event categories distinguished by likeness to the ggF or VBF production mechanism.

In the first search presented in Chapter 5, the heavy Higgs boson search was conducted in the $H \to ZZ^{(*)} \to 4\ell$ decay channel. This search utilised 20.3 fb^{-1} of pp collision data recorded at $\sqrt{s} = 8$ TeV. The results of this search were presented as model-independent upper limits on the heavy Higgs boson production cross-section times $H \to ZZ^{(*)}$ branching ratio separately for the ggF and VBF production. The event rates obtained in this search were compatible with the background predictions and no excess was observed. For the ggF mode, a 95% CL$_S$ upper limit of 330 fb was set at $m_H = 200$ GeV and of 38 fb at $m_H = 1$ TeV with an expected limit ranging from 329 fb to 43 fb. The corresponding limit obtained for the VBF mode was 277 fb at $m_H = 200$ GeV and 35 fb at $m_H = 1$ TeV with expected limits ranging from 179 fb to 41 fb.

In the second analysis of this thesis described in Chapter 6, the search in the $H \to ZZ^{(*)} \to 4\ell$ decay channel was combined with corresponding searches performed with the three additional $H \to ZZ^{(*)}$ search channels: $2\ell 2\nu$, $2\ell 2q$ and 2ν2q. The outcome of this analysis was model-independent upper limits on the heavy Higgs boson production rate, among a 2HDM interpretation. For the model-independent results, no indiction of a heavy Higgs boson was observed. For the ggF event category, a 95% CL$_S$ upper limit was set from 359 fb at $m_H = 200$ GeV to 10 fb at $m_H = 1$ TeV with expected limits ranging from 324 fb to 11 fb. In the VBF event category, the

upper limit was set from 214 fb at $m_H = 200$ GeV to 13 fb at $m_H = 1$ TeV with expected limits from 135 fb to 11 fb. The results of this search were furthermore interpreted in the context of Type-1 and Type-2 2HDM. Here, exclusion contours were given on the $\cos(\beta - \alpha)$ vs. $\tan(\beta)$ and m_H versus $\tan(\beta)$ planes for $m_H = 200$ GeV. The comparison of these results to corresponding searches is discussed below.

The third analysis of this thesis outlined in Chapter 7 presented the continued search for a heavy Higgs boson in the $H \to ZZ^{(*)} \to 4\ell$ decay channel using 3.2 fb^{-1} of pp collision data recorded at $\sqrt{s} = 13$ TeV. This search constituted one of the first completed analyses performed by ATLAS with Run-2 data. This search relied on the existing analysis framework and strategy from the corresponding Run-1 search, meaning that only few changes were implemented. A single, inclusive event category was used, and results were presented as upper limits on the heavy Higgs boson production rate. No indication of a heavy Higgs boson was observed, and a 95% CL_S upper limit was set on $\sigma \times BR(H \to ZZ^{(*)} \to 4\ell)$ ranging from 4.5 fb at $m_H = 200$ GeV to 1 fb at $m_H = 1$ TeV, with an expected limit from 5.81 fb to 1.16 fb.

8.1.1 Comparison of Combined Run-1 Results

The model-independent results presented in Chapter 6 are not directly comparable with the previous corresponding search results from ATLAS performed with $\sqrt{s} = 7$ TeV data [87, 88, 89] because these assumed that the relative rate of ggF and VBF production was fixed to the prediction from the SM, which contradicts the approach employed in Chapter 6 allowing for the relative rates of ggF and VBF production to vary independently.

The complimentary heavy Higgs boson search performed by CMS with Run-1 data relied on a data-set consisting of 5.1 fb^{-1} recorded at $\sqrt{s} = 7$ TeV and 19.7 fb^{-1} recorded at $\sqrt{s} = 8$ TeV [146]. This search used the $WW \to \ell\nu\ell\nu$ and $WW \to \ell\nu qq$ decay channels, and also the ZZ decay channels used by ATLAS, excluding the $2\nu 2q$ decay channel. The results from this analysis cannot be directly compared to those presented in Chapter 6 for the same reason as described above.

The results of Chapter 6 are comparable to similar results produced by ATLAS in the corresponding search for a narrow, heavy Higgs boson in the $H \to WW$ decay channel [147], which was performed with the same data-set. In this search, by using the two WW decay channels mentioned above, model-independent upper limits were set on the heavy Higgs boson production rate in the NWA separately for ggF and VBF production. At $m_H = 300$ GeV, the obtained upper limits on $\sigma \times BR(H \to WW)$ were 830 fb for the ggF production mode and 240 fb for the VBF production mode. For the highest mass point tested in the search, $m_H = 1500$ GeV, the upper limits were 22

fb for the ggF mechanism and 6.6 fb for the VBF mechanism. As such, the ZZ search is more sensitive at low mass, while the sensitivity of the WW decay channel is comparable at higher mass. A combination of the ZZ channels with the WW decay channels would enhance the sensitivity further.

The 2HDM results obtained from the combined searches in Chapter 6 can be compared to indirect limits obtained from the coupling measurements of the SM Higgs boson. Compared to recent studies of indirect limits [148], the exclusion limits presented in Chapter 6 are considerably more stringent for Type-1 with $\cos(\beta-\alpha) < 0$ and $1 < \tan(\beta) < 2$, and for Type-2 with $0.5 < \tan(\beta) < 2$.

8.1.2 Sensitivity Comparison of the H → ZZ$^{(*)}$ → 4l Searches

Although the fundamentals of the two searches performed in the $H \to ZZ^{(*)} \to 4\ell$ decay channels differ, a comparison of their sensitivity can be performed with a simple back-of-the-envelope calculation relying on the results presented in Chapter 5 and Chapter 7. The calculation is performed by computing the number of signal events, S, in a benchmark scenario at a given value of m_H, and the number of background events, B, in a window around the signal of $m_H \pm 50$ GeV. For this simplified study, the production cross-section of the SM Higgs boson will be used as a benchmark for the signal.

The number of signal events at a given mass point is obtained from the cross-section values documented by the LHC Higgs Cross-Section Working Group at $\sqrt{s} = 8$ TeV and $\sqrt{s} = 13$ TeV [36]. Only ggF and VBF production will be considered in this projection. The number of Higgs bosons present in the 4ℓ final-state is calculated by multiplying the produced number of Higgs bosons per fb^{-1} with $BR(H \to ZZ^{(*)} \to 4\ell)$ (where $\ell = e, \mu$), and afterwards with the acceptance of the signal obtained in the two individual searches. For the Run-1 search, as an approximation of the ggF and VBF acceptance presented in Figure 5.8, a conservative value of 10% is applied across all m_H points. Correspondingly, a flat acceptance of 15% is applied for the Run-2 search as an approximation of Figure 7.4. For simplicity, no separation is done between events originating from the ggF and VBF production mechanisms, nor between events in the various 4ℓ final-states. The obtained number of signal events per fb^{-1} for a select number of m_H points is presented in Table 8.1 for $\sqrt{s} = 8$ TeV and Table 8.2 for $\sqrt{s} = 13$ TeV.

Only the $q\bar{q} \to ZZ^{(*)}$ and $gg \to ZZ^{(*)}$ processes are considered in this rough estimation, since these as demonstrated largely dominate. The number of events originating from these two processes are obtained in a range of $m_H \pm 50$ GeV from the simulated samples presented in Chapter 5 and Chapter 7 after applying the full event selection. In order to normalise the yield of these

processes to units of 1 fb^{-1}, the obtained number of events is divided by the integrated luminosity employed in the respective analyses. The obtained number of background events per fb^{-1} at $\sqrt{s} = 8$ TeV and $\sqrt{s} = 13$ TeV are presented in Table 8.1 and Table 8.2, respectively.

The sensitivity of the heavy Higgs boson search in the $H \to ZZ^{(*)} \to 4\ell$ decay channel with Run-1 and Run-2 data can be compared from Table 8.1 and Table 8.2. As seen, the S/B ratio with 21.3 fb^{-1} of data recorded at $\sqrt{s} = 8$ TeV is larger than that obtained with 3.2 fb^{-1} recorded at $\sqrt{s} = 13$ TeV at all the considered m_H values. At lower m_H, the S/B ratio from the Run-1 search is around twice as large as the value from the Run-2 search, however, this difference converges at larger m_H values. Table 8.3 presents the S/B ratio per fb^{-1} obtained at $\sqrt{s} = 13$ TeV divided by the corresponding quantity obtained at $\sqrt{s} = 8$ TeV. As observed, the S/B ratio obtained at $\sqrt{s} = 13$ TeV with 1 fb^{-1} is around 3 – 5 times larger than with the $\sqrt{s} = 8$ TeV data, meaning that the Run-2 search will obtain a sensitivity that is comparable to the Run-1 search with around 8 fb^{-1} at $m_H = 200$ GeV and around 4 fb^{-1} at $m_H = 1000$ GeV.

TABLE 8.1: Obtained number of signal (S) and background (B) events at $\sqrt{s} = 8$ TeV at select m_H values. S is calculated from the SM Higgs boson production cross-section obtained from the LHC Higgs Cross-Section Working Group [36], multiplied with the signal acceptance obtained in Chapter 5. B is calculated from the simulation of the $q\bar{q} \to ZZ^{(*)}$ and $gg \to ZZ^{(*)}$ backgrounds in Chapter 5 in a window around the signal of $m_H \pm 50$ GeV.

m_H [GeV]	S per fb^{-1}	B per fb^{-1}	S / B per fb^{-1}	S / B with 21.3 fb^{-1}
200	0.93	9.79	0.095	2.01
300	0.54	3.90	0.14	2.93
400	0.39	0.94	0.42	8.89
500	0.17	0.34	0.50	10.7
600	0.076	0.15	0.51	10.8
700	0.036	0.071	0.50	10.6
800	0.018	0.041	0.45	9.57
900	0.0097	0.023	0.42	9.01

TABLE 8.2: Obtained number of signal (S) and background (B) events at $\sqrt{s} = 13$ TeV at select m_H values. S is calculated from the SM Higgs boson production cross-section obtained from the LHC Higgs Cross-Section Working Group [36], multiplied with the signal acceptance obtained in Chapter 7. B is calculated from the simulation of the $q\bar{q} \to ZZ^{(*)}$ and $gg \to ZZ^{(*)}$ backgrounds in Chapter 7 in a window around the signal of $m_H \pm 50$ GeV.

m_H [GeV]	S per fb^{-1}	B per fb^{-1}	S / B per fb^{-1}	S / B with 3.2 fb^{-1}
200	3.52	14.09	0.25	0.80
300	2.30	5.62	0.41	1.31
400	1.86	1.36	1.37	4.40
500	0.89	0.49	1.82	5.83
600	0.43	0.21	2.02	6.45
700	0.22	0.10	2.17	6.94
800	0.12	0.058	2.13	6.81
900	0.072	0.033	2.19	7.00

TABLE 8.3: S/B ratio per fb^{-1} at $\sqrt{s} = 13$ TeV divided by the corresponding quantity obtained at $\sqrt{s} = 8$ TeV.

m_H [GeV]	$\frac{\text{S / B per fb}^{-1} \text{ at } \sqrt{s}=13 \text{ TeV}}{\text{S / B per fb}^{-1} \text{ at } \sqrt{s}=8 \text{ TeV}}$
200	2.64
300	2.98
400	3.29
500	3.63
600	3.98
700	4.35
800	4.74
900	5.17

CHAPTER 9

Characterization of Run-2 Minimum Bias Trigger Scintillators

9.1 Introduction

As mentioned in Chapter 3, the ATLAS MBTS fulfil the task of level-1 (L1) triggering on charged particles from low-intensity collisions with a minimal bias on the signature of the event. This ability is crucial for multiple physics tasks, such as luminosity determination [149], heavy ion physics [150] and the measurement of the inelastic proton-proton cross-section [151, 152]. Furthermore, the study of minimum bias and underlying event properties is a necessity for fundamental measurements such as determining the charged particle multiplicity, underlying event characteristics and rapidity gap [153, 154], which are used to characterise the Monte Carlo simulation tunes required to get the most precise predictions for close to all ATLAS analyses. In addition, the MBTS can be used for timing in physics analyses, since a time measurement relative to the LHC clock can be determined for both sides of ATLAS, which can be used to reject out of time signals corresponding to non-collision background or collisions between satellite bunches [150].

During Run-1, the MBTS were exposed to a radiation dose corresponding to 10^4 Gy [76]. This heavy dose significantly impaired the basic functionality due to transparency degradation of the scintillating medium. Because of this irreversible damage, the MBTS underwent a full replacement before the start of Run-2. In this chapter, the characterisation of a Run-2 MBTS counter with cosmic radiation is presented.

9.1.1 Objectives

All of the physics tasks listed above require triggering with excellent efficiency. As explained in Chapter 3, a MBTS signal is passed to the L1 trigger if it is above the threshold of the discriminator it is being read out with. When adjusting this threshold, a compromise must be made between noise suppression and efficiency; a high threshold might suppress noise, but may potentially also suppress the real signals coming from the detector – vice versa with a low threshold. In this context, the strength of a signal is quantified as the light yield coming from the MBTS counter. In order to determine the optimal discriminator threshold for the Run-2 counters, it was highly desirable to characterise the response from a MBTS counter before integration into ATLAS and thereby the full TileCal readout chain. Such a characterisation was the main motivation for the studies presented in the following. Therefore, light yield determination was performed with the two components of the MBTS requiring separate read-out, i.e. the inner and outer sector.

Another important objective concerned determining how many wavelength shifting fibers (WLS) as a minimum should be used in the read-out of the outer sector of the MBTS. As will be explained further below, the outer sector of the Run-2 MBTS can be read out with either 4 or 8 WLS. However, at the time of these studies it had not been verified experimentally if the former option would result in a light yield sufficient enough to distinguish the detector signals from the baseline. This matter was determined by measuring the light yield of the outer counter with both 4 and 8 WLS.

As the studies progressed, a third objective appeared. It was quickly realised that the clear fibers intended for guiding the light from the MBTS to the photomultipliers in the TileCal drawer attenuated the light significantly more than expected. Therefore, a series of measurements were performed to determine the attenuation length of the clear fibers and hence determine if these were suited for installation in ATLAS. This was done by measuring the response of the MBTS with different lengths of clear fiber.

Furthermore, in addition to the original three objectives, the measurements listed above were used to assess the basic performance of the detector and consistency between its behaviour and the predictions from its layout.

9.1.2 Author's Contribution

The studies presented in this chapter were conducted by the author under close supervision of collaborator Sune Jakobsen. In addition, the studies were planned and continuously discussed

with the TileCal community, in particular Ana Henriques, Oleg Solovyanov and Irene Vichou. In addition to being documented in this thesis, the studies of this chapter are documented in [76, 77].

9.2 Run-2 Upgrades of the MBTS

The Run-2 MBTS counters deploy the same geometry as the Run-1 version and facilitate the existing read-out scheme. However, several changes are implemented in the layout. The coverage is increased from 2.12< $|\eta|$ <3.85 to 2.07< $|\eta|$ <3.86, and the granularity of each wedge is reduced by merging the two-parted outer sectors into one piece. In addition, as illustrated in Figure 9.1, an updated routing scheme of the wavelength-shifting optical fibers (WLS) embedded in the scintillating material assures a more uniform detector response. Like in Run-1, the light from the outer sector of each MBTS wedge is collected with 8 WLS, which in Run-2 are divided into bundles of 4 on each surface of the scintillating tile. This new arrangement enhances the operational flexibility; in the early phases of Run-2, while the emitted amount of light is still plentiful, 4 WLS are predicted to be enough to collect a sufficient amount of light. However, once radiation damage has degraded the scintillator transparency, the light yield can be recuperated by opting for all 8 WLS in the read-out. When only 4 WLS are in use in the outer sectors, two neighbouring sectors share a PMT with 8 fiber inputs – this decreases the number of PMTs used by each MBTS disk from 16 to 12. As in Run-1, light will be transported to the PMTs with clear optical fibers. The scintillating material of a Run-2 MBTS is shown in Figure 9.2 and Figure 9.3.

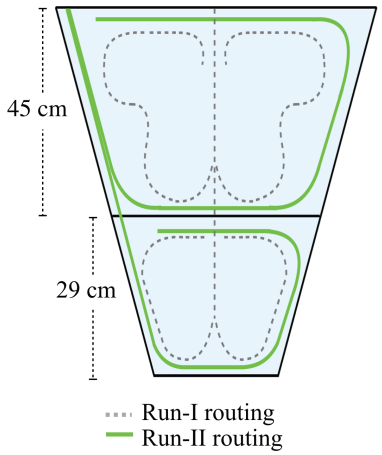

Figure 9.1: Layout of the Run-1 and Run-2 WLS routing scheme in the inner and outer sector of each MBTS wedge.

9.3 Calibrating the Photomultiplier to One Photoelectron

Once integrated into ATLAS, the MBTS will be read out with TileCal electronics. In the following measurements, it was desirable to remove any effects coming from these electronics on the light yield from the counter, and fewest possible components were hence used for read-out in the experimental setup. An 8-stage Hamamatsu PMT operated with a custom-made TileCal voltage divider (VD) was used to extract the signal from the MBTS, in this way avoiding the use of the full TileCal read-out chain. Two configurations of PMT and VD, specified in Table 9.1, were used. Both configurations were calibrated by determining the response induced by a single photoelectron (1PE).

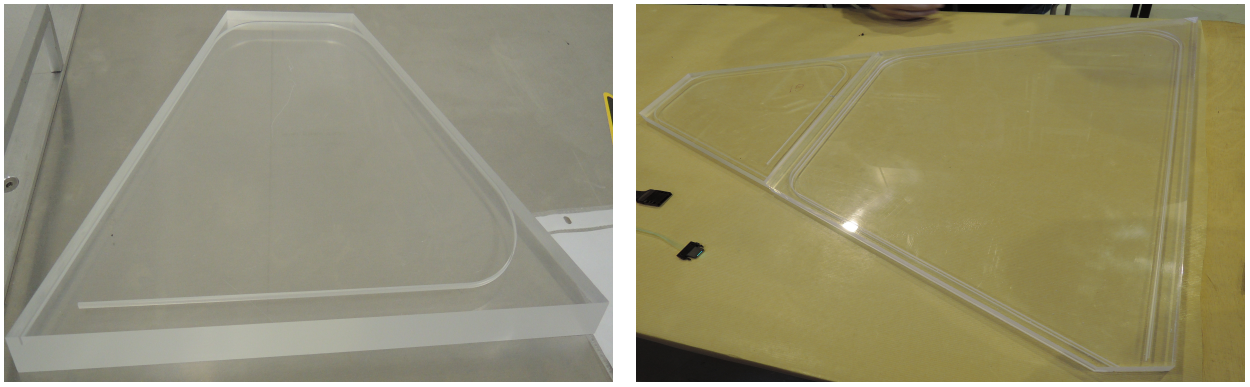

(A) (B)

FIGURE 9.2: The detecting medium from a Run-2 MBTS wedge.

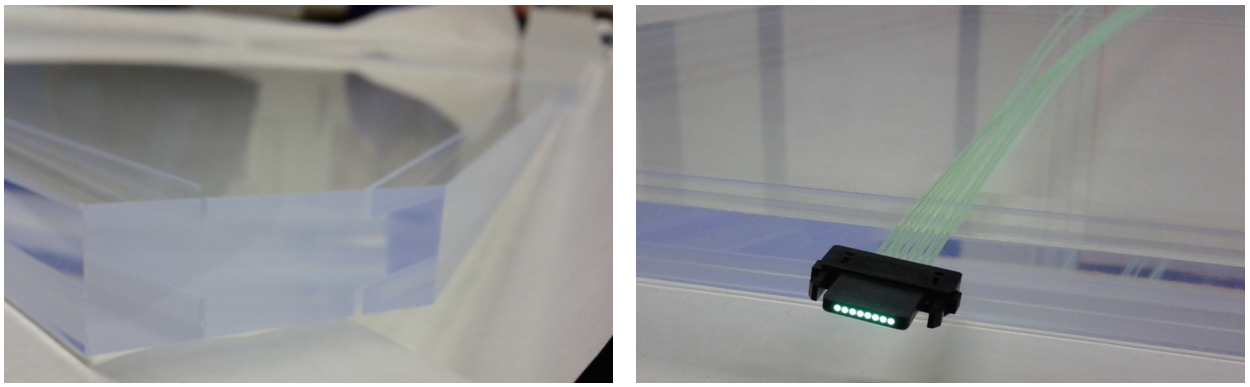

(A) (B)

FIGURE 9.3: The edges of a scintillating tile from an inner sector – the grooves used to embed the WLS are visible (A). A bundle of 8 WLS mounted onto a read-out connector before installation in the grooves (B).

This type of calibration is convenient because the light yield of the MBTS can be quantified directly in units of number of photoelectrons.

The 1PE calibration was performed in a light-proof chamber. An LED powered by a function-generator was installed inside the chamber and used as light source. The light output from the LED was adjusted such that the average number of photoelectrons detected by the PMT was well below one photoelectron. The rare signals corresponding to one or more photoelectrons would hence be clearly visible, and the 1PE response could be assessed with a fit to the spectrum. The PMT signal was extracted directly from the VD as seen in Figure 9.4 and fed to a LeCroy WaveRunner 104Xi 1 GHz oscilloscope. Data-taking was done on the oscilloscope by triggering on the signal from the pulser used to power the LED and recording the integrated pulse area of the PMT signal. To maximise the gain, the PMT was operated at the maximum safe value of 1 kV. Both configurations from Table 9.1 were calibrated with this method.

Table 9.1: Configurations of PMT and VD used for the measurements presented in this chapter.

Configuration	PMT type	PMT serial number	VD serial number
1	R7877	AA4688	108578
2	R11187	AA0205	2013112

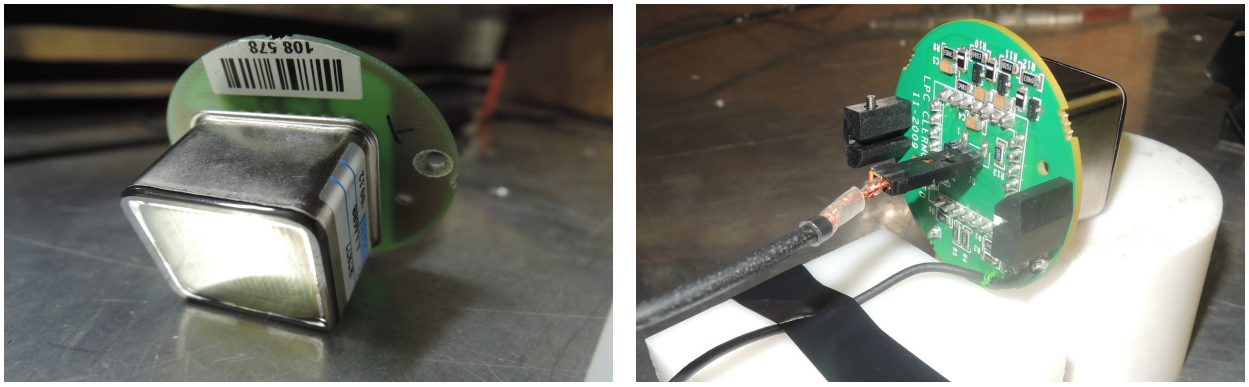

(A) (B)

Figure 9.4: A Hamamtsu R7877 PMT mounted to a TileCal VD (A). The PMT signal is extracted directly from the VD (B).

The calibration spectra obtained with the two PMT configurations are presented in Figure 9.5. The 1PE response is quantified by the variable $\mu_{1\text{PE}}$, defined as the average of each distribution. To obtain this, the spectra are fitted with the function taking the form:

$$f(x) = N \cdot \sum_{i=1}^{n} \left[\frac{e^{-\mu} \cdot \mu^i}{i!} \cdot \frac{1}{\sqrt{2\pi}\sqrt{i \cdot \sigma_{1\text{PE}}^2 + \sigma_{\text{ped}}^2}} \cdot e^{\frac{-(x-\mu_{\text{ped}}-i\cdot\mu_{1\text{PE}})^2}{2\cdot(i\cdot\sigma_{1\text{PE}}^2+\sigma_{\text{ped}}^2)}} \right] \tag{9.1}$$

This function takes two characteristics of the PMT into account: 1) the total number of photoelectrons following the amplification of a single photoelectron is Poisson distributed, and 2) the charge induced in a PMT by a certain number of photoelectrons will follow a Gaussian distribution. Hence, it is constructed from a Poissonian convoluted with a Gaussian. All parameters of this function are described in Table 9.2. The values obtained from fitting Equation 9.1 to the calibration spectra in Figure 9.5 are summarised in Table 9.3. From the fitted spectra in Figure 9.5, it is seen that the separation between the pedestal and 1PE contribution is visible with Configuration 1, but less pronounced with Configuration 2.

For the studies presented in this chapter, the uncertainty on the 1PE response is required. This quantity is defined as the error on the fitted parameter $\mu_{1\text{PE}}$, and is estimated by varying the range

and initial parameters of the fit. An uncertainty of 5% is attributed to $\mu_{1\text{PE}}$ from Configuration 1, and a conservative 20% to $\mu_{1\text{PE}}$ from Configuration 2. The large uncertainty on the latter reflects the poor separation between the pedestal and 1PE contribution.

TABLE 9.2: Parameters of Equation 9.1.

Parameter	Description
i	Number of photoelectrons
n	Maximum number of photoelectrons in fit
N	Normalisation factor
μ	Average number of photoelectrons
μ_{ped}	Charge of the pedestal
σ_{ped}	Charge spread of the pedestal
$\mu_{1\text{PE}}$	Charge of the 1PE contribution
$\sigma_{1\text{PE}}$	Charge spread of the 1PE contribution

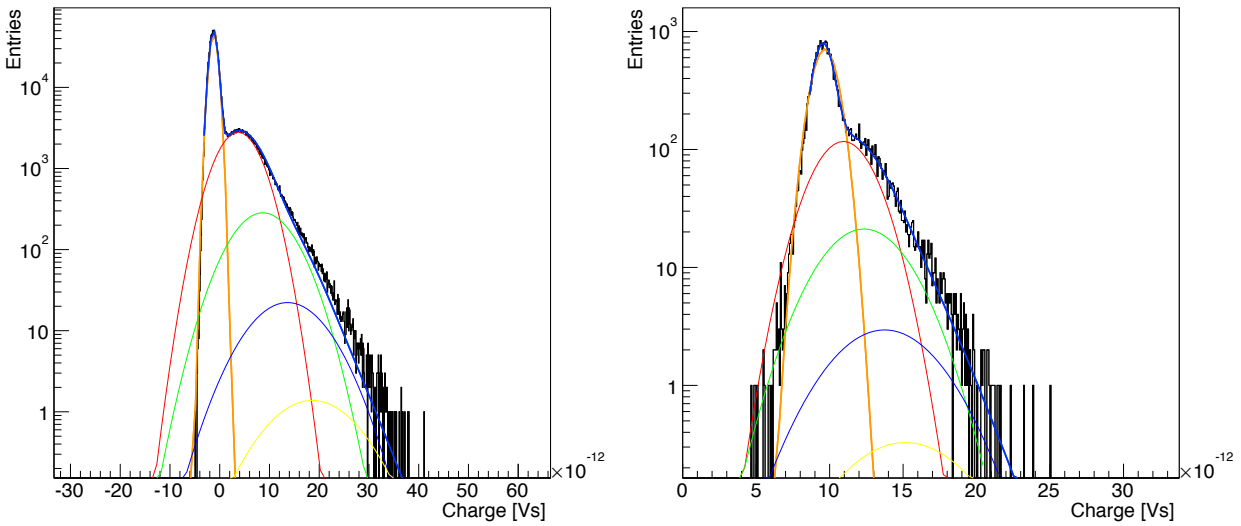

(A) (B)

FIGURE 9.5: The 1PE calibration spectra recorded with Configuration 1 (A) and 2 (B) from Table 9.1. The dominant peak on the lower side of the spectrum is the pedestal of the setup, which is fitted with a separate Gaussian distribution (orange curve). The blue curve is the global fit with Equation 9.1. The multi-coloured Gaussians under the global fit represent the contribution from 1, 2 and more photoelectrons, represented by the sum in Equation 9.1. All parameter values obtained from the fits are summarised in Table 9.3.

Table 9.3: Parameters obtained from fitting the calibration spectra in Figure 9.5. The quoted errors originate from the fit.

Parameter	Configuration 1	Configuration 2
μ	$(2.87 \pm 0.02) \times 10^{-1}$	$(5.12 \pm 0.15) \times 10^{-1}$
μ_{ped}	$(-1.24 \pm 0.01) \times 10^{-12}$	$(9.54 \pm 0.01) \times 10^{-12}$
σ_{ped}	$(7.52 \pm 0.01) \times 10^{-13}$	$(6.11 \pm 0.08) \times 10^{-13}$
μ_{1PE}	$(3.72 \pm 0.03) \times 10^{-12}$	$(1.40 \pm 0.06) \times 10^{-12}$
σ_{1PE}	$(3.77 \pm 0.02) \times 10^{-12}$	$(1.88 \pm 0.03) \times 10^{-12}$

9.4 Cosmic Setup

The light yield from one fully assembled MBTS counter was measured with cosmic rays in the dedicated setup shown in Figure 9.6. The counter was positioned horizontally on support structures in the light-proof chamber used for the 1PE calibration. An external trigger was provided by a two-fold coincidence in two 10×10 cm^2 scintillators placed above and below the surface of the counter. Cosmic rays impinging on a specific part of the MBTS counter were selected by positioning the trigger scintillators at the desired area. In the measurements presented in the following, the trigger scintillators were positioned at the centre of either the inner or outer sector. In order to block the low-energy electromagnetic component of the cosmic spectrum, two bricks of lead with a thickness of 2 cm were placed in between the trigger scintillators. Each trigger scintillator was connected to a Hamamatsu R7400p PMT operated at 900 V. As with the 1PE calibration, the read-out was done directly on the oscilloscope. The light from the MBTS was transported to the PMT with two different methods. In the first, the light from the MBTS was transported with a clear optical fiber that was routed to the PMT surface as seen in Figure 9.6. In the second, no clear fiber was used for light transport, and the PMT was hence positioned facing the MBTS read-out connector directly. Unless otherwise specified, the former approach was used. After each successful measurement, a pedestal was recorded with a random trigger.

9.5 Measurement Series

The light attenuation of the clear fibers was determined with a set of measurements in which the MBTS counter was read out with clear optical fibers of same lengths as used in ATLAS; 2.1 m and 3.6 m. These measurements were done with the inner sector of the MBTS and Configuration 1

from Table 9.1. A third measurement without any clear fiber was performed, i.e. with the PMT facing the MBTS connector directly as described above.

In the measurements that followed, the light yield of the outer sector when employing 4 or 8 WLS was determined. The reduction from 8 to 4 WLS was achieved by covering the two outermost WLS in each side of the connector. In this measurement, the MBTS counter was read out without any clear fiber and Configuration 1 from Table 9.1. The combination of this and the previous measurement series enabled a direct comparison of the light yield from the inner and outer sector.

A last measurement was performed with the outer sector with Configuration 2 from Table 9.1. No clear fiber was used in this measurement, and all 8 WLS were read out. With this it became possible to directly compare the two PMT configurations from Table 9.1.

9.6 Correcting for Light Loss in Connector

A correction had to be applied to all measurements performed without a clear optical fiber. This correction took into account a loss of light caused by a geometrical effect in the setup, which is illustrated in Figure 9.7.

The cladding of a fiber determines the maximum allowed emission angle of the light propagating from it. The WLS installed in the MBTS are double-cladded, meaning that the light coming from them can be emitted in an angle of maximum 45°. When the MBTS counter is read out with a clear optical fiber, there is direct contact between the WLS and the clear fibers, meaning that the majority of light emitted from the WLS is evacuated by the clear fibers and sent to the PMT, despite the large emission angle. Given that the MBTS connector is 10 mm deep, when the MBTS

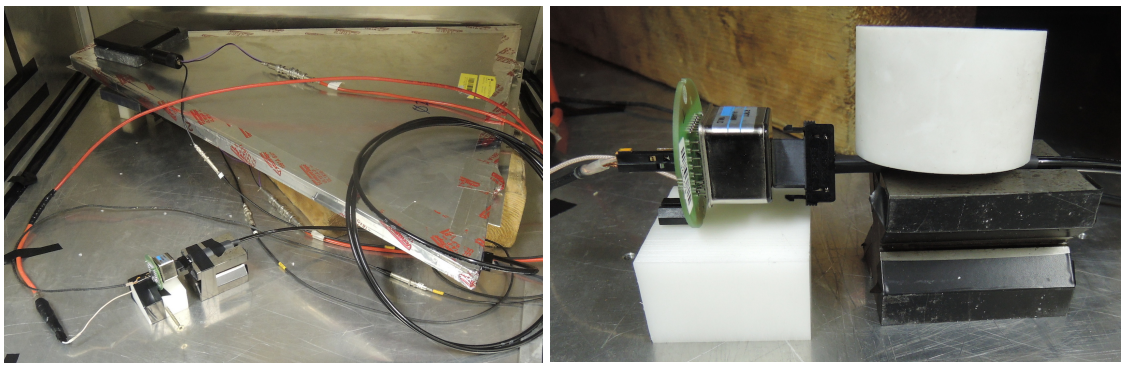

(A) (B)

FIGURE 9.6: Cosmic rays impinging the inner sector are selected by positioning the trigger scintillators at the centre of the inner sector (A). The clear fiber connected to the MBTS is routed to the PMT and kept in position with appropriate support structures (B).

is read out without a clear fiber but instead with the PMT positioned directly against the surface of the connector, a gap of 10 mm will be present between the WLS and the PMT. Over this distance, a portion of the light will be shadowed due to a reduction in the solid angle of the emitted light. From a geometrical viewpoint, the magnitude of the light loss will be proportional to the ratio between the area of the unshielded light cone versus the area of the connector where the light can propagate freely, as illustrated in Figure 9.7. From a geometrical perspective, a light loss of 85% was therefore expected to affect all the measurements performed without any clear fiber. However, since the reflectivity of the connector material was unknown, the magnitude of this light loss was measured directly.

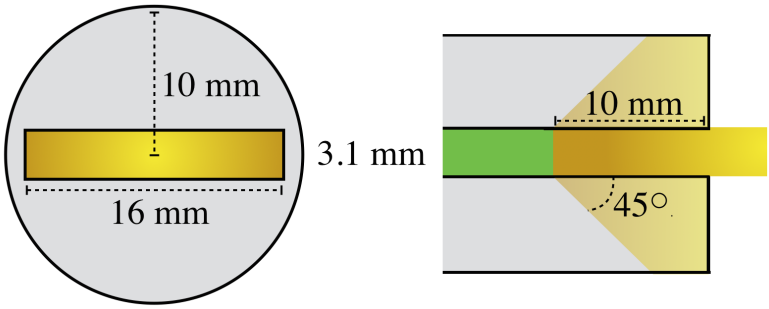

Figure 9.7: Illustration of the MBTS connector seen from the front (left). The yellow area represents the area of the MBTS connector, while the grey area represents the area of the light cone at the position of the PMT. Cross-section of the MBTS connector from the side (right). The green line represents the WLS, the yellow area the light being emitted from the WLS, and the grey area the connector material.

A separate experimental setup was constructed to measure the light loss caused by the geometry of the connector. This is shown in Figure 9.8. A bundle of WLS from the MBTS was installed in a light-proof chamber. An LED was used to excite the WLS and the light emitted from the WLS was detected with a pin-diode. The current from the pin-diode was read out with a pico-amp meter. A cap with identical dimensions and material as the MBTS connector was mounted onto the WLS bundle, hence attenuating the light in the same way as the MBTS connector. The current in the pin-diode was measured with and without the cap. The light attenuation was quantified as the difference in the magnitude of the two currents. For both 4 and 8 WLS, the light loss was found to be ~70%. This value is 15% smaller than predicted by the purely geometrical argument – the difference is ascribed to reflections in the connector. The measurement of the light attenuation was repeated multiple times to minimise the uncertainty on the scaling value.

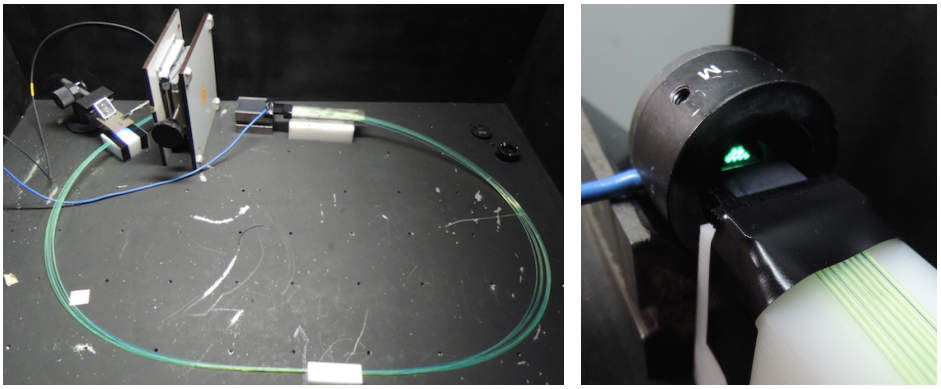

(A) (B)

FIGURE 9.8: The setup used to measure the light loss in the connector consisting of a WLS bundle, an LED, and a pin-diode (A), and a close-up of the WLS bundle facing the pin-diode (B).

9.7 Results

Examples of the obtained spectra are shown in Figure 9.9. To determine the light yield of each measurement, a fit with Equation 9.1 is imposed to all distributions. Initially, the pedestal, measured with a random trigger after each measurement is fitted with a Gaussian to determine the parameters μ_{ped} and σ_{ped}, describing the baseline of the experimental setup. From the fitted value of μ_{ped}, the value of μ_{1PE} can be determined by applying the distance between the pedestal and the 1PE contribution determined in the calibration. In summary, all parameters in Table 9.2 except N, μ and i are determined in the calibration. The parameter i is set to an arbitrary large number while N and μ are determined from the fit. The uncertainty on the fitted value of μ was defined from varying the fit range and initial parameters of the fit.

TABLE 9.4: Results obtained from the different measurements with the MBTS counter. The value μ denotes the average number of photoelectrons. The measurements performed with no use of clear fiber have been scaled with the light loss correction factor from Section 9.6.

Label	Sector	Measurement	Configuration	Light yield, μ [Vs]	Systematic error	1PE error	Total error
A	outer	4 WLS, no clear fiber	1	$20.93 \pm 9.27 \times 10^{-2}$	3.9%	5%	6.4%
B	outer	8 WLS, no clear fiber	1	$40.80 \pm 8.37 \times 10^{-2}$	1.6%	5%	5.3%
C	inner	8 WLS, no clear fiber	1	$27.87 \pm 8.70 \times 10^{-2}$	1.8%	5%	5.3 %
D	inner	8 WLS, 2.1 m fiber	1	$13.0 \pm 2.21 \times 10^{-2}$	1.7%	5%	5.3%
E	inner	8 WLS, 3.6 m fiber	1	$7.39 \pm 5.80 \times 10^{-2}$	1.2%	5%	5.2%
F	outer	8 WLS, no clear fiber	2	$19.63 \pm 4.93 \times 10^{-2}$	1.4%	20%	20.1%

The yield obtained with the various measurements are presented in Table 9.4 in units of number of photoelectrons. A label (A - F) has been assigned to each measurement to make relative

comparison easier. The measurements performed without a clear fiber have been scaled with the light loss correction factor from Section 9.6. Both the statistical error and uncertainty on $\mu_{1\text{PE}}$ are quoted in the table as well. The total error is obtained by folding the uncertainties in quadrature. To summarise further and enable direct comparison, Figure 9.10 presents all the fitted curves from Measurements A to E (with Configuration 1), with the pedestal from each measurement centred around 0.

9.7.1 Fiber Attenuation

The attenuation length of the clear fibers is estimated with a fit to the light yield values obtained from Measurement D and E. This is shown in Figure 9.11. Since the intensity of a propagating light beam decays exponentially [155], this fit is done with a function of the form $f(x) = I_0 \exp(-\mu x)$. The attenuation length is obtained from $\lambda = 1/|\mu|$. The upper and lower limits on the attenuation length are estimated by performing two additional fits. In the first, the datapoint at 2.1 m is shifted up by 1σ, and the datapoint at 3.6 m is shifted down by 1σ. The opposite is done in the subsequent fit. The attenuation lengths returned by these fits forms the uncertainty band on the central value. The obtained lower and upper attenuation lengths are 2.49 ± 0.65 m and 2.85 ± 0.84 m. As a sanity check, from Figure 9.11 it is noted that the light yield extrapolated back to 0 m, corresponding to the use of no clear fiber, is consistent with the obtained number of photoelectrons from Measurement C.

The observed attenuation length of ~2.5 m is surprisingly low; clear fibers of this caliber usually have an attenuation length greater than 10 m [156]. Multiple reasons can cause the observed value to be this low, damage being one of them. Another plausible explanation comes from the fact that the utilised clear fibers are single-clad only. Given that the WLS embedded in the MBTS counters are double-clad, the light from these will be emitted at angles where the single-clad fibers do not manage to trap a large portion of the light. Hence, employing double-clad clear fibers in the read-out could increase the amount of light being collected. At the time of these measurements, no such fibers were available, and it was therefore not possible to explore this hypothesis further.

9.7.2 MBTS Yield

The light yield of the outer sector read out with 4 and 8 of the available WLS is assessed with Measurement A and B. From a theoretical viewpoint, it would be intuitive to believe that the light yield of the latter measurement should be twice as large as the former. However, this behaviour is not evident, since the individual WLS might collect a different amount of light due to their relative positioning in the scintillator material. Given that the light yield from Measurement B is observed

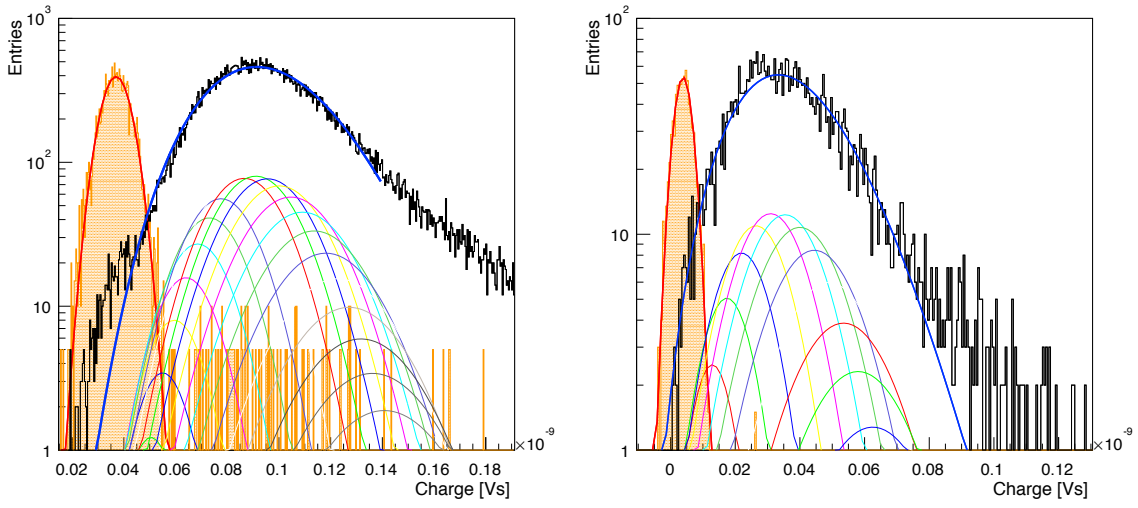

(A) (B)

FIGURE 9.9: Spectra obtained with the inner sector of the MBTS with measurement D (A) and E (B). The orange histogram is the pedestal recorded with a random trigger after each measurement, used to define the baseline of the experimental setup. The black histogram is the data recorded with the MBTS counter. A fit with Equation 9.1 is imposed to the data (blue curve).

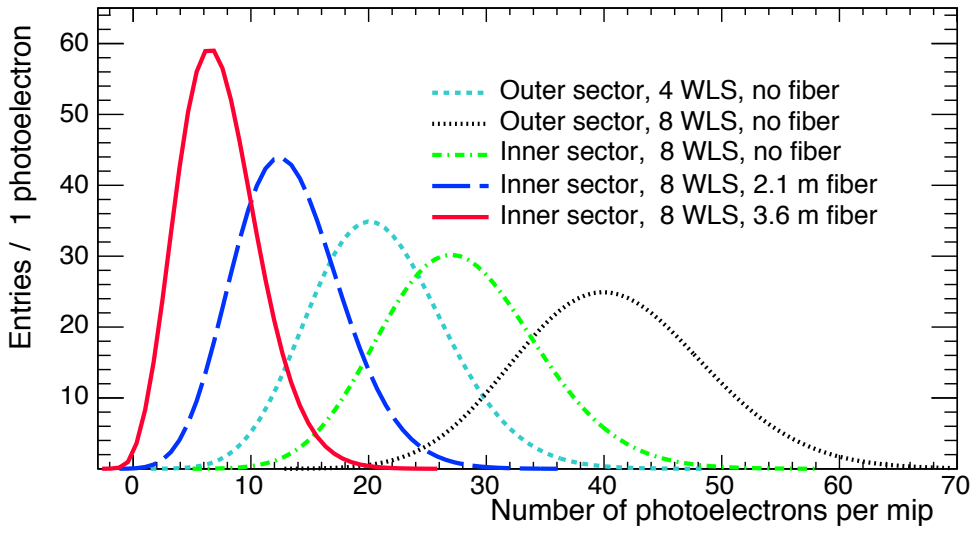

FIGURE 9.10: The fitted curves from Measurements A – E. The measurements performed with no use of clear fiber have been scaled with the light loss correction factor from Section 9.3. The x-axis is displayed in units of photoelectrons. The pedestal from all measurements has been centred around 0.

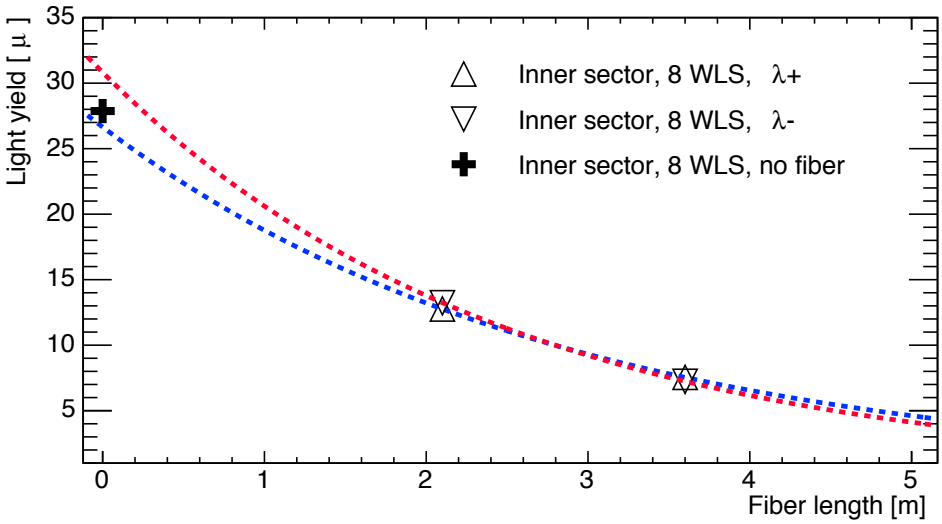

Figure 9.11: The upper and lower boundary on the light yield obtained from Measurement D and E in Table 9.4. The obtained attenuation lengths are 2.49 ± 0.65 m (blue) and 2.85 ± 0.84 m (red).

to be very close to twice as large as that from Measurement A, it can be concluded that the relative positioning of the WLS does not have any observable effect on the light yield. The question about whether 4 WLS provides a light yield that is sufficient to offset the MBTS signals from the baseline can be answered from Figure 9.10. As observed, the distance between the position of the pedestal (0) and the fitted curve from Measurement A is well defined, meaning that the use of 4 WLS results in an adequate amount of light.

In addition to the above, some interesting observations are made about the behaviour of the MBTS counter. By comparing Measurement B with C, the difference in light yield between the inner and outer sector when employing the same number of WLS, is assessed. As seen in Table 9.4, the light yield from the outer sector is ~45% larger than in the inner sector. This effect is somewhat surprising; given that the scintillation light has to travel a smaller distance in the inner sector before being evacuated by the WLS, the light yield of the inner sector could very well have been higher. However, when lowering the number of WLS in the large sector to 4, the light yield drops ~50% and falls below that of the inner sector. The implication of this is, that the use of 4 WLS in the read-out of the outer sector will make it more sensitive to efficiency degradation than the inner sector.

Ideally, a statement should be made about the two PMT configurations; by comparing Measurement B and F it is seen that Configuration 1 from Table 9.1 by far provides the highest light yield. However, due to the large uncertainty on Measurement F, the ratio between the light yields from the two configurations cannot be specified accurately.

9.8 Summary and Implications

The behaviour of a Run-2 MBTS counter and the clear fibers intended for read out was determined with cosmic rays in a dedicated setup in the TileCal laboratory at CERN. Several important observations were made, highlighting issues needing attention before the start of Run-2. Furthermore, the presented measurements served as a basic sanity check of the behaviour of the counters.

Firstly, in the presented measurements, the attenuation length of the clear fibers was determined. This was found to be around 2.5 m, which is a surprisingly low value compared to the norm, meaning that an unnecessarily large portion of the light emitted by the MBTS would be lost if these fibers were to be used in Run-2. Given that the transparency of the scintillating material in the MBTS inevitably will degrade from radiation damage, the loss of even a slight amount of light can be crucial to maintaining a signal of adequate magnitude and thus stable efficiency. Equipping the MBTS with double-clad fibers could potentially increase the amount of light being evacuated. Upon presenting the results in this chapter, new double-clad clear fibers were procured and used for the installation of the Run-2 counters.

Furthermore, in these measurements it was investigated whether 4 WLS would be sufficient for the read-out of the outer sector, or whether all 8 WLS should be employed. The measurements revealed that 4 WLS provided a satisfactory light level good enough to distinguish the signals coming from the MBTS. It was in addition confirmed that light yield of the outer sector can be recuperated by opting for all 8 WLS – an option that might be implemented once the scintillating material in the counters has been damaged.

Lastly, the detailed detector characterisation presented throughout this chapter facilitated the task of adjusting the discriminator thresholds for the Run-2 MBTS counters after integration in the ATLAS DAQ chain, and thereby also the timing of the MBTS signals. The resulting, highly satisfactory, timing of the MBTS counters observed in Run-2 during $\sqrt{s} = 13$ TeV collisions is presented in Figure 9.12. The characterisation presented in this chapter will also be highly useful when the discriminators will have to be adjusted in the future.

All in all, the characterisation presented in this chapter has shown that the Run-2 MBTS counters are highly functional and have the potential to perform well throughout Run-2.

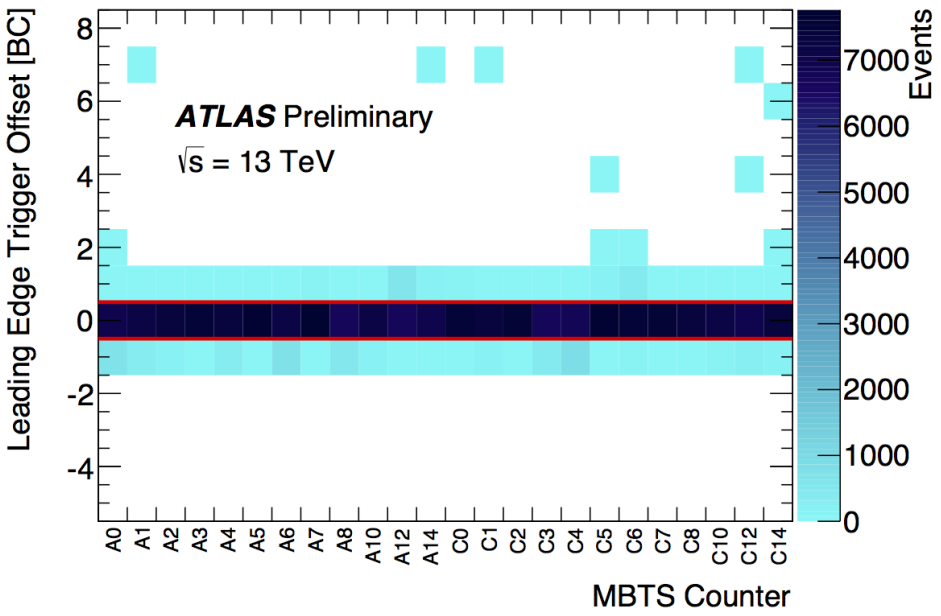

(a)

Figure 9.12: Relative timing of the rising edge of the 50 ns trigger signal from the different Minimum Bias Trigger Scintillator (MBTS) counters in units of 25 ns Bunch Crossing (BC) with respect to the bunch crossing position where beams were colliding in ATLAS. 12 MBTS counters are located at $z = +3560$ mm from the Interaction Point (IP) (A side) and 12 at $z = -3560$ mm from the IP (C side). Counters $0 - 7$ form an inner ring around the beam pipe, while counters 8, 10, 12 and 14 form an outer ring at larger radius. The $\sqrt{s} = 13$ TeV collision candidate events were selected with a two-sided coincidence MBTS trigger. For physics operation, the trigger signal is combined with the LHC fill pattern recovering the signal from counters whose rising edge is one BC early. The in-time BC is highlighted with a red border. MBTS PMTs were at a nominal setting of 830 V, NIM model 715 constant fraction discriminators were used to issue the trigger signal with a 200 mV threshold. The discriminators variable threshold range is $25 - 1000$ mV [157].

CHAPTER 10

Sommaire de la thése en français

10.1 Introduction

En 2012, les expériences ATLAS et CMS auprès de grand collisionneur de particules LHC de l'Organisation Européenne pour la Recherche Nucléaire (CERN), annoncérent la découverte d'un nouveau boson. En mesurant les propriétés de cette particule, il fut prouvé que cet objet était un scalaire CP-pair ayant une masse proche de 125 GeV, compatible avec le boson de Higgs prédit par le Modèle Standard. Cette découverte représenta une étape majeure dans l'étude des particules, car elle démontra que le mécanisme dénommé Electroweak Symmetry Breaking est responsable de la génération des masses des bosons vecteurs du Modèle Standard.

La découverte de ce nouveau boson ouvrit le champ à de nouvelles interrogations, à savoir si ce boson est le seul de ce type ou s'il fait partie d'un secteur de la physique tendue du Higgs. De nombreuses théories complémentaires au Modèle Standard prédisent l'existence d'autre bosons de Higgs: le 2-Higgs Doublet Model (2HDM) par exemple. La découverte de tout nouveau boson de Higgs indiquerait sans équivoque la présence de nouvelle physique au-delà du Modèle Standard.

Le sujet principal de cette thése porte sur les recherches de bosons de Higgs additionnels qui se décomposeraient en une paire de bosons Z, en utilisant les données enregistrées par l'expérience ATLAS. Le boson recherché est supposé être plus lourd que son compagnon découvert en 2012, CP-pair et ne pas posséder de charge électrique. Trois recherches indépendantes sont présentées dans ce travail, chacune des sections suivantes les décrivant.

10.2 Recherches dans le canal du Higgs se désintégrant en ZZ en quatre leptons, avec les données à 8 TeV

Le chapitre 5 présente les recherches d'un boson de Higgs lourd se désintégrant en ZZ en quatre leptons. L'analyse repose sur l'ensemble des données enregistrées par ATLAS lors des collisions proton-proton à des énergies de 8 TeV dans le centre de masse, correspondant à une luminosité intégrée de 20.3 fb^{-1}. Le spectre de masse étudié s'étend de 140 GeV à 1 TeV.

Afin d'obtenir une bonne sensitivité pour un grand nombre de signaux, les recherches sont définies de manière à être les moins dépendantes de modèles en évitant toute hypothèse associée à ces derniers. L'approximation de la largeur étroite (NWA) est utilisée, pour le signal sur l'ensemble du spectre étudié de la masse du Higgs (m_H). En procédant ainsi, il est possible de supprimer la dépendance de la largeur naturelle du boson de Higgs lourd vis-à-vis de sa masse, qui est pourtant présente dans le Modèle Standard. Cette approximation permet aussi de négliger deux types d'interférences intervenant dans le mécanisme de production du boson de Higgs lourd: il s'agit des interférences entre les bosons de Higgs lourd et léger et entre le boson de Higgs lourd et le continuum du bruit de fond ZZ. L'indépendance aux modéles est assurée en refusant toute hypothèse concernant la production relative aux modes ggF, VBF et VH. Ainsi, les événements sont segmentés en catégories orthogonales, qui sont définies comme étant compatibles avec un des trois modes de production ci-dessus cités. Afin de mesurer les rendements de ces modes de manière indépendante, un paramétre de force du signal est défini pour chacune des catégories ggF et VBF (μ_{ggF} et μ_{VBF}). Cette définition permet une détermination indépendante des rendements dans le fit final de l'analyse.

Le signal est modélisé avec l'approximation de largeur étroite et a une distribution de type Breit-Wigner avec une largeur de 4.07 MeV (largeur du boson de Higgs du modèle Standard). Le choix spécifique de la largeur n'a pas grande importance dès l'instant où cette dernière est bien plus inférieure à la résolution expérimentale. L'algorithme *Kernel Estimating Your Shape* est utilisé sur des ensembles de données simulées (Monte Carlo) et permet de déterminer la forme du signal. Pour certaines valeurs de mH où aucun Monte Carlo n'est disponible, la forme du signal est obtenue comme mélange des formes récupérées aux valeurs de m_H les plus proches.

Le bruit de fond dominant dans cette analyse vient du continuum ZZ produit par les désintégrations $q\bar{q} \rightarrow ZZ$ ou $gg \rightarrow ZZ$. La contribution de ces composantes est entiérement estimée par la simulation. La détermination des contributions mineures des bruits de fond Z+jets, $t\bar{t}$ et désintégrations de di-bosons, est axée sur les données.

Les résultats de cette analyse sont donnés sous forme de limites supérieures du produit de la

section efficace de production du boson de Higgs lourd par le rapport d'embranchement $H \to ZZ$. Ces limites sont calculées séparément pour les catégories ggF et VBF, comme fonction de m_H en suivant la procédure des CL_S. Dans la figure 10.1, la courbe noire en pointillés représente la limite attendue sous l'hypothése de bruit de fond seul, alors que les points noirs correspondent aux limites observées. Les incertitudes sur cette limite sont matérialisées par les bandes verte et jaune, pour les déviations à $\pm 1\sigma$ et $\pm 2\sigma$. Avec cette convention, un signal se manifesterait comme excès au-dessus des limites observées. Ainsi, les résultats sont compatibles à $\pm 2\sigma$ près avec les prédictions sur l'ensemble du spectre m_H considéré. Il n'y a donc aucune indication de la présence d'un boson de Higgs lourd. La limite sur $\sigma \times BR(H \to ZZ^{(*)})$ pour un CL de 95% dans la catégorie ggF est de 330 fb pour $m_H = 200$ GeV, et 38 fb pour $m_H = 1$ TeV. Les mêmes limites sont calculées pour la catégorie VBF et sont de 277 fb pour $m_H = 200$ GeV, et 35 fb pour $m_H = 1$ TeV.

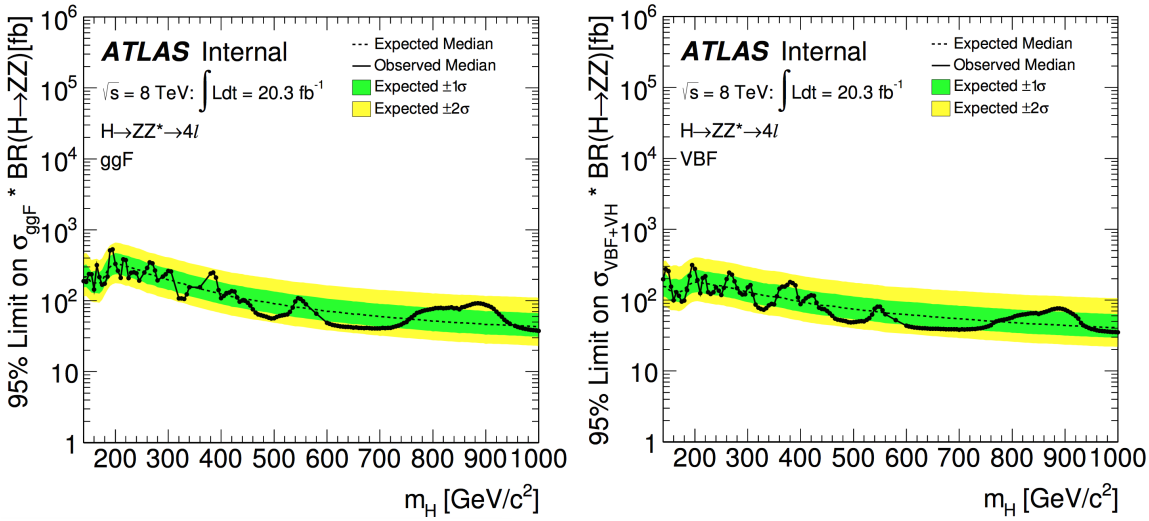

(A) (B)

Figure 10.1: Limites sur $\sigma \times BR(H \to ZZ^{(*)})$ pour un CL de 95% en fonction de m_H dans les catégories (A) ggF et (B) VBF. La courbe noire et les points indiquent les limites observées. La ligne pointillée noire représente les limites prédites, alors que les bandes verte et jaune symbolisent les déviations à 1σ et 2σ sur la limite attendue.

10.3 Combinaison des recherches avec les données à 8 TeV

Dans le chapitre 6, la sensibilité des recherches $H \to ZZ \to 4\ell$ est accrue en combinant les résultats obtenus avec d'autres études menées dans les trois autres processus $H \to ZZ^{(*)}$, $ZZ^{(*)} \to 2\ell 2\nu$, $2\ell 2q$ et $2\nu 2q$. Comme pour $ZZ^{(*)} \to 4\ell$, les recherches additionnelles sont basées sur des stratégies indépendantes des modèles en utilisant l'approximation NWA, et en segmentant les événements selon deux catégories ggF et VBF pour $2\ell 2\nu$ et $2\ell 2q$. La combinaison des résultats permet d'étendre les limites obtenues, et ce d'autant plus que les différentes recherches ont des sensitivités complémentaires dans différentes régions du spectre de masse.

La combinaison permet d'améliorer les résultats découlant de recherches précédentes menées par ATLAS, qui comportaient moins de processus de désintégration et utilisaient un ensemble de données réduit de 4.8 fb^{-1} à 7 TeV. En outre, ces précédentes recherches n'avaient pas été combinées, signifiant que le travail présenté dans cette thése est une première en la matière pour les études de $H \to ZZ^{(*)}$ par l'expérience ATLAS.

Dans cette combinaison, les fonctions de vraisemblance individuelles sont assemblées de telle sorte qu'un fit global est fait simultanément sur le signal et les régions de contrôle des quatre recherches. Une des parties cruciales de la méthode réside dans la définition du schéma de corrélation entre les quatre processus, qui permet la prise en compte des erreurs systématiques.

Les limites supérieures sur le produit de la section efficace de la production du boson de Higgs lourd par le rapport d'embranchement $H \to ZZ^{(*)}$ obtenues avec la combinaison sont présentées en figure 10.2. Ces limites sont calculées en utilisant la procédure des CL_S, séparément pour les catégories ggF et VBF. Les limites attendues sont aussi représentées pour comparaison. Ainsi, la chaîne 4ℓ a une meilleure sensitivité à basse masse, juste au-dessus de la chaîne $2\ell 2\nu$. Les observations ne dévient pas de la bande de 2σ dans le spectre de masse considéré (de 140 GeV à 1TeV). Les limites observées s'étendent de 359 fb à $m_H = 200$ GeV jusqu'à 10 fb à $m_H = 1$ TeV pour la catégorie ggF, et de 214 fb à $m_H = 200$ GeV jusqu'à 13 fb à $m_H = 1$ TeV pour la catégorie VBF.

Les résultats offrent également une interprétation en considerant le modèle 2HDM: des limites directes dans l'espace défini par $\tan(\beta)$ et $\cos(\beta - \alpha)$ sont calculées, ainsi que des limites sur $\tan(\beta)$ en fonction de m_H. Ces limites sont restreintes aux espaces permis par l'approximation NWA. Comme la largeur naturelle du boson de Higgs est ici assimilée à la résolution expérimentale des quatre processus, la largeur maximale tolérée est déterminée par les analyses ayant la meilleure résolution, à savoir 4ℓ et $2\ell 2q$. Un seuil limite de largeur de 0.5% m_H est utilisé comme maximum toléré pour tous les points de l'espace de paramétres du 2HDM. La figure 10.3 présente les limites d'exclusion dans le plan $\cos(\beta - \alpha)$ et $\tan(\beta)$ pour les 2HDM de Type-1 et Type-2, supposant un

boson de Higgs lourd ayant une masse de 200 GeV. Cette masse est choisie de telle sorte que l'hypothèse NWA soit valide dans la plupart des points de l'espace, tout en conservant une sensitivité maximale. Tout en calculant les limites à un point donné de ce plan, les rendements relatifs de ggF et VBF dans le fit sont fixés selon les prédictions du 2HDM pour ce couple de paramétres. Les régions en blanc montrent les régions de points non exclus par la présente analyse, dans laquelle la section efficace prédite par le 2HDM est en dessous de la sensitivité expérimentale. Les régions hachurées en rouge indiquent les limites d'exclusion observées, avec les bords matérialisés par les courbes rouges. La courbe bleue en pointillés représente le contour attendu, et les bandes verte et jaune, les erreurs relatives à 1σ et 2σ sur les prédictions.

La figure 10.4 présente les limites d'exclusion sur $\tan(\beta)$ en fonction de m_H pour les 2HDM de Type-1 et Type-2. Dans ces scenarios, l'hypothése $\cos(\beta - \alpha) = \pm 0.1$ est prise en considération. Ce point de l'espace de paramétres du 2HDM est suffisamment proche de la limite d'alignement, prenant en compte le fait que les couplages du Higgs ne sont pas changés vis-à-vis de leur valeur dans le Modèle Standard à un facteur 2 près. Dans cette figure, les aires grises masquent les régions dans lesquelles la largeur du boson est supérieure au seuil, ce qui est théoriquement impossible.

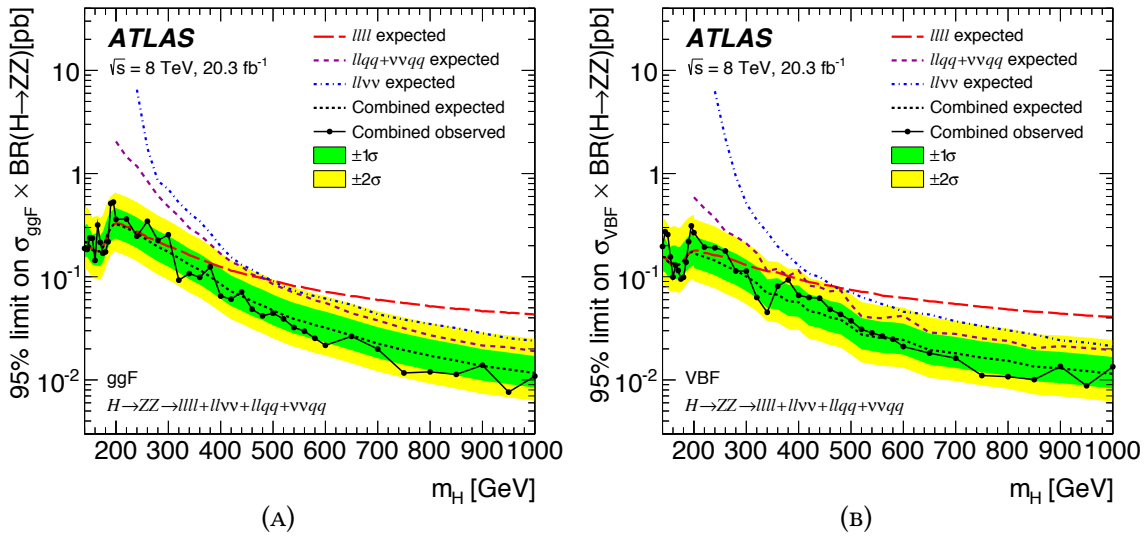

(A) (B)

FIGURE 10.2: Limites supérieures sur $\sigma \times \mathrm{BR}(H \to ZZ)$ en utilisant la méthode des $\mathrm{CL_S}$, en fonction de m_H, obtenues par combinaison des quatre recherches dans les catégories (A) ggF et (B) VBF. La courbe noire et les points indiquent la limite observée. La courbe noire en pointillés représente la limite attendue, tandis que les bandes verte et jaune matérialisent les incertitudes à 1σ et 2σ sur la limite attendue. Les courbes colorées en pointillés symbolisent les limites obtenues pour les différentes recherches individuelles.

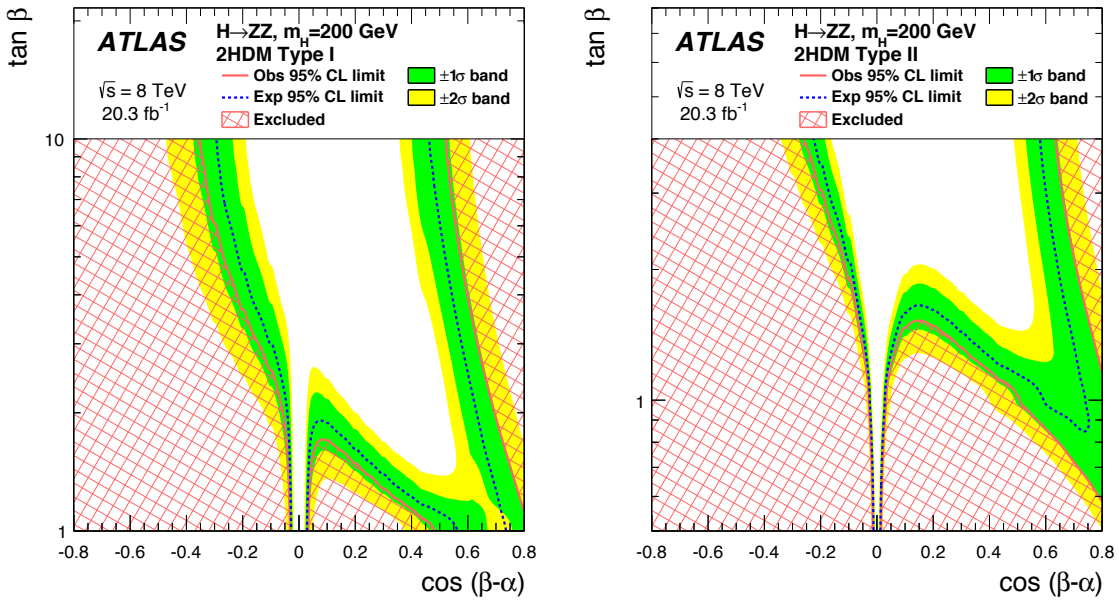

(A) (B)

FIGURE 10.3: Contours d'exclusion dans les 2HDM de (A) Type-1 et (B) Type-2 pour $m_H = 200$ GeV, dans les espaces de paramètres $\cos(\beta - \alpha)$ et $\tan(\beta)$. Les aires rouges hachurées montrent les limites d'exclusion obersvées, avec les bords soulignés par les courbes rouges. La courbe bleue en pointillés représente le contour d'exclusion attendu, et les bandes verte et jaune les incertitudes à 1σ et 2σ sur la valeur attendue. L'échelle de l'axe vertical est choisie de telle sorte que des régions pour lesquelles les couplages du boson de Higgs lèger sont trois fois plus grand que ceux du Modèle Standard, sont exclues.

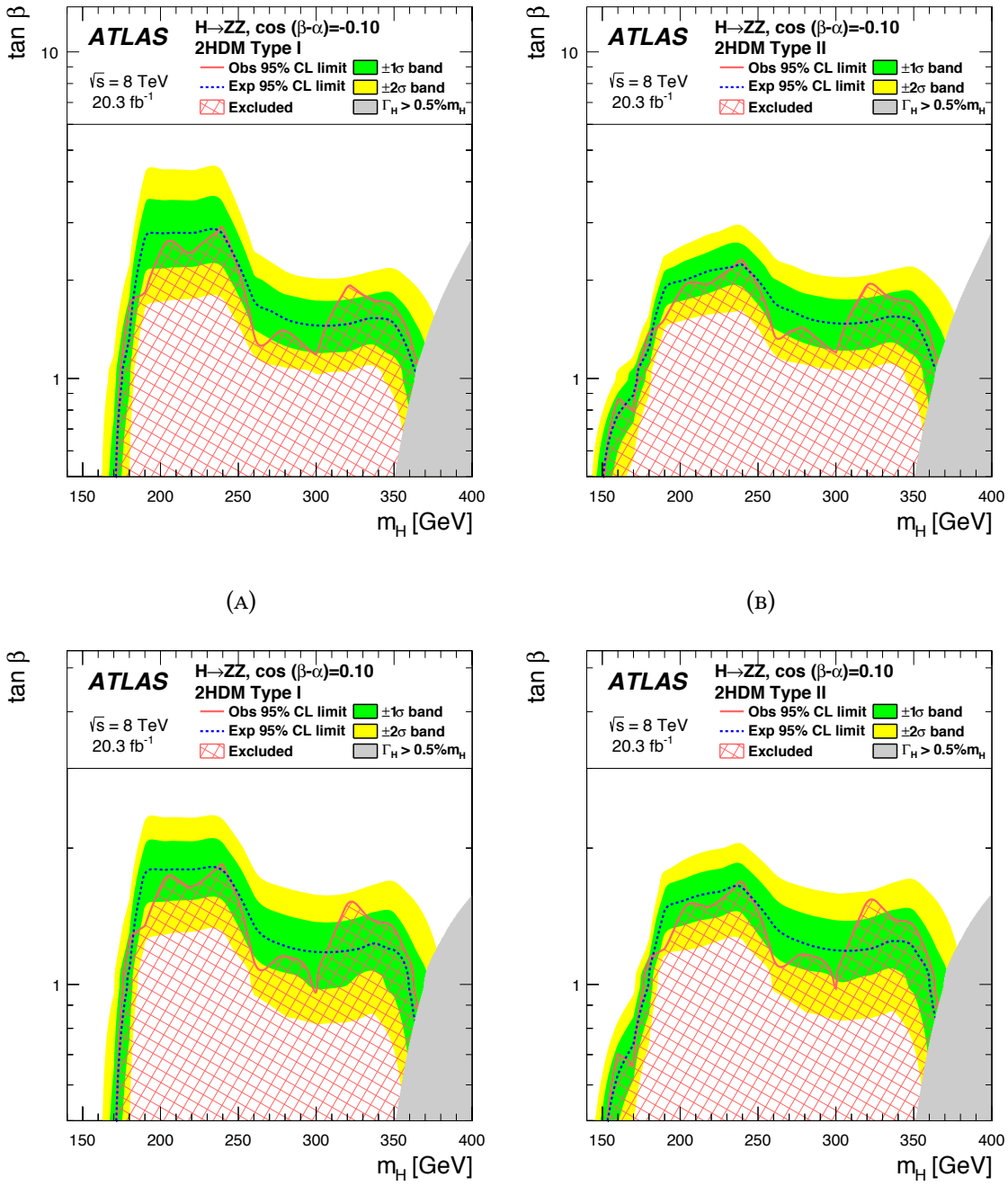

Figure 10.4: Contours d'exclusion dans 2HDM de (A) Type-1 et (B) Type-2 pour (C) $\cos(\beta-\alpha) = -0.1$ et (D) $\cos(\beta-\alpha) = 0.1$, en fonction de m_H et de $\tan(\beta)$. L' aire rouge hachurée montre la région d'exclusion observée. La courbe bleue représente le contour d'exclusion attendu et les bandes verte et jaune symbolisent les incertitudes à 1σ et 2σ sur ce contour. L'aire grise masque les régions pour lesquelles la largeur du boson est supérieure à 0.5% de m_H.

10.4 Recherches dans le canal du Higgs se désintégrant en ZZ en quatre leptons, avec les données à 13 TeV

Le chapitre 7 détaille la continuation des recherches d'un boson de Higgs lourd en utilisant les premiéres données du Run−2 (3.2 fb^{-1} à 13 TeV). Ce travail est la suite directe de l'analyse présentée dans le chapitre 5, et vise à rechercher la présence d'un boson de Higgs lourd ayant une largeur étroite dans l'intervalle de masses allant de 200 GeV à 1 TeV dans le canal $H \rightarrow ZZ^{(*)} \rightarrow 4\ell$. Les mêmes stratégies utilisées pour le Run−1, incluant la sélection des événements, l'estimation du bruit de fond et la méthode de traitement statistique, sont réutilisées ici. La principale différence réside dans le fait que le signal est modélisé avec une approche analytique et qu'il n y a pas de catégorisation selon le mécanisme de production. Ainsi, un unique ensemble de limites supérieures est inclus dans les résultats.

De la même maniére, les résultats sont présentés comme limites supérieures sur le produit de la section efficace de production du boson de Higgs lourd par le rapport d'embranchement $H \rightarrow ZZ^{(*)} \rightarrow 4\ell$. Les limites sont calculées en utilisant la procédure CL$_S$ et les résultats sont présentés en figure 10.5. Pour la plupart des masses testées, la limite observée entre dans les bandes de 1σ. Autour de $m_H = 450$ GeV, les résultats dévient jusqu'à 2σ mais la signification locale n'excède pas les 3σ. Les limites supérieures à 95% CLs s'étendent de 4.6 fb à $m_H = 200$ GeV jusqu'à 1.0 fb à $m_H = 1$ TeV.

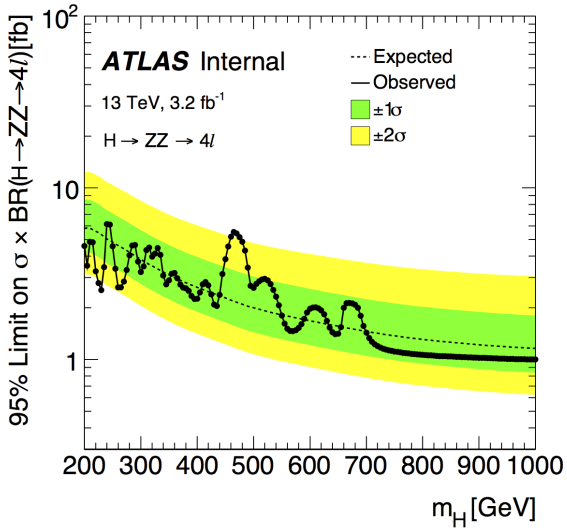

FIGURE 10.5: Limites supérieures à 95% CL$_S$ sur le produit $\sigma \times BR(H \rightarrow ZZ^{(*)} \rightarrow 4\ell)$ en fonction de m_H. La courbe noire et les points présentent les limites observées. La courbe noire en pointillés indique la limite attendue et les bandes verte et jaune montrent les déviations à 1σ et 2σ sur la prédiction.

10.5 Caractérisation des scintillateurs du déclencheur à biais minimum

Le chapitre 9 développe la caractérisation des nouveaux scintillateurs pour le déclencheur à biais minimum (MBTS), qui ont été déployés par ATLAS pour la prise de données du Run 2. Ces scintillateurs ont pour tâche de déclencher l'enregistrement (niveau 1) des événements composés de particules chargées émanant de collision à faible intensité avec un biais minimal pour la signature de l'événement. Durant le Run−1, les MBTS furent exposés à des doses de radiation de l'ordre de 10^4 Gy. Ceci endommagea les fonctions primaires des appareils de maniére importante, du fait de la dégradation de la transparence des milieux scintillants. À cause de ces altérations irréparables, les MBTS durent être entièrement remplacés avant le début du Run−2. L'agencement des nouveaux MBTS est similaire à ceux du Run−1, étant également segmentés en un secteur intérieur ($3.75 < |\eta| < 2.78$) et extérieur ($2.78 < |\eta| < 2.08$). Le secteur intérieur transmet ses données via 4 fibres optiques à décalage de longueur d'onde (WLS), alors que le secteur extérieur transmet ses données via 4 ou 8 WLS.

Afin de caractériser les nouveaux MBTS sous radiations cosmiques, un banc spécial fut construit dans le laboratoire TileCal du CERN. Trois grandeurs devaient être déterminées: 1) le rendement lumineux du secteur extérieur lorsque utilisé avec 4 ou 8 WLS, 2) la comparaison entre les rendements lumineux des secteurs intérieur et extérieur et 3) l'atténuation des fibres transparentes utilisées pour le transport des signaux. Afin de remplir ces trois objectifs, le plan de mesures décrit dans le tableau 10.1 fut mis en place.

Les résultats des mesures sont regroupés dans la derniére colonne du tableau 10.1. Le premier objectif est déterminé en comparant les mesures A et B. Le rendement lumineux est deux fois plus élevé lorsque deux fois plus de WLS sont utilisées. Le second objectif est établi en comparant les résultats B et C. Le rendement lumineux est du secteur extérieur est 1.5 fois plus supérieur à celui du secteur intérieur. Enfin, le troisième objectif s'obtient en imposant un fit aux mesures C, D et E. La longueur d'atténuation résultante est environ de 2.5 m, qui est 4 fois moindre que la norme industrielle pour ce type de fibre.

À la suite de ces mesures, deux actions spécifiques ont été menées avant l'installation dans le détecteur d'ATLAS. Tout d'abord, il a été décidé de n'utiliser que 4 WLS pour le secteur extérieur, car le rendement lumineux obtenu est suffisant d'après les mesures effectuées. Ensuite, de nouvelles fibres transparentes ont été mises pour l'installation.

Table 10.1: Résultats des mesures avec le compteur MBTS. Le rendement lumineux est mesuré en unités de nombre de photoélectrons.

Label	**Secteur**	**Mesure**	**Fibre transparente**	**Rendement lumineux (en nombre de photoelectrons)**
A	Extérieur	4 WLS	Aucune	21
B	Extérieur	8 WLS	Aucune	41
C	Intérieur	8 WLS	Aucune	28
D	Intérieur	8 WLS	2.1 m	13
E	Intérieur	8 WLS	3.6 m	7

APPENDIX A

Auxiliary Material for the Combination of the four $H \to ZZ^{(*)}$ Searches

Control Regions Discriminants of the 2l2q and 2v2q Decay Channels

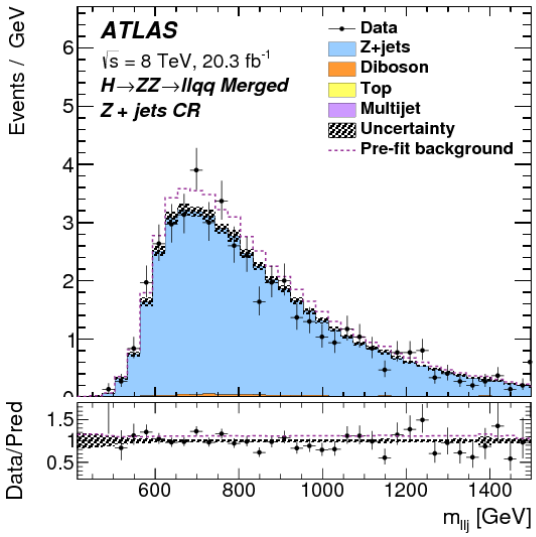

(A) Merged-jet ggF channel

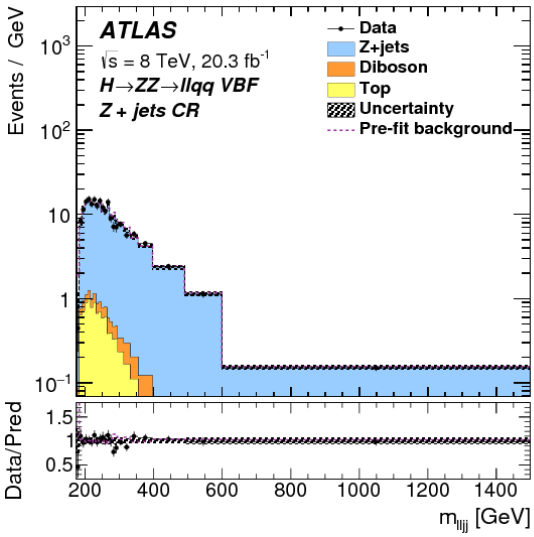

(B) VBF channel

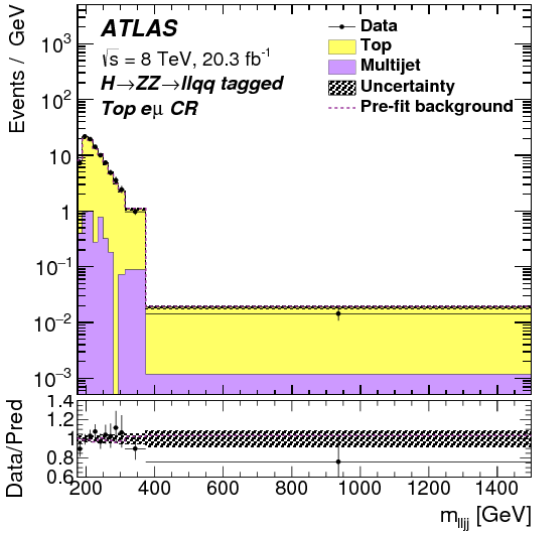

(C) Merged-jet ggF channel

FIGURE A.1: The distributions of $m_{\ell\ell jj}$ or $m_{\ell\ell j}$ in the Z+jets control region of the $H \to ZZ^{(*)} \to 2\ell 2q$ search in merged-jet ggF (A), VBF (B) event categories and the distribution of $m_{\ell\ell jj}$ in the $e\mu$ top-quark control region (C). The dashed line shows the total background used as input to the fit. The contribution labelled as "Top" includes both the $t\bar{t}$ and single-top processes. The bottom panels show the ratio of the observed data to the predicted background

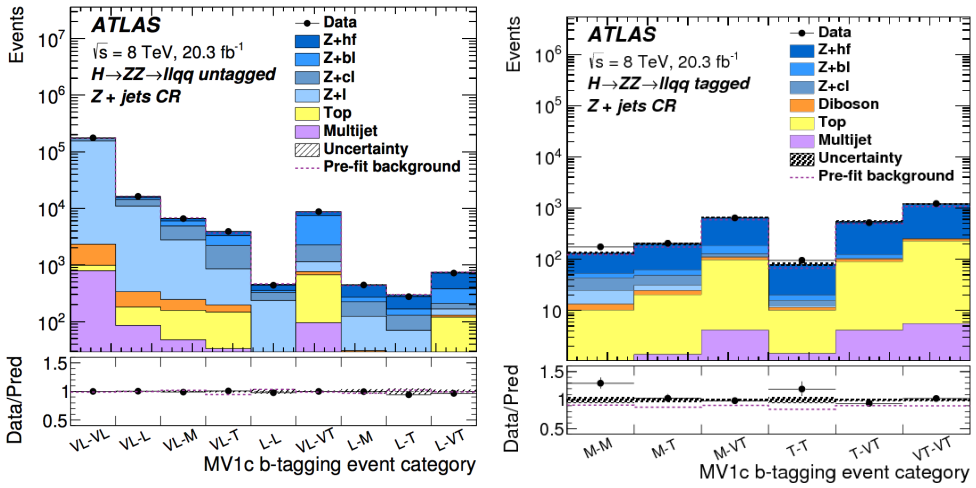

(A) Untagged (B) Tagged

Figure A.2: The distribution of the MV1c b-tagging event categories, based on the two signal jets, in the Z+jets control region in the untagged ggF (A) and tagged ggF (B) channels of the $H \to ZZ^{(*)} \to 2\ell 2q$ search. The b-jet purity generally increases from left to right. The dashed line shows the total background used as input to the fit. The contribution labelled as "Top" includes both the $t\bar{t}$ and single-top processes. The bottom panels show the ratio of the observed data to the predicted background.

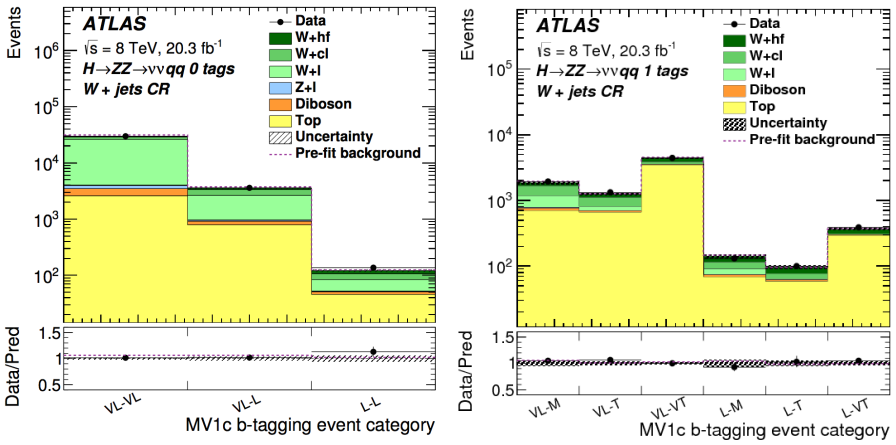

(A) 0-b-tag control region. (B) 1-b-tag control region.

Figure A.3: The distribution of the MV1c b-tagging event categories, based on the two signal jets, in the $W^{\pm}$+jets 0-b-tag (A) and 1-b-tag (B) control regions of the $H \to ZZ^{(*)} \to 2\nu 2q$ search. The b-jet purity generally increases from left to right. The dashed line shows the total background used as input to the fit. The contribution labelled as "Top" includes both the $t\bar{t}$ and single-top processes. The bottom panels show the ratio of the observed data to the predicted background.

APPENDIX B

Minimum Bias Trigger Scintillators for ATLAS: Commissioning and Run-2 Initial Operation

The following material was presented by the author at the conference ”Frontier Detectors for Frontier Physics: 13th Pisa Meeting on Advanced Detectors”, 2015, La Biodola, Isola d’Elba, Italy. The following material is published in Nuclear Instruments and Methods in Physics Research A 824 (2016) 24 - 26.

13th Pisa Meeting on Advanced Detectors

Minimum Bias Trigger Scintillators for ATLAS Commissioning and Run-2 Initial Operation

Overview

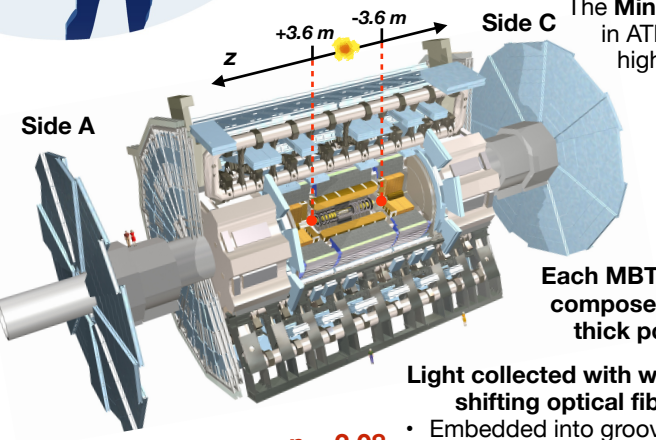

The **Minimum Bias Trigger Scintillators (MBTS)** were successfully deployed and operated in ATLAS during the running period of 2010 - 2013, known as LHC Run-1. They provided highly efficient triggering for minimum-bias proton-proton and heavy-ion collisions. The radiation dose from Run-1 (~10^4 Gy) degraded the transparency of the scintillating medium heavily (~50%). Therefore, the MBTS underwent a complete replacement in preparation for LHC Run-2 (2015-2017).

MBTS Layout for LHC Run-2

Each MBTS counter composed of 2 cm thick polystyrene

Light collected with wavelength shifting optical fibers (WLS)
- Embedded into grooves at the edges of each MBTS counter

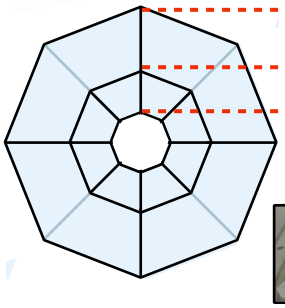

WLS connected to clear optical fibers transporting light to PMTs
- PMTs read out with electronics from the ATLAS Tile Calorimeter

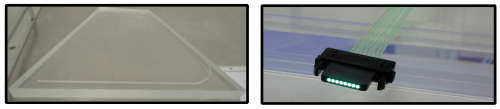

Reduced granularity and improved WLS routing scheme
- Segmentation of both inner and outer sector reduced from two pieces to one
- New WLS routing scheme maximises and homogenises light yield

More flexible readout
- 8 WLS are installed in both inner and outer sector
- Outer sector foreseen to be read out with 4 WLS in the early phase of Run 2
- When radiation damage has degraded the scintillator transparency, light yield can be recuperated by opting for all 8 WLS

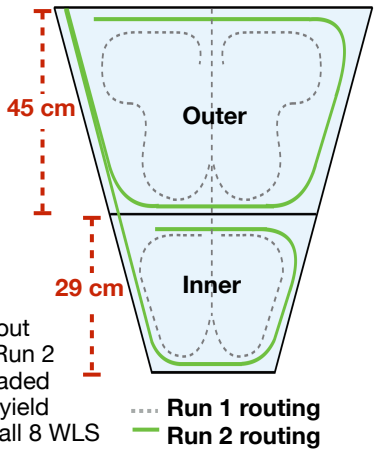

Commissioning with Cosmic Rays

A MBTS counter was characterised with cosmic radiation in a laboratory setup in order to study
- The yield from the two sectors
- The attenuation of the single-clad clear fibers intended for installation

Light yield determined with fit to spectra of integrated charge

$$f(x) = N \cdot \sum_{i=1}^{n} \left[\frac{e^{-\mu} \cdot \mu^i}{i!} \cdot \frac{1}{\sqrt{2\pi}\sqrt{i \cdot \sigma_{1PE}^2 + \sigma_{ped}^2}} \cdot e^{\frac{-(x-\mu_{ped}-i\cdot\mu_{1PE})^2}{2\cdot(i\cdot\sigma_{1PE}^2+\sigma_{ped}^2)}} \right]$$

- Convolution of *N* Gaussians with Poissonians
- μ, determined from the fit, is a direct measure of the number of photoelectrons
- Remaining parameters characterise the PMT and are determined from the calibration

Measured yield in agreement with expectations from detector design
- Yield from outer sector with 4 WLS 33% smaller than in inner
- Yield from outer sector with 8 WLS 48% larger than in inner
- 100% yield increase in outer sector when using 8 w.r.t. 4 WLS

Attenuation of clear fibers found to be unacceptably high. Double-clad fiber model procured and installed for Run 2

Performed measurements		
Sector	#WLS	Clear fiber
Outer	4	None
Outer	8	None
Inner	8	None
Inner	8	2.1 m
Inner	8	3.6 m

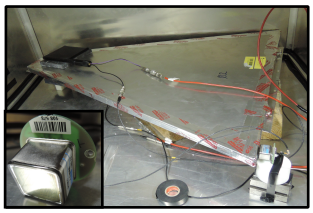

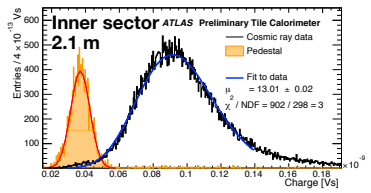

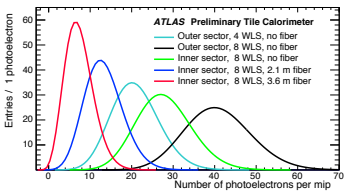

Initial Run-2 Operation

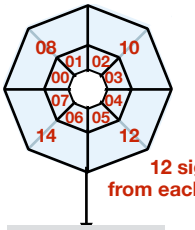

The Run-2 MBTS counters were integrated into the DAQ system in Summer 2014

12 signal outputs from each MBTS disk

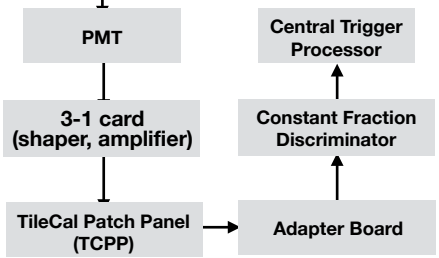

The former leading edge discriminators replaced with constant fraction discriminators
- Reduced time walk caused by the large dynamical range of MBTS signals
- Duration of discriminator output signals reduced from 200 to 50 ns

The timing of the MBTS trigger signals determined with first LHC Run-2 beam splashes (events induced by dumping beam on collimator)
- Timing w.r.t. independent, single-sided ATLAS calorimeter trigger on outgoing splash particles

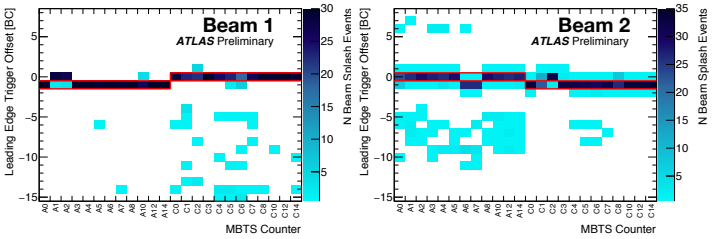

Operations under beam-splash events indicate that the MBTS are well-timed in and ready for LHC Run-2

Maria Hoffmann (CEA-Saclay) for the ATLAS Collaboration

APPENDIX C

Probing Compositeness with Higgs Boson Decays at the LHC

Introduction

An interesting BSM physics proposal is that of *compositeness*, which like 2HDM is a broader framework encompassing multiple theories. These theories predict the existence of a new, strongly interacting sector that couples to the SM particles. In compositeness models, the Higgs boson emerges as a massive pseudo-Goldstone boson. Furthermore, three heavy spin-1 resonances emerge in this theory, one neutral and two charged: ρ^0, ρ^+ and ρ^-. In the following study, it is investigated whether the decay of these ρ resonances involving Higgs bosons can be used as a probe of compositeness at the LHC. More specifically, the potential of the $\rho \to VH$ signature is assessed, where the Higgs boson and the associated Gauge boson have a high boost due to the massiveness of the ρ resonances. The discovery potential for the upcoming LHC operating periods is presented, showing that compositeness scales up to 3 TeV can be probed at the LHC with an integrated luminosity of 3000 fb^{-1} collected at $\sqrt{s}$ =13 TeV.

Author's Contribution

The following study was performed in close collaboration with Anna Kaminska, Rosy Nikolaidou (supervisor of the author) and Stathes Paganis. The author contributed to the following publication by generating the required samples, performing the baseline analysis, producing the final results, and writing the experimental sections. The upcoming study was performed in the very beginning of the duration of this thesis (in late 2013) and published in EPJ C [158] (in late 2014).

Eur. Phys. J. C (2014) 74:3181
DOI 10.1140/epjc/s10052-014-3181-z

THE EUROPEAN PHYSICAL JOURNAL C

Regular Article - Theoretical Physics

Probing compositeness with Higgs Boson decays at the LHC

Maria Hoffmann[1,a], **Anna Kaminska**[2], **Rosy Nicolaidou**[1], **Stathes Paganis**[3,4]

[1] DSM/IRFU (Institut de Recherches sur les Lois Fondamentales de l'Univers), CEA Saclay (Commissariat a l'Energie Atomique), 91191 Gif-sur-Yvette, France
[2] Deutsches Elektronen-Synchrotron DESY, 22607 Hamburg, Germany
[3] Department of Physics, National Taiwan University, No. 1, Sec. 4, Roosevelt Road, 10617 Taipei, Taiwan
[4] Department of Physics and Astronomy, The University of Sheffield, Sheffield S3 7RH, UK

Received: 31 July 2014 / Accepted: 12 November 2014 / Published online: 26 November 2014

Abstract A method is proposed to directly probe the Higgs boson compositeness using the unique characteristics of a boosted Higgs boson produced in association with a weak gauge boson ($W^{\pm}$, Z). The discovery potential for the upcoming LHC running is presented, showing that compositeness scales up to 3 TeV can be probed at the LHC with an integrated luminosity of $\mathcal{L} = 3000\ \text{fb}^{-1}$ collected at $\sqrt{s} = 13$ TeV.

1 Introduction

After the discovery of a particle consistent with the standard model (SM) Higgs boson [1–3] by the ATLAS and CMS Collaborations [4,5], intense research for the understanding of the details of the Higgs mechanism has commenced. Experimental data does not rule out a possible composite nature of the Higgs boson. In composite Higgs models, the Higgs boson is a (pseudo-) Goldstone boson emerging as a result of spontaneously broken global symmetry of a new, strong dynamics. Like in QCD, there is a new fermion sector causing spin-1 ρ-like bound states with masses at the compositeness energy scale.

The ρ-like bound states (ρ^0, ρ^+, ρ^-) couple to SM particles and can hence be directly probed at the LHC through searches for single lepton events ($\rho^{\pm} \to \ell^{\pm}\nu$) and searches for resonances decaying to two ($\rho^0 \to \ell^+\ell^-$) and three charged leptons ($\rho^{\pm} \to W^{\pm}Z \to \ell^{\pm}\nu\ell^+\ell^-$).

Currently, the dilepton searches set the best limits on compositeness [6,7]. However, for a large part of the compositeness model phase space, the branching ratio (BR) of $\rho^0 \to \ell^+\ell^-$ falls very fast with the ρ mass. Meanwhile, the BR of $\rho \to VH$, where V = W$^{\pm}$, Z, reaches a maximum. An observation of VH events in excess of what is expected by the SM and with an invariant mass at the TeV scale would be strong evidence for compositeness.

The decay products originating from heavy ρ decays are characterized by a very high transverse momentum ($p_{\perp}$). By exploiting this feature we propose a method to explore the presence of compositeness via the search for Higgs bosons with high $p_{\perp}$. This search is complementary to current searches using the dilepton invariant mass, and it may be more powerful than the latter in the parts of the compositeness model phase space where the $\text{BR}(\rho^0 \to \ell^+\ell^-) \lesssim 0.5\,\%$.

In this work we search for Higgs boson decays in the two channels providing the experimentally cleanest signatures for reconstructing the Higgs; the "golden" decay to four leptons, $H \to ZZ^* \to 4\ell$, where $\ell = e, \mu$, and the decay to two photons, $H \to \gamma\gamma$. The addition of the $H \to b\bar{b}$ mode is also discussed.

Since a Higgs originating from heavy ρ decays will carry a large $p_{\perp}$, all non-SM backgrounds for $H \to ZZ^* \to 4\ell$ and $H \to \gamma\gamma$ decays are expected to be small and SM Higgs backgrounds will thus dominate. In the $H \to b\bar{b}$ channel the non-Higgs background is still significant. The SM backgrounds can be strongly suppressed with a high Higgs $p_{\perp}$ requirement, which is the approach employed in this work. With the proposed method we are able to set a direct limit on the existence of compositeness and its energy scale.

2 Spin-1 resonances as a signal of composite Higgs

In this section we examine theories where the Higgs boson is a composite pseudo-Nambu–Goldstone boson (PGB) [8]. In these theories, a new strongly interacting sector with global symmetry $\mathcal{G}$ is present at the $\gtrsim$1 TeV compositeness scale (f). A composite Higgs boson emerges, much like the pion of QCD, as the PGB of a global symmetry breaking $\mathcal{G} \to \mathcal{H}$ of that sector. The explicit symmetry breaking is induced by

[a] e-mail: maria.hoffmann@cern.ch

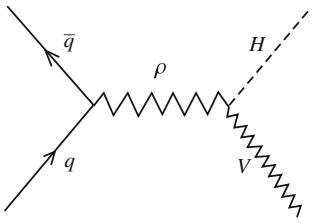

Fig. 1 Diagram depicting the process $pp \to \rho \to VH$

interactions of the SM gauge bosons and fermions with the strong sector.

The simplest example of such a strong sector is $SO(5) \to SO(4)$ [8], where $SO(4) \sim SU(2)_L \times SU(2)_R$, and the $10 - 6 = 4$ pseudo-Goldstones form a complex scalar field $SU(2)_L$ doublet that plays the role of the Higgs. The $SO(4) \sim SU(2)_L \times SU(2)_R$ global symmetry is gauged by the electroweak symmetry $\mathcal{G}_{\rm SM} = SU(2)_L \times U(1)_Y$ of the SM, which is external to the new strong sector. This means that the SM gauge bosons are external and couple to the strong sector. Interactions of the SM gauge bosons and fermions with the strong sector are responsible for the explicit breaking of the global symmetry $\mathcal{G}$. In this picture, loops of SM fermions and gauge bosons generate a Higgs potential which eventually breaks electroweak symmetry at scale v. This dynamically generated electroweak scale v may be lower than the strong sector (compositeness) breaking scale f. The ratio between the two scales $\xi = (v/f)^2$ is determined by the orientation of the electroweak group $\mathcal{G}_{\rm SM}$ with respect to the unbroken strong sector group $\mathcal{H} = SU(2)_L \times SU(2)_R$ in the true vacuum. If these two groups are misaligned, the electroweak symmetry is broken. Three composite pseudo-Goldstones become the longitudinal degrees of freedom of the weak gauge bosons and the fourth PGB defined along the misalignment angle θ is the light Higgs boson (Fig. 1).

In such composite Higgs models, vector meson ρ-like resonances appear and mix with the gauge bosons building new spin-1 eigenstates. Fermion resonances from the strong sector mix with SM fermions allowing them to interact directly with ρ resonances.

In this paper we consider the simplest case of the Minimal Composite Higgs Model (MCHM) [8]. The phenomenology of ρ resonances in this model, transforming in the adjoint representation of $SU(2)_L$, is representative of the entire family of composite Higgs models. It is expected that $SU(2)_L \times SU(2)_R \subset \mathcal{H}$ for any $\mathcal{G} \to \mathcal{H}$ composite Higgs model, in order to have custodial symmetry embedded in the construction. Since vector meson resonances appear in representations of the unbroken global group $\mathcal{H}$, ρ resonances transforming as $(3, 1)$ of $SU(2)_L \times SU(2)_R$ are a generic prediction of theories with a composite Higgs boson. Such resonances are expected to have substantial interactions with SM particles due to their natural mixing with W_μ fields. General properties of $SU(2)_L$ ρ mesons are well described in the framework of MCHM.

In the following analysis we consider ρ resonances transforming as a triplet of $SU(2)_L$, generically expected in composite Higgs models as discussed above. For the effective description of spin-1 resonances we follow the CCWZ approach [9,10], just as is done in [11] and presented in the appendix. This approach is fully equivalent to the Hidden Local Symmetries formalism [12]. Hence it is compatible with any generic composite Higgs construction used in the literature on the level of effective Lagrangian description. Moreover, it has a direct connection with deconstruction of extra dimensions, as discussed in [13].

When mixing effects in the spin-1/2 sector are neglected, compositeness models with a single vector meson can be described by just three parameters: the ρ mass, m_ρ, the ρ self-coupling g_ρ, and the parameter ξ. Based on naive dimensional analysis (NDA), the mass scale of ρ resonances is expected to be $m_\rho \sim g_\rho f$, where $1 < g_\rho < 4\pi$. The ρ production cross section is dominated by the Drell–Yan process. Neutral ρ decays to dileptons are particularly appealing to experimental searches for compositeness at the LHC. In particular for small $m_\rho (< 2$ TeV) and small values of parameter $\xi (\lesssim 0.1)$ the BR of $\rho^0 \to \ell^+\ell^-$ is large. However, observation of an excess in this channel would not by itself be sufficient to claim the observation of a composite ρ. Observation of the rest of the modes shown in Fig. 2 would be required.

Electroweak precision observables (see for example the discussion in [14]) and LHC collider data are sensitive to compositeness and can set limits in parts of the parameter space. Significant enhancement in the $H \to Z\gamma$ yield can also be induced by compositeness effects [16]. ATLAS and CMS have set limits on the ξ parameter using Higgs couplings $\xi < 0.22$ at 95 % CL, restricting the compositeness scale to $f > 0.5$ TeV [17,18]. It is safe to say that $\xi = 0.1$ at this point is still consistent with both electroweak precision constraints and LHC Higgs data, hence it will be used as a benchmark value in this paper. The compositeness scale can also be probed by direct searches for lightest vector resonances, though there is no strict relation between m_ρ and f. However, as mentioned before, by NDA we can expect $m_\rho \sim g_\rho f$. Using this assumption, the LHC narrow mass dilepton searches place limits in the region of $f \lesssim 1.5$ TeV$/g_\rho$ [6,7]. These searches are most efficient for exploring the light ρ resonance ($m_\rho \lesssim 2$ TeV) parameter space with substantial branching ratios into lepton pairs. However, for a big part of the parameter space the dilepton BR drops quickly to zero as a function of m_ρ, while the BR of $\rho \to VH$ tends to a maximum of about 70 %. The ρ BRs as a function of the m_ρ are shown in Fig. 2 for the benchmark parameter values of $\xi = 0.1$ and $g_\rho = 4$. Naively one would expect the BRs into VV and into VH to be equal. However, the fact

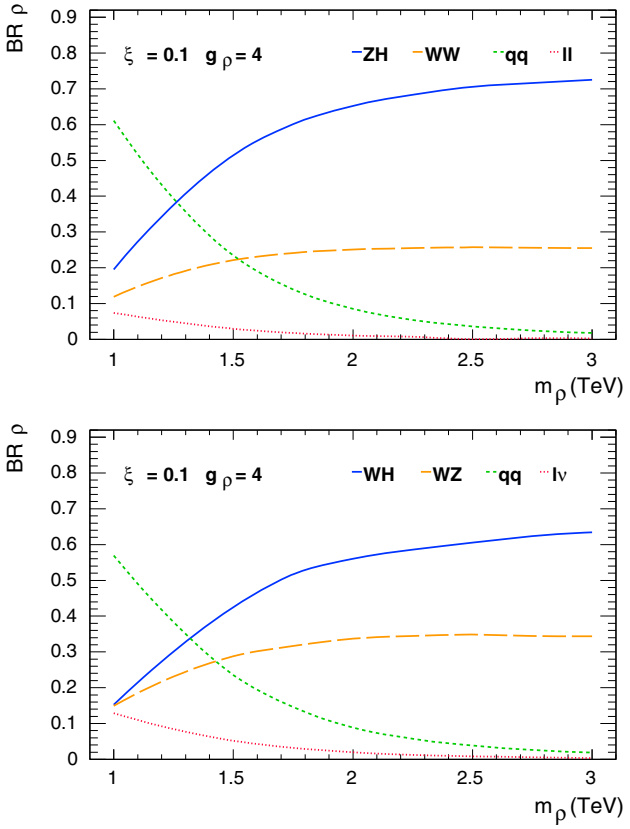

Fig. 2 Branching ratios of ρ^0 (*top*) and $\rho^{\pm}$ (*bottom*) decay modes for the benchmark parameters $\xi = 0.1$ and $g_\rho = 4$. The dilepton BR drops quickly to zero as a function of m_ρ while the BR of $\rho \to VH$ tends to a maximum of about 70 %

that the cosine of the Weinberg angle $\cos\theta_W$ is not equal 1 leads to substantial differences in the ρ couplings to W and Z bosons in some parts of the parameter space (especially for $g_\rho \lesssim 6$). For $m_\rho > 2$ TeV, the $\mathrm{BR}(\rho^0 \to \ell^+\ell^-)$ drops to values below 1 %. The branching ratios of ρ mesons do not depend strongly on the choice of g_ρ, but the production cross section behaves roughly as $1/g_\rho^2$, hence exclusion limits for ρ are g_ρ dependent. In general it is expected that g_ρ is substantially larger than the weak couplings g, g'. The ρ meson of QCD is described by $g_\rho \sim 6$. In this paper we consider $g_\rho = 4$ as a benchmark value, which is sufficiently above the weak couplings scale but still allows for significant ρ production at the LHC.

The large expected VH branching ratio of the ρ meson and the fact that both charged and neutral ρ's are involved offers a new possibility in experimental searches. We propose to search for boosted Higgs bosons produced by ρ^0, ρ^+, ρ^- decays in association with gauge bosons. For $\mathrm{BR}(\rho^0 \to \ell^+\ell^-) \gtrsim 0.5\,\%$ the proposed search is complementary to the dilepton search and can add information on the origin of a potential excess seen in the dilepton mass spectrum. For smaller $\mathrm{BR}(\rho^0 \to \ell^+\ell^-)$, the VH search becomes the most powerful in exploring the compositeness parameter space. In addition, a salient feature of the VH decay is that the Higgs invariant mass may be used to suppress the background.

3 Monte Carlo samples

The results presented in this paper are based on Monte Carlo (MC) samples generated with MadGraph5 [23] and parton showered with PYTHIA [24]. To simulate the response of an LHC-like experiment, realistic resolution and reconstruction efficiencies for electrons, muons, photons and jets were applied with the Delphes framework [25].

The signal samples include the processes $pp \to \rho \to VH$, where the definitions from Sect. 1 apply. These samples were generated at $\sqrt{s} = 13$ TeV with the benchmark parameter values $\xi = 0.1$ and $g_\rho = 4$. Typical values for the ρ production cross section as a function of the ρ mass computed with MadGraph5 are presented in Table 1. Numerical values of the BR for the processes $\rho^0 \to ZH$, $\rho^0 \to \ell^+\ell^-$, $\rho^\pm \to W^\pm H$, and $\rho^\pm \to \ell^\pm\nu$ are shown in Table 2.

The Higgs boson in the signal samples decays via either of the two channels $H \to \gamma\gamma$ or $H \to ZZ^* \to 4\ell$, where $\ell = e, \mu$. The vector boson produced in association with

Table 1 Total and individual cross sections for the process $pp \to \rho$ as a function of m_ρ. The cross sections were computed at $\sqrt{s} = 13$ TeV with the parameter values $\xi = (v/\Lambda_c)^2 = 0.1$, $g_\rho = 4$. The statistical uncertainty is less than 10^{-7} fb, and therefore not quoted in this table

m_ρ [TeV]	σ_{ρ^0} [fb]	σ_{ρ^+} [fb]	σ_{ρ^-} [fb]	Total [fb]
1.50	59.11	92.27	32.94	184.3
1.75	27.92	45.25	14.91	88.08
2.00	13.94	23.35	7.172	44.46
2.25	7.245	12.48	3.606	23.33
2.50	3.873	6.835	1.874	12.58
2.75	2.121	3.807	0.992	6.920
3.00	1.118	2.144	0.543	3.805

Table 2 Branching ratios for the decays $\rho^0 \to ZH \to \ell^+\ell^- H$, $\rho^\pm \to W^\pm H$, and $\rho^\pm \to \ell^\pm\nu$ as a function of m_ρ. The branching ratios were computed with the parameter values $\xi = (v/\Lambda_c)^2 = 0.1$, $g_\rho = 4$

m_ρ [TeV]	$\rho^0 \to ZH$	$\rho^0 \to \ell^+\ell^-$	$\rho^\pm \to W^\pm H$	$\rho^\pm \to \ell^\pm\nu$
1.50	0.515	0.0297	0.416	0.0716
1.75	0.603	0.0179	0.499	0.0442
2.00	0.653	0.0110	0.551	0.0277
2.25	0.683	0.00703	0.584	0.0180
2.50	0.704	0.00469	0.604	0.0120
2.75	0.714	0.00316	0.617	0.00833
3.00	0.725	0.00229	0.627	0.00593

the Higgs boson is constrained to decay hadronically, i.e. $V \to jj$.

As already mentioned, the main source of background in this search is SM Higgs production. In this study we consider the three main Higgs production mechanisms at the LHC; gluon–gluon fusion (ggF), vector boson fusion (VBF) and associated production (WH/ZH).[1] All samples were generated with a Higgs mass of $m_H = 125$ GeV, and scaled with the relevant cross sections and branching ratios reported by the LHC Higgs cross-section working group and the Particle Data Group [15,28].

In the following we further assess the improvement of the search when adding the high BR channel $H \to b\bar{b}$. This is done by extrapolating the results obtained for the $H \to \gamma\gamma$ channel using results from a recent combination reported by the LHC experiments in [21,22].

4 Analysis strategy

The analysis method presented in this paper aims toward optimizing the discovery potential of a composite Higgs during the upcoming LHC runs. A discovery could come in the form of a direct observation of Higgs boson events with anomalously high $p_\perp$ or ρ decays to VH along with an excess of events with dilepton invariant mass at the TeV scale.

The distribution of the transverse momentum of SM Higgs bosons and of Higgs bosons produced from ρ decays is shown in Fig. 3. Given the noticeable difference in the shape of the distributions, the transverse momentum can be used as a discriminating variable to suppress the SM background. The large transverse boost of these Higgs events causes the opening angle $\Delta R = \sqrt{\Delta\eta^2 + \Delta\phi^2}$ between the decay products (ZZ and $\gamma\gamma$) to be significantly smaller than that from a SM Higgs, which is shown in Fig. 4. The characteristic ΔR is not exploited in the present analysis strategy, but may be used in future searches to increase the sensitivity.

4.1 Event selection

A simple event selection inspired by the analysis strategies of ATLAS and CMS is implemented. The $H \to \gamma\gamma$ signal is selected by requiring two hard photons with E_T of the leading (subleading) photon being ≥ 40 (30) GeV. Events from the $H \to ZZ^* \to 4\ell$ decay are selected by requiring two pairs of oppositely charged, same-flavor leptons. The three leptons in the quadruplet with the largest transverse momentum must, in descending order, satisfy $p_\perp \geq 20$, 15, 10 GeV. Muons, electrons and photons must, respectively, satisfy $|\eta| < 2.7$, 2.47, 2.37. Common for the channels is that the invariant mass of the Higgs final states[2] must be in the range 100–150 GeV. To suppress the SM backgrounds, an additional requirement on the transverse momentum of the Higgs system of $p_\perp \geq 550$ GeV is applied.

Since the applied event selection is simplified with respect to that of the LHC experiments, all samples are multiplied with analysis efficiencies representative of those presented by ATLAS and CMS. These values were obtained at $\sqrt{s} = 8$ TeV [19,20], and have been scaled to $\sqrt{s} = 13$ TeV by assuming a slight increase in efficiency. A factor of 0.4 is applied to the signal samples in both Higgs decay channels. The factor applied to the $H \to ZZ^* \to 4\ell (H \to \gamma\gamma)$ background sample is 0.3(0.4) for ggF, 0.2(0.5) for VBF, and 0.5(0.5) for WH/ZH. Furthermore, the signal is multiplied by a scale factor accounting for the increased detector fiducial acceptance, which is a consequence of the boost that causes the Higgs to be emitted at lower η. The scale factor applied

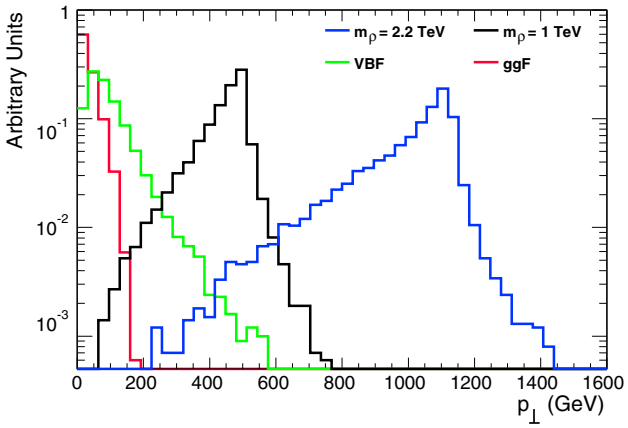

Fig. 3 The distribution of transverse momentum $p_\perp$ of SM Higgs bosons and of Higgs bosons originating from the $\rho \to VH$ decay

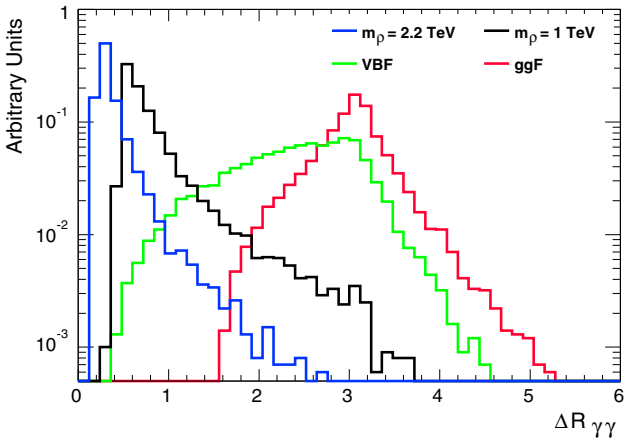

Fig. 4 The opening angle $\Delta R = \sqrt{\Delta\eta^2 + \Delta\phi^2}$ between two photons from SM Higgs boson decays and from $\rho \to VH \to V\gamma\gamma$ decays

[1] The cross section of a Higgs boson produced in association with a pair of top or b quarks ($t\bar{t}H$ or $b\bar{b}H$) is ≈ 3 times lower than the WH/ZH production at $\sqrt{s} = 13$ TeV and therefore not considered in this study.

[2] i.e. The 4ℓ and $\gamma\gamma$ system.

Table 3 Number of background events remaining after the full selection in Sect. 4.1 with an integrated luminosity of $\mathcal{L} = 1$ fb^{-1} at $\sqrt{s} = 13$ TeV

SM production	$H \to ZZ^* \to 4\ell$	$H \to \gamma\gamma$
ggF	0	0
VBF	1.1×10^{-4}	5.2×10^{-3}
ZH	4.0×10^{-5}	5.6×10^{-4}
WH	6.3×10^{-5}	8.8×10^{-4}

Table 4 Number of signal events remaining after the full selection in Sect. 4.1 with an integrated luminosity of $\mathcal{L} = 1$ fb^{-1} at $\sqrt{s} = 13$ TeV

m_ρ [TeV]	$H \to ZZ^* \to 4\ell$	$H \to \gamma\gamma$
1.50	3.8×10^{-3}	6.0×10^{-2}
1.75	2.6×10^{-3}	3.9×10^{-2}
2.00	1.5×10^{-3}	2.3×10^{-2}
2.25	8.9×10^{-4}	1.5×10^{-2}
2.50	5.1×10^{-4}	8.3×10^{-3}
2.75	2.9×10^{-4}	4.7×10^{-3}
3.00	1.6×10^{-4}	2.6×10^{-3}

to the $H \to \gamma\gamma$ channel is 1.2, while 1.3 is applied to $H \to ZZ^* \to 4\ell$.

The contribution from the non-resonant QCD background in the $\gamma\gamma + jj$ final state is estimated by extrapolating the obtained number of background events reported in [29] with the expected increase in production cross section [30], multiplied with the selection efficiency of the $p_\perp$ requirement. This efficiency is estimated with a $pp \to \gamma\gamma + jj$ sample generated with MadGraph and found to be on the order of 10^{-4}. With an integrated luminosity of 3,000 fb^{-1} the number of expected events from this process is more than one order of magnitude smaller than what is expected from the dominant SM Higgs background. This particular background is therefore considered safe to ignore. Similarly, the contribution from the ZZ continuum ($pp \to ZZ$) is assumed to be negligible after the rather tight $p_\perp$ requirement.

The numbers of signal and background events per fb^{-1} remaining after the full selection are presented in Tables 3 and 4. As seen, the contribution from ggF production is completely suppressed.

5 Results: discovery potential at the LHC

The analysis described in Sect. 4 is used to assess the compositeness discovery potential at the LHC. The results are presented in terms of significance defined as $Z = \sqrt{2\left[(s+b)\ln(1+s/b) - s\right]}$ [26], with s and b being the number of signal and background events remaining after the full selection.

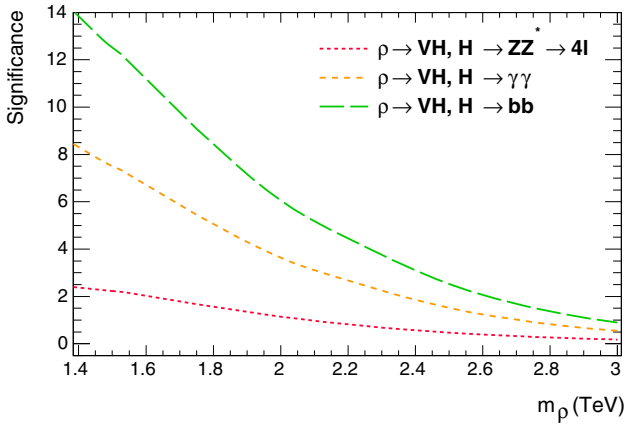

Fig. 5 Expected significance as a function of m_ρ obtainable with a single LHC experiment using the $H \to \gamma\gamma$, $H \to ZZ^* \to 4\ell$, and $H \to b\bar{b}$ decay channels. The latter was obtained with an optimistic extrapolation of the results obtained with the $H \to \gamma\gamma$ channel with the results reported in [21,22]. The significance was computed with an integrated luminosity of $\mathcal{L} = 300$ fb^{-1} collected at $\sqrt{s} = 13$ TeV with the parameter values $\xi = (v/\Lambda_c)^2 = 0.1$, $g_\rho = 4$

The expected impact of the inclusion of the $H \to b\bar{b}$ channel is also considered.The problem with this channel is the presence of significant QCD non-SM Higgs background requiring careful subtraction and detailed treatment of systematics. A realistic estimate of the impact of $H \to b\bar{b}$ can be obtained using existing analyses in similar event topologies to the VH. Recent studies at the LHC [21,22] showed that when searching for a Higgs boson produced via the $t\bar{t}H$ production mechanism, the expected significance increases by a factor of 1.7 when combining the $H \to \gamma\gamma$ channel with $H \to b\bar{b}$. The result reported in [21,22] is based on a detailed, full simulation including all systematics. Therefore, to realistically include the impact of the $H \to b\bar{b}$ channel, the significance obtained here with the $H \to \gamma\gamma$ channel is extrapolated by the factor 1.7.

The significance as a function of the ρ mass scale (m_ρ) is considered for two integrated luminosity points: $\mathcal{L} = 300$ fb^{-1} and $\mathcal{L} = 3000$ fb^{-1}. These sample sizes correspond to the expected integrated luminosity recorded after LHC and HL-LHC operation anticipated around the years 2020 and 2030, respectively [27]. The results obtained for the individual channels at $\sqrt{s} = 13$ TeV are presented in Figs. 5 and 6 for m_ρ in the interval 1.4–3 TeV.

As observed in Figs. 5 and 6 the diphoton channel is more sensitive than the four-lepton channel. This feature is a result of the BR($H \to \gamma\gamma$) being more than an order of magnitude larger than BR($H \to ZZ^* \to 4\ell$). The drop in significance with increasing m_ρ is a result of the ρ production cross section decreasing with higher m_ρ. From Fig. 5 we see that a single LHC experiment with a data sample of $\mathcal{L} = 300$ fb^{-1} is able to observe a signal with a significance of 3σ at $m_\rho \sim 2.5$ TeV. With $\mathcal{L} = 3000$ fb^{-1} the search is sensi-

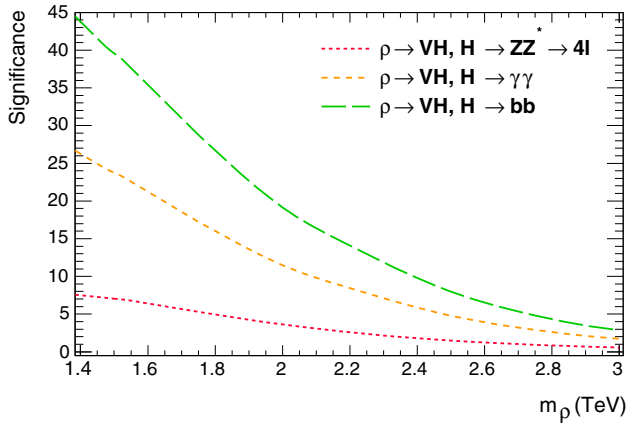

Fig. 6 Expected significance as a function of m_ρ obtainable with a single LHC experiment using the $H \to \gamma\gamma$, $H \to ZZ^* \to 4\ell$, and $H \to b\bar{b}$ decay channels. The latter was obtained with an optimistic extrapolation of the results obtained with the $H \to \gamma\gamma$ channel with the results reported in [21,22]. The significance was computed with an integrated luminosity of $\mathcal{L} = 3000\ \text{fb}^{-1}$ collected at $\sqrt{s} = 13$ TeV with the parameter values $\xi = (v/\Lambda_c)^2 = 0.1$, $g_\rho = 4$

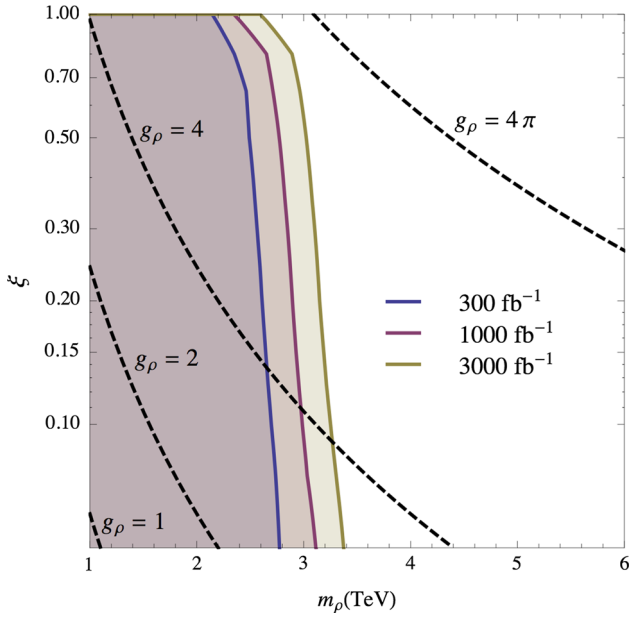

Fig. 7 Summary of the 95 % CL expected sensitivity for a single LHC experiment at $\sqrt{s} = 13$ TeV. The bands show the regions on the (ξ, m_ρ) plane that can be excluded using the combination of the channels $H \to \gamma\gamma$, $H \to ZZ^* \to 4\ell$, and $H \to b\bar{b}$. The latter was obtained with an optimistic extrapolation of the results obtained with the $H \to \gamma\gamma$ channel with the results reported in [21,22]. The $g_\rho = 4\pi$ line defines the perturbativity boundary above which the effective lagrangian description breaks down

tive all up to $m_\rho \sim 3$ TeV. A combination of ATLAS and CMS measurements with $\mathcal{L} = 3000\ \text{fb}^{-1}$ can hence allow sensitivity to compositeness scales up to $m_\rho \sim 3$–4 TeV.

The 95 % CL sensitivity expected for the combination of the three channels for the $SO(5)/SO(4)$ model considered here with $m_\rho \sim g_\rho f$ on the (ξ, m_ρ) plane is presented in Fig. 7 for three different luminosity scenarios. The non-perturbative limit $g_\rho = 4\pi$, where g_ρ the physical coupling of the three ρ resonances, is also shown.

It is worth noting that this result might be modified if the impact of fermion resonances is taken into account. This effect is highly model-dependent and relevant only if the ρ resonances interact directly with fermion resonances. In this case the interactions of vector mesons with third generation quarks can be enhanced due to partial compositeness. This does not affect the ρ production cross sections, but modifies the ρ decay widths into third generation quarks. Moreover, if the fermion resonances are light (which is motivated by naturalness arguments) the decays of the vector meson into a SM fermion and a fermion resonance, and the decays of ρ into two fermion resonances, might become kinematically available. This would make the impact on the width and branching ratios of the vector meson even stronger.

6 Summary and conclusions

In this paper the compositeness discovery potential for the upcoming LHC runs was presented. A method was proposed to directly probe the Higgs boson compositeness by identifying boosted Higgs events from $\rho \to VH$ decays. We have demonstrated that a search for compositeness is feasible with a data sample as small as $\mathcal{L} = 300\ \text{fb}^{-1}$ collected at $\sqrt{s} = 13$ TeV, which corresponds to the data sample recorded by the LHC in the year 2020.

The main result of this work is that compositeness scales up to $g_\rho f \sim 3$–4 TeV can be probed at the LHC with $\mathcal{L} = 3000\ \text{fb}^{-1}$ by alone using the VH decay mode. Combining the VH channel with dilepton and dijet searches could further increase the sensitivity and reach of the search. The proposed search can immediately be employed in the Higgs analyses currently performed by the ATLAS and CMS experiments.

Acknowledgments AK would like to thank the Mainz Institute for Theoretical Physics (MITP) for its hospitality and support during the completion of this work.

7 Appendix: Effective Lagrangian for a ρ resonance

Following [11], the PNG bosons $\Pi(x) = \Pi^{\hat{a}}(x)\, T^{\hat{a}}$ of $\mathcal{G} \to \mathcal{H}$ symmetry breaking can be described by $U(\Pi) = e^{i\Pi(x)/f}$ transforming as

$$U(\Pi) \to g\, U(\Pi)\, h^\dagger(\Pi, g), \qquad g \in \mathcal{G},\ h \in \mathcal{H}. \tag{1}$$

The leading-order effective Lagrangian term describing self-interactions of these bosons takes the form

$$\mathcal{L}^{\Pi} = \frac{f^2}{4}\mathrm{Tr}\left\{d_\mu d^\mu\right\} \tag{2}$$

where d_μ is defined by

$$-iU^\dagger D_\mu U = d_\mu^{\hat{a}} T^{\hat{a}} + E_\mu^a T^a = d^a + E^a \tag{3}$$

and $T^{\hat{a}}$, T^a are the broken and unbroken generators of $\mathcal{G}$. The covariant derivative takes into account the external gauging and introduces interactions of PNG bosons with electroweak bosons. For the description of the vector meson transforming as

$$(T^a \rho_\mu^a) \;\rightarrow\; h\,(T^a \rho_\mu^a)\,h^\dagger - \frac{i}{g_\rho} h\partial_\mu h^\dagger, \quad h \in \mathcal{H}, \tag{4}$$

(where in our case T^a are $SU(2)_L$ generators), we use the general leading-order effective Lagrangian

$$\mathcal{L}^{\rho} = -\frac{1}{4g_\rho^2}\rho_{\mu\nu}^a \rho^{a\,\mu\nu} + \frac{m_\rho^2}{2g_\rho^2}\left(\rho_\mu^a - E_\mu^a\right)^2. \tag{5}$$

The connection term E_μ^a introduces interactions of ρ mesons with PNG bosons and electroweak bosons.

References

1. F. Englert, R. Brout, Broken symmetry and the mass of gauge vector mesons. Phys. Rev. Lett. **13**, 321 (1964)
2. P.W. Higgs, Broken symmetries and the masses of gauge bosons. Phys. Rev. Lett. **13**, 508 (1964)
3. G. Guralnik, C. Hagen, T. Kibble, Global conservation laws and massless particles. Phys. Rev. Lett. **13**, 585 (1964)
4. C.M.S. Collaboration, Observation of a new boson at a mass of 125 GeV with the CMS experiment at the LHC. Phys. Lett. B **716**, 30 (2012)
5. ATLAS Collaboration, Observation of a new particle in the search for the standard model Higgs boson with the ATLAS detector at the LHC. Phys. Lett. B **716**, 1 (2012)
6. CMS Collaboration, Search for narrow resonances in dilepton mass spectra in pp collisions at $\sqrt{s} = 7$ TeV. arXiv:1206.1849 [hep-ex] (2013)
7. ATLAS Collaboration, Search for high-mass dilepton resonances in pp collisions at $\sqrt{s} = 8$ TeV with the ATLAS detector. arXiv:1405.4123 [hep-ex] (2014)
8. R. Contino, The Higgs as a composite Nambu–Goldstone boson. arXiv:1005.4269 [hep-ph] (2010)
9. S.R. Coleman, J. Wess, B. Zumino, Structure of phenomenological Lagrangians. 1. Phys. Rev. **177**, 2239 (1969)
10. C.G. Callan Jr, S.R. Coleman, J. Wess, B. Zumino, Structure of phenomenological Lagrangians. 2. Phys. Rev. **177**, 2247 (1969)
11. R. Contino, D. Marzocca, D. Pappadopulo, R. Rattazzi, On the effect of resonances in composite Higgs phenomenology. JHEP **1110**, 081 (2011)
12. M. Bando, T. Kugo, K. Yamawaki, Nonlinear realization and hidden local symmetries. Phys. Rept. **164**, 217 (1988)
13. G. Panico, A. Wulzer, The discrete composite Higgs model. JHEP **1109**, 135 (2011)
14. R. Contino, C. Grojean, D. Pappadopulo, R. Rattazzi, A. Thamm, Strong Higgs interactions at a linear collider. JHEP **1402**, 006 (2014)
15. LHC Higgs Cross-Section Working Group, Handbook of LHC Higgs Cross Sections: 3. Higgs Properties. arXiv:1307.1347 [hep-ph] (2013)
16. A. Azatov, R. Contino, A. Di Iura, J. Galloway, New prospects for Higgs compositeness in $h \rightarrow Z\gamma$. Phys. Rev. D **88**, 075019 (2013)
17. ATLAS Collaboration, Constraints on new phenomena via Higgs boson coupling measurements with the ATLAS detector, ATLAS-CONF-2014-10 (2014)
18. A. Azatov, J. Galloway, Electroweak symmetry breaking and the Higgs boson: confronting theories at colliders. Int. J. Mod. Phys. A **28**, 1330004 (2013)
19. ATLAS Collaboration, Measurements of Higgs boson production and couplings in the four-lepton channel in pp collisions at center-of-mass energies of 7 and 8 TeV with the ATLAS detector. arXiv:1408.5191 [hep-ph] (2014)
20. CMS Collaboration, H to ZZ to 4l, CMS-PAS-FTR-13-003 (2013)
21. ATLAS Collaboration, Search for $H \rightarrow \gamma\gamma$ produced in association with top quarks and constraints on the top quark-Higgs boson Yukawa coupling using data taken at 7 TeV and 8 TeV with the ATLAS detector, ATLAS-CONF-2014-043 (2014)
22. ATLAS Collaboration, Search for the standard model Higgs boson produced in association with top quarks and decaying to $b\bar{b}$ in pp collisions at $\sqrt{s}$ =8 TeV with the ATLAS detector at the LHC, ATLAS-CONF-2014-011 (2014)
23. J. Alwall et al. Madgraph 5 : Going beyond. arXiv:1106.0522v1 [hep-ph] (2011)
24. T. Sjostrand, S. Mrenna, P. Skands, A brief introduction to PYTHIA 8.1. Comput. Phys. Commun. **178**, 852 (2008)
25. S. Ovyn, X. Rouby, V. Lemaitre, DELPHES, a framework for fast simulation of a generic collider experiment. arXiv:0903.2225 [hep-ph] (2009)
26. G. Cowan, K. Cranmer, E. Gross, O. Vitells, Asymptotic formulae for likelihood-based tests of new physics. Eur. Phys. J. C **71**, 1–19 (2011)
27. ECFA high luminosity LHC experiments workshop: physics and technology challenges. 94th Plenary ECFA meeting (2013)
28. J. Beringer et al., Review of particle physics (RPP). Phys. Rev. D **86**, 010001 (2012)
29. ATLAS Collaboration, Measurement of Higgs boson production in the diphoton decay channel in pp collisions at center-of-mass energies of 7 and 8 TeV with the ATLAS detector. arXiv:1408.7084 [hep-ex] (2014)
30. ATLAS Collaboration, Projections for measurements of Higgs boson cross sections, branching ratios and coupling parameters with the ATLAS detector at a HL-LHC, ATL-PHYS-PUB-2013-014 (2013)

Bibliography

[1] S. L. Glashow. "Partial Symmetries of Weak Interactions". In: *Nucl. Phys.* 22 (1961), pp. 579–588. DOI: 10.1016/0029-5582(61)90469-2.

[2] A. Salam. "Weak and Electromagnetic Interactions". In: *Proceedings of the 8th Nobel symposium, Ed. N. Svartholm, Almqvist & Wiskell, 1968,* Conf. Proc. C680519 (1968), pp. 367–377. URL: {http://inspirehep.net/record/53083}.

[3] G. 't Hooft et al. "Regularization and Renormalization of Gauge Fields". In: *Nucl. Phys.* B44 (1972), pp. 189–213. DOI: 10.1016/0550-3213(72)90279-9.

[4] S. Weinberg. "A Model of Leptons". In: *Phys. Rev. Lett.* 19 (1967), pp. 1264–1266. DOI: 10.1103/PhysRevLett.19.1264.

[5] K. A. Olive et al. "Review of Particle Physics". In: *Chin. Phys.* C38 (2014), p. 090001. DOI: 10.1088/1674-1137/38/9/090001.

[6] The CMS Collaboration. "Observation of a new boson at a mass of 125 GeV with the CMS experiment at the LHC". In: *Phys. Lett.* B716 (2012), pp. 30–61. DOI: 10.1016/j.physletb.2012.08.021. arXiv: 1207.7235 [hep-ex].

[7] The ATLAS Collaboration. "Observation of a new particle in the search for the Standard Model Higgs boson with the ATLAS detector at the LHC". In: *Phys. Lett.* B716 (2012), pp. 1–29. DOI: 10.1016/j.physletb.2012.08.020. arXiv: 1207.7214 [hep-ex].

[8] T. Kibble. "Symmetry breaking in non-Abelian gauge theories". In: *Phys. Rev.* 155 (1967), pp. 1554–1561. DOI: 10.1103/PhysRev.155.1554.

[9] P. W. Higgs. "Spontaneous symmetry breakdown without massless bosons". In: *Phys. Rev.* 145 (1966), pp. 1156–1163. DOI: 10.1103/PhysRev.145.1156.

[10] G. Guralnik et al. "Global conservation laws and massless particles". In: *Phys. Rev. Lett.* 13 (1964), pp. 585–587. DOI: 10.1103/PhysRevLett.13.585.

[11] P. W. Higgs. "Broken symmetries and the masses of gauge bosons". In: *Phys. Rev. Lett.* 13 (1964), pp. 508–509. DOI: 10.1103/PhysRevLett.13.508.

[12] P. W. Higgs. “Broken symmetries, massless particles and gauge fields”. In: *Phys. Lett.* 12 (1964), pp. 132–133. DOI: 10.1016/0031-9163(64)91136-9.

[13] I. van Vulpen. ”Lecture notes in The Standard Model Higgs Boson”. Part of the Lecture Particle Physics II, UvA Particle Physics Master 2013-2014. Oct. (2013). URL: https://www.nikhef.nl/~ivov/HiggsLectureNote.pdf.

[14] T. Plehn et al. “The quartic higgs coupling at hadron colliders”. In: *Phys. Rev.* D72 (2005), p. 053008. DOI: 10.1103/PhysRevD.72.053008. arXiv: hep-ph/0507321 [hep-ph].

[15] J. Goldstone et al. “Broken Symmetries”. In: *Phys. Rev.* 127 (3 Aug. 1962), pp. 965–970. DOI: 10.1103/PhysRev.127.965. URL: http://link.aps.org/doi/10.1103/PhysRev.127.965.

[16] Y. Nambu et al. “Dynamical Model of Elementary Particles Based on an Analogy with Superconductivity. I”. In: *Phys. Rev.* 122 (1961), pp. 345–358. DOI: 10.1103/PhysRev.122.345.

[17] J. T. Seeman. “The Stanford Linear Collider”. In: *Ann. Rev. Nucl. Part. Sci.* 41 (1991), pp. 389–428. DOI: 10.1146/annurev.ns.41.120191.002133.

[18] ”LEP design report”. Copies shelved as reports in LEP, PS and SPS libraries. Geneva: CERN, 1984. URL: https://cds.cern.ch/record/102083.

[19] ”Design Report Tevatron 1 project”. Tech. rep. FERMILAB-DESIGN-1984-01. 1984. URL: https://cds.cern.ch/record/1478620.

[20] J. Ellis et al. “The Probable Fate of the Standard Model”. In: *Phys. Lett.* B679 (2009), pp. 369–375. DOI: 10.1016/j.physletb.2009.07.054. arXiv: 0906.0954 [hep-ph].

[21] The LEP Collaborations, the LEP EW Working Group and the SLD Heavy Flavour Group. “A Combination of preliminary electroweak measurements and constraints on the standard model”. In: (2004). arXiv: hep-ex/0412015 [hep-ex].

[22] The OPAL, DELPHI, ALEPH and L3 Collaboration. “Search for the standard model Higgs boson at LEP”. In: *Phys. Lett.* B565 (2003), pp. 61–75. DOI: 10.1016/S0370-2693(03)00614-2. arXiv: hep-ex/0306033 [hep-ex].

[23] The CDF and D0 Collaboration. “Higgs Boson Studies at the Tevatron”. In: *Phys. Rev.* D88.5 (2013), p. 052014. DOI: 10.1103/PhysRevD.88.052014. arXiv: 1303.6346 [hep-ex].

[24] T. Hambye et al. “Matching conditions and Higgs mass upper bounds revisited”. In: *Phys. Rev.* D55 (1997), pp. 7255–7262. DOI: 10.1103/PhysRevD.55.7255. arXiv: hep-ph/9610272 [hep-ph].

[25] ”ALEPH: technical report 1983”. Geneva: CERN, 1983. URL: https://cds.cern.ch/record/300680.

[26] ”DELPHI: technical proposal”. Tech. rep. CERN-LEPC-83-3. DELPHI-83-66. LEPC-P-2. 1983. URL: https://cds.cern.ch/record/300668.

[27] ”Technical proposal: L3”. Tech. rep. CERN-LEPC-83-5. LEPC-P-4. 1983. URL: https://cds.cern.ch/record/297266.

[28] ”The OPAL detector: technical proposal”. Tech. rep. CERN-LEPC-83-4. LEPC-P-3. 1983. URL: https://cds.cern.ch/record/300669.

[29] ”The CDF-II detector: Technical design report”. Tech. rep. FERMILAB-DESIGN-1996-01. FERMILAB-PUB-96-390-E. 1996. URL: https://cds.cern.ch/record/1478626.

[30] ”An Experiment at D0 to Study anti-Proton - Proton Collisions at 2-TeV: Design Report”. Tech. rep. FERMILAB-PUB-83-111-E. PRINT-84-0306 (FERMILAB). FERMILAB-DESIGN-1983-04. 1983. URL: https://cds.cern.ch/record/1478625.

[31] The CMS Collaboration. “Study of the Mass and Spin-Parity of the Higgs Boson Candidate Via Its Decays to Z Boson Pairs”. In: *Phys. Rev. Lett.* 110.8 (2013), p. 081803. DOI: 10.1103/PhysRevLett.110.081803. arXiv: 1212.6639 [hep-ex].

[32] The CMS Collaboration. “Precise determination of the mass of the Higgs boson and tests of compatibility of its couplings with the standard model predictions using proton collisions at 7 and 8 TeV”. In: *Eur. Phys. J.* C75.5 (2015), p. 212. DOI: 10.1140/epjc/s10052-015-3351-7. arXiv: 1412.8662 [hep-ex].

[33] The ATLAS Collaboration. “Evidence for the spin-0 nature of the Higgs boson using ATLAS data”. In: *Phys. Lett.* B726 (2013), pp. 120–144. DOI: 10.1016/j.physletb.2013.08.026. arXiv: 1307.1432 [hep-ex].

[34] The ATLAS Collaboration. “Measurements of Higgs boson production and couplings in diboson final states with the ATLAS detector at the LHC”. In: *Phys. Lett.* B726 (2013). [Erratum: Phys. Lett.B734,406(2014)], pp. 88–119. DOI: 10.1016/j.physletb.2014.05.011, 10.1016/j.physletb.2013.08.010. arXiv: 1307.1427 [hep-ex].

[35] The ATLAS and CMS Collaboration. “Combined Measurement of the Higgs Boson Mass in pp Collisions at $\sqrt{s} = 7$ and 8 TeV with the ATLAS and CMS Experiments”. In: *Phys. Rev. Lett.* 114 (2015), p. 191803. DOI: 10.1103/PhysRevLett.114.191803. arXiv: 1503.07589 [hep-ex].

[36] J. R. Andersen et al. "Handbook of LHC Higgs Cross Sections: 3. Higgs Properties". In: (2013). Ed. by S Heinemeyer et al. DOI: 10.5170/CERN-2013-004. arXiv: 1307.1347 [hep-ph].

[37] The ATLAS Collaboration. "Constraints on the off-shell Higgs boson signal strength in the high-mass ZZ and WW final states with the ATLAS detector". In: *Eur. Phys. J.* C75.7 (2015), p. 335. DOI: 10.1140/epjc/s10052-015-3542-2. arXiv: 1503.01060 [hep-ex].

[38] I. Brock et al. "Physics at the Terascale". Physics textbook. Wiley, 2011. ISBN: 978-3-527-41001-9. URL: https://books.google.ch/books/about/Physics_at_the_Terascale.html?id=eWyqcQAACAAJ&redir_esc=y.

[39] M. Klasen et al. "Indirect and direct search for dark matter". In: *Prog. Part. Nucl. Phys.* 85 (2015), pp. 1–32. DOI: 10.1016/j.ppnp.2015.07.001. arXiv: 1507.03800 [hep-ph].

[40] S. Perlmutter et al. "Measurements of Omega and Lambda from 42 high redshift supernovae". In: *Astrophys. J.* 517 (1999), pp. 565–586. DOI: 10.1086/307221. arXiv: astro-ph/9812133 [astro-ph].

[41] The Super-Kamiokande Collaboration. "Evidence for Oscillation of Atmospheric Neutrinos". In: *Phys. Rev. Lett.* 81 (8 1998), pp. 1562–1567. DOI: 10.1103/PhysRevLett.81.1562. URL: http://link.aps.org/doi/10.1103/PhysRevLett.81.1562.

[42] E. K. Akhmedov et al. "Seesaw mechanism and structure of neutrino mass matrix". In: *Phys. Lett.* B478 (2000), pp. 215–223. DOI: 10.1016/S0370-2693(00)00282-3. arXiv: hep-ph/9911364 [hep-ph].

[43] A. Djouadi. "The Anatomy of electro-weak symmetry breaking. II. The Higgs bosons in the minimal supersymmetric model". In: *Phys. Rept.* 459 (2008), pp. 1–241. DOI: 10.1016/j.physrep.2007.10.005. arXiv: hep-ph/0503173 [hep-ph].

[44] G. C. Branco et al. "Theory and phenomenology of two-Higgs-doublet models". In: *Phys. Rept.* 516 (2012), pp. 1–102. DOI: 10.1016/j.physrep.2012.02.002. arXiv: 1106.0034 [hep-ph].

[45] N. Craig et al. "Exclusive Signals of an Extended Higgs Sector". In: *JHEP* 11 (2012), p. 083. DOI: 10.1007/JHEP11(2012)083. arXiv: 1207.4835 [hep-ph].

[46] J. F. Gunion et al. "The CP conserving two Higgs doublet model: The Approach to the decoupling limit". In: *Phys. Rev.* D67 (2003), p. 075019. DOI: 10.1103/PhysRevD.67.075019. arXiv: hep-ph/0207010 [hep-ph].

[47] The ATLAS Collaboration. "Constraints on New Phenomena via Higgs Coupling Measurements with the ATLAS Detector". In: (2014).

[48] N. Craig et al. "Searching for Signs of the Second Higgs Doublet". In: (2013). arXiv: 1305.2424 [hep-ph].

[49] N. Greiner et al. "Interference contributions to gluon initiated heavy Higgs production in the Two-Higgs-Doublet Model". In: *Eur. Phys. J.* C76.3 (2016), p. 118. DOI: 10.1140/epjc/s10052-016-3965-4. arXiv: 1512.07232 [hep-ph].

[50] D. E. De Florian Sabaris et al. "Handbook of LHC Higgs cross sections: 4. Deciphering the nature of the Higgs sector". In: (2016). URL: https://cds.cern.ch/record/2215893.

[51] The CMS Collaboration. "Search for a standard-model-like Higgs boson with a mass in the range 145 to 1000 GeV at the LHC". In: *Eur. Phys. J.* C73 (2013), p. 2469. DOI: 10.1140/epjc/s10052-013-2469-8. arXiv: 1304.0213 [hep-ex].

[52] L. Evans et al. "LHC Machine". In: *JINST* 3 (2008), S08001. DOI: 10.1088/1748-0221/3/08/S08001.

[53] J. Haffner. "The CERN accelerator complex." In: (2013). General Photo. URL: https://cds.cern.ch/record/1621894.

[54] P. Grafstrom et al. "Luminosity determination at proton colliders". In: *Prog.Part.Nucl.Phys.* 81 (2015), pp. 97–148. DOI: 10.1016/j.ppnp.2014.11.002.

[55] R. Bruce et al. "Calculations of safe collimator settings and β^* at the CERN Large Hadron Collider". In: *Phys. Rev. ST Accel. Beams* 18 (6 2015), p. 061001. DOI: 10.1103/PhysRevSTAB.18.061001. URL: http://link.aps.org/doi/10.1103/PhysRevSTAB.18.061001.

[56] M. Giovannozzi. "Optics options for the 2015 LHC run". In: (2014). arXiv: 1410.7055 [physics.acc-ph].

[57] M. Lamont. "Status of the LHC". In: *Journal of Physics: Conference Series* 455.1 (2013), p. 012001. URL: http://stacks.iop.org/1742-6596/455/i=1/a=012001.

[58] W. J. Stirling. "Parton luminosity and cross section plots". Private communication. URL: http://www.hep.ph.ic.ac.uk/~wstirlin/plots/plots.html.

[59] The ATLAS Collaboration. "The ATLAS Experiment at the CERN Large Hadron Collider". In: *Journal of Instrumentation* 3.08 (2008), S08003. URL: http://stacks.iop.org/1748-0221/3/i=08/a=S08003.

[60] The CMS Collaboration. "The CMS experiment at the CERN LHC". In: *Journal of Instrumentation* 3.08 (2008), S08004. URL: http://stacks.iop.org/1748-0221/3/i=08/a=S08004.

[61] The ALICE Collaboration. "The ALICE experiment at the CERN LHC". In: *Journal of Instrumentation* 3.08 (2008), S08002. URL: http://stacks.iop.org/1748-0221/3/i=08/a=S08002.

[62] The LHCb Collaboration. "The LHCb Detector at the LHC". In: *JINST* 3 (2008), S08005. DOI: 10.1088/1748-0221/3/08/S08005.

[63] The TOTEM Collaboration. "The TOTEM experiment at the CERN Large Hadron Collider". In: *JINST* 3 (2008), S08007. DOI: 10.1088/1748-0221/3/08/S08007.

[64] The MoEDAL Collaboration. "Technical Design Report of the MoEDAL Experiment". Tech. rep. CERN-LHCC-2009-006. MoEDAL-TDR-001. Geneva: CERN, 2009. URL: https://cds.cern.ch/record/1181486.

[65] The LHCf Collaboration. "The LHCf detector at the CERN Large Hadron Collider". In: *JINST* 3 (2008), S08006. DOI: 10.1088/1748-0221/3/08/S08006.

[66] J. Pequenao. "Computer generated image of the whole ATLAS detector". 2008. URL: http://cds.cern.ch/record/1095924.

[67] The ATLAS Collaboration. "The ATLAS TRT Barrel Detector". In: *Journal of Instrumentation* 3.02 (2008), P02014. URL: http://stacks.iop.org/1748-0221/3/i=02/a=P02014.

[68] The ATLAS Collaboration. "The ATLAS TRT End-Cap detectors". In: *Journal of Instrumentation* 3.10 (2008), P10003. URL: http://stacks.iop.org/1748-0221/3/i=10/a=P10003.

[69] The ATLAS Collaboration. "Track Reconstruction Performance of the ATLAS Inner Detector at $\sqrt{s} = 13$ TeV". Tech. rep. ATL-PHYS-PUB-2015-018. Geneva: CERN, 2015. URL: http://cds.cern.ch/record/2037683.

[70] The ATLAS Collaboration. "ATLAS liquid argon calorimeter: Technical design report". In: (1996).

[71] The ATLAS Collaboration. "Design, Construction and Installation of the ATLAS Hadronic Barrel Scintillator-Tile Calorimeter". Tech. rep. ATL-TILECAL-PUB-2008-001. ATL-COM-TILECAL-2007-019. Geneva: CERN, 2007. URL: http://cds.cern.ch/record/1071921.

[72] The ATLAS Collaboration. "New Small Wheel Technical Design Report". Tech. rep. CERN-LHCC-2013-006. ATLAS-TDR-020. ATLAS New Small Wheel Technical Design Report. Geneva: CERN, 2013. URL: https://cds.cern.ch/record/1552862.

[73] K. Bachas et al. "Performance of the Muon Spectrometer in the high pseudo-rapidity region $|\eta| > 2.5$". Tech. rep. ATL-MUON-INT-2012-002. Geneva: CERN, 2012. URL: https://cds.cern.ch/record/1442569.

[74] The ATLAS Collaboration. "Muon reconstruction performance of the ATLAS detector in proton–proton collision data at $\sqrt{s} = 13$ TeV". Tech. rep. ATL-COM-PHYS-2015-1564. Geneva: CERN, 2015. URL: https://cds.cern.ch/record/2116829.

[75] Y. Nakahama. "The ATLAS Trigger System: Ready for Run-2". Tech. rep. ATL-DAQ-PROC-2015-006. 8. Geneva: CERN, 2015. URL: https://cds.cern.ch/record/2015211.

[76] M. Hoffmann. "Commissioning and Initial LHC Run-2 operation of the ATLAS minimum bias trigger scintillators". In: *Nuclear Instruments and Methods in Physics Research Section A: Accelerators, Spectrometers, Detectors and Associated Equipment* (2015), pp. –. ISSN: 0168-9002. DOI: http://dx.doi.org/10.1016/j.nima.2015.09.053. URL: http://www.sciencedirect.com/science/article/pii/S0168900215011080.

[77] M. Hoffmann et al. "Determination of Light Yield of an ATLAS Minimum Bias Trigger Scintillator for LHC Run II with Cosmic Radiation". Tech. rep. ATL-TILECAL-INT-2015-003. Geneva: CERN, 2015. URL: https://cds.cern.ch/record/1994354.

[78] The ATLAS Collaboration. "ATLAS Computing: technical design report". Technical Design Report ATLAS. Geneva: CERN, 2005. URL: https://cds.cern.ch/record/837738.

[79] R. Brun et al. "ROOT: An object oriented data analysis framework". In: *Nucl. Instrum. Meth.* A389 (1997), pp. 81–86. DOI: 10.1016/S0168-9002(97)00048-X.

[80] P. J. Laycock et al. "Derived Physics Data Production in ATLAS: Experience with Run 1 and Looking Ahead". In: *Journal of Physics: Conference Series* 513.3 (2014), p. 032052. URL: http://stacks.iop.org/1742-6596/513/i=3/a=032052.

[81] I. Vukotic. "Optimization and performance measurements of ROOT-based data formats in the ATLAS experiment". In: *Journal of Physics: Conference Series* 331.3 (2011), p. 032032. URL: http://stacks.iop.org/1742-6596/331/i=3/a=032032.

[82] A. Buckley et al. "Report of the xAOD design group". Tech. rep. ATL-COM-SOFT-2013-022. Geneva: CERN, 2013. URL: https://cds.cern.ch/record/1598793.

[83] The ATLAS Collaboration. "The ATLAS Simulation Infrastructure". In: *Eur. Phys. J.* C70 (2010), pp. 823–874. DOI: 10.1140/epjc/s10052-010-1429-9. arXiv: 1005.4568 [physics.ins-det].

[84] C Debenedetti. "Concepts for fast large scale Monte Carlo production for the ATLAS experiment". In: (2013). URL: https://cds.cern.ch/record/1605835.

[85] T. Sjostrand et al. "PYTHIA 6.4 Physics and Manual". In: *JHEP* 05 (2006), p. 026. DOI: 10.1088/1126-6708/2006/05/026. arXiv: hep-ph/0603175 [hep-ph].

[86] S. Agostinelli et al. "GEANT4: A Simulation toolkit". In: *Nucl. Instrum. Meth.* A506 (2003), pp. 250–303. DOI: 10.1016/S0168-9002(03)01368-8.

[87] The ATLAS Collaboration. "Search for a standard model Higgs boson in the H → ZZ → $\ell^+\ell^-\nu\bar{\nu}$ decay channel using 4.7 fb^{-1} of $\sqrt{s} = 7$ TeV data with the ATLAS detector". In: *Phys. Lett.* B717 (2012), pp. 29–48. DOI: 10.1016/j.physletb.2012.09.016. arXiv: 1205.6744 [hep-ex].

[88] The ATLAS Collaboration. "Search for a standard model Higgs boson in the mass range 200-600 GeV in the $H \to ZZ \to \ell^+\ell^- q\bar{q}$ decay channel with the ATLAS detector". In: *Phys. Lett.* B717 (2012), pp. 70–88. DOI: 10.1016/j.physletb.2012.09.020. arXiv: 1206.2443 [hep-ex].

[89] The ATLAS Collaboration. "Search for the Standard Model Higgs boson in the decay channel $H \to ZZ^{(*)} \to 4\ell$ with 4.8 fb^{-1} of pp collision data at $\sqrt{s} = 7$ TeV with ATLAS". In: *Phys. Lett.* B710 (2012), pp. 383–402. DOI: 10.1016/j.physletb.2012.03.005. arXiv: 1202.1415 [hep-ex].

[90] The ATLAS Collaboration. "Search for an additional, heavy Higgs boson in the $H \to ZZ$ decay channel at $\sqrt{s} = 8$ TeV in pp collision data with the ATLAS detector". In: *Eur. Phys. J.* C76.1 (2016), p. 45. DOI: 10.1140/epjc/s10052-015-3820-z. arXiv: 1507.05930 [hep-ex].

[91] Z. Marshall et al. "Simulation of Pile-up in the ATLAS Experiment". In: *Journal of Physics: Conference Series* 513.2 (2014), p. 022024. URL: http://stacks.iop.org/1742-6596/513/i=2/a=022024.

[92] The ATLAS Collaboration. "Luminosity Public Results Run-1". URL: https://twiki.cern.ch/twiki/bin/view/AtlasPublic/LuminosityPublicResults#Publications_and_Conference_Resu.

[93] The ATLAS Collaboration. "ATLAS Data Quality Information". 2015. URL: http://twiki.cern.ch/twiki/bin/view/AtlasPublic/RunStatsPublicResults2010.

[94] T. Hryn'ova et al. "Trigger Menu Strategy for Run 2". Tech. rep. ATL-COM-DAQ-2014-054. Geneva: CERN, 2014. URL: https://cds.cern.ch/record/1703730.

[95] The ATLAS Collaboration. "Electron efficiency measurements with the ATLAS detector using the 2012 LHC proton-proton collision data". Tech. rep. ATLAS-CONF-2014-032. Geneva: CERN, 2014. URL: http://cds.cern.ch/record/1706245.

[96] W. Lampl et al. "Calorimeter Clustering Algorithms: Description and Performance". Tech. rep. ATL-LARG-PUB-2008-002. ATL-COM-LARG-2008-003. Geneva: CERN, 2008. URL: https://cds.cern.ch/record/1099735.

[97] J. Alison et al. "Description and Performance of the Electron Likelihood Tool at ATLAS using 2012 LHC Data". Tech. rep. ATL-COM-PHYS-2013-378. Geneva: CERN, 2013. URL: https://cds.cern.ch/record/1537410.

[98] S. Hassani et al. "A muon identification and combined reconstruction procedure for the ATLAS detector at the LHC using the (MUONBOY, STACO, MuTag) reconstruction packages". In: *Nucl. Instrum. Meth.* A572 (2007), pp. 77–79. DOI: 10.1016/j.nima.2006.10.340.

[99] R. Nicolaidou et al. "Muon identification procedure for the ATLAS detector at the LHC using Muonboy reconstruction package and tests of its performance using cosmic rays and single beam data". In: *Journal of Physics: Conference Series* 219.3 (2010), p. 032052. URL: http://stacks.iop.org/1742-6596/219/i=3/a=032052.

[100] The ATLAS Collaboration. ""Measurement of the muon reconstruction performance of the ATLAS detector using 2011 and 2012 LHC proton-proton collision data"". In: *Eur. Phys. J.* C74.11 (2014), p. 3130. DOI: 10.1140/epjc/s10052-014-3130-x. arXiv: 1407.3935 [hep-ex].

[101] M. Cacciari et al. "The Anti-k(t) jet clustering algorithm". In: *JHEP* 04 (2008), p. 063. DOI: 10.1088/1126-6708/2008/04/063. arXiv: 0802.1189 [hep-ph].

[102] The ATLAS Collaboration. "Pile-up subtraction and suppression for jets in ATLAS". Tech. rep. ATLAS-CONF-2013-083. Geneva: CERN, 2013. URL: https://cds.cern.ch/record/1570994.

[103] The ATLAS Collaboration. "ATLAS Jet Cleaning Procedure". 2012. URL: http://twiki.cern.ch/twiki/bin/view/AtlasProtected/HowToCleanJets2012.

[104] B. Lenzi et al. "Developments on the software package for calorimetric isolation and energy loss measurements for muons in ATLAS". Tech. rep. ATL-COM-SOFT-2009-010. Geneva: CERN, 2009. URL: https://cds.cern.ch/record/1198692.

[105] B. Lenzi et al. "TrackInCaloTools: A package for measuring muon energy loss and calorimetric isolation in ATLAS". In: *Journal of Physics: Conference Series* 219.3 (2010), p. 032049. URL: http://stacks.iop.org/1742-6596/219/i=3/a=032049.

[106] S. Alioli et al. "NLO Higgs boson production via gluon fusion matched with shower in POWHEG". In: *JHEP* 04 (2009), p. 002. DOI: 10.1088/1126-6708/2009/04/002. arXiv: 0812.0578 [hep-ph].

[107] P. Nason et al. "NLO Higgs boson production via vector-boson fusion matched with shower in POWHEG". In: *JHEP* 02 (2010), p. 037. DOI: 10.1007/JHEP02(2010)037. arXiv: 0911.5299 [hep-ph].

[108] D. de Florian et al. "Transverse-momentum resummation: Higgs boson production at the Tevatron and the LHC". In: *JHEP* 11 (2011), p. 064. DOI: 10.1007/JHEP11(2011)064. arXiv: 1109.2109 [hep-ph].

[109] P. Golonka et al. "PHOTOS Monte Carlo: A Precision tool for QED corrections in Z and W decays". In: *Eur. Phys. J.* C45 (2006), pp. 97–107. DOI: 10.1140/epjc/s2005-02396-4. arXiv: hep-ph/0506026 [hep-ph].

[110] K. S. Cranmer. "Kernel estimation in high-energy physics". In: *Comput. Phys. Commun.* 136 (2001), pp. 198–207. DOI: 10.1016/S0010-4655(00)00243-5. arXiv: hep-ex/0011057 [hep-ex].

[111] W. Verkerke et al. "The RooFit toolkit for data modeling". In: *eConf* C0303241 (2003). [,186(2003)], MOLT007. arXiv: physics/0306116 [physics].

[112] M. Baak et al. "Interpolation between multi-dimensional histograms using a new non-linear moment morphing method". In: *Nucl. Instrum. Meth.* A771 (2015), pp. 39–48. DOI: 10.1016/j.nima.2014.10.033. arXiv: 1410.7388 [physics.data-an].

[113] H.-L. Lai et al. "New parton distributions for collider physics". In: *Phys. Rev.* D82 (2010), p. 074024. DOI: 10.1103/PhysRevD.82.074024. arXiv: 1007.2241 [hep-ph].

[114] F. Cascioli et al. "ZZ production at hadron colliders in NNLO QCD". In: *Phys. Lett.* B735 (2014), pp. 311–313. DOI: 10.1016/j.physletb.2014.06.056. arXiv: 1405.2219 [hep-ph].

[115] A. Bierweiler et al. "Vector-boson pair production at the LHC to $O(\alpha^3)$ accuracy". In: *JHEP* 12 (2013), p. 071. DOI: 10.1007/JHEP12(2013)071. arXiv: 1305.5402 [hep-ph].

[116] J. Baglio et al. "Massive gauge boson pair production at the LHC: a next-to-leading order story". In: *Phys. Rev.* D88 (2013), p. 113005. DOI: 10.1103/PhysRevD.88.113005. arXiv: 1307.4331.

[117] S. Gieseke et al. "Vector-boson pair production and electroweak corrections in HERWIG++". In: *Eur. Phys. J.* C74.8 (2014), p. 2988. DOI: 10.1140/epjc/s10052-014-2988-y. arXiv: 1401.3964 [hep-ph].

[118] J. Meyer et al. "Theoretical uncertainties and inputs occurring in$H \to ZZ$ analyses". Tech. rep. ATL-COM-PHYS-2015-1278. Authors: The HZZ group. Geneva: CERN, 2015. URL: https://cds.cern.ch/record/2058253.

[119] J. M. Campbell et al. "Bounding the Higgs width at the LHC using full analytic results for $gg- > e^-e^+\mu^-\mu^+$". In: *JHEP* 04 (2014), p. 060. DOI: 10.1007/JHEP04(2014)060. arXiv: 1311.3589 [hep-ph].

[120] M. Bonvini et al. "Signal-background interference effects for $gg \rightarrow H \rightarrow W^+W^-$ beyond leading order". In: *Phys. Rev.* D88.3 (2013), p. 034032. DOI: 10.1103/PhysRevD.88.034032. arXiv: 1304.3053 [hep-ph].

[121] M. L. Mangano et al. "ALPGEN, a generator for hard multiparton processes in hadronic collisions". In: *JHEP* 07 (2003), p. 001. DOI: 10.1088/1126-6708/2003/07/001. arXiv: hep-ph/0206293 [hep-ph].

[122] S. J. et al. "The tau decay library TAUOLA, version 2.4". In: *Comp. Phys. Comm.* 76 (1993), p. 361.

[123] P. Golonka et al. "The Tauola photos F environment for the TAUOLA and PHOTOS packages: Release. 2." In: *Comput. Phys. Commun.* 174 (2006), pp. 818–835. DOI: 10.1016/j.cpc.2005.12.018. arXiv: hep-ph/0312240 [hep-ph].

[124] S. H. Abidi et al. "Event selection and background estimation for the measurement of the properties of the Higgs particle in the four lepton decay channel with the ATLAS detector". Tech. rep. ATL-COM-PHYS-2013-1599. Geneva: CERN, 2013. URL: https://cds.cern.ch/record/1634096.

[125] The ATLAS Collaboration. "Jet energy measurement and its systematic uncertainty in proton-proton collisions at $\sqrt{s} = 7$ TeV with the ATLAS detector". In: *Eur. Phys. J.* C75 (2015), p. 17. DOI: 10.1140/epjc/s10052-014-3190-y. arXiv: 1406.0076 [hep-ex].

[126] S. H. Abidi et al. "Supporting documentation for the indirect Higgs width measurement in the high mass $gg \rightarrow H \rightarrow ZZ$ and $gg \rightarrow H \rightarrow WW$ channels". Tech. rep. ATL-COM-PHYS-2014-408. Geneva: CERN, 2014. URL: https://cds.cern.ch/record/1699634.

[127] P. Calpin et al. "$H \rightarrow WW \rightarrow l\nu l\nu$ high-mass analysis with 20 fb^{-1} of data collected with the ATLAS detector at $\sqrt{s} = 8$ TeV". Tech. rep. ATL-COM-PHYS-2014-193. Geneva: CERN, 2014. URL: https://cds.cern.ch/record/1667586.

[128] C. D. Burgard et al. "Analysis of $H \rightarrow WW \rightarrow \ell\nu\ell\nu$ ggF and VBF production modes with 20 fb^{-1} and 5 fb^{-1} of data collected with the ATLAS detector at $\sqrt{s} = 8$ and 7 TeV". Tech. rep. ATL-COM-PHYS-2014-466. Geneva: CERN, 2014. URL: https://cds.cern.ch/record/1702035.

[129] A. L. Read. "Presentation of search results: The CL(s) technique". In: *J. Phys.* G28 (2002). [,11(2002)], pp. 2693–2704. DOI: 10.1088/0954-3899/28/10/313.

[130] G. Cowan et al. “Asymptotic formulae for likelihood-based tests of new physics”. In: *Eur. Phys. J.* C71 (2011). [Erratum: Eur. Phys. J.C73,2501(2013)], p. 1554. DOI: 10.1140/epjc/s10052-011-1554-0, 10.1140/epjc/s10052-013-2501-z. arXiv: 1007.1727 [physics.data-an].

[131] C. Bini. ”Data analysis in Experimental Elementary Particle Physics”. Lecture notes. 2013-2014. URL: http://www.roma1.infn.it/people/bini/StatEPP.pdf.

[132] The CMS Collaboration. “Constraints on the Higgs boson width from off-shell production and decay to Z-boson pairs”. In: *Phys. Lett.* B736 (2014), pp. 64–85. DOI: 10.1016/j.physletb.2014.06.077. arXiv: 1405.3455 [hep-ex].

[133] H. Okawa et al. ”Search for a Higgs boson in the $H \to ZZ \to \ell\ell\nu\nu$ Channel”. Tech. rep. ATL-COM-PHYS-2014-270. Geneva: CERN, 2014. URL: https://cds.cern.ch/record/1693161.

[134] The ATLAS Collaboration. ”Performance of missing transverse momentum reconstruction for the ATLAS detector in the first proton-proton collisions at $\sqrt{s}$= 13 TeV”. Tech. rep. ATL-PHYS-PUB-2015-027. Geneva: CERN, 2015. URL: https://cds.cern.ch/record/2037904.

[135] The ATLAS Collaboration. Search for a heavy Higgs boson in the mass range 200-1000 GeV in the $H \to ZZ \to \ell\ell qq$ channel”. Tech. rep. ATL-COM-PHYS-2014-269. Geneva: CERN, 2014. URL: https://cds.cern.ch/record/1693159.

[136] The ATLAS Collaboration. ”Expected performance of the ATLAS b-tagging algorithms in Run-2”. Tech. rep. ATL-PHYS-PUB-2015-022. Geneva: CERN, 2015. URL: https://cds.cern.ch/record/2037697.

[137] The ATLAS Collaboration. “Calibration of the performance of b-tagging for c and light-flavour jets in the 2012 ATLAS data”. In: ATLAS-CONF-2014-046 (2014).

[138] C. Wang et al. ”Search for a high mass Higgs boson in the $H \to ZZ \to \nu\nu qq$ decay channel with the ATLAS Detector”. Tech. rep. ATL-COM-PHYS-2014-262. Geneva: CERN, 2014. URL: https://cds.cern.ch/record/1692942.

[139] The ATLAS Collaboration. ”Likelihood Combination Tool”. 2015. URL: https://twiki.cern.ch/twiki/bin/viewauth/AtlasProtected/LikelihoodCombinationTool.

[140] F. Ahmadov et al. ”Supporting Document for the Search for the bb decay of the Standard Model Higgs boson in associated (W/Z)H production with the ATLAS detector”. Tech. rep. ATL-COM-PHYS-2014-051. Geneva: CERN, 2014. URL: https://cds.cern.ch/record/1645654.

[141] The ATLAS Collaboration. "Luminosity Public Results Run-2". URL: https://twiki.cern.ch/twiki/bin/view/AtlasPublic/LuminosityPublicResultsRun2.

[142] D. J. Lange. "The EvtGen particle decay simulation package". In: *Nuclear Instruments and Methods in Physics Research Section A: Accelerators, Spectrometers, Detectors and Associated Equipment* 462.1–2 (2001). BEAUTY2000, Proceedings of the 7th Int. Conf. on B-Physics at Hadron Machines, pp. 152 –155. ISSN: 0168-9002. DOI: http://dx.doi.org/10.1016/S0168-9002(01)00089-4. URL: http://www.sciencedirect.com/science/article/pii/S0168900201000894.

[143] S. H. Abidi et al. "Common supporting note for the $H \to 4\ell$ channel: Event selection, background estimates, performance studies, etc.". Tech. rep. ATL-COM-PHYS-2015-1277. Geneva: CERN, 2015. URL: https://cds.cern.ch/record/2058249.

[144] G. Artoni et al. "Support Note for 2015 Muon Combined Performance Paper". Tech. rep. ATL-COM-PHYS-2015-1149. Support note for ATL-COM-PHYS-2015-1564. Geneva: CERN, 2015. URL: https://cds.cern.ch/record/2052558.

[145] The ATLAS Collaboration. ""Muon reconstruction performance of the ATLAS detector in proton–proton collision data at $\sqrt{s} = 13$ TeV"". In: (2016). arXiv: 1603.05598 [hep-ex].

[146] The CMS Collaboration. "Search for a Higgs Boson in the Mass Range from 145 to 1000 GeV Decaying to a Pair of W or Z Bosons". In: *JHEP* 10 (2015), p. 144. DOI: 10.1007/JHEP10(2015)144. arXiv: 1504.00936 [hep-ex].

[147] The ATLAS Collaboration. "Search for a high-mass Higgs boson decaying to a W boson pair in pp collisions at $\sqrt{s} = 8$ TeV with the ATLAS detector". In: *JHEP* 01 (2016), p. 032. DOI: 10.1007/JHEP01(2016)032. arXiv: 1509.00389 [hep-ex].

[148] B. Dumont et al. "Addendum to "Constraints on and future prospects for Two-Higgs-Doublet Models in light of the LHC Higgs signal"". In: (2014). arXiv: 1409.4088 [hep-ph].

[149] D. Berge et al. "Luminosity Measurement using the ATLAS Minimum Bias Trigger Scintillator System". Tech. rep. ATL-LUM-INT-2010-004. Geneva: CERN, 2010. URL: https://cds.cern.ch/record/1256521.

[150] A. Angerami. "Jet Quenching in Relativistic Heavy Ion Collisions at the LHC". PhD thesis. Columbia U., 2012. arXiv: 1208.5043 [nucl-ex]. URL: http://inspirehep.net/record/1181772/files/arXiv:1208.5043.pdf.

[151] The ATLAS Collaboration. "Measurement of the Inelastic Proton-Proton Cross-Section at $\sqrt{s} = 7$ TeV with the ATLAS Detector". In: *Nature Commun.* 2 (2011), p. 463. DOI: 10.1038/ncomms1472. arXiv: 1104.0326 [hep-ex].

[152] The ATLAS Collaboration. "Measurement of the Inelastic Proton-Proton Cross Section at $\sqrt{s} = 13$ TeV with the ATLAS Detector at the LHC". Tech. rep. ATLAS-CONF-2015-038. Geneva: CERN, 2015. URL: https://cds.cern.ch/record/2045064.

[153] M. Leyton. "Minimum Bias and Underlying Event Studies at ATLAS and CMS". In: *QCD and high energy interactions. Proceedings, 44th Rencontres de Moriond, La Thuile, Italy, March 14-21, 2009*. 2009, pp. 281–285. arXiv: 0905.3684 [hep-ex]. URL: http://inspirehep.net/record/821251/files/arXiv:0905.3684.pdf.

[154] A. Sidoti. "Minimum Bias Trigger Scintillators in ATLAS Run II". Tech. rep. ATL-DAQ-PROC-2014-010. 10. Geneva: CERN, 2014. URL: https://cds.cern.ch/record/1708408.

[155] W. R. Leo. "Techniques for Nuclear and Particle Physics Experiments". Springer, 1987.

[156] L. KURARAY CO. Plastic Scintillating Fibers (Materials and Structures). URL: http://kuraraypsf.jp/psf/.

[157] The ATLAS Collaboration. "Minimum Bias Trigger Public Results". URL: https://twiki.cern.ch/twiki/bin/view/AtlasPublic/MinBiasTriggerPublicResults.

[158] M. Hoffmann et al. "Probing compositeness with Higgs Boson decays at the LHC". In: *The European Physical Journal C* 74.11 (2014), pp. 1–7. ISSN: 1434-6052. DOI: 10.1140/epjc/s10052-014-3181-z. URL: http://dx.doi.org/10.1140/epjc/s10052-014-3181-z.

université PARIS-SACLAY | ÉCOLE DOCTORALE PHENIICS

Titre: Recherche d'un boson de Higgs additionnel de plus haute masse via sa désintégration en une paire de bosons de jauge Z avec le détecteur ATLAS au LHC

Mots clés: LHC, ATLAS, Higgs, BSM, Minimum Bias Trigger Scintillators

Le sujet principal de cette thèse porte sur la recherche d'un boson de Higgs additionnel de plus haute masse à travers sa désintégration en une paire de bosons de jauge Z ($H \rightarrow ZZ^{(*)}$) en utilisant les données enregistrées avec l'expérience ATLAS auprès du Grand Collisionneur de Hadrons (LHC). Quatre analyses distinctes sont présentées en fonction du mode de désintegration du boson Z soit une paire de leptons chargés (électrons ou muons), soit une paire de neutrinos soit une paire de quarks; ces analyses sont appelés $ZZ \rightarrow 4l$, $2l2\nu$, $2l2q$ et $2\nu2q$. L'étude utilise 20.3 fb^{-1} de données de collisions proton-proton enregistrées au cours de la première phase du LHC (Run-1) à une énergie dans le centre de masse de 8 TeV. La stratégie de recherche segmente les données en supposant que les mécanismes de production de bosons de Higgs additionnel sont les mêmes que dans le Modèle Standard (SM), et modélise le signal avec une largeur qui est faible par rapport à la résolution de la masse invariante.

La region de masse du boson de Higgs considéré étend de 140 GeV jusqu'à 1 TeV. Aucun nouveau boson de Higgs n'a été trouvé. La combinaison de resultats de quatre modes de désintégration donne des limites supérieures sur la section efficace σ de ce boson de Higgs additionel ($\sigma \times H \rightarrow ZZ^{(*)}$) qui étend de 359 fb à m_H = 200 GeV à 11 fb à m_H = 1TeV. Les résultats sont également interprétés dans le contexte des modèles au-delà du SM, à savoir les modèles à deux doublets.

L'analyse $H \rightarrow ZZ^{(*)} \rightarrow 4l$ est egalement réalisée au cours de la deuxième phase du LHC (Run-2) en utilisant 3.2 fb^{-1} de données de collisions de proton-proton enregistrées en 2015 à une énergie à une énergie dans le centre de masse de 13 TeV. Aucun excès significatif d'événements sur la prédiction du MS est trouvé. Les limites supérieures sur la section efficace ($\sigma \times H \rightarrow ZZ^{(*)} \rightarrow 4l$) sont de 4.5 fb à m_H = 200 GeV et 1 fb à m_H = 1 TeV.

La dernière partie de la thèse porte sur la caractérisation des détecteurs à scintillation d'ATLAS pour le déclenchement d'un biais minimal dans la région avant (le Minimum Bias Trigger Scintillators (MBTS)) en utilisant les rayons cosmiques. En raison de la dégradation des matériaux provoquée par des dommages dus à l' irradiation dans la première phase de fonctionnement du LHC, les MBTS devaient être remplacés lors de l'arrêt du LHC qui a eu lieu en 2014. Avant leur installation dans ATLAS, ces détecteurs ont été caractérisés en laboratoire en utilisant les rayons cosmiques.

Title: The Search for a Heavy Higgs Boson in the H→ ZZ Decay Channels with the ATLAS Detector

Keywords: LHC, ATLAS, Higgs, BSM, Minimum Bias Trigger Scintillators

The main subject of this thesis is the search for an additional heavy Higgs boson through its decay into a pair of Z bosons ($H \rightarrow ZZ^{(*)}$) using data recorded with the ATLAS experiment installed at the Large Hadron Collider (LHC). Four distinct analyses are presented, which are distinguished by the decay mode of the Z boson into either a pair of charged leptons (electrons or muons), into a pair of neutrinos or into a pair of quarks, denoted according to final-state, i.e. as $4l$, $2l2\nu$, $2l2q$ and $2\nu2q$. The study is performed using 20.3 fb^{-1} of proton-proton collision data recorded during the first phase of LHC operation (Run-1) at centre-of-mass energy of $\sqrt{s}$ = 8 TeV. A search strategy is employed which segments the data according to the Higgs boson production mechanism, assuming that these are the same as in the Standard Model (SM). Furthermore, the signal is modelled with a width that is small compared to the experimental mass resolution. The Higgs boson mass range considered extends up to 1 TeV for all four decay modes and down to as low as 140 GeV, depending on the decay mode. No significant excess of events over the Standard Model prediction is found. A simultaneous fit to the four decay modes yields upper limits on the heavy Higgs boson production cross-section times $H \rightarrow ZZ$ branching ratio ranging from 359 fb at m_H = 200 GeV to 11 fb at m_H = 1 TeV for the gluon-fusion production mechanism, and from 214 fb at m_H = 200 GeV to 13 fb at m_H = 1 TeV for the vector-boson fusion production mechanism. The results from these four searches are also interpreted in the context of models beyond the SM, namely the Type-1 and Type-2 2 Higgs Doublet Model.

The heavy Higgs boson search is also performed with the $H \rightarrow ZZ^{(*)} \rightarrow 4l$ decay mode alone using 3.2 fb^{-1} of proton-proton collision data recorded during the second phase of LHC operation (Run-2) at an increased centre-of- mass energy of $\sqrt{s}$ = 13 TeV. No significant excess of events over the Standard Model prediction is found. Upper limits are set on the heavy Higgs boson production cross-section times $H \rightarrow ZZ^{(*)} \rightarrow 4l$ branching ratio of 4.5 fb at m_H = 200 GeV and 1 fb at m_H = 1 TeV.

Lastly, a project of a more technical character is presented. In this study, the scintillation detectors employed by ATLAS for triggering with minimal bias in the forward region, the Minimum Bias Trigger Scintillators (MBTS), are characterised. Due to material degradation caused by radiation damage in the early phases of LHC operation, the MBTS had to be replaced during the LHC shutdown taking place in 2014. Before installation in ATLAS, these detectors were characterised in appropriate laboratory facilities using cosmic radiation.

Université Paris-Saclay
Espace Technologique / Immeuble Discovery
Route de l'Orme aux Merisiers RD 128 / 91190 Saint-Aubin, France